



UNIVERSITÉ D'ORLÉANS



**ÉCOLE DOCTORALE Santé, Sciences Biologiques et Chimie du Vivant
(SSBCV)**

Centre de Biophysique Moléculaire

THÈSE présentée par :

Fatima OUKHATAR

soutenue le : **21 Décembre 2012**

pour obtenir le grade de : **Docteur de l'université d'Orléans**

Discipline/ Spécialité : Chimie

**Design, Synthesis and Characterization of Neurotransmitter
Responsive Probes for Magnetic Resonance and Optical
Imaging**

THÈSE dirigée par :

Dr. Eva JAKAB TOTH
Prof. Nikos LOGOTHETIS

Directrice de Recherche CNRS, Orléans
Professeur, Max Planck Institute for Biological
Cybernetics, Tübingen, Allemagne

RAPPORTEURS :

Prof. Carlos GERALDES
Prof. Lothar HELM

Professeur, Université de Coimbra, Portugal
Professeur, Ecole Polytechnique Fédérale de
Lausanne, Suisse

JURY :

Prof. Carlos GERALDES
Prof. Lothar HELM

Professeur, Université de Coimbra, Portugal
Professeur, Ecole Polytechnique Fédérale de
Lausanne, Suisse

Dr. Philippe DURAND
Prof. Stéphane PETOUD
Dr. Goran Angelovski

Chargé de Recherche CNRS, Gif/Yvette
Directeur de Recherche INSERM, Orléans
Dr. Privatdozent, Max Planck Institute for Biological
Cybernetics, Tübingen, Allemagne

Dr. Éva JAKAB TOTH

Directrice de Recherche CNRS, Orléans

Acknowledgments

Undertaking this PhD project has been a truly life-changing experience for me and it would not have been possible to accomplish in due time without the help and guidance that I received from many people.

Foremost, I would like to express my deepest gratitude to my principal supervisor Dr. Éva Jakab Tóth, for giving me the chance to work on this project and for her supervision and guidance. I was most privileged to have her as my thesis advisor. Thanks for help and continuous support through the difficult and short time of writing this manuscript. I thank my second supervisor Prof. Nikos Logothetis for the opportunity of working in his esteemed department and for providing scientific support and excellent research facilities that have been of great importance to me in completing this thesis.

I would also like to thank Dr. Goran Angelovski for his assistance and guidance in throughout the course of this thesis. Thanks to all other chemists of our MPI chemistry group: Dr. Ilgar Mamedov, Karolina Jankowska, Dr. Pascal Kadjné, Dr. Matteo Placidi, Sandip Vibhute and Serhat Gündüz for your support and enjoyable working conditions. Additionally, I would also like to thank all members of our group in CBM, namely André Martins, Agnès Pallier, Dr. Jean-François Morfin, Dr. Célia Bonnet and Dr. Sara Lacerda. I am indebted to you for your friendly support and assistance during the experiments and deeply appreciate your optimism, humor and joyful atmosphere during my stays in Orleans. Special thanks to Célia and Sara for their generous time in reviewing my thesis chapters and giving valuable comments and suggestions.

I would further like to extend my gratitude to the people who made the excellent experimental contributions described in this manuscript. In particular, I acknowledge Dr. Svetlanna Eliseeva for performing the near-infrared measurements described in chapter 3, Dr. Hervé Meudal for doing the NMR experiments on the ternary complex YL5, and Dr. Carlos Platas-Iglesias (from the University of Coruña) for the computational analysis.

I would like to express my special appreciation and thanks to the members of the thesis jury: Dr. Philippe DURAND, Prof. Stéphane PETOUD, Prof. Carlos GERALDES and Prof. Lothar HELM for agreeing to be part of my committee and for the time they invested to read and evaluate this work.

I also thank all those who could not find a separate name, but have helped in one way or another to complete my project work.

Abbreviations

A/\hbar	hyperfine or scalar coupling constant
Ar	aromatique
Bn	benzyl
^t Bu or tert-Bu	tert-Butyl
dd	doublet of doublet
LiAlH ₄	Lithium Aluminium Hydride
Cbz	chlorobenzoformate
CDCl ₃	chloroform deuterated
CH ₂ Cl ₂	dichloromethane
CH ₃ CN	acetonitrile
C _L	concentration of ligand
DCC	N,N'-dicyclohexylcarbodiimide
D_{GdH}	diffusion coefficient
DIBAL-H	diisobutylaluminium hydride
DIPEA	diisopropylethylamine
DMF	N,N-Dimethylformamide
D ₂ O	deuteriumoxid
E_R	activation energy for the rotational correlation time
ESI-MS	electron Spray Ionization-Mass Spectrometry
Et	ethyl
E_{DGdH}	activation energy for the diffusion
Et ₂ O	diethyl ether
EtOAc	ethyl acetate
E_v	activation energy for the modulation of the ZFS
g	gram (s)
GABA	gamma-amino butyric acid
H ₂	hydrogen
HBTU	O-Benzotriazole-N,N,N',N'-tetramethyl-uronium-hexafluoro-phosphate
DO2A	1,4,7,10-tetraazacyclododecane-N,N'-bisacetatic acid
DOTA	1,4,7,10-tetraazacyclododecane-N,N',N'',N'''-tetraacetatic acid
HCl	hydrochloric acid
HCOOH	formic acid
HOBt	Hydroxybenzotriazole
HPLC	High Performance Liquid Chromatography
HRMS-ESI	Electron Spray Ionization-High Resolution Mass Spectrometry
HSQC	Heteronuclear Single Quantum Coherence
Hz	hertz
J	coupling constant (NMR)
K ₂ CO ₃	potassium carbonate
k_{ex}	water exchange rate
λ	lambda
LiOH	Lithium hydroxide

Ln	lanthanide
Me	methyl
MeOH	methanol
MeOD	methanol-deuterated
mg	milligram
mL	milliliter (s)
mmol	millimole
mM	millimole.L ⁻¹
MRI	Magnetic Resonance Imaging
Na ₂ CO ₃	sodium carbonate
NaHCO ₃	sodium bicarbonate
NaOH	sodium hydroxide
Na ₂ SO ₄	sodium sulphate
NEt ₃	triethylamine
p-	para-
NMe ₄ Cl	Tetramethylammonium chloride
NMe ₄ OH	Tetramethylammonium hydroxide
NMM	N-methylmorpholine
NMR	Nuclear Magnetic Resonance
NMRD	Nuclear Magnetic Resonance Dispersion
Pd-C	palladium carbon
Ph	phenyl
Ra-Ni	Raney nickel
R_1	longitudinal relaxation rate = $1/T_1$
r_1	longitudinal proton relaxivity
r_{GdO}	mean Gd(III) coordinated water oxygen distance
s	singlet (NMR)
THF	tetrahydrofuran
t	Triplet (NMR)
T_{1e}	(electronic) longitudinal relaxation time
T_{2e}	(electronic) transverse relaxation time
q	quartet
q	hydration number
quint	quintet
UV	ultraviolet
UV-vis	ultraviolet-visible spectroscopy
ΔH^\ddagger	activation enthalpy for the water exchange
ΔS^\ddagger	activation entropy
τ_m	mean residence time of a bound water molecule

Table of contents

CHAPTER 1. INTRODUCTION: LANTHANIDE BASED PROBES FOR MOLECULAR IMAGING .. 10

1.1. MAGNETIC RESONANCE IMAGING	14
1.1.1. Basic principles of MRI	14
1.1.1.1. Relaxation times	15
1.1.1.2. Contrast and constructing an image in MRI.....	17
1.1.2. Advantages over non MR techniques	19
1.1.3. MRI contrast agents	21
1.1.3.1. Gadolinium chelates as T_1 -contrast agents.....	21
1.1.3.2. Mechanism of action; solvation spheres	24
1.1.4. Contribution of molecular parameters to the inner-sphere relaxivity	25
1.2. TIME-RESOLVED LUMINESCENCE	28
1.2.1. Lanthanides and their photophysical characteristics.....	29
1.2.2. Sensitization of lanthanide luminescence (antenna effect).....	33
1.2.3. Quenching process and hydration state (q)	35
1.2.4. Quantum yield	37
1.2.5. Long-wavelength sensitization and near-infrared emission	38
1.3. LANTHANIDE BASED PROBES FOR MOLECULAR IMAGING.....	40
1.3.1. Classes of contrast agents	40
1.3.1.1. Targeted contrast agents	41
1.3.1.2. Smart contrast agents (SCAs)	41
a) pH-activated contrast agents.	42
b) Enzyme-activated contrast agents.....	43
c) Metal ion responsive contrast agents	45
1.4. FUNCTIONAL MOLECULAR IMAGING OF BRAIN ACTIVITY	48
1.4.1. Introduction.....	48
1.4.2. Potential targets in neuroimaging	50
1.5. OBJECTIVES OF THE THESIS.....	51
1.6. REFERENCES	53

CHAPTER 2. LANTHANIDE-BASED SMART CONTRAST AGENTS FOR SENSING

NEUROTRANSMITTERS	62
2.1. INTRODUCTION	64
2.1.1. Detection of neurotransmitters	66
2.1.1.1. Voltammetry.....	66
2.1.1.2. Microdialysis.....	66
2.1.2. MRI contrast agents sensitive to dopamine.....	68
2.2. DESIGN OF Ln^{3+}-BASED COMPLEXES RESPONSIVE TO NEUROTRANSMITTERS	69

2.3 SYNTHESIS OF THE COMPLEXES.....	73
2.3.1 Synthesis of ligands L ⁵⁻⁶	74
2.3.2 Synthesis of ligand L ⁷	77
2.3.3.Synthesis of ligand L ¹⁰	78
2.3.4.Synthesis of ligand L ¹¹	78
2.4. RESULTS AND DISCUSSION	79
2.4.1.pH-potentiometry	80
2.4.2.Luminescence studies: assessment of the number of coordinated water molecules for LnL ⁵ and LnL ⁶ complexes	82
2.4.3.UV-Vis measurements	82
2.4.4. ¹ H NMRD and ¹⁷ O NMR measurements of the Gd ³⁺ complexes	83
2.4.5.Binding assays.....	90
2.4.5.1. Relaxometric titrations.....	90
2.4.5.2. Luminescence studies	94
2.4.5.3. ¹ H & 2D NMR experiments to assess the interaction of -NH ₃ ⁺ with the crown ether	95
2.4.5.4. Computational study of the ternary complex YL ⁵ -Gly	98
2.5. CONCLUSION:	100
2.6. EXPERIMENTAL PROCEDURES AND MATERIALS.....	102
2.7. REFERENCES	122
CHAPTER 3. ATTEMPTS TO IMPROVE THE LIGAND DESIGN FOR NEUROTRANSMITTERS	
DETECTION	126
3.1. DESIGN OF THE COMPLEXES	128
3.2. SYNTHESIS OF THE COMPLEXES.....	132
3.2.1.Synthesis of Ligand L ⁸	132
3.2.2.Synthesis of ligand L ⁹	133
3.3. RESULTS AND DISCUSSION	136
3.3.1.Photophysical characterization	136
3.3.1.1. Luminescence emission of EuL ⁸	136
3.3.1.2. Near-infrared emission of YbL ⁸ and NdL ⁸	137
3.3.2. ¹⁷ O NMR measurements	140
3.3.3.Binding Assays	144
3.3.3.1. Relaxometric titrations of GdL ⁸ and GdL ⁹	144
3.3.3.2. Luminescence emission of EuL ⁸	147
3.3.3.3. Near-infrared emission of NdL ⁸ and YbL ⁸	149
3.4. CONCLUSIONS.....	163
3.5. EXPERIMENTAL PROCEDURES AND MATERIALS.....	165

3.6. REFERENCES	181
CHAPTER 4. ATTEMPTS TO SYNTHESIZE L¹⁻⁴	184
4.1 ATTEMPTS TO SYNTHESIZE L¹⁻²	186
4.1.1 Coupling via amid-bond formation	186
4.1.2. Coupling via alkylation.....	189
4.1.3. Coupling via reductive amination.....	190
a) Preparation of aldehyde by deprotection of acetal.....	192
b) Preparation of aldehyde by reduction of nitrile	193
c) Preparation of aldehyde by oxidation of alkene.....	194
d) Preparation of aldehyde by Swern oxidation	195
4.2. ATTEMPTS TO SYNTHESIZE LIGANDS L³⁻⁴	195
4.2.1. Coupling <i>via</i> alkylation	195
4.2.2. Coupling via reductive amination.....	196
a) Preparation of aldehyde by deprotection of acetal.....	197
b) Preparation of aldehyde by reduction of Weinreb amide:.....	197
SUMMARY AND CONCLUSIONS	199
APPENDIX	202
A.1. Most common neurotransmitters, their functions and the disorders associated with their dysfunctions.....	204
A.2. Reported concentration of some neurotransmitters.....	205
A.3. ¹ H & ¹³ C NMR spectra of L ⁵⁻¹¹ and ¹ H NMR spectra of EuL ⁵⁻⁸	206
A.4. Equations used for the fits of ¹⁷ ONMR and ¹ HNMRD Data.....	215
A.5. SPECFIT data (absorption titrations of YbL ⁸).....	220
RESUME FRANÇAIS.....	226

1

Introduction: Lanthanide Based Probes for Molecular Imaging

CHAPTER 1. INTRODUCTION: LANTHANIDE BASED PROBES FOR MOLECULAR IMAGING .. 10

1.1. MAGNETIC RESONANCE IMAGING	14
1.1.1. Basic principles of MRI.....	14
1.1.1.1. Relaxation times.....	15
1.1.1.2. Contrast and constructing an image in MRI.....	17
1.1.2. Advantages over non MR techniques.....	19
1.1.3. MRI contrast agents.....	21
1.1.3.1. Gadolinium chelates as T ₁ -contrast agents.....	21
1.1.3.2. Mechanism of action; solvation spheres	24
1.1.4. Contribution of molecular parameters to the inner-sphere relaxivity	25
1.2. TIME-RESOLVED LUMINESCENCE	28
1.2.1. Lanthanides and their photophysical characteristics	29
1.2.2. Sensitization of lanthanide luminescence (antenna effect).....	33
1.2.3. Quenching process and hydration state (<i>q</i>)	35
1.2.4. Quantum yield	37
1.2.5. Long-wavelength sensitization and near-infrared emission	38
1.3. LANTHANIDE BASED PROBES FOR MOLECULAR IMAGING	40
1.3.1. Classes of contrast agents	40
1.3.1.1. Targeted contrast agents	41
1.3.1.2. Smart contrast agents (SCAs).....	41
<i>a</i>) pH-activated contrast agents.....	42
<i>b</i>) Enzyme-activated contrast agents	43
<i>c</i>) Metal ion responsive contrast agents.....	45
1.4. FUNCTIONAL MOLECULAR IMAGING OF BRAIN ACTIVITY	48
1.4.1. Introduction	48
1.4.2. Potentials targets in neuroimaging	50
1.5. OBJECTIVES OF THE THESIS.....	51
1.6. REFERENCES	53

1. Lanthanide based probes for molecular Imaging

In medicine there is an increasing requirement to provide more precise and detailed images of specific molecular pathways and biomarkers *in vivo*, particularly those that are key targets in disease processes which will contribute to an increasing understanding of the molecular basis of diseases. The current assessment of disease is mostly based on anatomic or physiologic changes that are a late manifestation of the molecular changes that truly underline disease. The need for direct and in real time imaging of these molecular changes has made molecular imaging to be a rapidly growing discipline which offers another level of knowledge beyond anatomy. The term Molecular imaging has been applied to many modalities and research areas [1, 2] which all seek the same purposes: better understanding of mechanistic pathways, efficient and early diagnosis of the disease, in addition to earlier and direct molecular assessment of treatment effects. Among these modalities, MRI has emerged as the most promising method, due particularly to its noninvasive nature and outstanding high spatial resolution.

1.1. Magnetic Resonance Imaging

Over the past few decades magnetic resonance imaging has been refined into a widely used technique in clinical diagnostics and biomedical research. A method known as magnetic particle imaging, used in chemistry, has now been devised which offers an inner view of the human body. The high spatial resolution and the undisputed capacity of differentiating soft tissues have highly contributed to the widespread use of this imaging modality. MRI allows realistic three dimensional imaging of biological media, where the signal is based upon the relaxation times of water protons. MRI is primarily used for producing anatomical images, but it also gives information on the physicochemical state of tissues, flow, diffusion, motion and, more recently, molecular targets.

1.1.1. Basic principles of MRI

MRI provides information that differs from other imaging modalities. Although the word “nuclear has disappeared from the name (primarily due to negative connotation), the basic

principles of MRI are the same as those of Nuclear Magnetic Resonance (NMR) [3]. We derive images from the magnetic resonance properties of nuclear particles (nuclei) that contain an odd number of protons and/or neutrons and have a characteristic motion or *precession*. Thus, in principle it is possible to obtain MR images with many different nuclei, as is the case in the human body, in decreasing order of abundance, with hydrogen (^1H), Fluor (^{19}F), Sodium (^{23}Na), and Phosphorus (^{31}P). However, because the body is mainly made up of water, a large proportion of which is hydrogen, hydrogen is the major species that is MR sensitive and therefore the MRI technique refers essentially to proton imaging. The use of other nuclei in MRI is discussed in chapter one of *The Chemistry of Contrast Agents in Medical Magnetic Resonance Imaging* edited by Merbach and Toth [4].

1.1.1.1. Relaxation times

Because proton nuclei have a magnetic moment, when placed in a uniform magnetic field B_0 , most of the free hydrogen nuclei orient themselves along the direction of the magnetic field behaving like little magnets, rotate around the axis of the field (to be in resonance) and create a net magnetic moment, M , parallel to B_0 . This behavior is termed *Larmor precession*. The frequency of Larmor precession is proportional to the applied magnetic field strength as defined by the *Larmor frequency* ω (eq. 1):

$$\omega = \gamma B_0 \quad (1)$$

Where γ is the *gyromagnetic ratio* and B_0 is the strength of the applied magnetic field. The gyromagnetic ratio is a nuclei specific constant. For hydrogen, $\gamma = 42.6$ MHz/Tesla.

Next, a radio-frequency (RF) pulse is applied to the field B_0 . This pulse, with a frequency equal to the Larmor frequency, causes M to tilt away from B_0 (Figure 1.1.a) and the hydrogen spins flip, becoming oriented in a specific direction. Once the RF signal is removed, the nuclei realign themselves such that their net magnetic moment, M , is again parallel with B_0 . This return to equilibrium is referred to as relaxation. During relaxation, the

nuclei lose energy by emitting back the radiation or what we call their own RF signal. This signal is referred to as the free-induction decay (FID) response signal.



Figure 1.1. Following application of a radio frequency (RF) field B_1 , the net magnetization M is tipped away from the longitudinal direction (a). The resulting vector has both longitudinal M_z and transverse M_{xy} components (b)

The return to equilibrium after the initial RF pulse is not instantaneous and it occurs with characteristic time constants T_1 and T_2 .

Longitudinal relaxation time T_1 , is known as the 'spin-lattice' relaxation time because, following termination of an RF pulse, nuclei dissipate their excess energy as heat to the surrounding environment (or lattice) and revert to their equilibrium position. Realignment of the nuclei along B_0 , through a process known as recovery, leads to a gradual increase in the longitudinal magnetization M_z . The time taken for a nucleus to relax back (T_1) to its equilibrium state depends on the rate that excess energy is dissipated to the lattice. With M_{0-long} the amount of magnetization parallel with B_0 before the 90° RF pulse and M_{long} the z component of M at time t , it follows that:

$$M_{long} = M_{0-long}(1 - e^{-t/T_1}) \quad (2)$$

Transverse relaxation time T_2 , also known as the 'spin-spin' relaxation time because of its origin in the interactions between the magnetic moments that cause a fast decrease in transverse magnetization (M_{xy}). The decay in transverse magnetization (which does not involve the emission of energy) has the time constant T_2^* which characterizes de-phasing due to both B_0 inhomogeneity and transverse relaxation:

$$M_{trans} = M_{0-trans} e^{-t/T_2^*} \quad (3)$$

$$\frac{1}{T_2^*} = \frac{1}{T_2} + \frac{1}{T_2(inhomogeneity)} \quad (4)$$

Where $M_{0-trans}$ is the amount of transverse (M_{xy}) magnetization just after the end of the 90° RF pulse. These equations fitting allows to extract T_2 which is even longer than T_2^* .

Both forms of relaxation T_1 and T_2 take place separately and simultaneously and they both vary exponentially, however, T_1 relaxation is often slower than T_2 relaxation. The crucial point in imaging is that different tissues, because of their different chemical constitutions and different physical states, have different relaxation times. These relaxation time differences can be used to reconstruct for each dimension to generate MR image contrast by encoding the FID response.

1.1.1.2. Contrast and constructing an image in MRI

An MRI image is a collection of small volumes (voxels) inside of which all the spins contribute to only one signal value. This means that within each of these voxels the signal assigned is an average of the signals of all the individual spins. This difference in spin quantity (spin density) is due to the different tissues it encompasses. Image contrast is defined as the relative difference between the signals of adjacent voxels. The intensity of each voxel is directly related to the intensity of the local MR signal which in turn is dependent on the intrinsic parameters of the tissue; relaxation times (T_1 and T_2) and the proton (spin) density; the higher the proton density, the stronger the FID response signal. The contrast of MR image is always proportional to the spin density, while the main factor determining the tissue contrast is the choice of sequence and its parameters, since for a particular sequence each tissue will have a particular signal height. The parameters that define a pulse sequence are the repetition time (TR) and the echo time (TE):

- a. Repetition time (TR) is the time between consecutive 90° RF pulses. The sequence can be repeated for instance if it is necessary to improve the signal to noise ratio. A long

repetition time allows the protons in all of the tissues to relax back into alignment with the main magnetic field. A short repetition time will result in the protons from some tissues not having fully relaxed back into alignment before the next measurement is made, decreasing the signal from this tissue.

- b. Echo time (TE) is the time between the initial 90° RF pulse and the echo, the time at which the MR signal is measured. A long echo time results in reduced signal in tissues since the protons are more likely to become out of phase. A short echo time reduces the amount of dephasing that can occur in tissue.

By changing these pulse sequence parameters, it is possible to manipulate an MR image contrast. The most basic pulse sequences used in MRI are: gradient echo pulse sequence, spin echo pulse sequence (figure 1.2) and inversion recovery pulse sequence [5, 6].

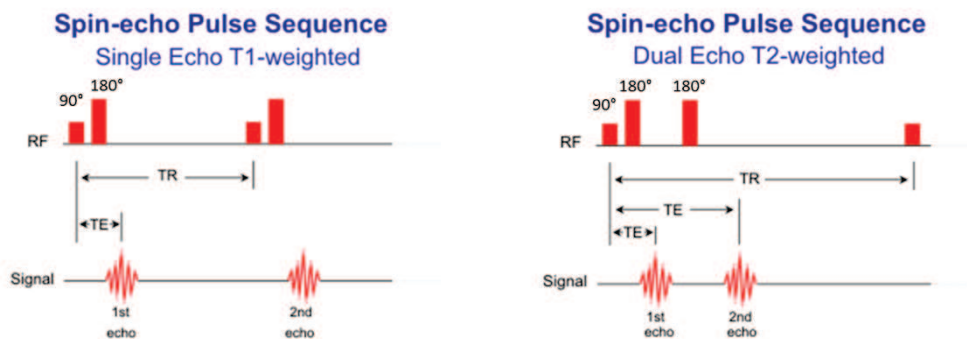


Figure 1.2. 90° and 180° Pulses timing used in Spin-echo sequences for T_1 -weighted and T_2 -weighted imaging.

T_1 -weighted imaging

T_1 -weighted scans refer to a set of standard scans that depict differences in the spin-lattice (or T_1) relaxation time of various tissues within the body. To obtain a T_1 weighted image, the spin echo sequence is repeated but with a short TR. This means that the net magnetizations of the tissues with short T_1 will have time to recover to equilibrium but the magnetizations of the tissues with long T_1 will have no time to recover. In this way tissues with shorter T_1

will show brighter signals than the tissues with longer T_1 . By varying the value of TR the contrast between the tissues with different values of T_1 can be adjusted.

T_2 -weighted imaging

T_2 -weighted scans refer to an image where most of the contrast between tissues or tissue states is due to differences in tissue T_2 created typically by using longer TE and TR times. Therefore, T_2 weighted image contrast state is obtained by imaging with a TR long compared to tissue T_1 (to reduce T_1 contribution to image contrast) and a TE between the longest and shortest tissue T_2 of interest. A TR greater than 3 times the longest T_1 is required for the T_1 effect to be less than 5%.

When we try to have no contrast from either T_2 or T_1 decay, the only signal change results from differences in the amount of available spins (hydrogen nuclei in water). It uses a short TE and long TR. The obtained MR image, in this case, is called spin density (SD) weighted image (figure 1.3)

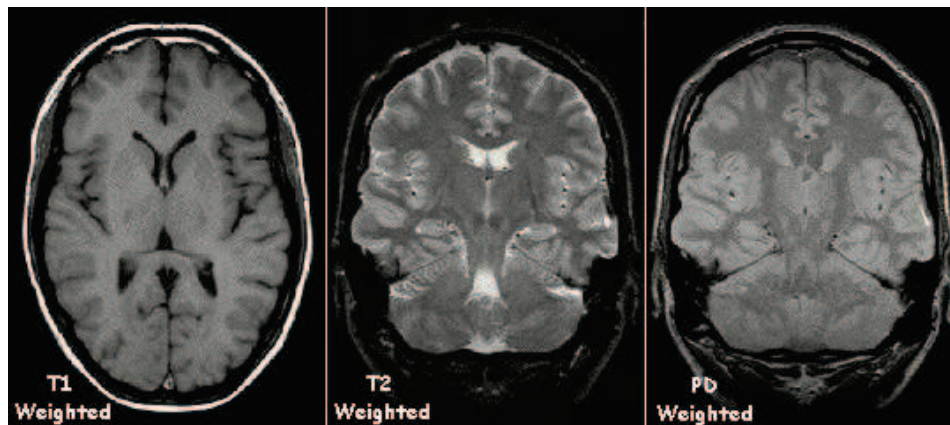


Figure 1.3. Three types of MR image of brain: the T_1 weighted image depicts relatively bright grey matter and dark CSF; the T_2 weighted image highlights the CSF, while the SD weighted image shows little contrast between tissues.

1.1.2. Advantages over non MR techniques

MRI is a powerful diagnostic imaging method which has many advantages over other imaging techniques (table 1.1) [7, 8]:

- **High spatial resolution.** It is a major technological advantage. MRI can characterize and discriminate among tissues using their physical and biochemical properties (water, iron, fat and extravascular blood). The contrast resolution of MR is ~ 10 times better than that of conventional radiography thereby making it a modality-of-choice with high diagnostic potentials. It is possible to measure signals from cubes (voxels) of tissue as small as ~ 0.3 mm from the human brain, generating the high-quality images used in clinical MRI.
- **Non-invasiveness.** It also owes its widespread use to its non-invasiveness. Both biochemical spectroscopy and spatial information (imaging) can be easily performed without destroying the sample, which is a great asset for biomedical and physiological research. It uses radiowaves to extract the information unlike the majority of non-NMR-based techniques which make use of potentially damaging ionizing radiation. For instance, computer assisted tomography (CT) uses X-rays, and nuclear medicine based techniques like gamma scintigraphy and positron emission tomography (PET) involves the administration of radioactive tracers (Table 1.1). Even traditional studies of metabolic processes in intact cells and organs use compounds labelled with radioactive isotopes of hydrogen and/or carbon. PET has a relatively poor spatial resolution (~ 3 mm), so that correlation of the results with anatomy is difficult without the use of other supplementary techniques like CT etc. PET imaging can also detect activity-induced increases in blood flow. Even though nuclear medicine techniques have the advantage of high penetration and sensitivity and the ability to pick up micro- or nonomolar tissue concentration, they usually lack chemical specificity. Similarly, while CT can provide rapid, relatively high-resolution cross-sectional images, it cannot provide soft-tissue details and metabolic or physiological information.
- **Flexibility.** MR Imaging differs from other imaging modalities because signal and contrast are multiparametric in both the intrinsic MR properties of the tissue and the method of measurement (the sequence & scan parameters chosen). This flexibility in controlling the final contrast in the image is one of the great advantages of MRI from its clinical application point of view where the visualization of subtle anatomical differences between the healthy and diseased tissue is required.

Table 1.1. Some of the most commonly applied imaging modalities and their parameters [7]. The imaging techniques are classified according to the energy used to provide the information (X-ray to radio wave), the spatial resolution reported (macroscopic to microscopic) and the nature of the information determined (Anatomical to molecular).

Technique	Reporting unit	Resolution	Depth	Target
MRI	Complexes of Gd^{3+} , Mn^{2+} or Fe^{3+}	10 – 100 μm	No limit	Anatomical Physiological Molecular
Ultrasound	Microbubbles	50 μm	cm	Anatomical Physiological
FRI	Fluorochromes	2 - 3 mm	< 1 cm	Molecular
CT	Iodinated molecules	50 μm	No limit	Anatomical Physiological
PET	Radioisotopes ^{18}F , ^{64}Cu or ^{11}C	1 – 2 mm	No limit	Physiological Molecular
SPECT	Radioisotopes ^{99}Tc or ^{111}In	1 - 2 mm	No limit	Physiological Molecular

1.1.3. MRI contrast agents

As outlined above, the overriding challenge with MRI is its relatively low sensitivity since the intrinsic contrast provided by the water relaxation times and changes in their values due to tissue pathology are often too small to enable a sensitive and specific diagnostics. In order to induce additional and specific contrast, exogenous molecules can be introduced to affect some property of the water protons to such an extent that an observable effect is achieved. Such molecules are called MRI paramagnetic contrast agents [4, 9, 10]. Although some believe that the non-invasiveness of MRI is one of its strengths and should be kept that way, the clinical efficacy of the paramagnetic contrast has largely justified its use.

1.1.3.1. Gadolinium chelates as T_1 -contrast agents

Contrast agents generally work by increasing the longitudinal ($1/T_1$) and transverse ($1/T_2$) proton relaxation rates, thus they are usually categorized as T_1 or T_2 agents. Effects on

relaxation times are concentration dependent; the more agent present, the greater the effect.

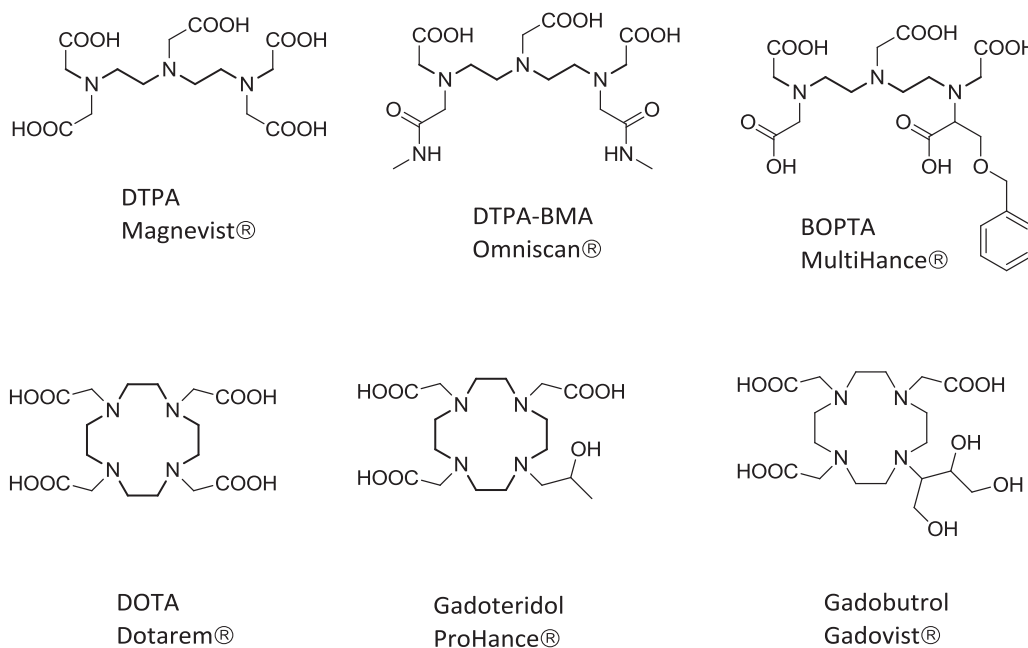
The most widely used, especially for clinical use, are gadolinium-based T_1 agents which increase the signal intensity on T_1 -weighted images. Gadolinium ion (Gd^{3+}) is the cation of choice because of its high number (seven) of unpaired electrons and its long electronic relaxation time [11]; It causes its own magnetic field to fluctuate strongly which is the origin of the proton relaxation rate enhancement. As free ion, Gd^{3+} is potentially toxic. Therefore, the ion should be coordinated to a protective multidentate ligand with high binding affinity to form non-toxic complex. Consequently, a critical criterion in designing gadolinium chelates is the high thermodynamic and kinetic stability to assure their tolerance and safe use *in vivo*.

Many gadolinium complexes have been reported [9, 12]. The commercially available chelates have favorable safety profiles at approved doses in patients with normal renal function [13, 14]. They are non-specific extracellular agents that show non-specific distribution pattern allowing measurement of physiological tissue parameters (e.g., vascular permeability, blood flow, and blood volume). Despite the variety in their chemical structure, these compounds have similar pharmacological properties (Table 1.2) and can be classified into acyclic and macrocyclic chelates (figure 1.4). Acyclic chelates include mainly derivatives of the aminopolycarboxylic acids, like diethylenetriaminepentaacetic acid (DTPA), as backbone. Commercially approved ones include the first MRI contrast agents, Gd-DTPA (gadopentetate, Magnevist[®]) and Gd-DTPA-BMA (OmniScan[®]) which were approved for human use. The cyclic commercially approved class of MRI contrast agents comprise Gd-HP-DO3A (ProHance[®]) and Gd-DOTA (Dotarem[®]). In this case, the ligands (macrocyclic chelates) are derivatives of 1,4,7,10-tetraazacyclododecane (cyclen). The tetraacetic acid derivative of cyclen, DOTA, forms gadolinium complexes with extraordinary kinetic inertness and very high thermodynamic stability [15].

Table 1.2. Thermodynamic stabilities and relaxivities of the commercial extracellular agents [16]

Chemical Name	Generic Name	Brand Name	$1/T_1$ relaxivity ($\text{mM}^{-1}\text{s}^{-1}$)	Log K (therm)
$[\text{Gd}(\text{DTPA})(\text{H}_2\text{O})]^{2-}$	Gadopentetate	Magnevist [®]	4.30 ^{a,b}	22.46 ^h
$[\text{Gd}(\text{DOTA})(\text{H}_2\text{O})]^-$	Gadoterate	Dotarem [®]	4.20 ^{a,b}	25.30 ⁱ
$[\text{Gd}(\text{DTPA-BMA})(\text{H}_2\text{O})]$	gadodiamide	Omniscan [®]	4.39 ^{a,g}	16.85 ^j
$[\text{Gd}(\text{HP-DO3A})(\text{H}_2\text{O})]$	gadoteridol	ProHance [®]	3.70 ^{c,d}	23.80 ^k
$[\text{Gd}(\text{DO3A-butrol})(\text{H}_2\text{O})]$	gadobutrol	Gadovist [®]	3.60 ^{c,e}	21.80 ^l
$[\text{Gd}(\text{DTPA-BMEA})(\text{H}_2\text{O})]$	gadoversetamide	OptiMARK [®]	4.70 ^{c,f}	16.84 ⁱ

^aRelaxivities in water at 20 MHz and 25°C. ^cRelaxivities in water at 20 MHz and 40°C. ^bAime et al. Magn. Reson. Chem., **1991**, 29, 923-7. ^dShukla et al. Magn. Reson. Chem., **1996**, 35, 928-931. ^eVolger et al. Eur. J. Radiol., **1995**, 21, 1-10. ^fPerissamy et al. Invest Radiol., **1991**, 26, S217-S220. ^gPowell et al. J. Am. Chem. Soc., **1996**, 118, 9333-9346. ^hSmith et al. **1997**, NIST Standard Reference Database#46, 3.0 ed. ⁱKumar et al. Inorg. Chem, **1994**, 33, 3567-3575. ^jCacheris et al. Magn. Reson. Imaging, **1990**, 8, 467-481. ^lToth et al. Inorg. Chim. Acta., **1996**, 249, 191-199.

**Figure 1.4.** Chemical structure of the ligand in some commercially available Gd³⁺-based agents

The efficiency of a given MR contrast agent is measured in terms of its relaxivity, r_1 , which is defined as the paramagnetic relaxation rate enhancement $\Delta(1/T_1)$ of water protons observed for a 1mM solution of contrast media. It is typically expressed in units of $\text{mM}^{-1}\text{s}^{-1}$ and is both field and temperature dependent (Eq.5).

$$r_1 = \frac{\Delta\left(\frac{1}{T_1}\right)}{[\text{Gd}^{3+}]}, \quad \Delta\left(\frac{1}{T_1}\right) = \frac{1}{T_{1,obs}} - \frac{1}{T_{1,d}} \quad (5)$$

Where $1/T_{1,obs}$ represents the observed solvent relaxation rate and $1/T_{1,d}$ is the diamagnetic relaxation rate which corresponds to the relaxation rate of the solvent nuclei in the absence of the paramagnetic solute. From equation (5), it is obvious that the T_1 shortening is linearly dependent on the concentration of the gadolinium complex injected, which is valid at least in highly diluted solutions.

1.1.3.2. Mechanism of action; solvation spheres

The relaxivity of paramagnetic metal complexes depends on many factors and can be described by a complex theory with numerous terms (Solomon-Bloembergen-Morgan theory of paramagnetic relaxation) [17-21]. Some of these terms are dependent not only on the chemical structure of the molecule but also on the environment around the agent. Therefore, unlike PET or CT agents, which have fixed physical properties providing signal for imaging, there is a possibility for designing MRI contrast agents that have varying signal enhancement in response to the environment.

The gadolinium complex can be viewed as having separate water-coordination spheres (figure 1.5). The inner sphere (IS) consists of water molecule(s) directly bound to the metal ion. For contrast agents like GdDOTA (table 1.2), the inner hydration sphere is one water molecule. The second coordination sphere (SS) is less well defined and can be described as being the solvent molecules that are not directly bound but may remain in the proximity of the paramagnetic metal for a relatively long time, e. g. due to hydrogen bonds to the ligand or to the solvent molecule(s) in the first coordination sphere. We define the second sphere

in terms of water residency time, τ'_m , which must be longer than the diffusion correlation time of water. The second-sphere relaxivity can be described by the same theory as the inner-sphere term. Very often this contribution is difficult to separate and evaluate, thus it is neglected or simply taken into account as an increase in the outer-sphere term. The outer sphere (OS) is a less organized structure and consists of freely diffusing water. Relaxivity can be factored into contributions arising from water in each coordination sphere:

$$r_1^{obs} = r_1^{IS} + r_1^{SS} + r_1^{OS} \quad (6)$$

where r^{OS} , r^{SS} , r^{OS} describe the inner sphere, second, sphere and the outer sphere relaxivities, respectively.

For monomer Gd^{3+} complexes the inner sphere and outer sphere mechanisms contribute more or less to the same extent to the overall paramagnetic relaxation enhancement. However, the development of high relaxivity contrast agents mainly involves increasing the inner sphere contribution since the outer sphere term can hardly be modified.

1.1.4. Contribution of molecular parameters to the inner-sphere relaxivity

The inner sphere contribution to the longitudinal relaxation rate $1/T_1$ is given by the following equation:

$$r_1^{IS} = \frac{cq}{55.5} \left(\frac{1}{T_{1m} + \tau_m} \right) \quad (7)$$

where c is the molar concentration, q is the number of bound water molecules per Gd^{3+} , τ_m is the life-time of the water molecule in the inner sphere of the complex (equal to the reciprocal water exchange rate, $1/k_{ex}$) and T_{1m} is the relaxation time of the bound water protons (figure 1.5).

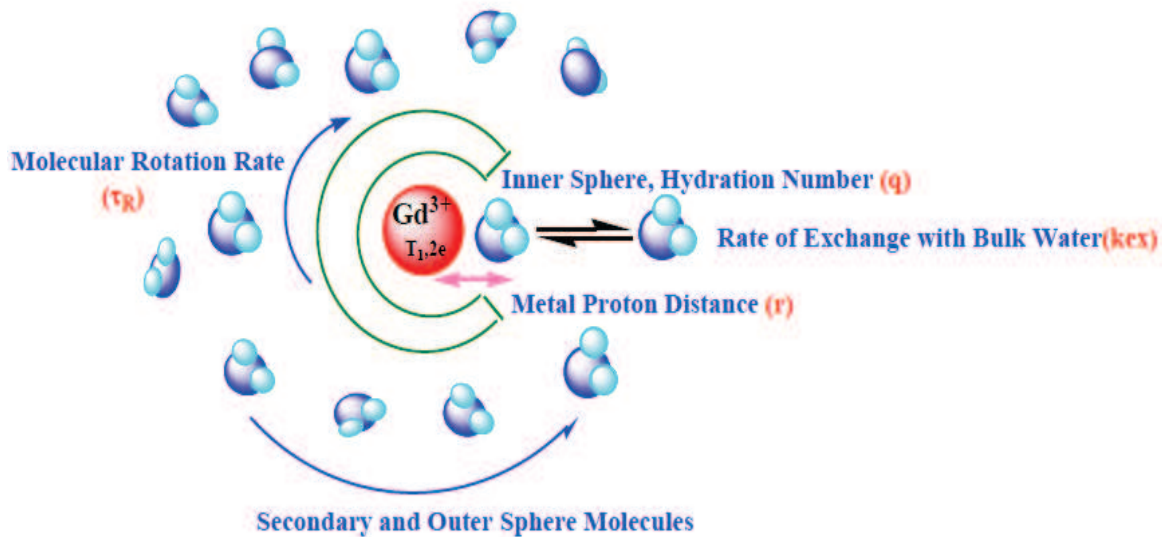


Figure 1.5. Schematic representation of a model Gd-complex with one inner sphere coordinated water molecule in solution (bulk water) and the parameters influencing the relaxation of a Gd³⁺ complex.

It is apparent from equation (7) that the parameters which can be modified in order to boost relaxivity are the following:

- a) **Inner-sphere hydration number, q .** The inner sphere relaxivity is directly proportional to the number of inner sphere water molecules, q . All approved Gd³⁺-based contrast agents have one water molecule in their inner sphere. Theoretically, high relaxivity can be achieved by increasing this low hydration number. However, this is not easily applicable due to toxicity concerns, since increasing q leads to a decrease of the stability of the metal complex. The complex needs to be sufficiently stable not to release the Gd³⁺ ion during the time course of an MRI examination.
- b) **Gd-H distance.** The distance between the coordinated water proton and the Gd³⁺ electron spin has a crucial role in determining the relaxivity, but it is a parameter that is difficult to measure experimentally. Generally it can be deduced from the Gd³⁺-coordinated water oxygen distance which is easier to obtain. Attempts have been made to determine $r_{\text{Gd-H}}$ by various means [22-26]. Nonetheless, given the fact that the tilt

angle of the plane of the bound water molecule is not well defined in solution, the obtained $r_{\text{Gd-H}}$ values are merely estimations.

- c) **Water exchange rate, k_{ex} .** The relaxivity depends inversely on the water residency time which is the time needed for the relaxed bound water molecule(s) to exchange with the solvent water molecules. This rate needs to be situated within an optimal range [27-29]. Obviously, if τ_m becomes too long, there is a little or no exchange of the relaxed water with the bulk and the relaxivity will be limited. On the other hand, a very short τ_m results in an increased T_{1m} (relaxation of the bound water is less efficient); the bound water molecule will not have enough time to feel the paramagnetic effect of the metal and the relaxivity is affected. The water exchange rate is closely related to the inner sphere structure of Gd^{3+} . The factors that influence the water residence lifetime (or rate of exchange) include the charge on the complex [30], solvent accessibility (the steric environment around the metal centre), the mechanism of the water exchange and for DOTA derivatives the relative population of their structural isomers [31].
- d) **Rotational correlation time, τ_R .** The rotational correlation time refers to how rapidly the molecule tumbles in solution. For small complexes currently used as (commercial) contrast agents, fast tumbling limits the relaxivity [16]. The Solomon-Bloembergen-Morgan theory predicts that the relaxivity of a Gd^{3+} complex with optimally fast water exchange rate ($k_{\text{ex}} = 10^8 \text{ s}^{-1}$ at ~20-60 MHz) can be drastically increased upon slowing its molecular tumbling. This can be achieved through incorporation of the complex into macromolecules or nanosized structures such as proteins [32, 33], micelles [34, 35], dendrimers [36-38], cyclodextrins [39], etc. An increase in τ_R with increasing molecular weight is frequently observed, though the increase is not linearly proportional to the molecular weight.
- e) **Electronic relaxation (T_{1e} and T_{2e}).** Both the longitudinal and transverse electronic relaxation times influence the relaxivity and it is difficult to correlate their effect with the structural features of the ligands. They are dependent on the magnetic field strength (B_0), and the theory that describes the electronic relaxation parameters is limited and is only valid over a small range of B_0 , in which a mono-exponential electronic

relaxation process is occurring. Outside this range, the process becomes multi-exponential and the parameters become difficult to determine.

Taking into account all above-mentioned parameters, it is possible to conceive MRI contrast agents endowed with higher relaxivity. According to the Solomon-Bloembergen-Morgan theory, a simultaneous optimization of all these parameters could lead to a relaxivity of about $100 \text{ mM}^{-1}\text{s}^{-1}$ (at 20 MHz); while the current contrast agent have relaxivities around 4-5 $\text{mM}^{-1}\text{s}^{-1}$ at the same field. The parameters q , τ_m and τ_R are the easier to predict, thus the most amenable to modulation by an appropriate ligand design. For instance, the nature and position of the Gd^{3+} chelate substituents contribute mainly in optimizing the number and exchange rate of coordinated water molecules [12, 28, 40].

1.2. Time-Resolved Luminescence

Although MRI is the most important and prominent technique in diagnostic clinical medicine and biomedical research due to its high resolution and its versatility that cover a broad range of *in vivo* applications, it is characterized by inherently low sensitivity due to the low quantum energy involved. To overcome this issue, the use of millimolar concentration of contrast agents is needed, an aspect that prevents the current contrast agents from being used in targeted imaging. Indeed, many useful targets associated with disease are present at nM- μM concentrations, which are too low to be detected by MRI. The search for a better sensitivity led to the development of new fields and methodologies in order to overcome the MRI limitation; one way consists of using nano-sized systems such as liposomes, micelles, microemulsions, polymers, etc. that are able to carry a huge payload of Gd^{3+} complexes in order to get an amplification effect [41, 42]. A straightforward extension of this approach involves the use of naturally occurring nanosized aggregates such as apoferritin [43, 44] and lipoproteins [45, 46]. High field MRI is also a growing field meant to achieve the same purpose. Special contrast agents need to be developed and optimized for such high fields [47].

Another tendency to surmount the low sensitivity of MRI involves using optical emissive probes that combine high signal-to-noise ratio and high temporal resolution. A variety of

different imaging and spectroscopic modes are available: absorption and scattering microscopy [48], fluorescence [49] and bioluminescence [50]. The majority of optical probes are based on organic fluorophores which have short lifetimes (nanosecond range) and endogenous molecules will frequently interfere with their light of excitation and/or emission. In contrast, luminescent lanthanide probes display long-lived emissions (up to ms) at a large range of wavelengths (visible to near infrared). These very long luminescence lifetimes are ideal for the direct, time-gated detection of an analyte in a complex biological medium such as a cell with regards to the background autofluorescence [51-54]. Accordingly, combining the excellent resolution of MRI and high sensitivity of luminescent-based optical offers the possibility for applying a multimodal approach, where a bimodal agent that satisfies requirements for both modalities within a single molecule can be used as optical and MR imaging probes [55-57]. Such bimodal compounds are based on the unusual spectral properties of lanthanide ions.

1.2.1. Lanthanides and their photophysical characteristics

The lanthanides comprise the fourteen elements of the top row in the 'f-block' of the periodic table and have the electronic configuration $[\text{Xe}] 4f^n 5s^2 5p^6$ where n varies from 0 to 14 (table 1.3). They are also known as 'rare earth elements' and include Yttrium (Y) and Scandium (Sc), because of their chemical similarity.

Lanthanides have found uses in a wide variety of industries and materials, such as catalysts, glasses, ceramics, permanent magnets, optics and electronics [58-60]. Europium, cerium and terbium are major contributors to commercial markets in fluorescent lighting and color displays. Various lanthanide ions can be used in lasers, with neodymium as the most famous in yttrium aluminum garnet (Nd-YAG). The green, blue and red luminescent bands in Euro banknotes are attributed to Eu^{3+} and Eu^{2+} complexes [61]. Certain lanthanides (Eu, La, Lu, Nd, Pr, Sm, Tm and Yb) are used as tracers in wine chemistry to discriminate wines according to geographical region [62]. The following are some of the general characteristics of lanthanide series:

a) Oxidation state. In aqueous solution, lanthanides are most stable in the +3 oxidation state. In reducing conditions, europium, samarium and ytterbium can be stable in the divalent form; cerium has also been known to adopt a +4 oxidation state. Lanthanide ions possess relatively high charge densities and have a strong electrostatic nature in their bonding, as the ions are polarizing and can be classified as hard Lewis acids. The 4f orbitals in Ln^{3+} ions are well shielded by the 5s and 6p orbitals, and therefore do not participate directly in bonding. Therefore, coordination to trivalent lanthanides tends to be more ionic (electrostatic) in character, which leads to a strong preference for negatively charged or neutral donor groups possessing large ground state dipole moments. Therefore, combinations of amines and carboxylic acid groups are often used in lanthanide complexation [63]. This ionic character of binding also means lanthanide complexes tend to undergo facile exchange of ligands [61].

Table 1.3. Selected properties of lanthanide ions [61]

Atomic Number	Name	Symbol	Electronic configuration		Ground term	Radius M^{3+} (Å)
			Atom	M^{3+}		
57	Lanthanum	La	[Xe] 5d ¹ 6s ²	[Xe]	¹ S ₀	1.17
58	Cerium	Ce	[Xe] 4f ¹ 5d ¹ 6s ²	[Xe] f ¹	² F _{5/2}	1.15
59	Praseodymium	Pr	[Xe] 4f ² 6s ²	[Xe] f ²	³ H ₄	1.13
60	Neodymium	Nd	[Xe] 4f ³ 6s ²	[Xe] f ³	⁴ I _{9/2}	1.12
61	Promethium	Pm	[Xe] 4f ⁴ 6s ²	[Xe] f ⁴	⁵ I ₄	1.11
62	Samarium	Sm	[Xe] 4f ⁵ 6s ²	[Xe] f ⁵	⁶ H _{5/2}	1.10
63	Europium	Eu	[Xe] 4f ⁶ 6s ²	[Xe] f ⁶	⁷ F ₀	1.09
64	Gadolinium	Gd	[Xe] 4f ⁷ 6s ²	[Xe] f ⁷	⁸ S _{7/2}	1.08
65	Terbium	Tb	[Xe] 4f ⁸ 6s ²	[Xe] f ⁸	⁷ F ₆	1.06
66	Dysprosium	Dy	[Xe] 4f ⁹ 6s ²	[Xe] f ⁹	⁶ H _{15/2}	1.05
67	Holmium	Ho	[Xe] 4f ¹⁰ 6s ²	[Xe] f ¹⁰	⁵ I ₈	1.04
68	Erbium	Er	[Xe] 4f ¹¹ 6s ²	[Xe] f ¹¹	⁴ I _{15/2}	1.03
69	Thulium	Tm	[Xe] 4f ¹² 6s ²	[Xe] f ¹²	³ H ₆	1.02
70	Ytterbium	Yb	[Xe] 4f ¹³ 6s ²	[Xe] f ¹³	² F _{7/2}	1.01
71	Lutetium	Lu	[Xe] 4f ¹⁴ 5d ¹ 6s ²	[Xe] f ¹⁴	¹ S ₀	1.00

- b) The coordination number.** The coordination number of the aqua ions $[\text{Ln}(\text{H}_2\text{O})_n]^{3+}$ is 9 for the early lanthanides (La-Eu) and 8 for those later in the series (Dy-Lu), with the intermediate metals (Sm-Dy) exhibiting a mixture of species. The coordination number of the lanthanide complexes can be dictated by the steric bulk of the coordinating ligands, and species with coordination numbers as low as 2 and as high as 12 are known [61].
- c) Ionic radius.** As the 4f electrons of the lanthanides are well shielded from the environment, the spectroscopic and magnetic properties of these ions are largely independent of environment (solvent, coordinated ligands, etc.). Filling of the inner 4f electron shell across the lanthanide series results in a diminution of the ionic radius by as much as 15% from lanthanum to lutetium (table 1.3), referred to as the lanthanide contraction.[64] This causes neighbouring lanthanides to have similar, but not identical, properties. In other words, the lanthanides are chemically similar but have specific magnetic and photophysical properties. Thus, we can use lanthanide substitution as a tool to tune the magnetic and optical properties in a lanthanide complex without changing its chemical behaviour.
- d) Toxicity.** Lanthanides are highly toxic as they mimic the behaviour of Ca^{2+} due to the similarity of their ionic radii [65]. They can interfere with processes that are dependent on Ca^{2+} influx (by blocking the cellular voltage-gated channels, even when present at low concentrations). This can result in contraction of the smooth, skeletal and cardiac muscle, alter the transmission of nervous influx and blood coagulation [66]. Lanthanides have also been shown to inhibit the activity of certain enzymes, for example Ca^{2+} activated ATP-ases of the endoplasmic reticulum [67].
- e) Luminescence properties.** With the exceptions of the $4f^0$, $4f^1$, $4f^{13}$ and $4f^{14}$ species (La^{3+} , Ce^{3+} , Yb^{3+} and Lu^{3+} , respectively), all lanthanide ions absorb electromagnetic radiation, primarily in the visible region, which is manifested in f-electrons from the partially filled 4f subshell being excited from the ground state to an excited state. These f–f transitions are Laporte forbidden [68] and are responsible for the interesting photophysical

properties of the lanthanide ions, such as long-lived luminescence and sharp absorption and emission lines which are being exploited in sensory applications.

Narrow emission bands. Luminescent lanthanides can have emission bands ranging from UV to NIR regions, depending on the nature of lanthanide cations. The emission bands are very narrow and do not overlap completely one with another (figure 1.6) [68]. As a consequence, multiple lanthanide probes can be employed concurrently to monitor several analytes simultaneously and the response of each probe is a function solely of the targeted analyte.

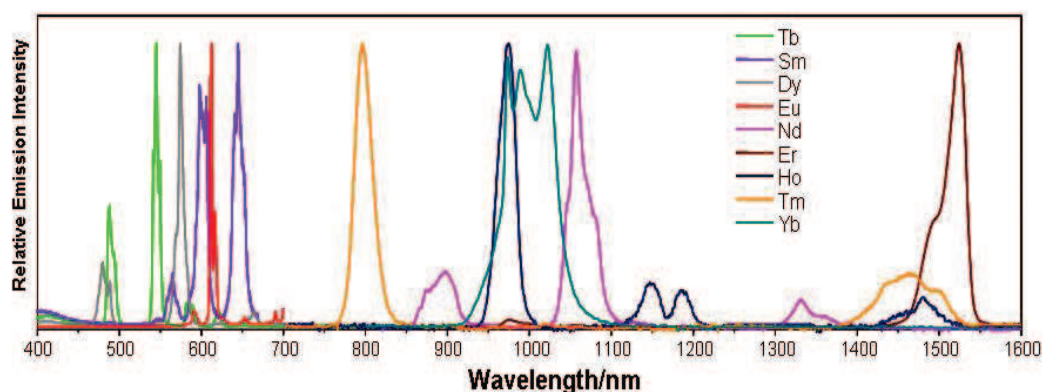


Figure 1.6. Emission spectra of some lanthanides (III) [68].

Large Stokes shift. Lanthanides emission gives rise to a large Stokes shift between the absorption band and the emission of the lanthanide, thus minimizing luminescence reabsorption and corresponding quantification artefacts.

Long-lived luminescence lifetimes allow time-gated detection where the background luminescence is allowed to decay to zero leaving only the longer-lived lanthanide emissions before measuring the luminescence of the complex [69]. Consequently, the luminescence intensity is a function only of the concentrations of the lanthanide probe and its targeted analyte, and is unaffected by the presence of any other chromophore in the medium. Hence, time gating facilitates the intracellular spatial and quantitative determination of the concentration of a desired analyte [51, 70].

1.2.2. Sensitization of lanthanide luminescence (antenna effect)

A direct consequence of the Laporte-forbidden nature of f-f transition luminescence is the low absorption coefficient of the lanthanide ion making direct photoexcitation of lanthanide ions difficult [58, 71]. They can only be effectively excited directly by lasers. Lanthanide luminescence can be significantly enhanced *via* a process called 'sensitization' [72, 73]. It consists of covalently or non-covalently attaching to the chelating agent an antenna or chromophore with high extinction coefficient. In order to act as an efficient antenna, the chromophore (usually an aromatic or unsaturated organic molecule) must absorb radiation effectively and pass it as much as possible, nonradiatively, to the lanthanide emissive state. Population of the lanthanide emissive state *via* sensitized emission may occur through various processes. The nature of the process will depend on a number of factors, principally the lanthanide ion involved and the associated thermodynamic and photophysical properties of the antenna unit. The processes in question will not be discussed here; we will briefly discuss the most common one which is triplet-mediated. For an in-depth view there are many reviews [64, 74, 75].

Triplet-mediated process

The triplet-mediated mechanism of luminescence sensitization is as follows: the first step involves the absorption of a photon of a suitable wavelength by the chromophore, promoting an electron into the singlet-excited state [72]. This can either lose energy and return to the ground state through fluorescence or alternatively in the presence of a heavy atom (such as Lanthanide) undergo non-radiative intersystem crossing resulting in a triplet state. At this point, it can phosphoresce to the ground state or populate the lanthanide emissive state through energy transfer, where luminescence can result (figure 1.7).

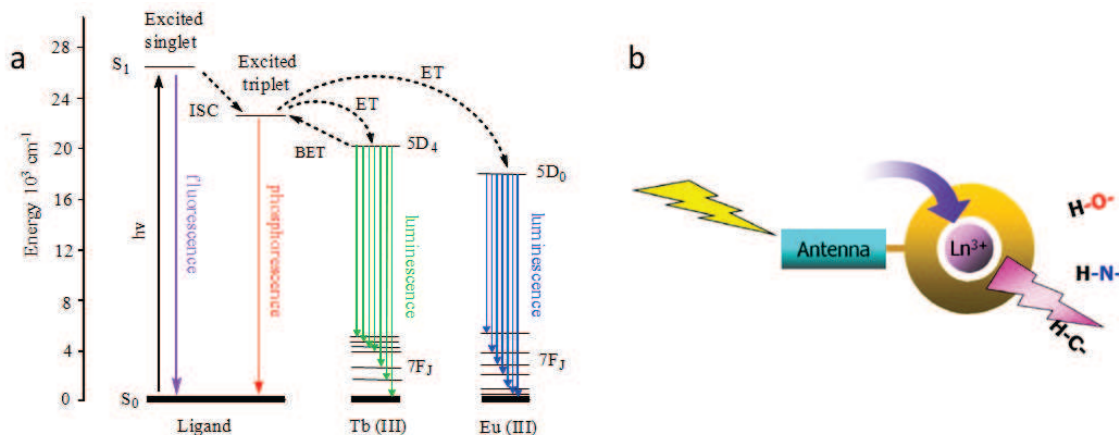


Figure 1.7. Simplified Jablonski diagram showing the main energy flow paths during sensitization of lanthanide luminescence *via* its antenna. This energy transfer is generally believed to occur through the triplet state (a). Indirect excitation of a lanthanide ion *via* a sensitizer that is bound to the ligand (b). ET stands for energy transfer.

For this process to occur efficiently, the energy of the triplet state is critical and needs to be at least 1500 cm^{-1} higher in energy than the respective lanthanide emissive state. If not, thermally activated back-energy transfer (BET) can occur repopulating the triplet state. This state can be depopulated by collision with molecular oxygen, ultimately rendering the lanthanide emission sensitive to the degree of aeration. To ensure that this energy gap is reasonably large, chromophores that absorb in the ultraviolet region are used to sensitise the visible emission from certain lanthanides and this has obvious problems for application *in vivo*. Research has focused on the use of chromophores that have a small singlet-triplet energy gap. Such systems enable longer wavelength sensitisation of visible emission. Although the energy difference between the triplet excited state and the best accepting level is of first importance, other parameters such as the kinetic of the energy transfer (ET) and the geometry of the complexes also play a relevant role. As an example, Beeby et al. used benzophenone as sensitizer in order to obtain unity quantum yield of formation of the triplet excited state, combined with a highly efficient ET (0.99). However, “only” 27% and 9.5% luminescence quantum yields were obtained for the terbium and europium

complexes, respectively, as a result of poor metal centered efficiency for those complexes [76].

Of all the lanthanides, Eu^{3+} , Tb^{3+} and Gd^{3+} are the best ions in terms of efficient excited state population, with energy gaps of 12,300 cm^{-1} (${}^5\text{D}_0 \rightarrow {}^7\text{F}_6$), 14,800 cm^{-1} (${}^5\text{D}_4 \rightarrow {}^7\text{F}_0$) and 32,200 cm^{-1} (${}^6\text{P}_{7/2} \rightarrow {}^8\text{S}_{7/2}$), respectively [77]. Nevertheless, while europium and terbium both emit in the visible region, gadolinium has high energy levels and emits in the ultraviolet, making it unusable in most luminescence sensing applications *in vivo* due to significant absorption and emission interference of these high-energy wavelengths.

1.2.3. Quenching process and hydration state (q)

Once formed, the lanthanide excited state can be quenched by natural, non-radiative processes and energy transfer to the stretching modes of X-H oscillators. These X-H oscillations are closely diffusing O-H, amide N-H and methylene C-H oscillators [78]. All these processes obviously reduce the lifetime and intensity of the luminescence.

The intensity of the luminescence (I) as a function of time can be used to determine the rate constant (k_{obs}) and the lifetime (τ) for the decay of the luminescence of a given complex, this is depicted in equations 8-10.

$$I_t = I_0 e^{(-k_{obs}t)} \quad (8)$$

$$\tau = \frac{1}{k_{obs}} \quad (9)$$

$$k_{obs} = k_{nat} + k_{nr} + k_{X-H} \quad (10)$$

where k_{nat} is the natural radiative rate constant, k_{nr} is the rate constant for nonradiative de-excitation and k_{X-H} is the rate constant of the de-excitation by XH oscillators. The effects of the corresponding deuterated oscillators O-D, N-D and C-D are considered to be negligible [79], so subtracting the two rate constants in D_2O and H_2O will give the number of X-H oscillators that quench the luminescence.

$$\Delta k = k_{H_2O} - k_{D_2O} = \sum k_{X-H} \quad (11)$$

In aqueous media the dominating quenching group is the O-H of the water molecules. Therefore, Horrocks and Sudnick suggested that the difference in the observed rate constants in H₂O and D₂O could be used to determine the number of directly co-ordinated water molecules, denoted q [80].

$$q = A(k_{H_2O} - k_{D_2O}) \quad (12)$$

A is a proportionality constant specific to each lanthanide. Closely diffusing water molecules will also have a small but observable effect on the luminescence; so a further corrective term, B, is required. This is also specific to each lanthanide.

$$q_{corr} = A\Delta k - B \quad (13)$$

The different A and B values have been empirically determined for some lanthanide ions and are given in table [81].

Table 1.4. Correction factors for some of the Ln³⁺

Lanthanide	A	B
Nd ³⁺	130 ns	0.4 ns ⁻¹
Eu ³⁺	1.2 ms	0.25 (+ 0.075χ) ms ⁻¹
Tb ³⁺	5 ms	0.06 ms ⁻¹
Yb ³⁺	1.0 μs	0.1 μs ⁻¹

When applying the correction factors to Eu³⁺ complexes, a further term is required to account for the significant quenching effect of nearby N-H oscillators of amine or amide functional groups (χ). 75 μs⁻¹ is subtracted from the difference of the rate constants for each N-H oscillator present, to determine a more accurate q-value. The extent of quenching by the O-H oscillators is inversely proportional to the energy gap between the excited and

ground states of the lanthanide ion. Those with a larger energy gap will experience a lesser degree of quenching, as the O-H oscillators will need to be in a higher vibrational energy state to obtain effective overlap and allow energy transfer to occur. Thus, caution is required when interpreting hydration states [81].

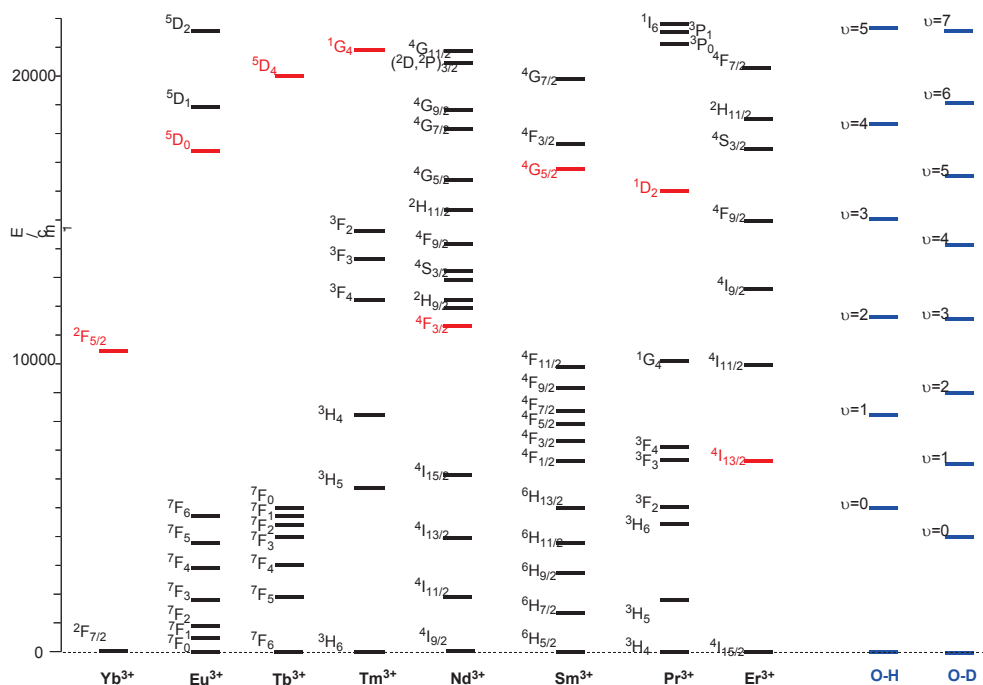


Figure 1.8. The energy states of some of the emissive lanthanides and the vibrational states of OH/OD oscillators. Luminescent states are indicated in red.

In figure 1.8, the emissive states of the lanthanides are highlighted in red and it can be seen how they align with the various vibrational harmonics of O-H/O-D oscillators. It also helps to explain why quenching is less pronounced in deuterated media, as higher vibrational harmonics of an O-D oscillator have less effective overlap with the emissive state of the lanthanide [82].

1.2.4. Quantum yield

The efficiency of energy transfer is proportional to the donor quantum yield. By lanthanide quantum yield here we mean the probability that the lanthanide will emit a photon given that the lanthanide is excited. This definition is very similar to that used with conventional

fluorophores. The quantum yield of sensitized lanthanide luminescence is dependent on four parameters:

- 1) The efficiency by which the triplet excited state of the antenna is populated.
- 2) The energy of the triplet excited state of the antenna relative to the excited state of the lanthanide ion. For intramolecular energy transfer to occur, the triplet excited state of the antenna must be higher in energy than the excited state of the lanthanide. Direct fluorescence from the antenna is observed if the triplet state of the antenna is too high or too low in energy. Furthermore, when the triplet state of the antenna is too close in energy to the state of the lanthanide, back energy transfer (BET) from the lanthanide to the antenna occurs with a consequent decrease in lanthanide emission.
- 3) The distance separating the antenna from the lanthanide ion.
- 4) The number of coordinated water molecules. Since the fourth overtone of the water O–H oscillator is lower in energy than the 5D states of Eu^{3+} and Tb^{3+} , energy transfer from the excited state of the lanthanide to coordinated water molecules can significantly reduce the quantum yield of the metal luminescence.

1.2.5. Long-wavelength sensitization and near-infrared emission

The lanthanides can be classified according to the nature of their emissions, predominantly visible and/or near infrared. This is expressed in table 1.5 along with the wavelengths of their main emissions [58].

The long-lived emission from lanthanides in the near infrared region (NIR) is highly desirable in the pursuit of optical imaging. Biological tissue is more transparent to light of this wavelength; also the excitation wavelength required is lower in energy than that for visible emitting systems which means that it causes less damage to biological samples and at the same time this will result in less interference from endogenous species present, in terms of competitive absorption and auto-fluorescence and there will be less light scattering. The lower scattering of NIR photons results in improved image resolution [68].

Table 1.5. The principal emission wavelengths, colours and electronic transitions of the emissive trivalent lanthanides

Ln^{3+}	λ_{em} nm	Emission colour(s)	Transition(s)
Pr	603, 1020, 1440	NIR, Orange	$^3\text{P}_0 \rightarrow ^3\text{H}_6, ^1\text{D}_2 \rightarrow ^3\text{F}_4, ^1\text{D}_2 \rightarrow ^1\text{G}_4$
Nd	1060	NIR	$^4\text{F}_{3/2} \rightarrow ^4\text{I}_{11/2}$
Sm	603	Orange	$^4\text{G}_{5/2} \rightarrow ^6\text{H}_{7/2}$
Eu	620	Red	$^5\text{D}_0 \rightarrow ^7\text{F}_3$
Gd	312	UV	$^6\text{P}_{7/2} \rightarrow ^8\text{S}_{7/2}$
Tb	550	Green	$^5\text{D}_4 \rightarrow ^7\text{F}_5$
Dy	570	Yellow	$^4\text{F}_{9/2} \rightarrow ^6\text{H}_{15/2}$
Ho	650, 970	Red, NIR	$^5\text{F}_5 \rightarrow ^5\text{H}_8, ^5\text{F}_5 \rightarrow ^5\text{H}_7$
Er	1530	NIR	$^4\text{I}_{13/2} \rightarrow ^4\text{I}_{15/2}$
Tm	480, 650	Blue	$^1\text{G}_4 \rightarrow ^3\text{H}_6, ^1\text{G}_4 \rightarrow ^3\text{H}_4$
Yb	980	NIR	$^2\text{F}_{5/2} \rightarrow ^2\text{F}_{7/2}$

Several sensitizers or antennae have been described for the sensitization of NIR emitting lanthanide cations [68, 72, 83].

1.3. Lanthanide based-probes for molecular imaging

The higher resolution and non-invasiveness of MRI make it an attractive modality for molecular imaging applications. The currently used clinical paramagnetic agents are nonspecific that give only anatomical information, and they are not capable of indicating the biochemical or physiologic abnormalities underlying diseases. On the basis of the above considerations and to keep up with that need for more specific and functional contrast, the research focus in MRI contrast agents has shifted in recent years to the development of new generations of contrast agents that have molecular, physiological, or biochemical specificity. They generally consist of a MRI reporting unit linked to a receptor or binding site that interacts selectively with the biomarker in question.

1.3.1. Classes of contrast agents

Based on the differing ways in which lanthanide-based MR contrast agents report their presence, these agents can be mainly categorized into targeted and responsive (smart) contrast agents [84]. Numerous are the publications that report different chemical designs for these contrast agents, but so far very few have been applied *in vivo*. Some examples are reviewed in the following section with special emphasis on smart contrast agents.

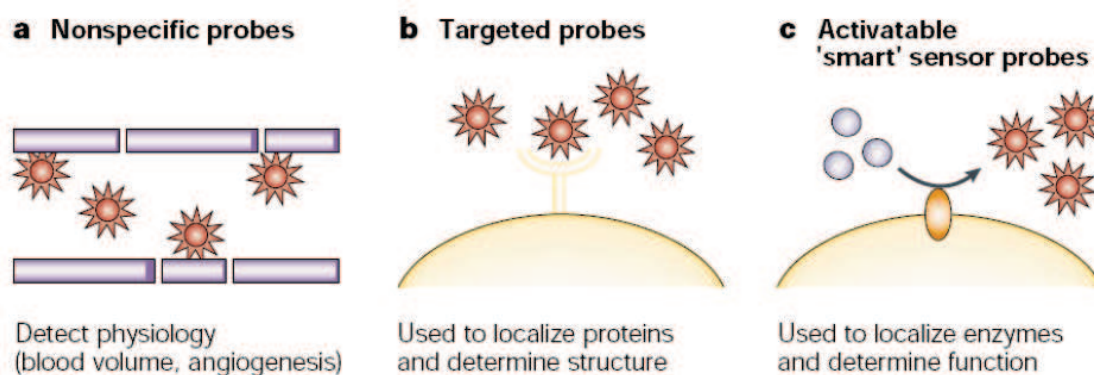


Figure 1.9. Different generations of MR contrast agents [85]. Whereas nonspecific MRI and optical contrast agents (a) show simple perfusion and/or permeability properties of the tissue, (b) targeted probes bind by specific ligands to protein structures on the cell surface (e.g., tumor associated receptors). (c) Smart probes are activated by a specific target interaction (e.g., enzymatic conversion).

1.3.1.1. Targeted contrast agents

They are also called as the affinity-targeted agents. They are linked to specific affinity ligands (vectors) such as peptides, antibody fragments, polysaccharides or small molecules having specificity to an organ or disease site. This concept has potential applications in imaging of important cellular and molecular moieties non-invasively in nano- and picomolar concentrations because they are directed to targets of interest more efficiently, thereby achieving higher local concentrations at lower dosages [86, 87].

Proteins such as intergrin [88, 89]; avidin [90]; folate receptors [91, 92] are some of reported targets. Many other cell receptors or molecular targets, especially those overexpressed in tumors, can be targeted by attaching an affinity ligand to the MR reporter [93-96]. For instance, incorporation of glucose Gd^{3+} -conjugates into the bilayer of nonionic vesicles allowed successful targeted imaging of tumors that overexpress glucose receptors [87, 97].

Combining efficient targeting strategy with sensitivity of optical imaging helps to resolve molecular targets in the nanomolar range *in vivo*. Thus, the detection of cell surface proteins (e.g., tumor associated receptors) is feasible with this approach [86].

1.3.1.2. Smart contrast agents (SCAs)

Also referred to as responsive or activated contrast agents. This class of agents is responsive to changes in physiological surrounding, which make them act as a reporter of their biochemical microenvironment [98]. The smart contrast agents undergo conformational changes upon interaction with the target. This results in significant change in their signal properties (e.g., shortening of T_1 relaxation time) by altering one of the parameters that determine the relaxivity. Frequently this is a change in the number of coordinated water molecules, but there is also the potential to alter the rotational correlation time or the mean water residence lifetime.

For lanthanide-based luminescent probes the change in signal can generally result through one of two methods. Either the metabolite coordinates directly to the metal ion displacing

the quenching water molecule(s), or it binds to another part of the complex altering the energy transfer processes involved in the luminescence. There have been several articles detailing the types and action of luminescence and MRI responsive probes [99-101].

In contrast to targeted contrast agents, the observed change in signal consists of an “off” or “on” status that occurs only in the presence of a threshold concentration of the specific molecule. This makes smart contrast agents ideal candidates for molecular imaging because they provide the highest signal-to-noise ratio for molecular target identification.

a) pH-activated contrast agents.

The main drive behind this area of smart contrast agents is based on the fact that the extracellular physiological pH in tumor and other pathological processes is somewhat more acidic than that of healthy tissue. Therefore triggering MRI contrast agents by pH variation seems like a promising method for highlighting tumors [102]. Many examples of pH-sensitive contrast agents have been reported [103-109]. They undergo relaxation changes by protonation/deprotonation of the complex, by changes in the complex configuration, or by the formation of aggregates as a consequence of changes in pH.

The Gd^{3+} complex of a DOTA- tetramide derivative has been prepared by Sherry et al. who observed an interesting behavior of the agent with change of pH (figure 1.10a) [103]. The relaxivity of the pH-sensitive contrast agent increases when pH increases from 4 to 6, but decreases between pH 6 to 8.5 and is constant between 8.5 and 10.5. Lowe *et al* employed a toluenesulphonamide as a pH labile ligation group in a Gd(DO3A) chelates; as the pH of a solution is reduced, the sulphonamide becomes protonated and dissociates from the metal center (Figure 1.10b) [110]. Later Woods *et al* observed a similar pH-sensitive dissociation in complexes with one *p*-nitrophenolic ligating group (Figure 1.10c) [111]. More recently, Gianolio et al developed a new ratiometric method for measurement the pH based on inclusion of the sulphonamide-based Gd-DO3A complex (R=OMe, figure 1.10b) in liposomes [109]. The amphiphilic metal complex, containing a moiety whose protonation changes the coordination properties of the metal chelate, experiences a difference in

distribution depending on the pH conditions. The ratiometric method consists of measuring the pH dependence of the ratio between the longitudinal paramagnetic contribution to the water proton relaxation rates at two different magnetic fields, thus removing the concentration dependence of the MR signal.

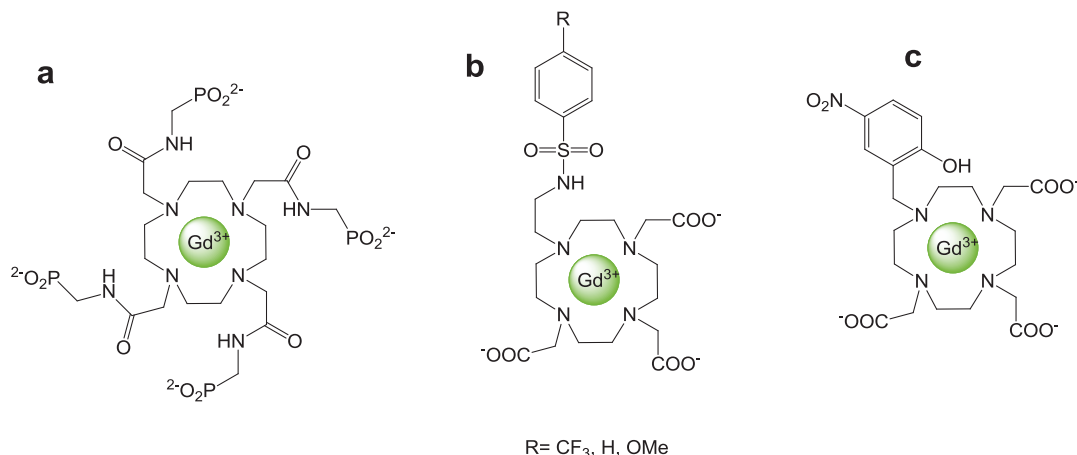


Figure 1.10. Some complexes reported as pH sensitive CAs.

b) Enzyme-activated contrast agents

Enzymes are highly specific biochemical catalysts that function by converting one molecule into another. They are essential for a countless number of biological transformations taking place inside the living organisms [112]. Therefore, the enzymatically modulated MRI CAs could provide an effective means of measuring enzyme activity and detecting enzyme location for disease detection and assaying gene expression purposes. Enzyme targeting has special advantage as a small concentration of the enzyme can catalytically convert a relatively high amount of the enzyme-responsive magnetic probe, decreasing considerably the limit of their detection compared with other biomolecular targets.

Meade and coworkers developed the first example of an enzyme-sensitive MRI CA for gene expression [113, 114]. They demonstrated the principle of enzymatic activation of an MRI CA by β -galactosidase, a frequently used marker enzyme in molecular biology. Attachment of the galactose group to the Gd^{3+} chelate was performed through a β -gal-cleavable linker (figure 1.11a). Enzyme cleavage of the complex results in an open coordination site available for water that creates a detectable MR contrast agent. It has been suggested that

there are two possible mechanisms of water exclusion that is significantly influenced by the linker between the macrocycle and the galactopyranose: one is a steric mechanism where the galactopyranose sugar blocks water from the Gd^{3+} center. The second is consistent with a mechanism in which a bidentate anion occupies two available coordination sites of Gd^{3+} in the precleavage state [115].

This approach for the development of enzymatically activated MR agents has been subject to further improvements, especially in terms of optical properties and cell internalization (figure 1.11b) [116-119].

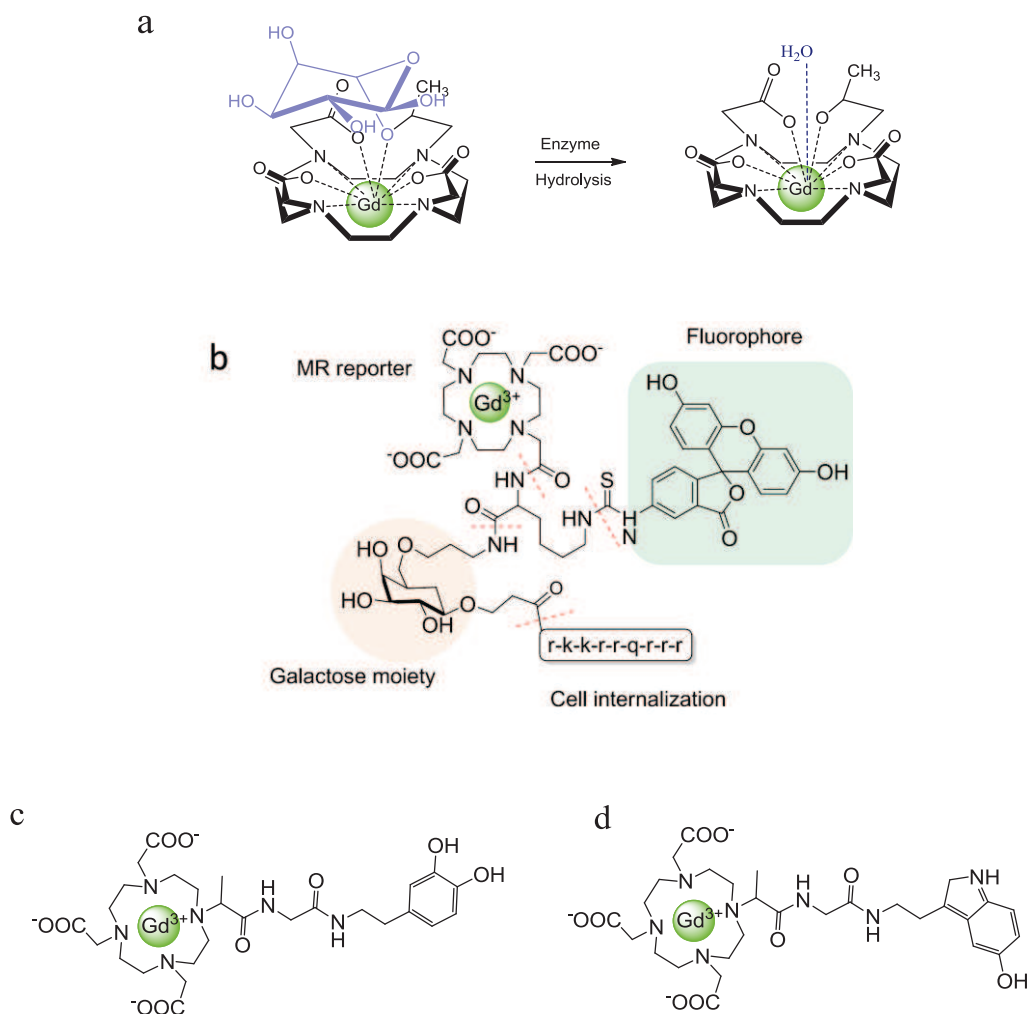


Figure 1.11. Reported compounds as enzyme sensitive CAs

Besides hydrolases, oxidoreductases have also been targets in the exploration of enzyme-sensitive paramagnetic CAs [120-122]. A MR signal amplification strategy has been developed based on enzyme-mediated polymerization of paramagnetic Gd^{3+} substrates into oligomers of higher magnetic relaxivity. Catechol and serotonin which are known to be substrates of oxidized peroxidase and myeloperoxidase respectively were linked to a Gd-DOTA chelate, and the resulting agent acted as a monomer (figures 1.11c-d). In the presence of peroxidase, the monomers were induced to form radical species that trigger the rapid condensation into paramagnetic oligomers leading to manifold increase in r_1 relaxivity due to an increase in τ_R . By this signal amplification mechanism, horseradish peroxidase (HRP) and myeloperoxidase (MPO) could be detected in the nanomolar range [123, 124]. These systems are of the very few examples of responsive Gd^{3+} -agents that have proceeded to *in vivo* experiments.

c) Metal ion responsive contrast agents

Many bivalent metal ions (i.e. Ca^{2+} , Zn^{2+} or Fe^{2+} , etc.) are important modulators of biological mechanisms. Besides, many diseases have been associated to altered metal ion concentration in the body. *In vivo* determination of metal ion distribution is thus highly desirable. A large number of metal-responsive MRI contrast agents, the majority based on Gd^{3+} complexes, have been reported in recent years [125, 126]. The contrast-enhancing properties of a Gd^{3+} complex can be most conveniently modulated by interaction with the sensed metal cation *via* changes in the number of water molecules directly bound to Gd^{3+} or changes in the size of the complex, which represent the two major strategies to develop metal sensitive MRI probes.

The pioneering work in this area was conferred by Li et al. who focused on the important role played by intracellular Ca^{2+} in signal transduction, having developed the complex shown in figure 1.12 [127, 128].

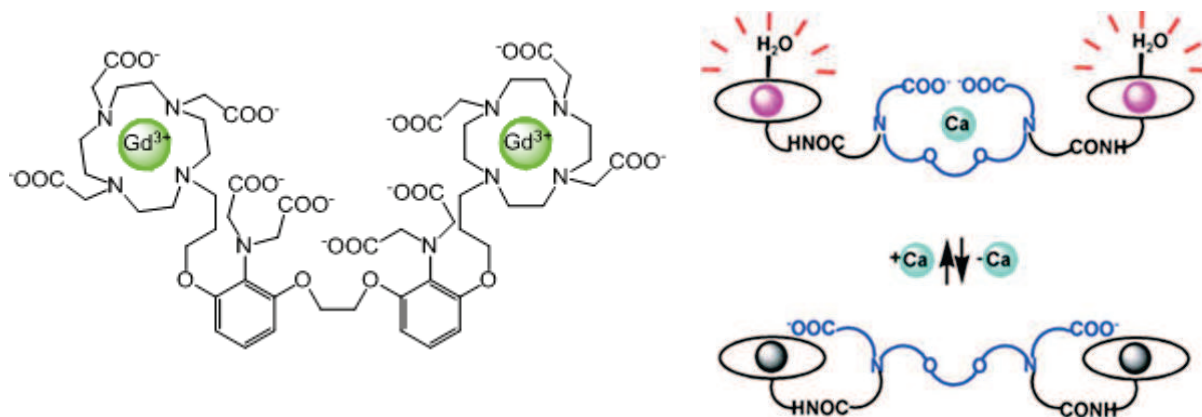


Figure 1.12: Left: GdDOPTA complex responsive to Ca^{2+} . Right: upon interaction with Ca^{2+} , water is allowed to access to the Gd^{3+} chelates exhibiting high and reversible relaxivity change [126].

The molecular design involves changes in the coordination sphere of the Gd^{3+} ion following coordination of Ca^{2+} , depicted in figure 1.12. The acetate arms of the Ca^{2+} chelate that coordinate to Gd^{3+} centre are displaced in the presence of Ca^{2+} . This allows one water molecule to coordinate to each Gd^{3+} centre resulting in an increased relaxivity. This approach represents the most widely used strategy to create Gd-based MRI contrast agents with a relaxivity response not only to calcium, but also to various metal ions.

Improvements to this GdPABTA have been made. For instance, higher relaxivity increase (around 100%) has been reported by Dhingra et al. for a monomeric Ca^{2+} sensitive contrast agent, Gd-DOPTRA (Figure 1.13a). This agent has a good Ca^{2+} selectivity in the presence of Mg^{2+} and Zn^{2+} . In the physiologically more relevant artificial cerebro-spinal fluid and artificial extracellular matrix, the relaxivity changes on Ca^{2+} binding were also as high as 36 and 25%, respectively. Corresponding bismacrocyclic agents containing BAPTA-bisamide (figure 1.13c) exhibit relaxivities comparable to that of monomeric agent. However, only an increase up to 15% has been shown in presence of Ca^{2+} . This change is likely insufficient for *in vivo* MRI detection.

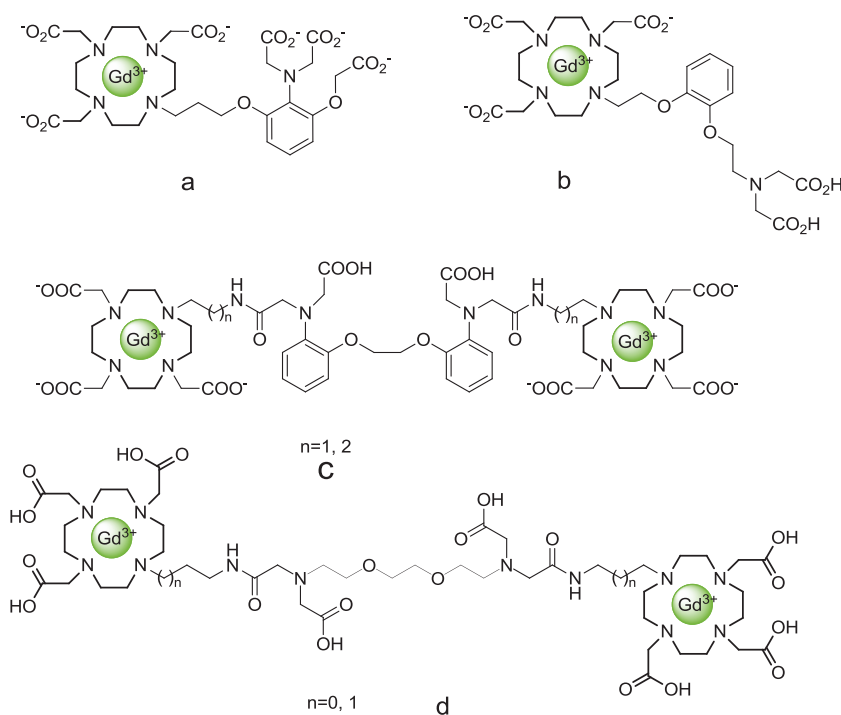


Figure 1.13: Ca^{2+} responsive contrast agents for neurological application.

Similarly, EGTA chelator-based contrast agents were developed (figure 1.13d) and showed up to 83% change in relaxivity *in vitro* and $\sim 10\%$ change under biologically relevant conditions in the relevant range of Ca^{2+} modulation in the brain (0.8–1.2 mM). Previous theoretical studies predict that $\sim 5\%$ signal change is detectable in a time-resolved *in vivo* experiment [129]. Another example of a Ca^{2+} responsive agent containing a catechol moiety (figure 1.13b) showed to be selective towards Ca^{2+} and exhibited a 63% change in relaxivity in presence of competing ions (Na^+ , K^+ , Mg^{2+} , Zn^{2+} and Cu^{2+}) [130]. Some of these Ca^{2+} -responsive agents are currently undergoing *in vivo* tests.

Zinc(II) is another significant metal ion that is considered to be the second most abundant transition metal in human body after iron. It is mostly bound to proteins that play a central role in controlling gene transcription and metalloenzyme function. Selectively sensing Zn^{2+} ions with contrast agents had been first studied by Hanaoka *et al* by using an agent based on the association of a GdDTPA core and *bis*-(2-pyridylmethyl)amine (DPA) (figures 1.14a-b) [131]. Many other examples of Zn^{2+} sensitive probes have been reported since

[132-135]. Que *et al* introduced a SCA (Figure 1.14c) sensitive to copper, [136, 137] an important catalytic co-factor for a variety of metabolic reactions in biological systems (iron transport, oxidative stress protection, cell growth, etc.).

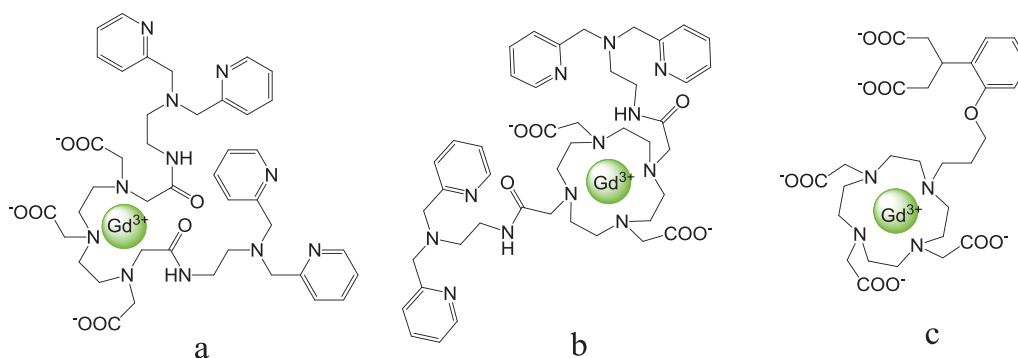


Figure 1.14. some reported SCAs for Zinc (a, b) and Copper (C) sensing.

Unlike targeted CAs, probe design and synthesis of SCAs are more complex, as finding a way to translate physiological activity into notable and measurable changes in MR image contrast, upon interaction with the target, is challenging. This makes this area of research still in a very experimental status and human applications of these probes may less likely be expected within the nearer future.

1.4. Functional molecular imaging of brain activity

1.4.1. Introduction

Neuroimaging studies in humans are highly inclusive, in that one can record activity from all brain areas at the same time, but they lack the ability to tell us anything about the local processes underlying the observed stimulus-induced activation patterns. Localization and comprehension of the neuro-physiological mechanisms underlying our perceptual or cognitive capacities is of obvious importance for a precise understanding of the neural mechanisms underlying dysfunctions, which an essential first step towards the development of pharmacological and behavioral therapies.

The research in the Max Planck Institute (MPI) for Biological Cybernetics concentrates on developing imaging methodologies which could address various intriguing questions regarding neural mechanisms of cognitive functions and *in vivo* connectivity in the primate [138]. Functional magnetic resonance imaging (fMRI) is the major technique that was first used for this purpose [139]. The term Functional Imaging in MRI is a very general term that covers any technique that gives functional information rather than just anatomical one (Flow, perfusion, diffusion, and brain activation). However, when functional magnetic resonance imaging (fMRI) is mentioned it is normally referred to brain activation (BOLD effect) whose signals are driven by the metabolic needs of the active brain cells. Actually, The 'Blood-oxygenation-level-dependent' (BOLD) contrast is based on the endogenous 'smart' contrast agent deoxyhemoglobin in the blood and is triggered by a combination of changes in local blood oxygenation (increase in oxygen consumption due to local increase in glucose), flow and volume that are in turn reflexively triggered by elevated neural activity [139]. The decrease in deoxyhemoglobin, because of its high paramagnetism, produces a decrease in local microscopic field gradients, which in turn produces an increase in T_2^* . This corresponds to an increase in signal, which is measured by the MR equipment.

Although BOLD fMRI still has a tremendous impact in neuroscience, the method provides only an indirect readout of neural activity since the relation between the neuronal activity and hemodynamics is unclear [139]. Efforts have begun to establish quantitative relationships between BOLD fMRI responses and underlying neurophysiology [140]. These studies suggested that the BOLD contrast is affected by the subject-specific cerebrovascular and baseline physiological factors, in addition to neural activity. Thus, this BOLD signal sensitivity to the vascular system complicates efforts to accurately determine the neural activity [140, 141]. Based on this finding, it has been concluded that the existing fMRI methods alone are not sufficient to tackle the brain function since it is unlikely that substantial improvements can still be made in the BOLD technique, because of the complexity of neurovascular coupling. This fact was the driving force behind development of multimodal approaches in the institute that aim to combine fMRI with invasive methods such as electrophysiological measurements (e.g. EEG, conducted with intracortical

microelectrodes which measure extracellular field potentials), neurochemistry and neuropharmacology, etc. Furthermore, the non-invasiveness aspect of fMRI has motivated a growing interest in MRI contrast agents' field as a substitute for BOLD imaging. Indeed, the use of smart MRI contrast agents to assess the neural function allows more precise and accurate measurements of brain function through direct visualization of neural activation independent of the state of the vascular system.

1.4.2. Potentials targets in neuroimaging

In principle, there are only a limited number of potential target events that could be useful for direct measurements of activation in the brain. They include measurements of:

- Changes in extracellular field or transmembrane potentials
- Changes in the concentration of ions (H^+ , Na^+ , K^+ , Cl^- , Ca^{2+} , Mg^{2+})
- Changes in the concentration of neurotransmitters (Gly, Asp, Glu, GABA, acetylcholine, dopamine, serotonin...)
- Changes in the concentration of molecules mediating the neurovascular-coupling (second messengers: cAMP, cGMP, arachidonic acid ...)
- Changes in the concentration of metabolites due to enhanced energy consumption (O_2)

Only the first three methods directly reflect neural activation. The time course of the changes mimics the exact activation of the cells and the spatial specificity of the changes is tightly overlapping with the regional activation induced by a stimulus. The last method relies on the concentration of metabolites and may suffer from some of the disadvantages known for methods relying on hemodynamic responses.

Currently, no suitable extracellular agents are available for monitoring concentration changes of ions or molecules involved in the neural signaling process. However, in principle, some (if not all) of the smart contrast agents mentioned earlier in this chapter might be envisaged as being useful model for designing agents for neural imaging [142].

1.5. Objectives of the thesis

The emerging need for suitable MR imaging probes that have an ability to translate neural activity into detectable MR signal was the drive to perform the present work. Precisely, the long run goal of this research project is to develop extracellular, neurotransmitter-sensitive smart contrast agents that are able to effectively track the brain activity status by contrast change in MR images. The probes are supposed to permit a direct visualization of neural activation independent of the hemodynamics and will reflect more directly changes in neuronal activity.

This thesis includes two major chapters:

Chapter 2 presents the efforts made towards the design and synthesis of lanthanide-based probes for T_1 -weighted MRI. In an attempt to understand the structural factors which govern the interaction of these probes with neurotransmitters, we envisaged a series of five CAs with structural variations in the family. To understand the chemical and coordination processes which are responsible for triggering the changes in the magnetic properties of these CAs, extensive physicochemical studies were conducted. Also, *in vitro* MR relaxation measurements simulating pH-physiological conditions in presence of different neurotransmitters were performed to assess the affinity of these agents to neurotransmitters. This mainly helped to establish a relationship between the relaxivity r_1 and the molecular structure of the responsive SCAs.

Based on the knowledge gained from studying the previous SCAs, chapter 3 focuses on optimizing two aspects *via* the synthesis of two novel smart contrast agents. First, we sought to improve the binding affinity in order to target neurotransmitters more selectively by modulating the SCA structure. Second, we incorporated an appropriate antenna to take advantage of combining optical and MRI modalities for future *in vivo* studies. The synthesis and applicability of this bimodal SCA is discussed in this chapter.

Ultimately, the structural and mechanistic insights drawn from these studies are crucial for future optimized design that can lead to more selective and sensitive SCAs for both optical and MR imaging.

1.6. References:

1. Ralph Weissleder, Mahmood U: **molecular imaging**. *Radiology* 2001(219):316-333.
2. Massoud TF, Gambhir SS: **Molecular imaging in living subjects: seeing fundamental biological processes in a new light**. *Genes & Development* 2003, **17**(5):545-580.
3. Foltz WD, Jaffray DA: **Principles of Magnetic Resonance Imaging**. *Radiat Res* 2012, **177**(4):331-348.
4. Merbach AE, Toth E: **The Chemistry of Contrast Agents in Medical Magnetic Resonance Imaging**: Wiley: New York; 2001.
5. Sharma HA, Lagopoulos J: **MRI physics: pulse sequences**. *Acta Neuropsychiatr* 2010, **22**(2):90-92.
6. Jackson EF, Ginsberg LE, Schomer DF, Leeds NE: **A review of MRI pulse sequences and techniques in neuroimaging**. *Surg Neurol* 1997, **47**(2):185-199.
7. Pysz MA, Gambhir SS, Willmann JK: **Molecular imaging: current status and emerging strategies**. *Clin Radiol* 2010, **65**(7):500-516.
8. James ML, Gambhir SS: **A MOLECULAR IMAGING PRIMER: MODALITIES, IMAGING AGENTS, AND APPLICATIONS**. *Physiol Rev* 2012, **92**(2):897-965.
9. Zhang ZD, Nair SA, McMurry TJ: **Gadolinium meets medicinal chemistry: MRI contrast agent development**. *Current Medicinal Chemistry* 2005, **12**(7):751-778.
10. Kubicek V, Toth E: **DESIGN AND FUNCTION OF METAL COMPLEXES AS CONTRAST AGENTS IN MRI**. In: *Advances in Inorganic Chemistry, Vol 61: Metal Ion Controlled Reactivity*. Edited by VanEldik R, Hubbard CD, vol. 61; 2009: 63-129.
11. Sherry AD, Caravan P, Lenkinski RE: **Primer on Gadolinium Chemistry**. *Journal of Magnetic Resonance Imaging* 2009, **30**(6):1240-1248.
12. Hermann P, Kotek J, Kubicek V, Lukes I: **Gadolinium(III) complexes as MRI contrast agents: ligand design and properties of the complexes**. *Dalton Transactions* 2008(23):3027-3047.
13. Brucher E: **Kinetic stabilities of gadolinium(III) chelates used as MRI contrast agents**. *Contrast Agents I* 2002, **221**:103-122.
14. Port M, Idee JM, Medina C, Robic C, Sabatou M, Corot C: **Efficiency, thermodynamic and kinetic stability of marketed gadolinium chelates and their possible clinical consequences: a critical review**. *Biomaterials* 2008, **21**(4):469-490.
15. Wang XY, Jin TZ, Comblin V, Lopezmut A, Merciny E, Desreux JF: **A KINETIC INVESTIGATION OF THE LANTHANIDE DOTA CHELATES - STABILITY AND RATES OF FORMATION AND OF DISSOCIATION OF A MACROCYCLIC GADOLINIUM(III) POLYAZA POLYCARBOXYLIC MRI CONTRAST AGENT**. *Inorganic Chemistry* 1992, **31**(6):1095-1099.
16. Caravan P, Ellison JJ, McMurry TJ, Lauffer RB: **Gadolinium(III) chelates as MRI contrast agents: Structure, dynamics, and applications**. *Chem Rev* 1999, **99**(9):2293-2352.
17. Bloembergen N, Purcell EM, Pound RV: **RELAXATION EFFECTS IN NUCLEAR MAGNETIC RESONANCE ABSORPTION**. *Physical Review* 1948, **73**(7):679-712.
18. Solomon I: **RELAXATION PROCESSES IN A SYSTEM OF 2 SPINS**. *Physical Review* 1955, **99**(2):559-565.
19. Solomon I, Bloembergen N: **NUCLEAR MAGNETIC INTERACTIONS IN THE HF MOLECULE**. *J Chem Phys* 1956, **25**(2):261-266.
20. Bloembergen N: **PROTON RELAXATION TIMES IN PARAMAGNETIC SOLUTIONS**. *J Chem Phys* 1957, **27**(2):572-573.
21. Bloembergen N, Morgan LO: **PROTON RELAXATION TIMES IN PARAMAGNETIC SOLUTIONS EFFECTS OF ELECTRON SPIN RELAXATION**. *J Chem Phys* 1961, **34**(3):842-&.

22. Steele ML, Wertz DL: **SOLUTE COMPLEXES IN AQUEOUS GADOLINIUM(III) CHLORIDE SOLUTIONS.** *J Am Chem Soc* 1976, **98**(15):4424-4428.
23. Yamaguchi T, Nomura M, Wakita H, Ohtaki H: **AN EXTENDED X-RAY ABSORPTION FINE-STRUCTURE STUDY OF AQUEOUS RARE-EARTH PERCHLORATE SOLUTIONS IN LIQUID AND GLASSY STATES.** *J Chem Phys* 1988, **89**(8):5153-5159.
24. Cossy C, Barnes AC, Enderby JE, Merbach AE: **THE HYDRATION OF DY-3+ AND YB-3+ IN AQUEOUS-SOLUTION - A NEUTRON-SCATTERING 1ST-ORDER DIFFERENCE STUDY.** *J Chem Phys* 1989, **90**(6):3254-3260.
25. Benazeth S, Purans J, Chalbot MC, Nguyen-van-Duong MK, Nicolas L, Keller F, Gaudemer A: **Temperature and pH dependence XAFS study of Gd(DOTA)(-) and Gd(DTPA)(2-) complexes: Solid state and solution structures.** *Inorganic Chemistry* 1998, **37**(15):3667-3674.
26. Caravan P, Astashkin AV, Raitsimring AM: **The gadolinium(III)-water hydrogen distance in MRI contrast agents.** *Inorganic Chemistry* 2003, **42**(13):3972-3974.
27. Toth E, Helm L, Merbach AE: **Relaxivity of MRI contrast agents.** *Contrast Agents I* 2002, **221**:61-101.
28. Caravan P, Farrar CT, Frullano L, Uppal R: **Influence of molecular parameters and increasing magnetic field strength on relaxivity of gadolinium- and manganese-based T(1) contrast agents.** *Contrast Media Mol Imaging* 2009, **4**(2):89-100.
29. Aime S, Botta M, Fasano M, Terreno E: **Prototropic and water-exchange processes in aqueous solutions of Gd(III) chelates.** *Accounts Chem Res* 1999, **32**(11):941-949.
30. Laurent S, Elst LV, Botteman F, Muller RN: **An Assessment of the Potential Relationship between the Charge of Gd-DTPA Complexes and the Exchange Rate of the Water Coordinated to the Metal.** *European Journal of Inorganic Chemistry* 2008(28):4369-4379.
31. Zhang SR, Kovacs Z, Burgess S, Aime S, Terreno E, Sherry AD: **(DOTA-bis(amide))lanthanide complexes: NMR evidence for differences in water-molecule exchange rates for coordination isomers.** *Chemistry-a European Journal* 2001, **7**(1):288-296.
32. Karfeld-Sulzer LS, Waters EA, Davis NE, Meade TJ, Barron AE: **Multivalent Protein Polymer MRI Contrast Agents: Controlling Relaxivity via Modulation of Amino Acid Sequence.** *Biomacromolecules* 2010, **11**(6):1429-1436.
33. Yang JJ, Yang J, Wei L, Zurkiya O, Yang W, Li S, Zou J, Zhou Y, Maniccia ALW, Mao H *et al*: **Rational design of protein-based MRI contrast agents.** *J Am Chem Soc* 2008, **130**(29):9260-9267.
34. Andre JP, Toth E, Fischer H, Seelig A, Macke HR, Merbach AE: **High relaxivity for monomeric Gd(DOTA)-based MRI contrast agents, thanks to micellar self-organization.** *Chemistry-a European Journal* 1999, **5**(10):2977-2983.
35. Torres S, Martins JA, Andre JP, Geraldes C, Merbach AE, Toth E: **Supramolecular assembly of an amphiphilic Gd-III chelate: Tuning the reorientational correlation time and the water exchange rate.** *Chemistry-a European Journal* 2006, **12**(3):940-948.
36. Wiener EC, Auteri FP, Chen JW, Brechbiel MW, Gansow OA, Schneider DS, Belford RL, Clarkson RB, Lauterbur PC: **Molecular dynamics of ion-chelate complexes attached to dendrimers.** *J Am Chem Soc* 1996, **118**(33):7774-7782.
37. Yan G, Ai C, Li L, Zong R, Liu F: **Dendrimers as carriers for contrast agents in magnetic resonance imaging.** *Chinese Science Bulletin* 2010, **55**(27-28):3085-3093.
38. Miyake Y, Kimura Y, Ishikawa S, Tsujita H, Miura H, Narazaki M, Matsuda T, Tabata Y, Yano T, Toshimitsu A *et al*: **Synthesis and functional evaluation of chiral dendrimer-triamine-coordinated Gd complexes as highly sensitive MRI contrast agents.** *Tetrahedron Letters* 2012, **53**(34):4580-4583.

39. Battistini E, Gianolio E, Gref R, Couvreur P, Fuzerova S, Othman M, Aime S, Badet B, Durand P: **High-relaxivity magnetic resonance imaging (MRI) contrast agent based on supramolecular assembly between a gadolinium chelate, a modified dextran, and poly-beta-cyclodextrin.** *Chemistry-a European Journal* 2008, **14**(15):4551-4561.
40. Jacques V, Dumas S, Sun WC, Troughton JS, Greenfield MT, Caravan P: **High-Relaxivity Magnetic Resonance Imaging Contrast Agents Part 2 Optimization of Inner- and Second-Sphere Relaxivity.** *Invest Radiol* 2010, **45**(10):613-624.
41. Botta M, Tei L: **Relaxivity Enhancement in Macromolecular and Nanosized GdIII-Based MRI Contrast Agents.** *European Journal of Inorganic Chemistry* 2012, **2012**(12):1945-1960.
42. Li Y, Beija M, Laurent S, vander Elst L, Muller RN, Duong HTT, Lowe AB, Davis TP, Boyer C: **Macromolecular Ligands for Gadolinium MRI Contrast Agents.** *Macromolecules* 2012, **45**(10):4196-4204.
43. Makino A, Harada H, Okada T, Kimura H, Amano H, Saji H, Hiraoka M, Kimura S: **Effective encapsulation of a new cationic gadolinium chelate into apoferritin and its evaluation as an MRI contrast agent.** *Nanomedicine-Nanotechnology Biology and Medicine* 2011, **7**(5):638-646.
44. Aime S, Frullano L, Crich SG: **Compartmentalization of a gadolinium complex in the apoferritin cavity: A route to obtain high relaxivity contrast agents for magnetic resonance imaging.** *Angewandte Chemie-International Edition* 2002, **41**(6):1017-+.
45. Briley-Saebo KC, Geninatti-Crich S, Cormode DP, Barazza A, Mulder WJM, Chen W, Giovenzana GB, Fisher EA, Aime S, Fayad ZA: **High-Relaxivity Gadolinium-Modified High-Density Lipoproteins as Magnetic Resonance Imaging Contrast Agents.** *Journal of Physical Chemistry B* 2009, **113**(18):6283-6289.
46. Cormode DP, Mulder WJM, Fisher EA, Fayad ZA: **Modified lipoproteins as contrast agents for molecular imaging.** *Future Lipidology* 2007, **2**(6):587-590.
47. Helm L: **Optimization of gadolinium-based MRI contrast agents for high magnetic-field applications.** *Future Medicinal Chemistry* 2010, **2**(3):385-396.
48. !!! INVALID CITATION !!!
49. Mansfield JR: **Distinguished Photons: A Review of In Vivo Spectral Fluorescence Imaging in Small Animals.** *Curr Pharm Biotechnol* 2010, **11**(6):628-638.
50. Prescher JA, Contag CH: **Guided by the light: visualizing biomolecular processes in living animals with bioluminescence.** *Curr Opin Chem Biol* 2010, **14**(1):80-89.
51. Bunzli JCG: **Lanthanide Luminescence for Biomedical Analyses and Imaging.** *Chem Rev* 2010, **110**(5):2729-2755.
52. Elbanowski M, Makowsaka B: **The lanthanides as luminescent probes in investigations of biochemical systems.** *J Photochem Photobiol A-Chem* 1996, **99**(2-3):85-92.
53. Yam VWW, Lo KKW: **Recent advances in utilization of transition metal complexes and lanthanides as diagnostic tools.** *Coord Chem Rev* 1999, **184**:157-240.
54. Petoud S, Shade CM, Uh H, Gogick K, Thompson ZP: **Luminescent dendrimer complexes for in vivo biologic imaging.** *Abstr Pap Am Chem Soc* 2009, **238**.
55. Bonnet CS, Buron F, Caille F, Shade CM, Drahos B, Pellegatti L, Zhang J, Villette S, Helm L, Pichon C *et al*: **Pyridine-Based Lanthanide Complexes Combining MRI and NIR Luminescence Activities.** *Chemistry-a European Journal* 2012, **18**(5):1419-1431.
56. Long NJ, Bottrill M, Sae-Heng M, So PW: **Probes for dual MRI-optical imaging.** *Abstr Pap Am Chem Soc* 2009, **238**.
57. Bonnet CS, Tóth É: **Towards highly efficient, intelligent and bimodal imaging probes: Novel approaches provided by lanthanide coordination chemistry.** *Comptes Rendus Chimie* 2010, **13**(6-7):700-714.

58. Bunzli JCG, Piguet C: **Taking advantage of luminescent lanthanide ions.** *Chemical Society Reviews* 2005, **34**(12):1048-1077.
59. Bunzli JCG: **Lanthanide-containing luminescent molecular edifices.** *J Alloy Compd* 2006, **408**:934-944.
60. Bunzli JCG, Eliseeva SV: **Lanthanide NIR luminescence for telecommunications, bioanalyses and solar energy conversion.** *J Rare Earths* 2010, **28**(6):824-842.
61. Simon C: **Lanthanide and Actinide Chemistry** West Sussex, England 2006.
62. Galgano F, Favati F, Caruso M, Scarpa T, Palma A: **Analysis of trace elements in southern Italian wines and their classification according to provenance.** *LWT - Food Science and Technology* 2008, **41**(10):1808-1815.
63. Petoud S, Cohen SM, Bunzli JCG, Raymond KN: **Stable lanthanide luminescence agents highly emissive in aqueous solution: Multidentate 2-hydroxyisophthalamide complexes of SM3+, Eu3+, Tb3+, Dy3+.** *Journal of the American Chemical Society* 2003, **125**(44):13324-13325.
64. Bunzli JCG: **Luminescent lanthanide probes as diagnostic and therapeutic tools.** *Metal Ions in Biological Systems, Vol 42: Metal Complexes in Tumor Diagnosis and as Anticancer Agents* 2004, **42**:39-75.
65. Shannon RD: **REVISED EFFECTIVE IONIC-RADII AND SYSTEMATIC STUDIES OF INTERATOMIC DISTANCES IN HALIDES AND CHALCOGENIDES.** *Acta Crystallographica Section A* 1976, **32**(SEP1):751-767.
66. Idee JM, Port M, Raynal I, Schaefer M, Le Greneur S, Corot C: **Clinical and biological consequences of transmetallation induced by contrast agents for magnetic resonance imaging: a review.** *Fundam Clin Pharmacol* 2006, **20**(6):563-576.
67. Itoh N, Kawakita M: **CHARACTERIZATION OF GD-3+ AND TB-3+ BINDING-SITES ON CA-2+, MG-2+-ADENOSINE TRIPHOSPHATASE OF SARCOPLASMIC-RETICULUM.** *J Biochem* 1984, **95**(3):661-669.
68. Uh H, Petoud S: **Novel antennae for the sensitization of near infrared luminescent lanthanide cations.** *Comptes Rendus Chimie* 2010, **13**(6-7):668-680.
69. Ramirez FD, Varbanov S, Cecile C, Muller G, Fatin-Rouge N, Scopelliti R, Bunzli JCG: **A p-tert-butylcalix 6 arene bearing phosphinoyl pendant arms for the complexation and sensitisation of lanthanide ions.** *Journal of the Chemical Society-Dalton Transactions* 2002(23):4505-4513.
70. Marriott G, Heidecker M, Diamandis EP, Yanmarriott Y: **TIME-RESOLVED DELAYED LUMINESCENCE IMAGE MICROSCOPY USING AN EUROPIUM ION CHELATE COMPLEX.** *Biophys J* 1994, **67**(3):957-965.
71. Eliseeva SV, Bunzli J-CG: **Lanthanide luminescence for functional materials and bio-sciences.** *Chemical Society Reviews* 2010, **39**(1):189-227.
72. D'Aleo A, Pointillart F, Ouahab L, Andraud C, Maury O: **Charge transfer excited states sensitization of lanthanide emitting from the visible to the near-infra-red.** *Coord Chem Rev* 2012, **256**(15-16):1604-1620.
73. Thibon A, Pierre VC: **Principles of responsive lanthanide-based luminescent probes for cellular imaging.** *Analytical and Bioanalytical Chemistry* 2009, **394**(1):107-120.
74. Parker D, Williams JAG: **Getting excited about lanthanide complexation chemistry.** *Journal of the Chemical Society-Dalton Transactions* 1996(18):3613-3628.
75. Bunzli JCG, Piguet C: **Lanthanide-containing molecular and supramolecular polymetallic functional assemblies.** *Chemical Reviews* 2002, **102**(6):1897-1928.

76. Beeby A, Bushby LM, Maffeo D, Williams JAG: **The efficient intramolecular sensitisation of terbium(III) and europium(III) by benzophenone-containing ligands.** *J Chem Soc-Perkin Trans 2* 2000(7):1281-1283.
77. Leonard JP, Nolan CB, Stomeo F, Gunnlaugsson T: **Photochemistry and photophysics of coordination compounds: Lanthanides.** In: *Photochemistry and Photophysics of Coordination Compounds II*. Edited by Balzani V, Campagna S, vol. 281. Berlin: Springer-Verlag Berlin; 2007: 1-43.
78. Dickins RS, Parker D, deSousa AS, Williams JAG: **Closely diffusing O-H, amide N-H and methylene C-H oscillators quench the excited state of europium complexes in solution.** *Chem Commun* 1996(6):697-698.
79. Beeby A, Clarkson IM, Dickins RS, Faulkner S, Parker D, Royle L, de Sousa AS, Williams JAG, Woods M: **Non-radiative deactivation of the excited states of europium, terbium and ytterbium complexes by proximate energy-matched OH, NH and CH oscillators: an improved luminescence method for establishing solution hydration states.** *J Chem Soc-Perkin Trans 2* 1999(3):493-503.
80. Horrocks WD, Sudnick DR: **LANTHANIDE ION PROBES OF STRUCTURE IN BIOLOGY - LASER-INDUCED LUMINESCENCE DECAY CONSTANTS PROVIDE A DIRECT MEASURE OF THE NUMBER OF METAL-COORDINATED WATER-MOLECULES.** *J Am Chem Soc* 1979, **101**(2):334-340.
81. Faulkner S, Pope SJA, Burton-Pye BP: **Lanthanide complexes for luminescence imaging applications.** *Applied Spectroscopy Reviews* 2005, **40**(1):1-31.
82. D Parker GW: **Responsive luminescent lanthanide complexes in Lanthanide ions and their interactions with biological systems:** Marcel Dekker New York; 2003.
83. Caille F, Bonnet CS, Buron F, Villette S, Helm L, Petoud S, Suzenet F, Toth E: **Isoquinoline-based lanthanide complexes: bright NIR optical probes and efficient MRI agents.** *Inorg Chem* 2012, **51**(4):2522-2532.
84. Strijkers GJ, Mulder WJM, van Tilborg GAF, Nicolay K: **MRI contrast agents: Current status and future perspectives.** *Anti-Cancer Agents in Medicinal Chemistry* 2007, **7**(3):291-305.
85. Vierling JMLaP: **The [18]-N3O3 aza-oxa Macrocyclic: a Selective Receptor Unit for Primary Ammonium Cations.** *Tetrahedron Letters* 1980, **21**:1323-1326.
86. Hellebust A, Richards-Kortum R: **Advances in molecular imaging: targeted optical contrast agents for cancer diagnostics.** *Nanomedicine* 2012, **7**(3):429-445.
87. Geraldine C, Djanashvili K, Peters JA: **Glycoconjugate probes and targets for molecular imaging using magnetic resonance.** *Future Medicinal Chemistry* 2010, **2**(3):409-425.
88. Caravan P: **Protein-Targeted Gadolinium-Based Magnetic Resonance Imaging (MRI) Contrast Agents: Design and Mechanism of Action.** *Accounts Chem Res* 2009, **42**(7):851-862.
89. Verwilt P, Eliseeva SV, Vander Elst L, Burtea C, Laurent S, Petoud S, Muller RN, Parac-Vogt TN, De Borggraeve WM: **A Tripodal Ruthenium-Gadolinium Metallostar as a Potential $\alpha(v)\beta(3)$ Integrin Specific Bimodal Imaging Contrast Agent.** *Inorganic Chemistry* 2012, **51**(11):6405-6411.
90. Mishra A, Pfeuffer J, Mishra R, Engelmann J, Mishra AK, Ugurbil K, Logothetis NK: **A new class of Gd-based DO3A-ethylamine-derived targeted contrast agents for MR and optical imaging.** *Bioconjugate chemistry* 2006, **17**(3):773-780.
91. Konda SD, Aref M, Wang S, Brechbiel M, Wiener EC: **Specific targeting of folate-dendrimer MRI contrast agents to the high affinity folate receptor expressed in ovarian tumor xenografts.** *Magnetic Resonance Materials in Physics Biology and Medicine* 2001, **12**(2-3):104-113.

92. Kalber TL, Kamaly N, So P-W, Pugh JA, Bunch J, McLeod CW, Jorgensen MR, Miller AD, Bell JD: **A Low Molecular Weight Folate Receptor Targeted Contrast Agent for Magnetic Resonance Tumor Imaging.** *Molecular Imaging and Biology* 2011, **13**(4):653-662.
93. Sukerkar PA, MacRenaris KW, Townsend TR, Ahmed RA, Burdette JE, Meade TJ: **Synthesis and Biological Evaluation of Water-Soluble Progesterone-Conjugated Probes for Magnetic Resonance Imaging of Hormone Related Cancers.** *Bioconjugate chemistry* 2011, **22**(11):2304-2316.
94. Pu Y, Wang WB, Tang GC, Zeng F, Achilefu S, Vitenson JH, Sawczuk I, Peters S, Lombardo JM, Alfano RR: **Spectral polarization imaging of human prostate cancer tissue using a near-infrared receptor-targeted contrast agent.** *Technology in Cancer Research & Treatment* 2005, **4**(4):429-436.
95. Sturzu A, Heckl S: **Magnetic Resonance Imaging of Human Glioma Cells by means of an Interleukin-6 Receptor-Targeted Contrast Agent.** *Chemical Biology & Drug Design* 2010, **75**(4):369-374.
96. Prata MIM, Santos AC, Torres S, Andre JP, Martins JA, Neves M, Garcia-Martin ML, Rodrigues TB, Lopez-Larrubia P, Cerdan S *et al*: **Targeting of lanthanide(III) chelates of DOTA-type glycoconjugates to the hepatic asialoglycoprotein receptor: cell internalization and animal imaging studies.** *Contrast Media Mol Imaging* 2006, **1**(6):246-258.
97. Alain Luciani, Jean-Christophe Olivier, Olivier Clement, Nathalie Siauve, Pierre-Yves Brillet, Bertrand Bessoud, Florence Gazeau, Ijeoma F. Uchegbu, Edmond Kahn, Guy Frija *et al*: **Glucose-Receptor MR Imaging of Tumors: Study in Mice with PEGylated Paramagnetic Niosomes.** *Radiology* 2004(231):135.
98. Chuqiao T, Osborne EA, Louie AY: **Activatable T1 and T2 Magnetic Resonance Imaging Contrast Agents.** *Ann Biomed Eng* 2011, **39**(4):1335-1348.
99. David P: **Luminescent lanthanide sensors for pH, pO₂ and selected anions.** *Coord Chem Rev* 2000(205):109-130.
100. Meade TJ, Taylor AK, Bull SR: **New magnetic resonance contrast agents as biochemical reporters.** *Curr Opin Neurobiol* 2003, **13**(5):597-602.
101. Major JL, Boiteau RM, Meade TJ: **Mechanisms of Zn(II)-Activated Magnetic Resonance Imaging Agents.** *Inorganic Chemistry* 2008, **47**(22):10788-10795.
102. Perez-Mayoral E, Negri V, Soler-Padros J, Cerdan S, Ballesteros P: **Chemistry of paramagnetic and diamagnetic contrast agents for Magnetic Resonance Imaging and Spectroscopy pH responsive contrast agents.** *Eur J Radiol* 2008, **67**(3):453-458.
103. Zhang SR, Wu KC, Sherry AD: **A novel pH-sensitive MRI contrast agent.** *Angewandte Chemie-International Edition* 1999, **38**(21):3192-3194.
104. Aime S, Delli Castelli D, Terreno E: **Novel pH-reporter MRI contrast agents.** *Angewandte Chemie-International Edition* 2002, **41**(22):4334-4336.
105. Kalman FK, Woods M, Caravan P, Jurek P, Spiller M, Tircso G, Kiraly R, Brucher E, Sherry AD: **Potentiometric and relaxometric properties of a gadolinium-based MRI contrast agent for sensing tissue pH.** *Inorganic Chemistry* 2007, **46**(13):5260-5270.
106. Giovenzana GB, Negri R, Rolla GA, Tei L: **Gd-Aminoethyl-DO3A Complexes: A Novel Class of pH-Sensitive MRI Contrast Agents.** *European Journal of Inorganic Chemistry* 2012(12):2035-2039.
107. Okada S, Mizukami S, Kikuchi K: **Switchable MRI contrast agents based on morphological changes of pH-responsive polymers.** *Bioorganic & Medicinal Chemistry* 2012, **20**(2):769-774.

108. Lokling KE, Fossheim SL, Skurtveit R, Bjornerud A, Klaveness J: **pH-sensitive paramagnetic liposomes as MRI contrast agents: in vitro feasibility studies.** *Magnetic Resonance Imaging* 2001, **19**(5):731-738.
109. Gianolio E, Porto S, Napolitano R, Baroni S, Giovenzana GB, Aime S: **Relaxometric Investigations and MRI Evaluation of a Liposome-Loaded pH-Responsive Gadolinium(III) Complex.** *Inorganic Chemistry* 2012, **51**(13):7210-7217.
110. Lowe MP, Parker D, Reany O, Aime S, Botta M, Castellano G, Gianolio E, Pagliarin R: **pH-dependent modulation of relaxivity and luminescence in macrocyclic gadolinium and europium complexes based on reversible intramolecular sulfonamide ligation.** *J Am Chem Soc* 2001, **123**(31):7601-7609.
111. Woods M, Kiefer GE, Bott S, Castillo-Muzquiz A, Eshelbrenner C, Michaudet L, McMillan K, Mudigunda SDK, Grin D, Tircso G *et al*: **Synthesis, relaxometric and photophysical properties of a new pH-Responsive MRI contrast agent: The effect of other ligating groups on dissociation of a p-nitrophenolic pendant arm.** *J Am Chem Soc* 2004, **126**(30):9248-9256.
112. van Beilen JB, Li Z: **Enzyme technology: an overview.** *Current Opinion in Biotechnology* 2002, **13**(4):338-344.
113. Moats RA, Fraser SE, Meade TJ: **A "smart" magnetic resonance imaging agent that reports on specific enzymatic activity.** *Angewandte Chemie-International Edition in English* 1997, **36**(7):726-728.
114. Louie AY, Huber MM, Ahrens ET, Rothbacher U, Moats R, Jacobs RE, Fraser SE, Meade TJ: **In vivo visualization of gene expression using magnetic resonance imaging.** *Nature Biotechnology* 2000, **18**(3):321-325.
115. Lauren M. Urbanczyk-Pearson, Frank J. Femia, Jeffrey Smith, Giacomo Parigi, Joseph A. Duimstra, Amanda L. Eckermann, Claudio Luchinat aTJM: **Mechanistic Investigation of beta-Galactosidase-Activated MR Contrast Agents**, vol. 47: *Inorganic Chemistry*; 2008.
116. Alauddin MM, Louie AY, Shahinian A, Meade TJ, Conti PS: **Receptor mediated uptake of a radiolabeled contrast agent sensitive to beta-galactosidase activity.** *Nuclear Medicine and Biology* 2003, **30**(3):261-265.
117. Hanaoka K, Kikuchi K, Terai T, Komatsu T, Nagano T: **A Gd³⁺-based magnetic resonance imaging contrast agent sensitive to beta-galactosidase activity utilizing a receptor-induced magnetization enhancement (RIME) phenomenon.** *Chemistry-a European Journal* 2008, **14**(3):987-995.
118. Keliris A, Ziegler T, Mishra R, Pohmann R, Sauer MG, Ugurbil K, Engelmann J: **Synthesis and characterization of a cell-permeable bimodal contrast agent targeting beta-galactosidase.** *Bioorganic & Medicinal Chemistry* 2011, **19**(8):2529-2540.
119. Chauvin T, Torres S, Rosseto R, Kotek J, Badet B, Durand P, Toth E: **Lanthanide(III) Complexes That Contain a Self-Immolative Arm: Potential Enzyme Responsive Contrast Agents for Magnetic Resonance Imaging.** *Chemistry-a European Journal* 2012, **18**(5):1408-1418.
120. Rodriguez E, Nilges M, Weissleder R, Chen JW: **Activatable Magnetic Resonance Imaging Agents for Myeloperoxidase Sensing: Mechanism of Activation, Stability, and Toxicity.** *J Am Chem Soc* 2010, **132**(1):168-177.
121. Querol M, Chen JW, Bogdanov AA: **A paramagnetic contrast agent with myeloperoxidase-sensing properties.** *Organic & Biomolecular Chemistry* 2006, **4**(10):1887-1895.
122. Ronald JA, Chen JW, Chen Y, Hamilton AM, Rodriguez E, Reynolds F, Hegele RA, Rogers KA, Querol M, Bogdanov A *et al*: **Enzyme-Sensitive Magnetic Resonance Imaging Targeting Myeloperoxidase Identifies Active Inflammation in Experimental Rabbit Atherosclerotic Plaques.** *Circulation* 2009, **120**(7):592-U592.

123. Bogdanov A, Matuszewski L, Bremer C, Petrovsky A, Weissleder R: **Oligomerization of paramagnetic substrates result in signal amplification and can be used for MR imaging of molecular targets.** *Molecular Imaging* 2002, **1**(1):16-23.
124. Chen JW, Pham W, Weissleder R, Bogdanov A: **Human myeloperoxidase: A potential target for molecular MR imaging in atherosclerosis.** *Magnetic Resonance in Medicine* 2004, **52**(5):1021-1028.
125. Bonnet CS, Toth E: **MRI probes for sensing biologically relevant metal ions.** *Future Medicinal Chemistry* 2010, **2**(3):367-384.
126. Cai K: **Magnetic resonance imaging of glutamate.** *Nature Medecine* 2012, **18**(2):302-306.
127. Li WH, Fraser SE, Meade TJ: **A calcium-sensitive magnetic resonance imaging contrast agent.** *J Am Chem Soc* 1999, **121**(6):1413-1414.
128. Li WH, Parigi G, Fragai M, Luchinat C, Meade TJ: **Mechanistic studies of a calcium-dependent MRI contrast agent.** *Inorganic Chemistry* 2002, **41**(15):4018-4024.
129. Jasanoff A, Shapiro MG, Atanasijevic T, Faas H, Westmeyer GG: **Dynamic imaging with MRI contrast agents: quantitative considerations.** *Magnetic Resonance Imaging* 2006, **24**(4):449-462462.
130. Mamedov I, Logothetis NK, Angelovski G: **Structure-related variable responses of calcium sensitive MRI probes.** *Org Biomol Chem* 2011, **9**(16):5816-5824.
131. Hanaoka K, Kikuchi K, Urano Y, Nagano T: **Selective sensing of zinc ions with a novel magnetic resonance imaging contrast agent.** *J Chem Soc-Perkin Trans 2* 2001(9):1840-1843.
132. Hanaoka K, Kikuchi K, Urano Y, Narazaki M, Yokawa T, Sakamoto S, Yamaguchi K, Nagano T: **Design and synthesis of a novel magnetic resonance imaging contrast agent for selective sensing of zinc ion.** *Chemistry & Biology* 2002, **9**(9):1027-1032.
133. Major JL, Parigi G, Luchinat C, Meade TJ: **The synthesis and in vitro testing of a zinc-activated MRI contrast agent.** *Proceedings of the National Academy of Sciences of the United States of America* 2007, **104**(35):13881-13886.
134. Xiao-an Z, Lovejoy KS, Jasanoff A, Lippard SJ: **Water-soluble porphyrins as a dual-function molecular imaging platform for MRI and fluorescence zinc sensing.** *Proceedings of the National Academy of Sciences of the United States of America* 2007, **104**(26):10780-10785.
135. Esqueda AC, Lopez JA, Andreu-de-Riquer G, Alvarado-Monzon JC, Ratnakar J, Lubag AJM, Sherry AD, De Leon-Rodriguez LM: **A New Gadolinium-Based MRI Zinc Sensor.** *J Am Chem Soc* 2009, **131**(32):11387-11391.
136. Que EL, Chang CJ: **A smart magnetic resonance contrast agent for selective copper sensing.** *J Am Chem Soc* 2006, **128**(50):15942-15943.
137. Que EL, Gianolio E, Baker SL, Aime S, Chang CJ: **A copper-activated magnetic resonance imaging contrast agent with improved turn-on relaxivity response and anion compatibility.** *Dalton Transactions* 2010, **39**(2):469-476.
138. Logothetis NK: **Intracortical recordings and fMRI: an attempt to study operational modules and networks simultaneously.** *NeuroImage* 2012, **62**(2):962-969.
139. Logothetis NK: **What we can do and what we cannot do with fMRI.** *Nature* 2008, **453**(7197):869-878.
140. Logothetis NK, Pauls J, Augath M, Trinath T, Oeltermann A: **Neurophysiological investigation of the basis of the fMRI signal.** *Nature* 2001, **412**(6843):150-157.
141. Kannurpatti SS, Motes MA, Rypma B, Biswal BB: **Neural and vascular variability and the fMRI-BOLD response in normal aging.** *Magnetic Resonance Imaging* 2010, **28**(4):466-476.
142. Bonnet CS, Toth E: **Smart MR imaging agents relevant to potential neurologic applications.** *AJNR American journal of neuroradiology* 2010, **31**(3):401-409.

2

Lanthanide-based Smart Contrast Agents for Sensing Neurotransmitters

CHAPTER 2. LANTHANIDE-BASED SMART CONTRAST AGENTS FOR SENSING

NEUROTRANSMITTERS	62
2.1. INTRODUCTION	64
2.1.1. Detection of neurotransmitters	66
2.1.1.1. Voltammetry.....	66
2.1.1.2. Microdialysis.....	66
2.1.2 MRI contrast agents sensitive to dopamine.....	68
2.2. DESIGN OF Ln^{3+}-BASED COMPLEXES RESPONSIVE TO NEUROTRANSMITTERS	69
2.3. SYNTHESIS OF THE COMPLEXES.....	73
2.3.1 Synthesis of ligands L^{5-6}	74
2.3.2 Synthesis of ligand L^7	77
2.3.3. Synthesis of ligand L^{10}	78
2.3.4. Synthesis of ligand L^{11}	78
2.4. RESULTS AND DISCUSSION	79
2.4.1. pH-potentiometry.....	80
2.4.2. Luminescence studies: assessment of the number of coordinated water molecules for LnL^5 and LnL^6 complexes	80
2.4.3. UV-Vis measurements	82
2.4.4. ^1H NMRD and ^{17}O NMR measurements of the Gd^{3+} complexes	83
2.4.5. Binding assays.....	90
2.4.5.1. Relaxometric titrations	90
2.4.5.2. Luminescence studies	94
2.4.5.3. ^1H & 2D NMR experiments to assess the interaction of $-\text{NH}_3^+$ with the crown ether.....	95
2.4.5.4. Computational study of the ternary complex $\text{YL}^5\text{-Gly}$	98
2.5. CONCLUSION	100
2.6. EXPERIMENTAL PROCEDURES AND MATERIALS.....	102
2.7. REFERENCES	122

2.1. Introduction

Neurotransmitters are essentially the brain's chemical messengers. They are responsible for intercellular communication between neurons by transmission of signals from one neuron to the next across synapses.

Some neurotransmitters are commonly described as excitatory or inhibitory according to their effects on postsynaptic neurons. Based on their size, neurotransmitters can be broadly split into two major groups, the relatively larger neuroactive peptides and the conventional small-molecule neurotransmitters [1]. The latter include acetylcholine, the biogenic amines (dopamine, noradrenaline, serotonin and histamine) (figure 2.1) and the amino-acids neurotransmitters, gamma-amino butyric acid (GABA), glutamate, aspartate and glycine (figure 2.2). Acetylcholine and biogenic amines exist in very restricted regions in the central nervous system (CNS) and at low concentrations. On the other hand, amino acid transmitters are considered to be the workhorses of the neurotransmitter family. By far, the most prevalent transmitter is glutamate [2], which is excitatory at well over 90% of the synapses in the human brain. Initially, scientists could not accept the implication of glutamate as a neurotransmitter because of its high concentration levels and wide distribution of glutamate in the CNS. The next most prevalent neurotransmitter is GABA, the major inhibitory neurotransmitter that is often referred to as valium-like substance. When GABA concentration is out of range, it is likely that an excitatory neurotransmitter is firing too often in the brain. GABA will be sent out to attempt to balance this stimulating over-firing.

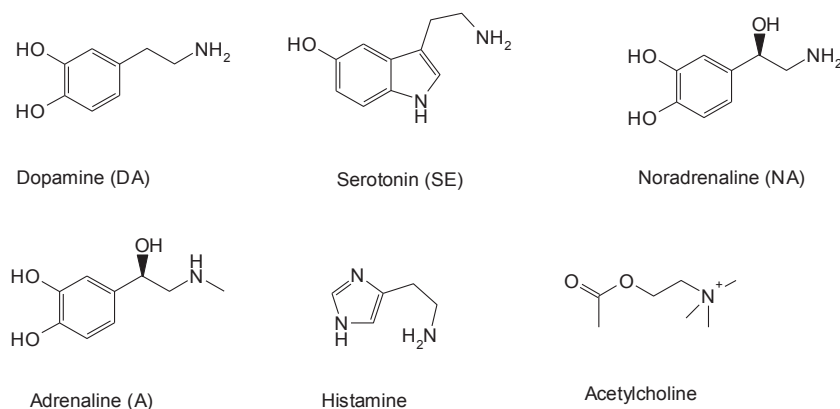


Figure 2.1. Chemical structures of biogenic amines and acetylcholine. DA, A and NA are categorized as catecholamines because they share the catechol moiety.

Neurotransmitters participate in complex neuronal processes, such as development, learning and memory, and even neuropathology [3, 4]. For instance, there is a link between acetylcholine and Alzheimer's disease: There is ca. 90% loss of acetylcholine in the brains of people suffering from Alzheimer's, which is a major cause of senility [5, 6]. Low serotonin levels are also associated with decreased immune system function [7, 8]. People with too little GABA tend to suffer from anxiety disorders, and drugs like Valium work by enhancing the effects of GABA [9].

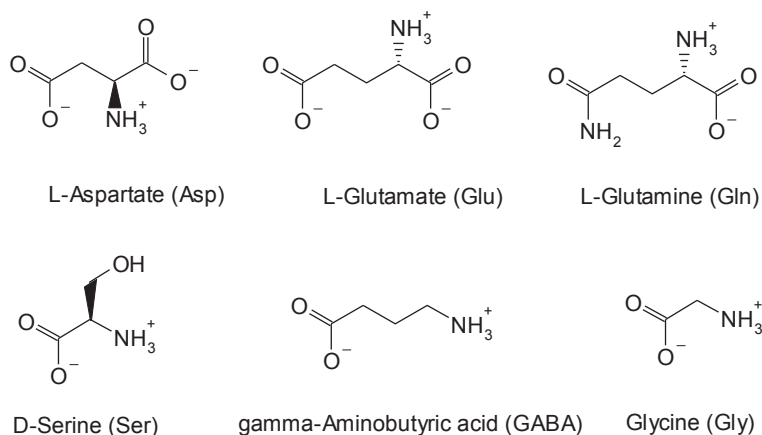


Figure 2.2. Chemical structures of amino-acid neurotransmitters and glutamine, a precursor for the biosynthesis of glutamate. They are found mostly as zwitterions at physiological pH, that is, with the carboxylate group deprotonated and the amino group protonated.

An overview of the processes where neurotransmitters are involved and their concentration in the brain are reported in the appendix.

There is no doubt that real-time imaging of neurotransmitter movement and concentration change will greatly enhance the understanding of the brain complexity. Advances that have been made in neuroscience are often directly linked to the development of new methods for their quantification and monitoring [10]. Still, monitoring the *in vivo* dynamics remains one of the most challenging assays that the brain researchers face today and progress in this research area is slow. The difficulties lie in a number of factors: 1) the synaptic release of NTs may occur in a few milliseconds. Under this time scale, any method that cannot respond fast enough would not be able to reveal the true behavior of neurotransmitters in CNS. 2) The dimensions of neurons are only at micrometer size and the cleft between the pre- and postsynaptic cells is

in the nanometer range. Thus, in order to obtain a data with good spatial resolution for such systems, the monitoring method should be able to match such dimensions. 3) The concentration of neurotransmitters present in extracellular fluids with normal neurotransmitter functions are usually very low, typically around mM to μM or even down to nM in the case of neuropeptides, especially. Altogether, a combination of high spatial and temporal resolution is required to make meaningful measurements.

2.1.1. Detection of neurotransmitters

In this section we explore the methods available to quantify and to monitor the activity of neurotransmitters in the CNS. The focus here will be on the two approaches that have undergone major development over the past decades and are still in frequent use in neuroscience, namely voltammetry and microdialysis.

2.1.1.1. Voltammetry

Voltammetry makes use of the fact that certain neurotransmitters (e.g. dopamine and serotonin), are electroactive [11]. The measurements are based on oxidizing or reducing the neurotransmitters at electrodes held at a potential characteristic for that specific neurotransmitter (the redox potential) with respect to a reference electrode. As neurotransmitter molecules get adsorbed at the electrode surface there is an exchange of electrons, leading to a net current into or out of the electrode. These redox currents are directly proportional to the neurotransmitter concentration and range from picoamperes to microamperes for physiological concentrations of neurotransmitters. The sensitivity of *in vivo* voltammetry varies depending upon the electrode and the voltammetric method. To date, the use of voltammetry has been limited to the detection of readily oxidizable species.

2.1.1.2. Microdialysis

Microdialysis consists of sampling the extracellular fluid of brain for *ex-vivo* analysis [12-15]. It involves introducing a dialysis membrane between the perfusion solution and the extracellular fluid to let molecules that are sufficiently small to pass through the dialysis membrane. For *ex-vivo* determination of collected analytes, microdialysis is usually coupled with liquid chromatography–mass spectrometry (LS-MS), use of fluorogenic reagents or enzymatic assays.

The latter are based on using an enzyme that is selective to a specific analyte and measuring the concentration of the assay products by various detection methods, which in turn can be related back to the analyte concentration. On the other hand, available fluorogenic reagents react mainly with primary amine neurotransmitters to give a by-product. This is particularly useful for detection of amino acid neurotransmitters. The range of chemicals that can be examined using *in vivo* microdialysis is limited only by the ability of a given compound to pass through the dialysis membrane and the availability of an appropriate analytical technique.

Technical improvements have advanced these neurochemical measurements to the real-time domain, but they have still been used extensively to monitor extracellular neurotransmitter concentrations. Although they dominate the modern area of *in vivo* neurochemical monitoring, one critical limitation is the highly invasive nature of implanting devices in the brain that results in several reactions within the CNS tissue [16]. Neuroinflammation not only alters the sampled microenvironment, but also results in a diffusion barrier that encapsulates the probe and therefore restricts access to released neurotransmitters. Knowledge of the time course of these events is critical in determining the interval during which microdialysis or voltammetry experiments can be performed with minimal interference from tissue reactions. This highly-invasive aspect makes the study of neurotransmitter dynamics largely confined to animal models.

Recently an imaging approach has been developed to measure changes in transmitter-receptor interactions in the living non-human primate and human brain. This approach uses positron emission tomography (PET) to quantify the binding of radiotracers that have been developed to occupy specific neuroreceptor subtypes in the brain [17]. *In vivo*, endogenous neurotransmitters can compete with the radiotracer for receptor occupancy and as a result, radiotracer binding may also provide an indirect measure of transmitter release. To date, research using this method has focused primarily on central DA-containing neurons. This is in part, due to the available ligands such as [11C]-raclopride, a suitable radiotracer for the DA D2/D3 receptor [9]. The limited spatial resolution of this approach makes it difficult to image transmitter dynamics in small nuclei such as the cell body region of most chemically-defined pathways. In addition, the level of sensitivity is not adequate for visualizing brain regions that

have a low density of receptors, as is the case for DA D2/D3 receptors in cortex. Finally, the method can only be applied to the study of transmitter systems for which well-characterized radiotracers are available.

Ultimately, no techniques without major limitations are currently available to monitor neurotransmitters. The ability to image neurotransmitters using electrode-free, noninvasive methodology with high spatial and temporal resolution clearly poses a particular challenge.

2.1.2. MRI contrast agents sensitive to dopamine

At the time this work was undertaken, neurotransmitter sensing had not been established for MRI. Jasanoff and coworkers have reported in 2010 for the first time a MRI contrast agent sensitive to dopamine, by applying a molecular engineering technique to a bacterial heme protein, cytochrome P450 domain (BM3h) [18]. They found that binding of a natural ligand, arachidonic acid, alters the T_1 relaxivity of BM3h by displacing a water molecule coordinated to the heme iron. The molecular engineering allowed tuning the BM3h binding specificity away from arachidonic acid and toward dopamine. The resulting sensors were shown to detect extracellular dopamine in both cell culture and rat brains with affinities of 3.3–8.9 μM .

Although low sensitivity is a problem for all MRI contrast agents, it is more of a challenge for existing biomolecular contrast agents than for synthetic agents. In this case, for instance, the protein T_1 agent BM3h has a relaxivity of $1.23 \text{ mM}^{-1}\text{s}^{-1}$ at 21 °C and 4.7 T, compared with 3–5 $\text{mM}^{-1}\text{s}^{-1}$ for Gd^{3+} compounds under similar conditions. With today's technology, a synthetic MRI contrast agent is therefore likely to be applicable at lower concentration and with lesser risk of physiological disruption or toxicity than a biomolecular probe. This is one reason why much effort has focused on detection systems in which small molecule synthetic contrast agents function as responsive agents and provide amplification as well as desirable targeting and specificity properties.

2.2. Design of Ln³⁺-based complexes responsive to neurotransmitters

This section discusses our attempts to develop synthetic MRI probes to study the feasibility of detecting neurotransmitters, essentially with MRI technique. For this purpose, our first aim was the design of Gd³⁺ chelates with appropriate recognition moieties that will be able to accomplish good binding with the targeted neurotransmitters with respect to the relaxivity modulation upon binding. Our choice has been addressed to target amino acid neurotransmitters which are zwitterionic. Since zwitterionic neurotransmitters are bifunctional guests, more effective receptors should have two binding sites highly complementary to the NH₃⁺ and COO⁻ groups. Multivalent interactions are known to be more potent and selective over the analogous monovalent interaction and contribute to the increased association strength of the entire complex [19, 20].

In the literature, there are many examples of recognition moieties which bind to carboxylate or ammonium groups. Particularly, binding of ammonium groups is a well documented field of supramolecular chemistry [21], due to the ubiquity of these small groups in molecular biology. The binding of primary, secondary and tertiary ammonium ions relies on hydrogen bonding to a large extent. Other types of interactions may act simultaneously, namely cation- π -interaction [22] and ion pairs and salt bridges [23]. A typical example of a salt bridge is the ammonium ion carboxylate ion pair. The complex stability depends on the number of H-bonds possible between host and guest [24], but also on the acidity of the ammonium ion. If exposed to a competing solvent such as water, a single hydrogen bond contributes much less to the binding energy; water has a high dielectric constant and competes strongly for H-bond sites reducing the effectiveness of hydrogen bonding and making molecular recognition in water a challenging topic of growing interest that has been reviewed [25]. Various approaches have been reported for the binding of ammonium ions and amino acids ranging from molecular receptors of varying sizes, shapes and complex structures, such as metal-complexing agents, crown ethers, calixarenes, porphyrins, cucurbiturils, cyclodextrins and cyclopeptides [26].

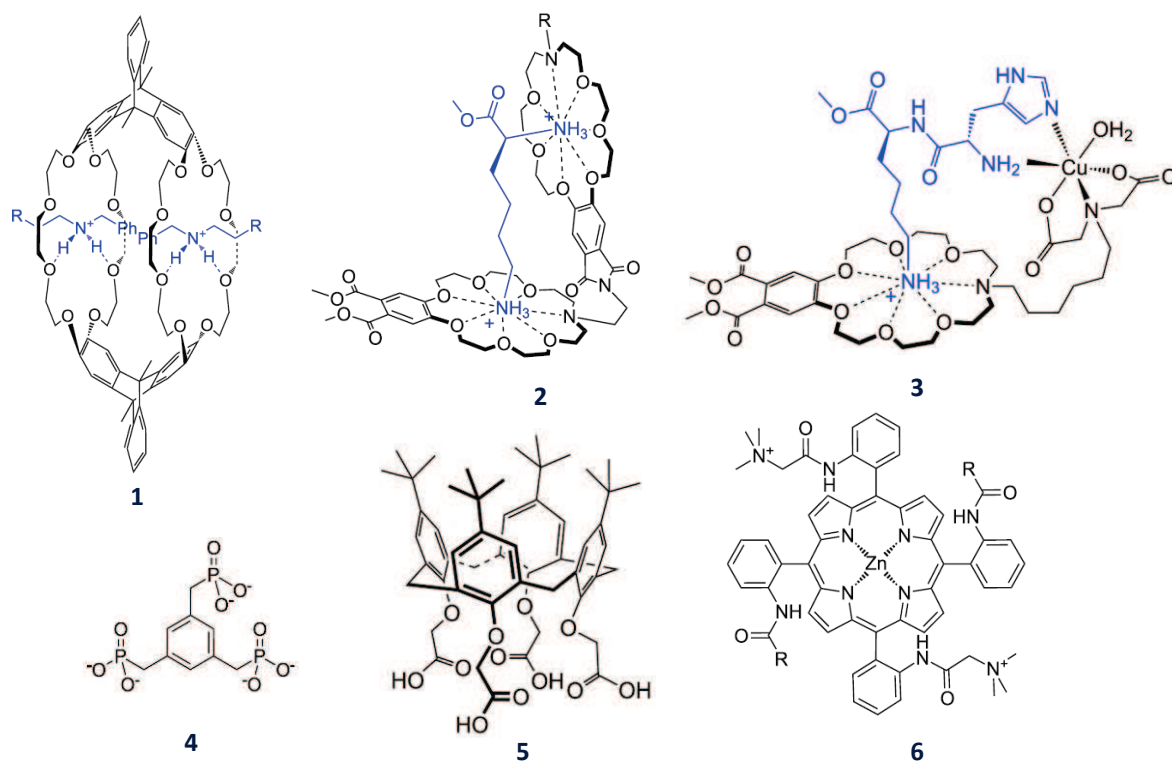
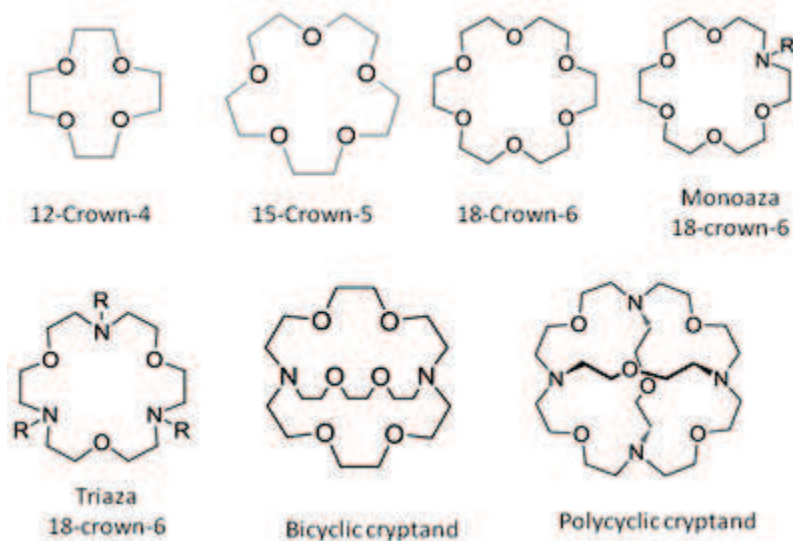


Figure 2.3. Reported molecular hosts for ammonium ions: crown-ether-based hosts for secondary ammonium (1) [27], lysine (2) [28] and His-Lys-OMe (3) [29]; a simple phosphonic acid-based host (4) [30]; the first example of a water soluble calixarene (5) [31] and a zinc porphyrin host (6) [32].

For the proof-of-concept study, we focused on the design of simple hosts which are relevant for us in terms of relaxivity change, our choice was restricted to crown-ether derivatives and phosphonates. Many different examples reported in literature show that crown ethers are one of the most versatile classes of synthetic receptors for the recognition of ammonium ions. Crown ethers recognize ammonium-ions typically by hydrogen-bond interactions. Therefore only ammonium ions of primary and secondary amines are typical guests and quaternary ammonium ions are not bound. Also, high binding affinities are observed in organic solvents, such as methanol. At physiological conditions in water, the binding constants are usually smaller. Selective recognition of ammonium ions (ionic radius 1.43 Å) by crown ethers require complementarity to the size of the crown-ether cavity to impart high selectivity over interfering cations of other sizes [33] or other interacting functional groups. 18-Crown-6 type structures typically show the highest affinity for primary ammonium ions (figure 2.4), while secondary ammonium ions prefer larger crown ethers [34].



Crown ether	Cavity size	Guest	logK
12-Crown-4	120-150 pm	BnNH ₃ Cl	0.8
15-crown-5	170-220 pm	BnNH ₃ Cl	2.74
18-crown-6	260-320 pm	BnNH ₃ Cl	4.43

Figure 2.4. Structures of typical examples of (aza)crown ethers and cryptand crown ethers (top). Binding constants of three crown ethers to benzylammonium chloride in methanol (bottom) that demonstrate the effect of the crown ether size on the binding constant.

On the basis of the above considerations, *de novo* design based on lanthanide-based DO2A unit was used for binding of zwitterionic neurotransmitters to which a monoaza-18-crown-6-ether moiety, a commercially available compound, is covalently connected. The DO2A unit was functionalized in such a way that the metal is coordinatively unsaturated and positively charged. Therefore, the carboxylate group of the neurotransmitter which is negatively charged will bind to the metal via the so-called charge-charge interaction. Such design allows a divalent interaction with the Ln³⁺-complex which serves to enhance the binding interaction (despite the competitive influence of the water) with neurotransmitters over other competitive ions, which can form monovalent interactions either with the crown ether or the lanthanide chelate. Moreover, with regard to optical detection, the (R)-methyl phenyl acetamide group serves as an antenna for sensitization of the Ln³⁺ in luminescence spectroscopy experiments and it also

introduces a chiral center in the ligand. Given the asymmetry of the designed ligands, this stereogenic center might help to obtain better defined and less flexible structures for NT binding by limiting the multiconformational behavior known for asymmetrical DOTA derivatives. The possible host-guest complex structure is depicted in figure 2.5.

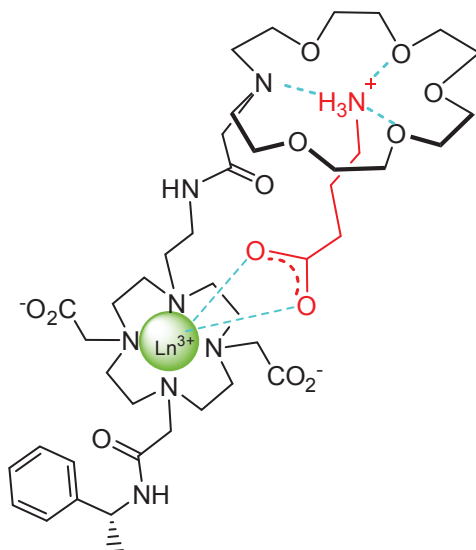


Figure 2.5. Schematic representation of the expected structure for host-guest complex with the zwitterionic neurotransmitter GABA.

The mechanism by which these Ln^{3+} complexes are supposed to work as responsive agents involves a displacement of the coordinated water upon binding with the targeted neurotransmitter. Specifically, this decrease of hydration number results in a “turn-off” response in relaxivity, thus in MRI, and a “turn-on” response in luminescence imaging due to the deactivation of the quenching of Ln^{3+} luminescence by water. It should be noted that for both MRI and optical imaging, turn-on sensors, whose signals increase upon binding of the target, are preferred over turn-off ones because they permit more easy and accurate measurement. Yet, it is not possible to attain bimodal turn-on sensors simultaneously for both MRI and luminescence, since the combined requirements for both imaging techniques are often considered to be non-compatible; that is, the presence of at least one bound water molecule is required for a good MRI efficiency, while water molecules are undesired for optical purposes since they strongly quench the luminescence. Therefore, a responsive MRI turn-on probe is necessarily an optical turn-off probe and *vice versa*.

2.3. Synthesis of the complexes

Initially, the aim was to synthesize the DOTA-bisamide ligands L^{1-2} and the DO3A-monoamide ligands L^{3-4} as shown in figure 2.6. However, attempts to synthesize these ligands were unsuccessful. Chapter 4 describes the different attempted synthetic pathways.

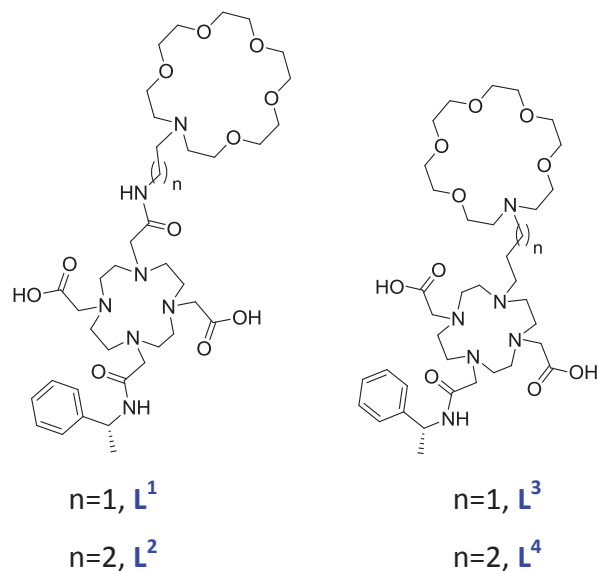


Figure 2.6. Structure of prospected ligands whose synthesis was not successful.

We have therefore moved on to the synthesis of a new series of ligands that differ only in the nature of the linker connecting the two macrocycles as shown in figure 2.7.

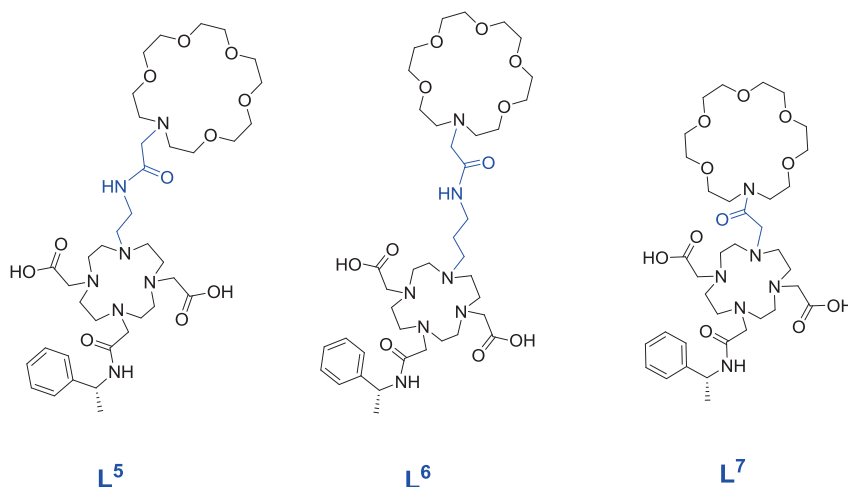


Figure 2.7. Structure of chelating agents L^{5-7} synthesized in this work.

For comparative purposes, ligands **L**¹⁰ and **L**¹¹ were also synthesized as models for ligands **L**⁶ and **L**⁷, respectively (figure 2.8). They are devoid of crown ether moiety. Subsequently, investigation of their affinity with neurotransmitters, in this case, would be an indirect way to gain insight into to what degree the crown ether moiety contributes to the overall complexes affinity.

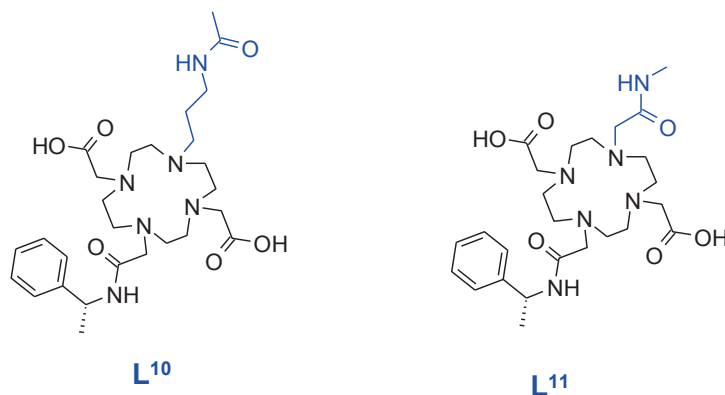
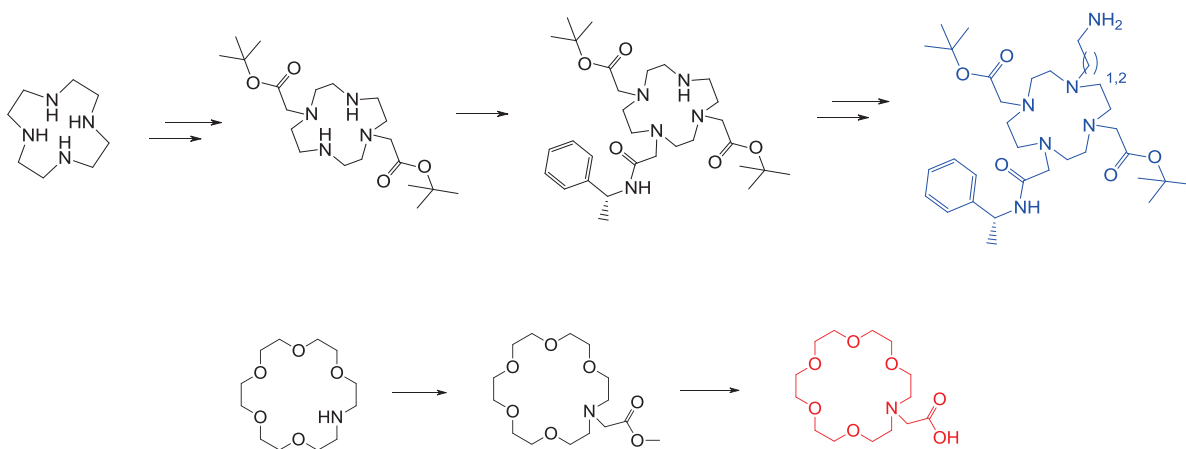


Figure 2.8. Structure of model chelating agents

2.3.1. Synthesis of ligands **L**⁵⁻⁶

Figure 2.9 depicts the synthetic approach used to obtain the chelating agents **L**⁵⁻⁶. These ligands were formed by coupling two macrocyclic building blocks; a crown-ether carboxylic acid and a cyclen moiety containing free primary amines (ethyl- and propylamine).



On the other hand, monoaza-crown ether carboxylic acid **6** (figure 2.11) was synthesized from 1-aza-18-crown-6-ether by reaction with the benzyl bromoacetate to get the intermediate **5**. The next step involved cleavage of the benzyl group to obtain acid **6**.

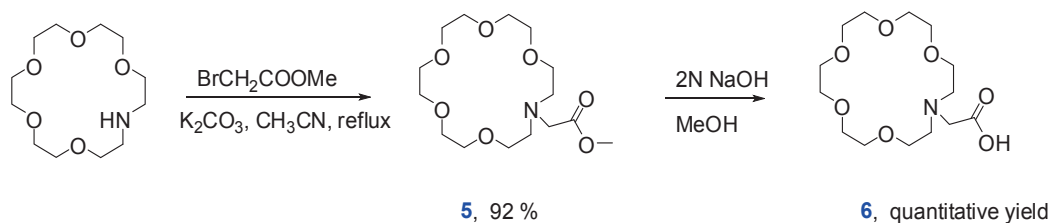


Figure 2.11

Finally, free amines **4a** and **4b** were coupled with the acid **6** to form **7a** and **7b**, respectively (figure 2.12). The reaction was performed at room temperature using HBTU as coupling reagent in DMF as solvent. The deprotection of tert-butyl esters using formic acid at reflux gave the ligands **L⁵** and **L⁶** with yields of 40 and 45%, respectively.

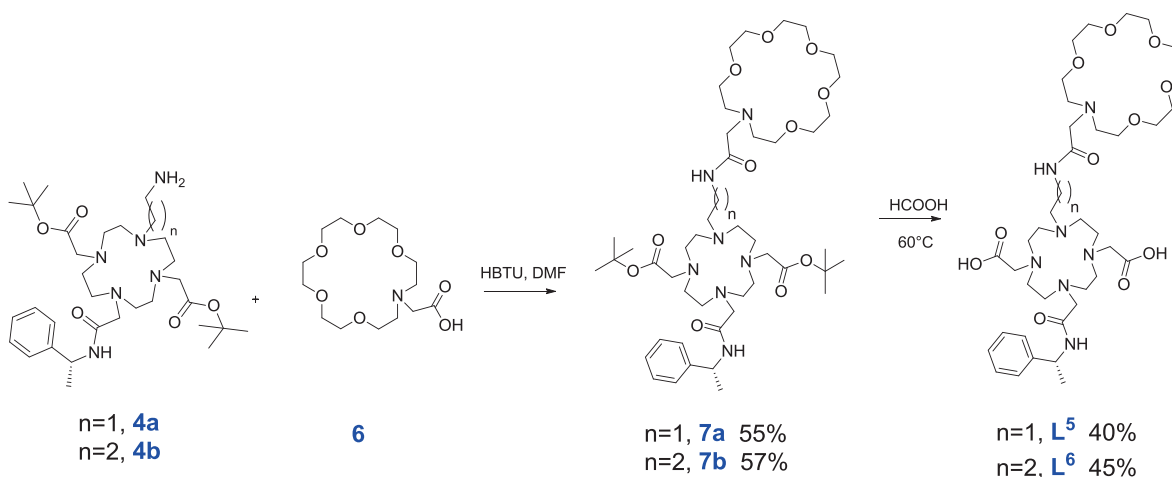


Figure 2.12

2.3.2. Synthesis of ligand **L**⁷

Ligand **L**⁷ was obtained by alkylation of precursor **2** (used in the synthesis of the ligands **L**⁵ and **L**⁶) with compound **8** which was formed by reacting 1-aza-18-crown-6 with chloroacetyl chloride (figure 2.13). Alkylation of precursor **2** with the intermediate acetyl chloride **8** gave compound **9** in near quantitative yield.

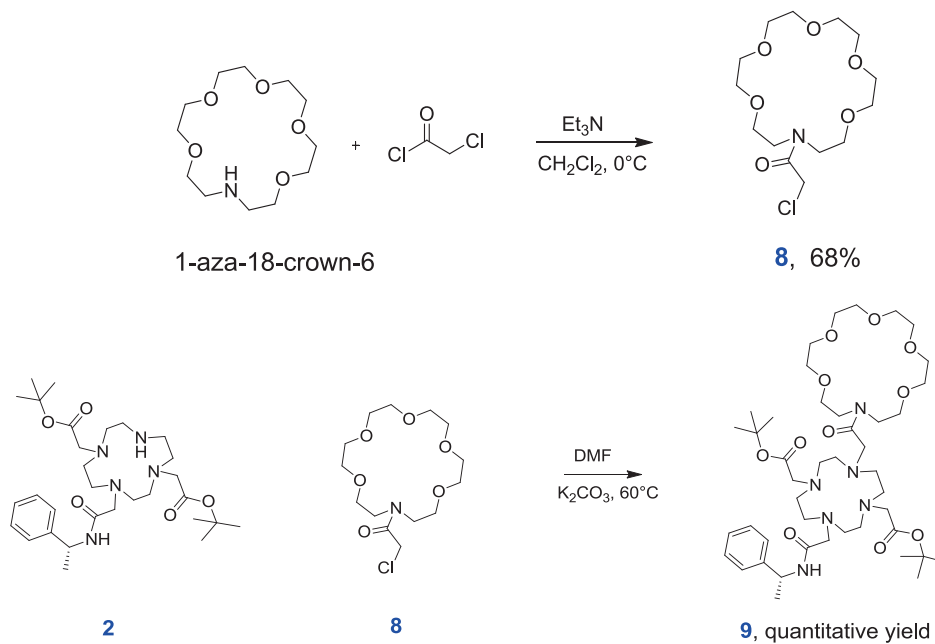


Figure 2.13

Finally, deprotection of **9** afforded **L**⁷ in 48 % after purification by HPLC (figure 2.14).

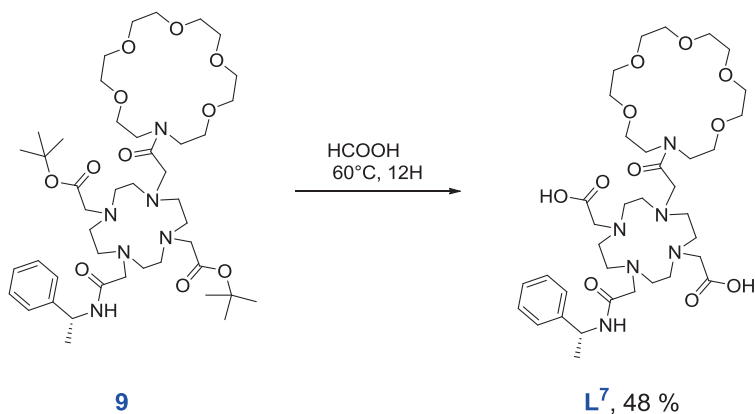


Figure 2.14

3.2.1. Synthesis of ligand L¹⁰

The synthesis route of ligand L¹⁰ is outlined in figure 2.15. It was obtained over 2 steps starting from the intermediate **4b**. Acetylation of the later using acetyl chloride, followed by removal of tert-butyl protecting groups afforded ligand L¹⁰.

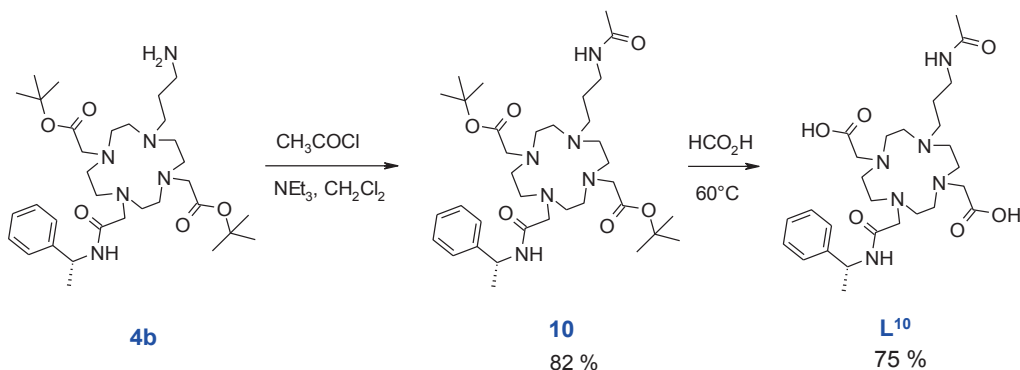


Figure 2.15

3.2.2. Synthesis of ligand L¹¹

Ligand L¹¹ was also synthesized over two steps from the previously prepared precursor **2**. Its reaction with 2-chloro-N-methylacetamide gave the intermediate **11**, which was then deprotected to obtain the ligand L¹¹ (figure 2.16).

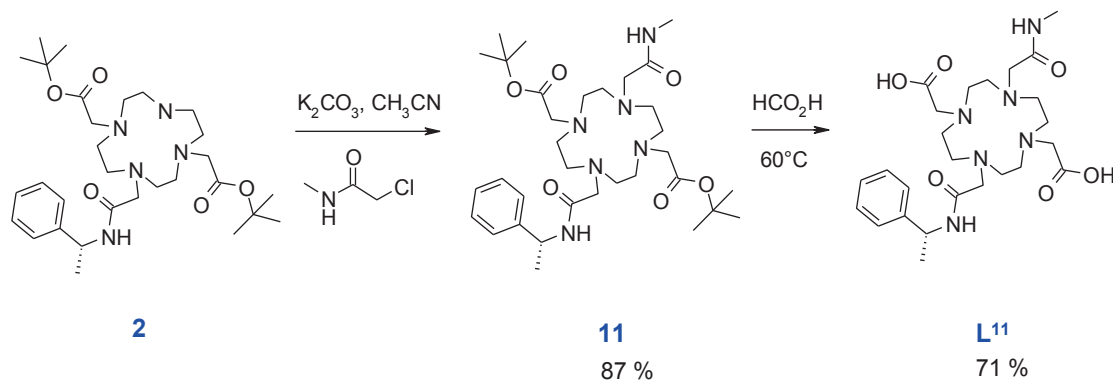


Figure 2.16

Complexation: Ligands L⁵⁻⁷ and L¹⁰⁻¹¹ were loaded with Ln³⁺ using lanthanide chloride salts (LnCl₃·6H₂O) in water while the pH was kept at 6-7 during the complexation. The solutions were heated at 60°C for 2 hours to allow complexation. All Ln³⁺ complexes were characterized by mass spectrometry, and the appropriate isotope pattern distribution characteristic for Ln³⁺

complexes was observed. No complexation of metal by crown ether was observed, contrary to what was reported by Gunnlaugsson and coworkers for a similar complex formed in methanol [36].

2.4. Results and discussion

2.4.1. pH-potentiometry

Protonation constants, as defined in equation 2.1, of ligands L^{5-7} were determined via pH-potentiometric titrations, performed at 25 °C in the pH range 2.1–11.9.

$$K_{Hi} = \frac{[H_iL]}{[H_1L][H^+]} \quad (2.1)$$

The potentiometric titrations were carried out both in KCl and in tetramethylammonium chloride, NMe_4Cl (0.1 molL^{-1}) to maintain the ionic strength by using KOH or tetramethylammonium hydroxide (NMe_4OH) as titrant. The potassium ion K^+ is known to bind strongly the crown ether. Indeed, the titration curves are slightly different in KCl or NMe_4Cl solution, in particular in the pH range 5-7 (see Figure 2.17 for L^5). The calculated values of the protonation constants are listed in Table 2.1.

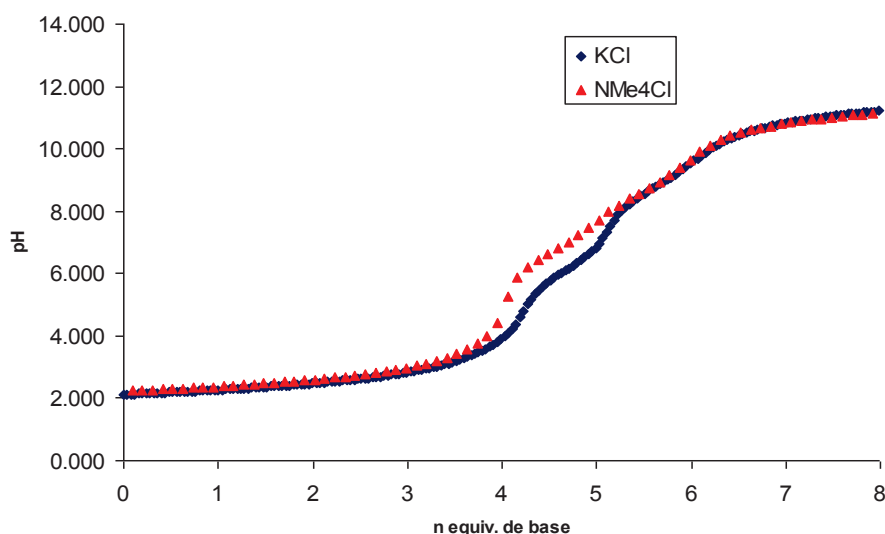


Figure 2.17. pH-potentiometric titration curves of the ligand H_5L^5 ($C_L = 3 \text{ mM}$, 1 equivalent HCl added) in the presence of 0.1 KCl or 0.1M NMe_4Cl ionic strength.

Table 2.1. The protonation constants ($\log K_i$) of L^{5-7} ($I = 0.1$ M KCl or 0.1 M NMe_4Cl , $25^\circ C$).

	L5		L6		L7	DOTA*
	0.1M KCl	0.1 M NMe_4Cl	0.1M KCl	0.1 M NMe_4Cl	0.1 M NMe_4Cl	0.1 M NMe_4Cl
$\log K_1$	10.64	11.02	10.9	10.86	11.19	11.08
$\log K_2$	8.62	8.60	8.55	8.62	9.07	9.23
$\log K_3$	6.2	6.8	6.15	6.62	2.8	4.24
$\log K_4$	3.50	3.44	4.04	4.38	2.4	4.18
$\log K_5$	2.85	1.68	3.20	3.7		1.88
$\log K_6$						1.71

*Protonation constants of DOTA at $25^\circ C$ obtained by potentiometry (0.1 M NMe_4Cl) [37].

By analogy to similar macrocyclic ligands, the first two protonation constants represent the protonation of opposite amine nitrogens of the cyclen ring, while the last two protonation steps occur on the carboxylates groups. In comparison to $DOTA^{4-}$, the first two protonation constants are slightly affected by the replacement of two acetates by amides; they are lower than those for DOTA. The ligands L^5 and L^6 displayed an additional protonation constant between 6 and 7, which corresponds to the protonation of the crown-ether nitrogen. The value of this protonation constant is strongly affected by the ionic strength; as expected, it is lower in KCl due to the coordination of the K^+ ion to the crown ether. We should note that in the lanthanide complexes, the protonation constant of this crown-ether nitrogen is expected to be lower than in the free ligand. Consequently, at physiological pH, this nitrogen is expected to be unprotonated, which is favourable for ammonium binding, as this prevents the electrostatic repulsion between the crown ether nitrogen and the protonated ammonium group of the amino-acid neurotransmitters.

2.4.2. Luminescence studies: assessment of the number of coordinated water molecules for LnL^5 and LnL^6 complexes

The hydration number of the Gd^{3+} complexes is a key parameter that determines their proton relaxivity. It is particularly important in our approach, since it is expected that binding of

the neurotransmitter molecules to the lanthanide complexes affects their hydration number, which is then translated to a relaxivity change.

Herein, luminescence studies served to determine the hydration number of Ln^{3+} complexes. The q was determined using Tb^{3+} and Eu^{3+} complexes. This involved measuring the luminescence lifetimes of the $^5\text{D}_0$ (Eu^{3+}) and $^5\text{D}_4$ (Tb^{3+}) excited states in H_2O and D_2O buffered solutions (25°C, HEPES 25mM, pH 7.4). The Eu^{3+} complexes were excited directly on the Eu^{3+} band at 395 nm. Lifetimes of Tb^{3+} complexes were measured by exciting the phenyl group at 257 nm, through sensitized emission. The emission spectra of Eu^{3+} and Tb^{3+} are depicted in figure 2.18

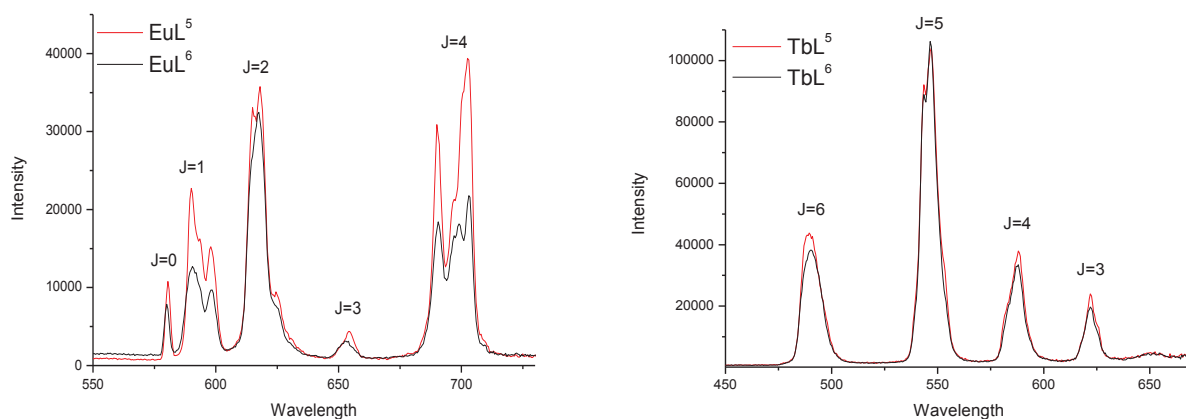


Figure 2.18. Left: the emission spectra of the complexes EuL^{5-6} (5mM) corresponding to the deactivation of the $^5\text{D}_0 \rightarrow ^4\text{F}_j$ transitions. Right: the emission spectra of the complexes TbL^{5-6} corresponding to the deactivation of the $^5\text{D}_4 \rightarrow ^4\text{F}_j$.

The hydration states for Eu^{3+} and Tb^{3+} complexes were estimated using equations 2.2 and 2.3, respectively, where x , in the case of Eu^{3+} , takes into account the effect of exchangeable amide N–H oscillators [38, 39]. In this case, $x=2$, assuming that the amide oxygen of the linker $\text{CH}_2(\text{CH}_2)_n\text{NHCO}$ is bound to the metal ion.

$$q_{\text{Eu}} = 1.2[(k_{\text{H}_2\text{O}} - k_{\text{D}_2\text{O}}) - 0.25 - 0.075x] \quad (2.2)$$

$$q_{\text{Tb}} = 5[(k_{\text{H}_2\text{O}} - k_{\text{D}_2\text{O}}) - 0.06] \quad (2.3)$$

Luminescence lifetimes along with the q values are shown in table 2.3. q was found to be 1 for Eu^{3+} and Tb^{3+} complexes. These q values are lower than expected on the basis of the high relaxivities measured for the complexes GdL^5 and GdL^6 (see below)¹. They are, however, consistent with those determined by ^{17}O chemical shifts measurements (see below).

Table 2.2. q values and lifetimes of the Eu^{3+} and Tb^{3+} excited states (298K, H_2O and D_2O , 25 mM HEPES, pH 7.3, $c_{\text{EuL}}=5$ mM and $c_{\text{TbL}}=50$ μM).

Complex	$\tau_{\text{H}_2\text{O}}$ (ms)	$\tau_{\text{D}_2\text{O}}$ (ms)	q
EuL^5	0.52	1.68	1.1
TbL^5	1.76	3.17	1.0
TbL^6	1.52	2.68	1.1
EuL^6	0.35	0.69	1.3

2.4.3. UV-Vis measurements

The q values obtained by the luminescence method described above or from the ^{17}O chemical shifts (below) are frequently not integer numbers but rather fractions. This can be due to inaccuracy of the measurement or to the existence of a hydration equilibrium between complexes with different q values. In order to accurately assess the hydration state, we recorded high resolution UV-Vis absorption spectra on the Eu^{3+} complexes as there is no direct way to check the presence of hydration equilibrium for a Gd^{3+} complex. Hydration equilibria can be characterised by the UV-Vis absorption spectrum of the corresponding Eu^{3+} complex, which has a $^5\text{D}_0 \leftarrow ^7\text{F}_0$ transition band around 578-582 nm, very sensitive to the coordination environment and the observation of a single band excludes the co-existence of differently hydrated species [40, 41].

The UV-Vis absorption spectra were recorded on EuL^5 and EuL^6 aqueous solutions. Both complexes show a single absorption band in the range 25 – 70 °C in the 578-582 nm region,

¹ For the sake of simplicity, charges and hydration water molecules are not indicated. GdL^5 and GdL^6 stand for $[\text{GdL}^5(\text{H}_2\text{O})]$ and $[\text{GdL}^6(\text{H}_2\text{O})]$, respectively, throughout the text.

corresponding to the ${}^5D_0 \leftarrow {}^7F_0$ transition (Figure 2.19). The presence of a single absorption band at both temperatures confirms the absence of hydration equilibrium.

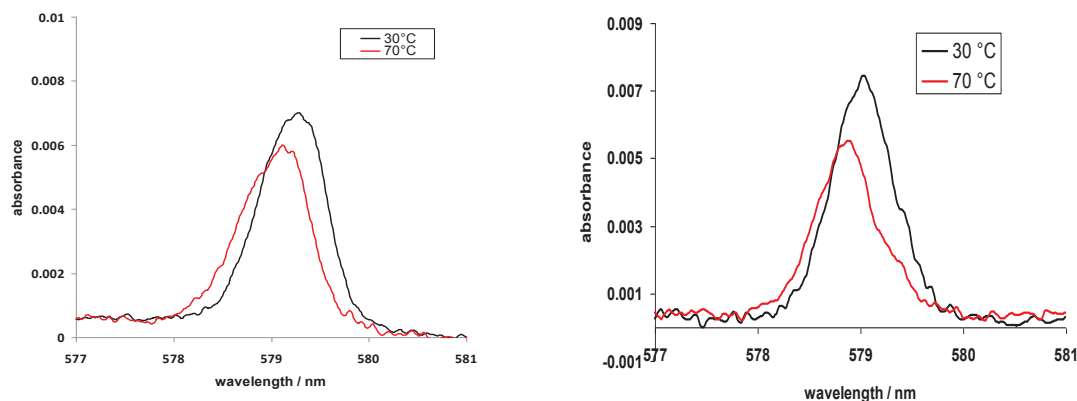


Figure 2.19. UV-Vis spectra of the ${}^5D_0 \leftarrow {}^7F_0$ transition measured in 0.02 M EuL^5 (left) and EuL^6 (right) solutions recorded at different temperatures (30 and 70°C). The position of the bands varies with temperature, which is a normal phenomenon for such Eu^{3+} spectra, and which is independent of any hydration equilibrium.

2.4.4. ${}^1\text{H}$ NMRD and ${}^{17}\text{O}$ NMR measurements of the Gd^{3+} complexes

The determination of the structural and dynamic parameters contributing to the observed relaxivity of Gd^{3+} complexes is possible through an array of different experimental techniques [42, 43], including ${}^1\text{H}$ Nuclear Magnetic Relaxation Dispersion (NMRD) and ${}^{17}\text{O}$ NMR spectroscopy [43]. ${}^1\text{H}$ NMRD profiles, where the relaxivity is measured as a function of the ${}^1\text{H}$ Larmor frequency, provide a snapshot of the different interaction mechanisms and dynamic processes that affect the relaxivity of a contrast agent. The features of the NMRD curve are influenced by the water exchange rate, electron relaxation parameters and rotational correlation times. However, due to the high number of parameters affecting relaxivity, their determination uniquely from the analysis of these curves can lead to false results. Therefore, it is usually combined with other techniques such as ${}^{17}\text{O}$ NMR spectroscopy. The presence of a water molecule in the inner-sphere of a paramagnetic lanthanide complex is obviously reflected in the ${}^{17}\text{O}$ NMR parameters of the bulk water. By performing variable temperature ${}^{17}\text{O}$ T_2 measurements, it is possible to accurately determine the water exchange rate. The rotational

correlation time can be assessed by performing variable temperature ^{17}O T_1 measurements. On the other hand, variable temperature measurements of the chemical shift difference between bulk and bound water ($\Delta\omega_r$), give an indication of the q value. A reliable determination of the interdependent parameters common to ^1H NMRD and ^{17}O NMR is often performed through the simultaneous least-squares fitting of all the data obtained.

The magnetic-field dependence of the proton longitudinal relaxation of complexes GdL^{5-7} were recorded as a series of ^1H NMRD profiles at 25°C and 37 °C over the frequency range 0.01 to 100 MHz (figure 2.20).

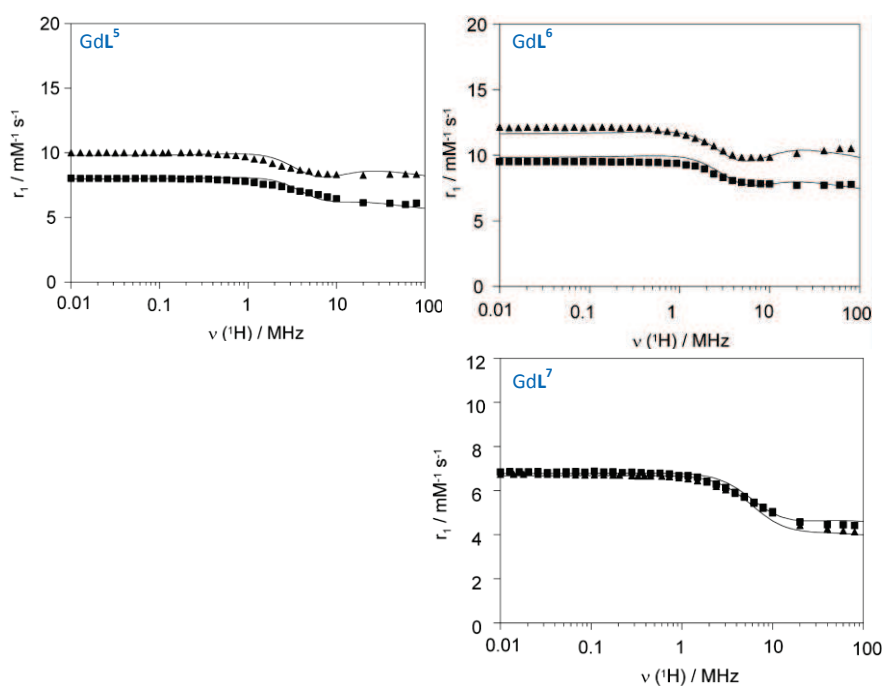


Figure 2.20. Proton relaxivities r_1 of GdL^{5-7} , as a function of the Larmor frequency at 25°C (\blacktriangle) and 37°C (\blacksquare). The lines represent the best fits to the experimental points.

The proton longitudinal relaxivity r_1 of complexes GdL^5 , GdL^6 , GdL^7 and GdL^{10} were measured to be 6.4, 7.8, 4.5 and 6.7 $\text{mM}^{-1}\text{s}^{-1}$ respectively in 25 mM HEPES buffered solution (37°C, 300 MHz, pH 7.4). In contrast to GdL^7 , complexes GdL^5 and GdL^6 showed a significant temperature dependency. This temperature dependence (r_1 decreases with increasing temperature) and the

shape of the NMRD curves follow the general trend observed for typical small molecular weight complexes, where the relaxivity is limited by the rotational correlation time.

Additionally, an ^{17}O NMR study has been performed on the complexes GdL^{5-7} and GdL^{10} . Figure 2.21 shows the measured temperature dependency of the reduced ^{17}O chemical shifts ($\Delta\omega_r$), and transverse ($1/T_{2r}$) and longitudinal ($1/T_{1r}$) relaxation rates. For complexes GdL^{5-6} and GdL^{10} , the transverse ^{17}O relaxation rate, $1/T_{2r}$, increases with decreasing temperature, indicating that these complexes are in the fast exchange regime. GdL^7 , in contrast, is in slow exchange regime all over the temperature range studied, as the reduced transverse relaxation rate decreases with decreasing temperature and correspondingly, the very small chemical shifts also point to slow exchange.

In the slow exchange regime, the reduced transverse relaxation rates are directly determined by the water exchange rate. In the fast exchange regime, on the other hand, the reduced transverse relaxation rate is defined by the transverse relaxation rate of the bound water oxygen, $1/T_{2m}$, which is in turn influenced by the water exchange rate, k_{ex} , the longitudinal electronic relaxation rate, $1/T_{1e}$, and the scalar coupling constant, A/\hbar . The reduced ^{17}O chemical shifts are determined by A/\hbar . Transverse ^{17}O relaxation is governed by the scalar relaxation mechanism, thus contains no information on the rotational motion of the system. In contrast to $1/T_{2r}$, the longitudinal ^{17}O relaxation rates, $1/T_{1r}$, are determined by dipole-dipole and quadrupolar relaxation mechanisms, both related to rotation. The dipolar term depends on the Gd^{3+} -water oxygen distance, r_{GdO} , while the quadrupolar term is influenced by the quadrupolar coupling constant, $\chi(1+\eta^2/3)^{1/2}$. The analysis of the experimental ^1H NMRD and ^{17}O NMR data for all three systems was performed according to the traditional Solomon-Bloembergen-Morgan theory. The theoretical equations used in the data analysis are shown in the Appendix. Ideally, simultaneous fitting of ^{17}O and ^1H NMRD data is more accurate as it puts more constraints on the parameters which are common to both ^{17}O and ^1H relaxation. In the case of GdL^5 and GdL^6 , however, the simultaneous fitting was not possible and fittings were done separately. The reason is that the description of the electron spin relaxation is not valid for all magnetic fields covered by the NMRD measurements (below ~ 6 MHz). On the other hand, GdL^7 is mainly in slow exchange which means that the reduced transverse relaxation

rates bear very limited information on the electron spin relaxation, therefore, a simultaneous fit would make less sense. All parameters obtained from the separate fits are shown in Table 2.3.

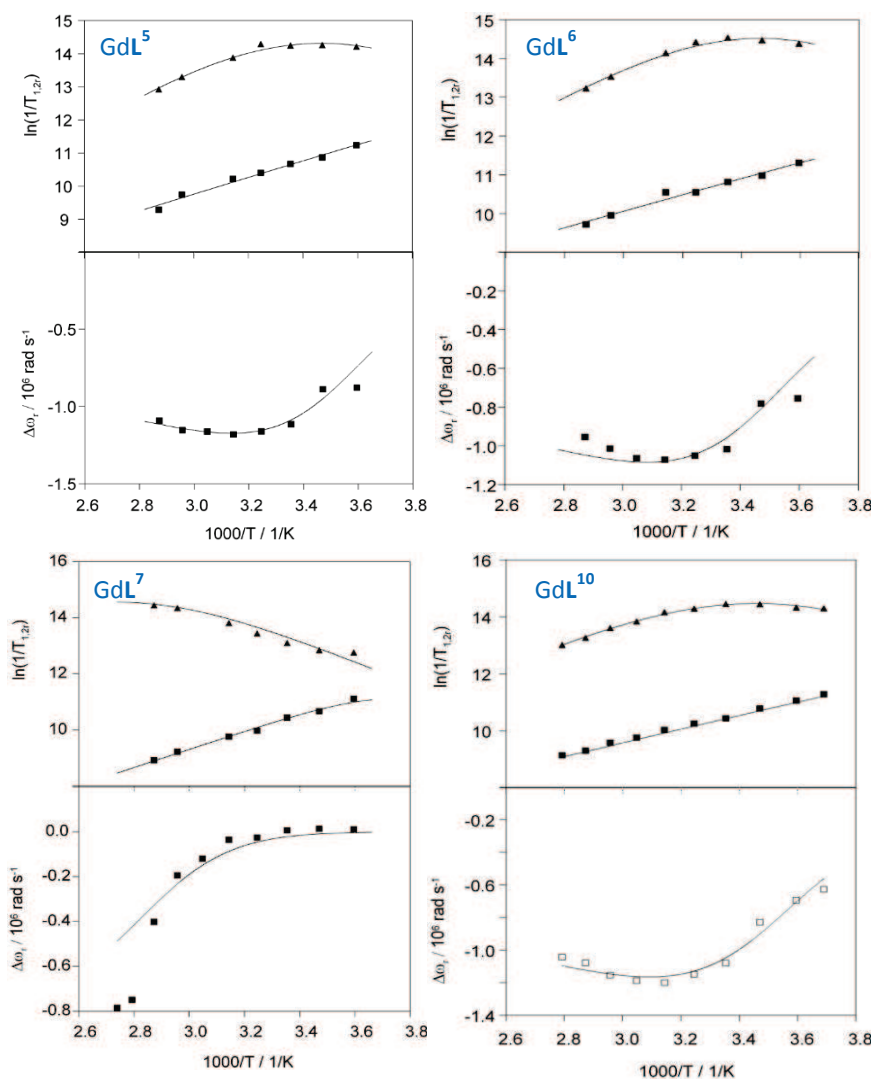


Figure 2.21. Temperature dependence of the reduced transverse ^{17}O relaxation rates, $1/T_{2r}$ (\blacktriangle), $1/T_{1r}$ (\blacksquare or \square) and the reduced ^{17}O chemical shifts, $\Delta\omega_r$ for GdL^{5-7} and GdL^{10} .

In the fitting procedure, r_{GdO} has been fixed to 2.50 \AA , based on available crystal structures [36, 44] and recent ESEEM results [45]. The quadrupolar coupling constant, $\chi(1+\eta^2/3)^{1/2}$, has been set to the value for pure water, 7.58 MHz. The following parameters have been adjusted: the

water exchange rate, k_{ex}^{298} , the activation entropy, ΔS^\ddagger , the activation enthalpy for water exchange, ΔH^\ddagger , the scalar coupling constant, A/\hbar , the rotational correlation time (τ_R^{298}) and its activation energy, E_R , and the parameters characterizing the electron spin relaxation, such as the correlation time for the modulation of the zero-field-splitting, τ_V^{298} , and its activation energy, E_V , and the mean-square zero-field-splitting energy, Δ^2 . The empirical constant describing the outer sphere contribution to the ^{17}O chemical shift, C_{os} , was also fitted and gave reasonable values. E_V was fixed to 1 kJ/mol, otherwise small negative values being obtained.

For GdL^5 , GdL^6 and GdL^{10} , all in the fast exchange regime, the reduced chemical shifts and, consequently the scalar coupling constant calculated, give a direct indication of the hydration state of the complexes. In all cases, the shifts are in accordance with one inner sphere water molecule, as it was concluded above for L^5 and L^6 from the luminescence on the corresponding Eu^{3+} and Tb^{3+} analogues.

The water exchange rates are considerably (twenty times) higher for GdL^5 , GdL^6 and GdL^{10} than for GdL^7 . This is directly related to the structure of the complexes. GdL^7 is a DOTA bisamide derivative, and as it was previously reported for many amide derivatives, the water exchange is diminished as compared to GdDOTA. According to the empirical rule that has been observed on a large number of amide derivative complexes, the water exchange is decreased to 1/3 by the replacement of each carboxylate by an amide function [43].

Table 2.3A: Parameters obtained from the fitting of the transverse and longitudinal ^{17}O NMR relaxation rates and chemical shifts as a function of temperature at 11.7 T, and of the NMRD profiles at 298K and 310K. Underlined parameters were fixed in the fit.

	GdL^5		GdL^6		GdL^{10}
	^{17}O NMR	NMRD	^{17}O NMR	NMRD	^{17}O NMR
$k_{\text{ex}}^{298} (10^6 \text{s}^{-1})$	14.2(7)	<u>14.2</u>	13.0(6)	<u>13.0</u>	13.5(<u>4</u>)
$\Delta H^\ddagger (\text{kJ}\cdot\text{mol}^{-1})$	38.3(8)	<u>38.3</u>	33.3(6)	<u>33.3</u>	33.8(<u>4</u>)
$\Delta S^\ddagger (\text{J}\cdot\text{mol}^{-1}\cdot\text{K}^{-1})$	+21(2)		+4(1)		1(<u>1</u>)
$\tau_{\text{R}}^{298} (\text{ps})$	250(12)	212(10)	292(15)	271(15)	214(<u>10</u>)
$E_{\text{R}} (\text{kJ}\cdot\text{mol}^{-1})$	21.1(2)	23.9(2)	17.6(2)	17.5(2)	20.0(<u>2</u>)
$\tau_{\text{V}}^{298} (\text{ps})^{[c]}$	2(0.2)	32.9(1)	2.0(1)	4.0(1)	5.0(<u>1</u>)
$\Delta^2 (10^{20} \text{s}^{-1})$	0.61(5)	0.30(3)	0.36(6)	0.19(6)	1.2(<u>0.1</u>)
$A/\hbar (10^6 \text{rad}\cdot\text{s}^{-1})$	-3.9(1)		-3.7(1)		-3.9(<u>1</u>)
C_{os}	0.20		0.21(5)		0.20(<u>5</u>)
$D_{\text{GdH}} (10^{-10} \text{m}^2\text{s}^{-1})$		<u>26</u>		<u>26</u>	
$E_{\text{DGdH}} (\text{kJ}\cdot\text{mol}^{-1})$		<u>35</u>		<u>35</u>	

The GdL^7 complex also falls into this rule. On the other hand, the three other complexes have faster water exchange than that on GdDOTA. This is likely the consequence of the coordination of the amide function which is oriented differently than in GdL^7 and which is relatively far and therefore induces more steric constraints around the water binding site. Higher steric constraint is known to lead to faster water exchange in dissociatively activated water exchange processes [46]. The rotational correlation times obtained in the fit are relatively long as compared to that of GdDOTA, which is the result of the larger molecular size of the chelates. The values obtained from the ^{17}O longitudinal relaxation rates are longer than those calculated from the ^1H NMRD data, reflecting the possible motion around the Gd-coordinated water oxygen axis. Similar data have been previously reported for different Gd-complexes [40].

Table 2.3B: Parameters obtained from the fitting of the transverse and longitudinal ^{17}O NMR relaxation rates and chemical shifts as a function of temperature at 11.7 T, and of the NMRD profiles at 298K and 310K. Underlined parameters were fixed in the fit.

	GdL⁷		GdDOTA^a
	^{17}O NMR	NMRD	^{17}O NMR
$k_{\text{ex}}^{298} (10^6 \text{s}^{-1})$	0.70(5)	<u>0.70</u>	4.1
$\Delta H^\ddagger (\text{kJ.mol}^{-1})$	30.8(5)	<u>30.8</u>	49.8
$\Delta S^\ddagger (\text{J.mol}^{-1}.\text{K}^{-1})$	-30(2)		+48.5
$\tau_{\text{R}}^{298} (\text{ps})$	204(10)	115(10)	77
$E_{\text{R}} (\text{kJ.mol}^{-1})$	27.1(4)	15.0(2)	16.1
$\tau_{\text{V}}^{298} (\text{ps})^{[c]}$	5.0(2)	12.2(8)	11
$\Delta^2 (10^{20} \text{s}^{-1})$	0.80(6)	0.98(6)	0.16
$A/\hbar (10^6 \text{rad.s}^{-1})$	-3.8(1)		-3.7
C_{os}	0.00(5)		0.21
$D_{\text{GdH}} (10^{-10} \text{m}^2 \text{s}^{-1})$		<u>26</u>	<u>22</u>
$E_{D_{\text{GdH}}} (\text{kJ.mol}^{-1})$		<u>35</u>	<u>20.2</u>

a) from [41].

2.4.5. Binding assays

2.4.5.1. Relaxometric titrations

The binding of the neurotransmitters to the complexes GdL^5 , GdL^6 , GdL^7 and GdL^{10} was investigated by monitoring the variation of the longitudinal water proton relaxation rates R_1 at 37°C and pH 7.4, following the addition of increasing amounts of a given neurotransmitter to the solution of the complex. Figures 2.22 and 2.23 display the change observed upon titration of the complexes GdL^5 and GdL^6 with acetylcholine, GABA, L-glutamate, glycine as well as L-glutamine, which is a non-neurotransmitter amino-acid. Figure 2.24 shows the titration curve of GdL^{10} with glycine. Since the behaviour of GdL^{10} was similar to that of GdL^6 , it was not further investigated with other neurotransmitters. The complexes GdL^7 and GdL^{10} displayed no change in relaxivity in presence of any of the amino acid neurotransmitters (curves not shown).

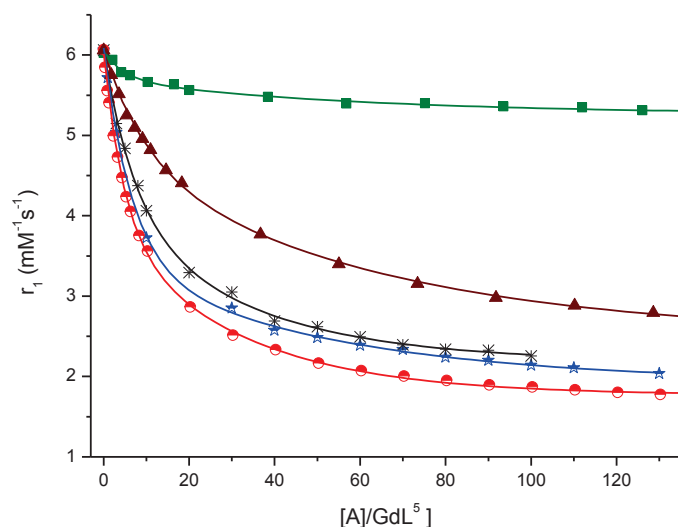


Figure 2.22. ^1H NMR relaxometric titrations of GdL^5 with different neurotransmitters at 60 MHz, pH 7.4 and 37°C. Ach (■), GABA (▲), Glu (*), Gln (★) and Gly (●).

GdL^5 showed a significant decrease of relaxivity when titrated with glutamine and glycine, and to a lower extent in the presence of GABA. The effect of acetylcholine, serotonin and noradrenaline is significantly smaller than that of the other amino acids. This is obviously due to the absence of a carboxylate group. The same trend was observed for GdL^6 which triggers a slightly increased response as compared to GdL^5 , especially in the case of acetylcholine and

GABA. This decrease in relaxivity clearly indicates that there is formation of ternary complexes which implies the partial or complete displacement of the water molecule in the inner coordination sphere.

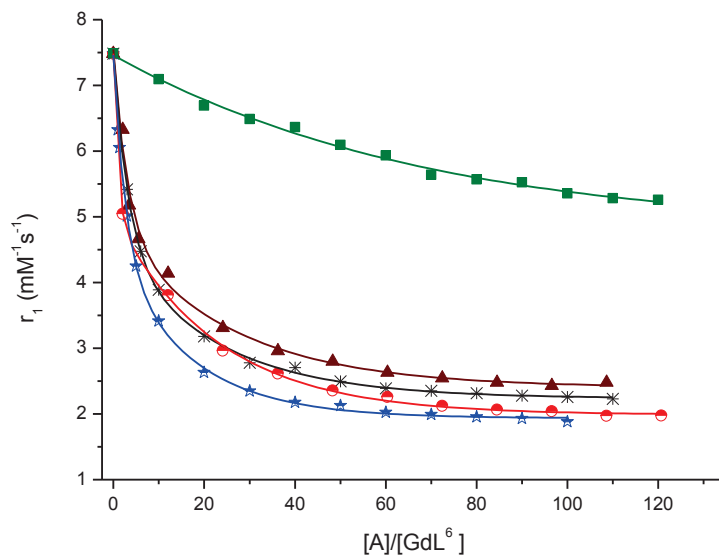


Figure 2.23. ^1H NMR relaxometric titrations of GdL^6 with different neurotransmitters at 60 MHz, 37°C and pH7.4 (HEPES 25mM), ~ 2 mM complex. The titration of glutamate was done at 300 MHz. Ach (■), GABA (▲), Glu (*), Gln (★) and Gly (●).

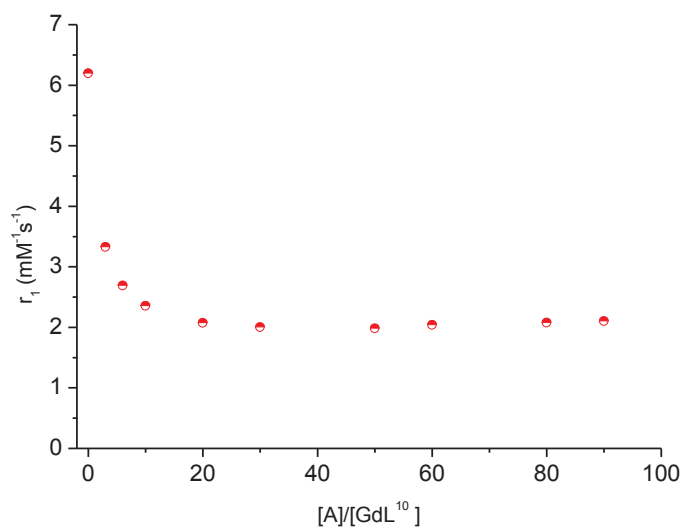


Figure 2.24. ^1H NMR relaxometric titration of GdL^{10} with glycine at 500 MHz, 37°C and pH7.4 (HEPES 25mM), ~ 2 mM complex.

Table 2.4 summarizes the relaxivity decrease observed for GdL⁵ and GdL⁶ upon interaction with neurotransmitters and other anions as well as the corresponding dissociation constants for the ternary complexes ($K_d = [\text{GdL}][\text{A}] / [\text{GdL-A}]$, where A stands for the analyte neurotransmitter or anion). The dissociation constants have been calculated by fitting the relaxation rates as a function of the analyte concentration as described in the experimental section.

Table 2.4. Dissociation constants and the percentages of the observed change in relaxivity upon interaction with neurotransmitters and small anions.

	GdL ⁵		GdL ⁶	
	K _d (mM)	r _{1p} (%)	K _d (mM)	r _{1p} (%)
Acetylcholine	-	12	-	30
GABA	28.2(8)	58	8.0(2)	67
Glycine	9.1(2)	71	5.6(2)	74
Glutamine ^a	9.8(4)	66	6.1(2)	75
Serotonin ^a	-	<10 ^b	-	-
Noradrenaline ^a	-	22 ^b	-	25 ^b
Carbonate	14.7(8)	67	-	-
Glutamate	19.8(3)	59	9.1(2)	69
Hydrogen phosphate	-	0	-	0

a) Titrations were conducted at 300MHz, 37°C. b) r_{1p} decrease after adding at once 50 equivalents of NT.

It is worth noting that GdL⁵ has selectivity for glycine and L-glutamine (α - amino acids) over GABA (a γ -amino acid), whilst this selectivity has diminished in the case of GdL⁶, having the longest linker. This observation leads to think that GABA is too big to form dual binding with both paramagnetic metal and crown ether. Thus, this suggests that the crown ether is important for binding strength. Thus, this suggests that the crown ether is important for binding strength. Chirality of the α -methyl group does not seem to contribute much to the binding selectivity, as the non-chiral glycine responds to a similar extent as L-glutamine. L-glutamine and L-glutamate have similar effects (we should note that the titration with L-glutamate was carried out at different magnetic field (300MHz)).

The effect of bicarbonate and phosphate ions was also investigated since these are two significant and often interfering components of physiological fluids. Bicarbonate is the most abundant anion in extracellular space and it is found in the range of 25 mM, compared with about 1 mM for hydrogenphosphate. However, so far it is not known how bicarbonate concentrations fluctuate within the brain following stimulation. Complex GdL^5 displayed a decrease in relaxivity upon titration with bicarbonate anion in to a similar extent as glutamine (figure 2.25). Similar effect is expected for GdL^6 with hydrogencarbonate (not measured). On the other hand, no decrease of relaxivity is observed when phosphate is added to the solution. The titration of GdL^5 with glutamine in the presence of a 100-fold excess of potassium has been also performed to check if the interaction potassium-crown ether interferes with the change in relaxivity. We have noticed that the initial relaxivity of the complex solution has slightly increased upon addition of K^+ (figure 2.25). This is might be due to a partial rearrangement of the coordination environment of Gd^{3+} upon potassium binding by crown-ether. That is, the ethyl amide group might partially dissociates from the gadolinium ion when the potassium is trapped by the crown-ether. This also points to the binding of the ethylamide carbonyl group to the metal ion. The total decrease in relaxivity has shifted from 66 % to 72 % in the presence of potassium ions.

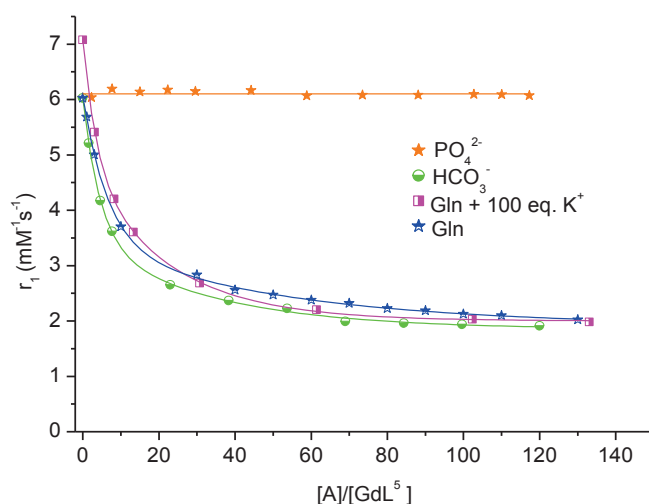


Figure 2.25. Change in r_1 of complex GdL^5 as function of added hydrogen phosphate, hydrogen bicarbonate, glutamine and glutamine in the presence of 100 eq. of K^+ . ~ 2 mM complex, 25 mM HEPES, 60 MHz, 37 °C, pH 7.4.

2.4.5.2 Luminescence studies

The results from the relaxometric titrations suggest that the coordinated water molecule is partially or entirely displaced by neurotransmitter binding. This process was detected and confirmed by changes in the luminescence lifetime of the excited states, determined in H₂O. The lifetimes of the EuL⁵ were measured in the absence and presence of added glutamate. The hydration number of EuL⁵ was found to decrease from 1.1 to 0.3 following addition of 60 equivalents of glutamate (figure 2.26), which explains the observed drop in relaxivity.

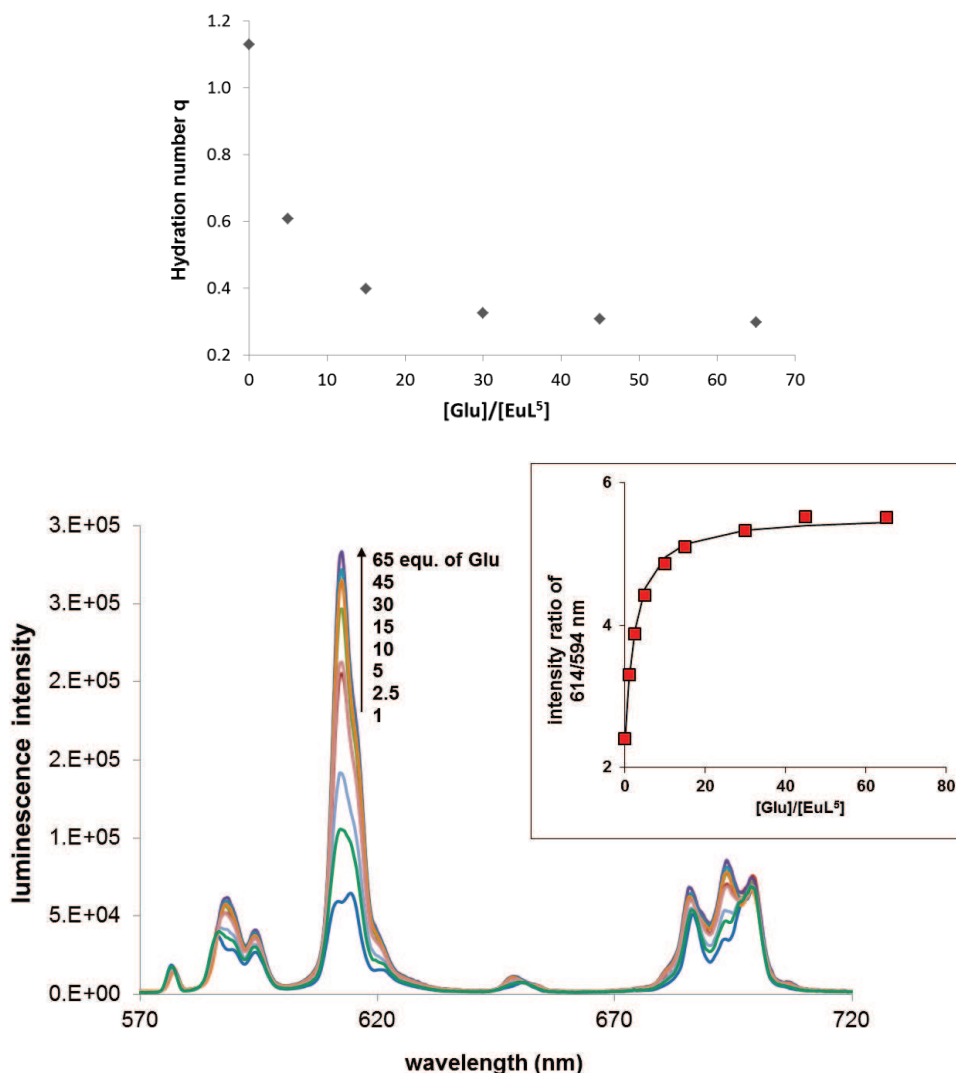


Figure 2.26. Changes in hydration number and luminescence emission of EuL⁵ upon addition of increasing amount of glutamate (5 mM complex, 25 mM HEPES, pH 7.3, excitation 391 nm).

Furthermore, the shape and intensity of some of the bands in the Eu^{3+} emission spectra are known to be highly sensitive to changes in the coordination environment of the lanthanide ion, whilst others remain unaffected [47, 48]. Thus, a change in the hydration state induces a change in the form of the emission spectra. We have examined the emission spectral properties of the EuL^5 complex. Upon addition of increasing amount of glutamate, there was a significant increase in the emission intensity ratio of 615 and 594 nm bands, from 2.4 to 5.5 (figure 2.26). This also suggests that the water molecule has been displaced, as the emission is enhanced due to the removal of the O-H vibrational quenching pathway. This phenomenon may open the possibility of ratiometric measurements to detect neurotransmitters, as previously used for the detection of hydrogencarbonate and citrate [27, 31]. Indeed, such ratiometric response allows eliminating the problem related to the unknown local concentration of the agent through concentration-independent measurements.

2.4.5.3 ^1H & 2D NMR experiments to assess the interaction of $-\text{NH}_3^+$ with the crown ether

The above described experiments (relaxometric titrations, luminescence) could not clearly show whether there is any interaction between the ammonium group of the neurotransmitters and the crown ether moiety of the Ln^{3+} complexes. Although there is a selectivity for glycine and glutamine (α - amino acids) over GABA (a γ -amino acid) which may lead to think that GABA is too big to form dual binding with both paramagnetic metal and crown ether, this discrimination may merely be due to steric factors making the Ln^{3+} ion less accessible to interact with the CO_2^- group of the neurotransmitter. We prepared the YL^5 complex, a diamagnetic analogue of GdL^5 in order to study the interactions by NMR. The ^1H NMR spectrum of YL^5 is shown in Figure 2.27.

In order to look at the spectral changes upon neurotransmitter binding, 6 equivalents of glutamate have been added to the YL^5 solution and the ^{13}C - ^1H HSQC spectrum has been recorded, as compared to the YL^5 solution without glutamate (Figure 2.28). The comparison of the spectra clearly shows that the binding of the glutamate has a strong effect on all the peaks, including those of the crown ether, except for the aromatic signals which remain unaffected. The same experiment has been performed on a solution containing 6 equivalents of

bicarbonate (Figure 2.29). In this case, all signals are shifted, including those of the aromatic ring. These results indicate that bicarbonate binding affects the conformation of the entire complex while glutamate binding has no observable effect on the aromatic ring. Consequently, no final conclusion can be drawn about the participation of the crown ether in the neurotransmitter binding. We should also note that hydrogen bonding between the hydrogencarbonate proton and the crown ether oxygens or nitrogen cannot be excluded either, which will evidently, strongly affect the crown ether signals. Unfortunately, all attempts to detect any NOE effect between the crown ether and glutamate nuclei were unsuccessful.

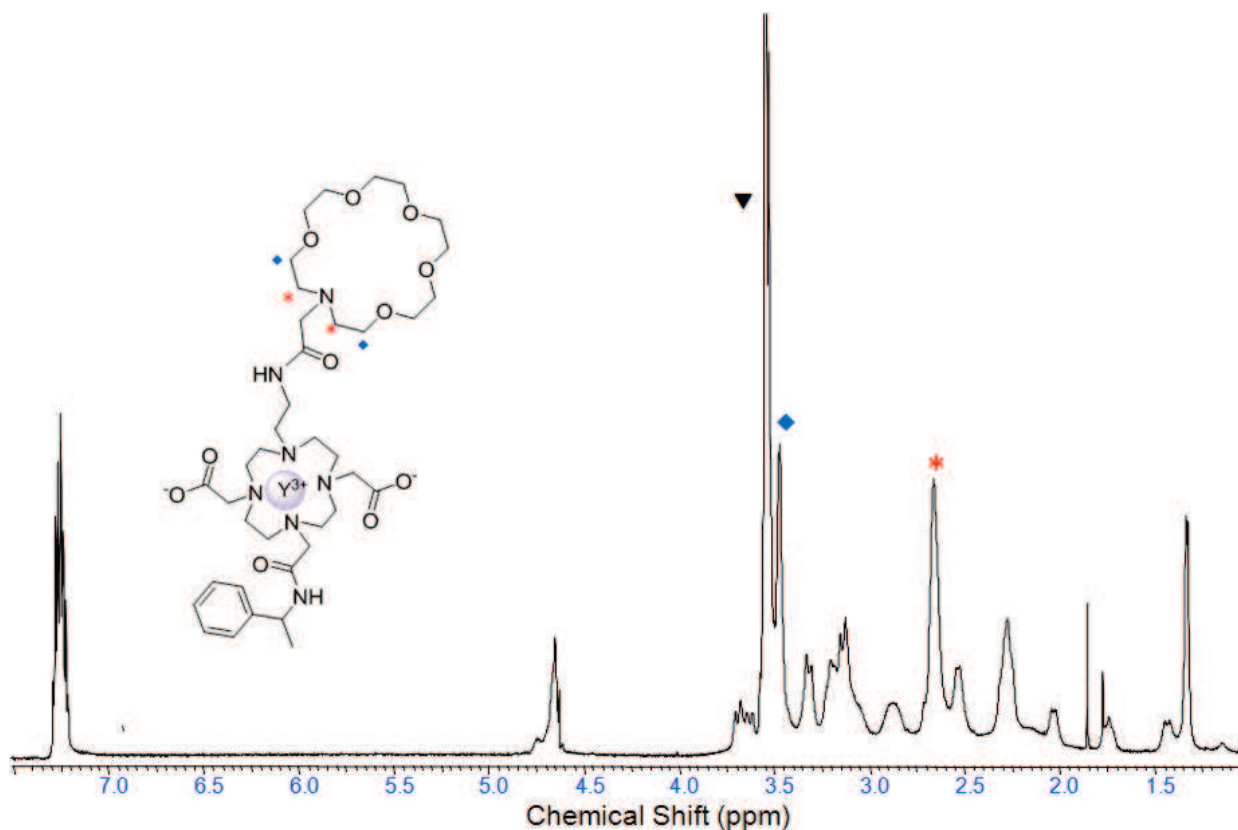


Figure 2.27. ^1H NMR spectrum of the complex YL⁵, highlighting the ^1H signals from the crown ether moiety (▼, * and ◆).

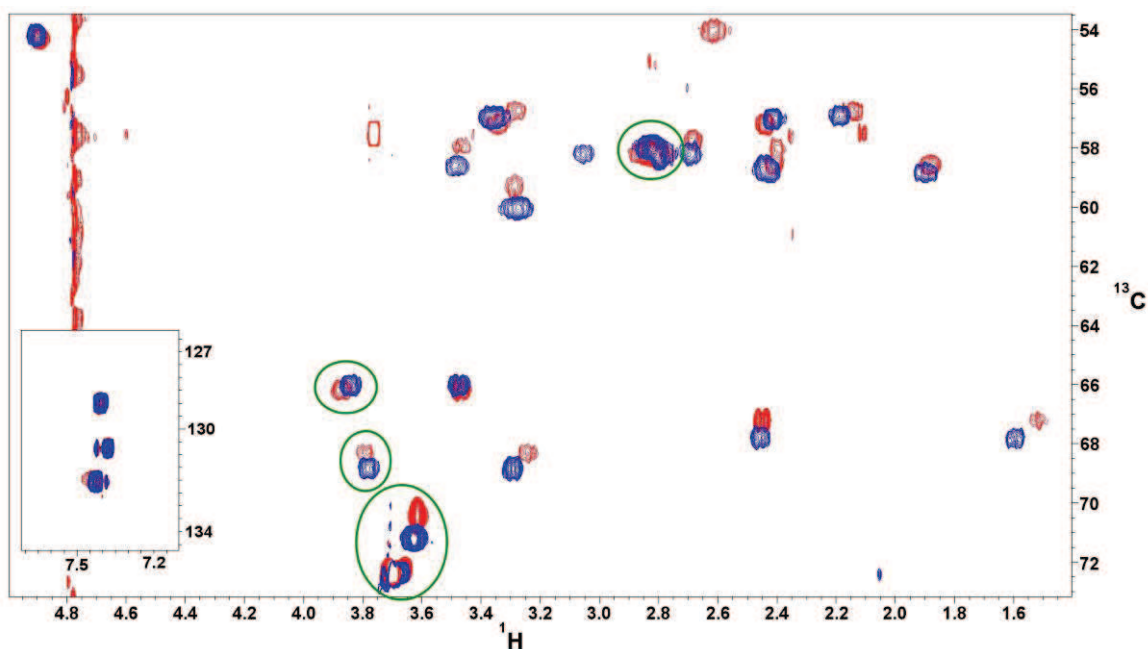


Figure 2.28. ^{13}C - ^1H HSQC spectra of YL^5 in the absence (blue) and in the presence of 6 equivalents of glutamate (red). The peaks of the crown ether are encircled and aromatic ones are shown in the inset. pH 7.4.

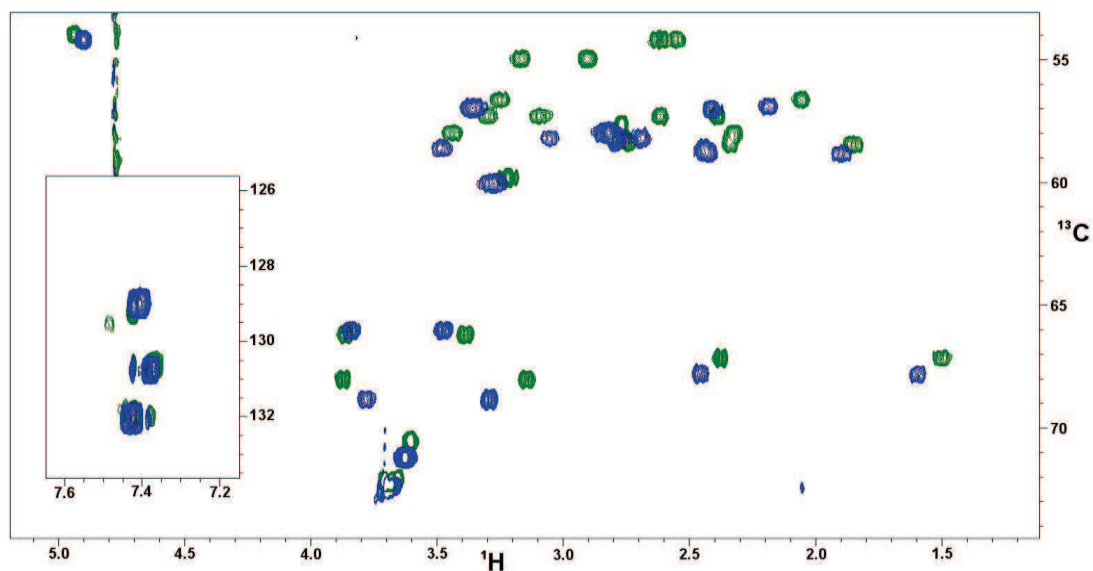


Figure 2.29. ^{13}C - ^1H HSQC spectra of YL^5 in the absence (blue) and in the presence (green) of 6 equivalents of HCO_3^- . The aromatic peaks are shown in the inset. pH 7.4.

2.4.5.4. Computational study of the ternary complex YL⁵-Gly

DFT calculations have been performed on the GdL⁵-Gly system by Carlos Platas at the University of Corunha, Spain. The objective of these calculations was first of all to show that ditopic binding of neurotransmitters to GdL⁵ is indeed feasible. In Eu³⁺ complexes of DOTA, DOTA-tetraamide and DO3A derivatives the signals of the *pseudo* axial protons on the cyclen rings are usually found between 24 and 45 ppm in the SAP isomer and below 20 ppm in the TSAP isomer [28, 29, 34, 49-51]. The spectrum recorded for EuL⁵ shows four resonances in the range 28.7-31.4 ppm (figure 2.23) that indicates that the complex presents a SAP coordination in solution. Thus, only the SAP form of the GdL⁵-Gly complex has been considered in our calculations. The ligand provides heptadentate binding to the metal ion through the four nitrogen atoms of the cyclen unit, and three oxygen atoms provided by two carboxylate groups and the acetamide group (figure 2.31). The calculated Gd-N bond distances fall in the range 2.65-2.76 Å with an average value of 2.71 Å. As expected due to their negative charge, the Gd-O distances involving oxygen atoms of carboxylate groups (2.35 and 2.38 Å) are shorter than the Gd-O_{amide} distance (2.42 Å). Overall, the distances between Gd³⁺ and the donor atoms of the ligand are in good agreement with those observed for different complexes of this ion with cyclen-based ligands [50]. Nine-coordination around Gd³⁺ is completed by the carboxylate unit of Gly, which is predicted to bind to Gd³⁺ in an asymmetrical bidentate fashion, with Gd-O distances of 2.48 and 2.63 Å. These distances are very similar to those calculated for the interaction of a DO3A derivative and the carboxylate group of 5-acetylneuraminic acid [29]. The mean twist angle of the two square faces defined by the four nitrogen atoms of the macrocycle and the donor atoms of the pendant arms and one oxygen atom of Gly (41.9°) is close to the ideal value expected for a SAP coordination (45°).

The -NH₃⁺ moiety of Gly interacts with the aza-18-crown-6 moiety through two approximately linear N-H...O and N-H...N hydrogen bonds [N...O 2.982 Å, NH...O 1.928 Å, N-H...O 176.7°; N...N 2.972 Å, NH...N 1.949 Å, N-H...N 168.3°] and a third weaker N-H...O interaction [N...O 2.932 Å, NH...O 2.003 Å, N-H...O 147.7°]. The distances between the donor N atom of Gly and all the six acceptor groups of the crown ether are short, indicating strong dipolar attractions [2.96-2.98 Å]. Both the interaction mode of Gly and the conformation of the

macrocyclic moiety calculated for GdL5-Gly are very similar to those observed in different complexes of alkylammonium guests with 18-crown-6 derivatives [47, 52].

Aiming to obtain a rough estimation of the binding energy for the interaction between the -NH_3^+ group of Gly and the crown moiety, we performed a geometry optimization of $\text{GdL}^5\text{-Gly}$ starting from a molecular geometry in which the crown moiety was brought away from the Gly unit. This was achieved by rotation of the C-N(H)-C(O)-C dihedral angle of the amide group linking the crown ether moiety and the cyclen unit. The energy difference between the two energy minima corresponding to $\text{-NH}_3^+\cdots\text{crown}$ bound and unbound forms amounts to 94.3 kJ/mol, which suggests that the binding of Gly through the crown moiety provides a substantial contribution to the overall stability of the $\text{GdL}^5\text{-Gly}$ system.

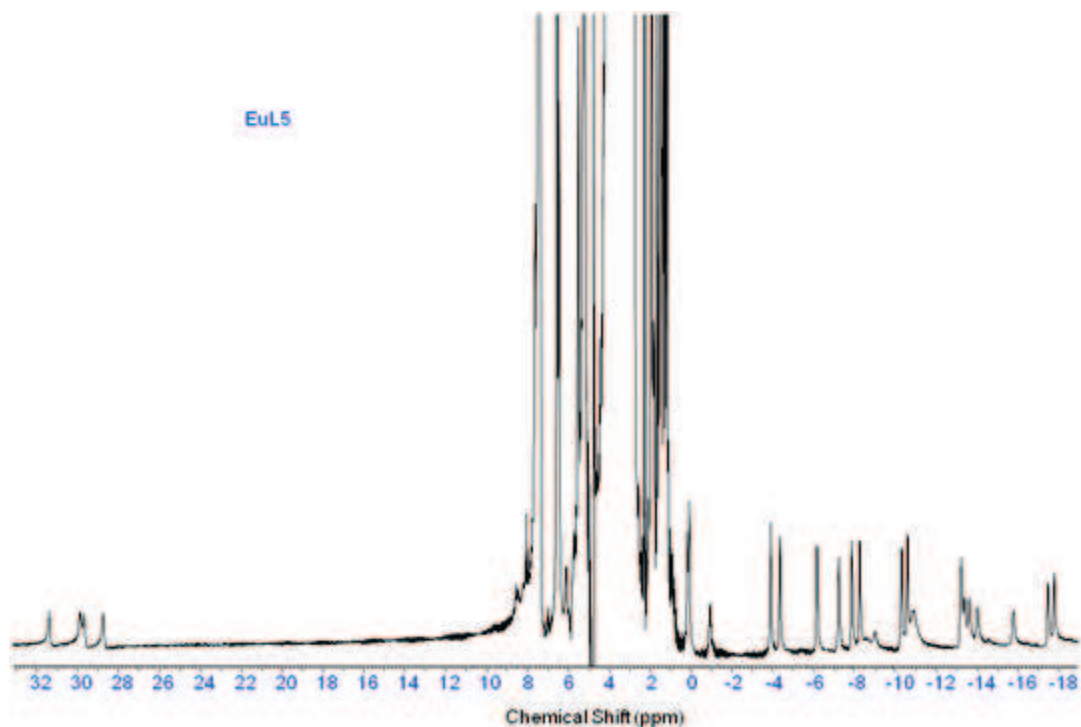


Figure 2.30. 500 MHz ^1H spectrum of the complex EuL^5 . pH 7.4

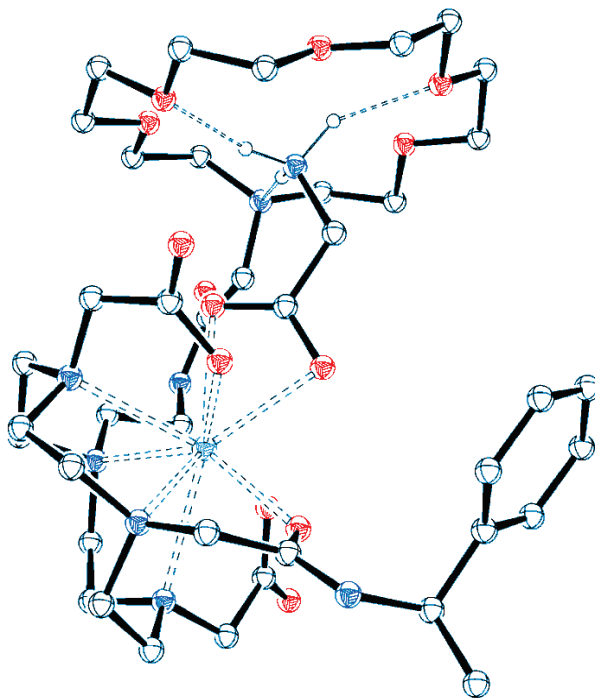


Figure 2.31. Molecular geometry of the ternary complex $\text{GdL}^5\text{-Gly}$ as optimized in aqueous solution at the TPPSh/ LCRECP /6-31G(d) level.

2.5. Conclusion:

In summary, we have described in this proof-of-concept study the design and synthesis of lanthanide-based probes in the objective of developing smart contrast agents sensitive to zwitterionic amino-acid neurotransmitters for potential use in MRI. Two of the synthesized Gd^{3+} -based SCAs exhibited, as expected, a decrease in proton relaxivity up to $\sim 70\%$ in the presence of the amino-acid neurotransmitters. These SCAs showed a good affinity for amino acid neurotransmitters in the mM range, which is suited for imaging in the extracellular media, where the concentration are typically in the range of mM for some neurotransmitters. They also displayed good selectivity over non-amino acid neurotransmitters (acetylcholine, serotonin and noradrenaline) and hydrogenphosphate. Unfortunately, the design did not prove to be selective, as the complexes also bind hydrogen bicarbonate to the same extent as glycine and glutamate.

The mechanism of the neurotransmitter-dependent-relaxivity change has been investigated by the measurements of luminescence lifetimes on the corresponding Eu^{3+} and Tb^{3+} complexes, suggesting that a decrease in hydration number is responsible for the relaxivity decrease. The change in the hydration state was also suggested by a change in the emission intensity bands of Eu^{3+} complex. Advantageously, these probes have shown a specific luminescence response, which might be valuable for the ratiometric measurement of neurotransmitter levels both for *in vitro* and *in vivo* assays.

The above results encouraged us to direct our efforts towards further improving the design of the SCAs at different levels as discussed in the next chapter.

2.6. Experimental procedures and materials

All commercial reagents and solvents were used as received from the suppliers unless otherwise indicated. Tetrahydrofuran (THF) was freshly distilled from the sodium complex of benzophenone before use.

Analytical ^1H and ^{13}C NMR spectra were recorded on a Bruker AvanceIII 300 MHz spectrometer operating at 300.17 and 75.48 MHz, for ^1H and ^{13}C , respectively. All experiments were performed at 25 °C.

Chromatographic methods: Flash column chromatography was performed using flash silica gel 60 (70-230 mesh ASTM). Analytical thin layer chromatography (TLC) was performed on aluminum sheet silica gel plates with silica gel 60 F254 (Merck). The compounds were visualized by UV254 light and/or developed with Dragendorff stain. Purification using reversed phase HPLC was on a Varian PrepStar Instrument, Australia, equipped with PrepStar SD-1 pump heads. UV absorbance was measured using a ProStar 335 photodiode array detector at 214 nm and 254 nm. This detector is equipped with a dual-path length flow cell which enables measurement of absorption of analytical and preparative samples without changing the flow cell. Reversed-phase analytical HPLC was performed in a stainless steel Chromsep (length 250 mm, internal diameter 4.6 mm, outside diameter 3/8 inch and particle size 8 μm) C18 column and preparative HPLC was performed in a stainless steel Chromsep (length 250 mm, internal diameter 41.4 mm, outside diameter 2 inch and particle size 8 μm) C18 column (Varian, Advanced Chromatographic Solutions). The three ligands were purified according to the same method (table). The flow rate used was 10 mL/min.

Electrospray ionization mass spectrometry (ESI-MS) spectra were performed on an SL 1100 system (Agilent) with ion trap detection in the positive and negative ion modes. FT-ICR-MS were performed on a Bruker FT-ICR Apex II spectrometer Agilent (Germany).

Table 2.5. Elution conditions for preparative HPLC. Solvents were buffered with 0.1% HCOOH.

Time (s)	%H ₂ O	% MeCN
0:00	90	10
1:00	85	15
14:00	85	15
15:00	78	22
21:00	78	22
22:00	10	90
25:00	10	90
26:00	90	10
30:00	90	10

Potentiometric Studies. Carbonate-free 0.1 molL⁻¹ NMe₄OH, KOH and 0.1 molL⁻¹ HCl were prepared from Fisher Chemicals concentrates. Potentiometric titrations were performed in 0.1 molL⁻¹ aqueous NMe₄Cl under nitrogen atmosphere and the temperature was controlled to ± 0.1 °C with a circulating water bath. The p[H] (p[H] = -log[H⁺], concentration in molarity) was measured in each titration with a combined pH glass electrode (Metrohm) filled with 3M KCl and the titrant addition was automated by use of a 702 SM titrino system (Metrohm). The electrode was calibrated in hydrogen ion concentration by titration of HCl with NMe₄OH in 0.1 molL⁻¹ electrolyte solution [48]. A plot of meter reading versus p[H] allows the determination of the electrode standard potential (E°) and the slope factor (f). Continuous potentiometric titrations with NMe₄OH 0.1 molL⁻¹ were conducted on aqueous solutions containing L⁵⁻⁷ (~ 3 mM) in the range 2-11.8. Experimental data were refined using the computer program Hyperquad 2008 [53]. All equilibrium constants are concentration quotients rather than activities. The ionic product of water at 25 °C and 0.1 molL⁻¹ ionic strength is pK_w = 13.77 [54]. Fixed values were used for total concentrations of ligand and base. All values and errors (one standard deviation) reported are at least the average of three independent experiments.

The ¹H NMRD profiles and 1/T₁ relaxation measurements: The 1/T₁ nuclear magnetic relaxation dispersion (NMRD) profiles of the water protons were recorded at 37 °C and 25 °C on a Stelar SMARTracer Fast Field Cycling NMR relaxometer (0.00024-0.24 T, 0.01-10 MHz ¹H Larmor frequency) and a Bruker WP80 NMR electromagnet adapted to variable field

measurements (0.47-1.88 T, 20-80 MHz ^1H Larmor frequency) controlled by the SMARTracer PC-NMR console. The temperature was controlled by a VTC91 temperature control unit and maintained by a gas flow, measured according to a previous calibration with a Pt resistance temperature probe. The relaxivities at 300 MHz was measured on a Bruker Avance 300 (7T) spectrometer. The least-squares fit of ^1H NMRD data were performed by using Micromath Scientist[®] version 2.0 (Salt Lake City, UT, USA).

^{17}O NMR Measurements. Variable temperature ^{17}O NMR measurements on aqueous solution of the Gd^{3+} complexes were obtained on a Bruker Avance 500 (11.75 T, 67.8 MHz) spectrometer. The temperature was calculated according to a previous calibration with ethylene glycol and MeOH [55]. Acidified water (HClO_4 , pH~4) was used as an external reference. Longitudinal ^{17}O relaxation times T_1 were measured by the inversion-recovery pulse sequence[56], and the transverse relaxation times (T_2) were obtained by the Carr-Purcell-Meiboom-Gill spin-echo technique[57]. Analysis of the ^{17}O NMR experimental data was performed with the Scientist[®] software. To eliminate the susceptibility corrections to the chemical shift [58], the samples were placed in a glass sphere fixed in a 10 mm NMR tube. For sufficient accuracy, at least 20 mM concentration of the Gd^{3+} complex has been used. To improve sensitivity, the amount of ^{17}O was enriched by adding H_2^{17}O (10% H_2^{17}O , CortecNet) to achieve approximately 1% ^{17}O content in the sample.

Luminescence measurements: The lifetime measurements were performed on a QuantaMasterTM 3 PH fluorescence spectrometer from Photon Technology International, Inc. (USA). The measurements were performed in H_2O and D_2O (25 °C, pH 7.4, HEPES) at a concentration of 5 mM for EuL^{5-6} and 50 μM for TbL^{5-6} . Excitation and emission slits were set to 2 nm and 1 nm for EuL and TbL respectively. The luminescence spectra were obtained after excitation at 394 nm for Eu^{3+} and at 257 nm for Tb^{3+} . Each reported luminescence lifetimes is the average 3 values involving 25 scans (decays data) and the curves are fitted with no improvement to the first order exponential decay.

UV-Vis spectrophotometry

The absorbance spectra were recorded on a Perkin-Elmer Lambda 19 spectrometer in thermostated cells between 25 and 50 °C for EuL⁵ ($c_{Eu} \approx 2.5$ mM, pH ~ 6.80) and EuL⁶ ($c_{Eu} \approx 2.4$ mM, pH ~ 6.90). The measurements were carried out in a 10 cm optical path length cylindrical cuvette between $\lambda = 577 - 581.0$ nm.

Neurotransmitter Binding Studies. Ternary complex formation between GdL⁸⁻⁹ complexes and neurotransmitters was assessed by performing relaxometric titrations at 37°C on a Stellar SMARTracer Fast Field Cycling NMR relaxometer at 37 °C (60 MHz) or on a Bruker AvanceIII 300 MHz spectrometer. The pH was maintained at 7.4 by a 25 mM HEPES buffer. A HEPES buffered solution of the neurotransmitter was added stepwise to the 1-2 mM GdL complex solutions of up to at least 100 equivalents. The concentration of the Gd³⁺ solutions was determined by bulk magnetic susceptibility method (BMS) using *tert*-butanol enriched samples [59]. The dissociation constants were determined according to the following equations where the paramagnetic relaxation rate $1/T_{1para}$ is the sum of the contributions originating from the free GdL complex and the GdL-analyte adduct (GdLA). The $1/T_{1para}$ values measured as a function of the analyte (neurotransmitter) concentrations have been fitted to the equations below:

$$1/T_{1para} = \left(r_1^{GdLA} \times Z + (c_{GdL} - Z) \times r_1^{GdL} \right) \times 1000$$

where

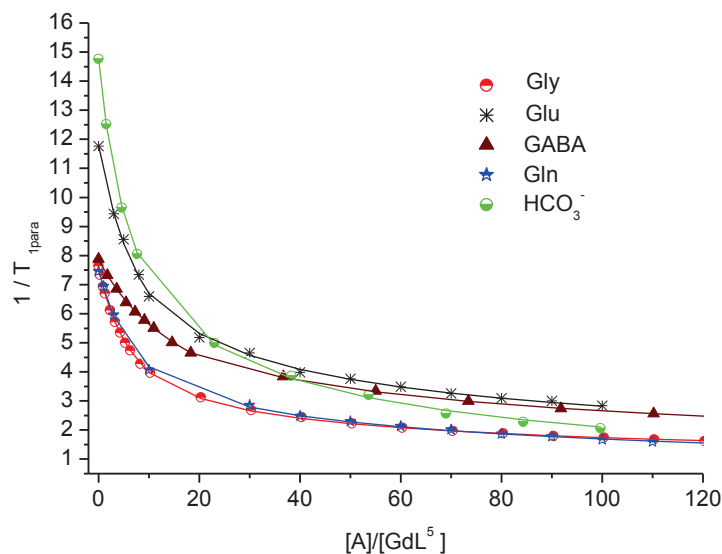
$$Z = \frac{\left(K_d + c_{GdL} + c_A \right) + \sqrt{\left(K_d + c_{GdL} + c_A \right)^2 - 4(c_A \times c_{GdL})}}{2}$$

The dissociation constant is defined as:

$$K_d = \frac{[A] \times [GdL]}{[GdLA]}$$

where r_1^{GdL} and r_1^{GdLA} are the relaxivities of the free complex and the fully bound complex, respectively. K_d is the dissociation constant, C_{GdL} and C_{CA} represent the concentrations of both GdL and analyte. Both K_d and r_1^{GdLA} have been obtained through a two parameter fitting of the

relaxation rate data measured at various analyte concentrations. Representative fits are shown below for GdL^5 .



NMR experiments (to assess the interaction NH_3^+ -crown ether)

Sample preparation:

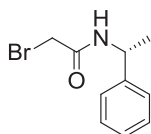
YL^5 was dissolved in 300 μL of D_2O in Shigemi tube with final concentration of 7.5 mM and $\text{pH}=7.4$. For the formation of the ternary complex we added 6 equivalents of glutamic acid and we adjusted the pH at 7.4. All two-dimensional $^1\text{H}, ^{13}\text{C}$ -HSQC spectra was collected at 298K on Varian INOVA 600-MHz equipped with a triple resonance HCN probe and Z-pulsed field gradients. The NMR data sets were processed using the NMRPipe/NMRDraw software package [59] and analysed using CCPN software[60].

Computational details of the ternary complex GdL^5 -Gly. All calculations were performed employing the Gaussian 09 package (Revision B.01). Full geometry optimizations of the GdL^5 -gly system were performed in aqueous solution employing DFT within the hybrid meta generalized gradient approximation (hybrid meta-GGA), with the TPSSh exchange-correlation functional [5]. It was shown that the TPSSh functional provides more accurate geometries of Ln^{3+} complexes than the popular B3LYP functional, as well as accurate ^{17}O hyperfine coupling constants of the

coordinated water molecule for different Gd^{3+} complexes with polyaminocarboxylate ligands [61]. In these calculations we employed the energy-consistent large-core quasirelativistic ECP of Dolg et al [7]. (LCRECP) and its associated [5s4p3d]-GTO valence basis set for the lanthanide, while the C, H, N and O atoms were described by using the standard 6-31G(d) basis set. No symmetry constraints have been imposed during the optimizations. The large-core RECP approach, which includes the 4f electrons in the core, avoids many difficulties associated to the computational treatment of open-shell systems, and despite their approximate nature it is an efficient computational tool that has proven to give good results in studies that focus on the structural features or the estimates of relative energies for Ln^{3+} complexes at both the HF and DFT level [8, 9]. The default values for the integration grid ("fine") and the SCF energy convergence criteria (10^{-8}) were used. Solvent effects were included by using the polarizable continuum model (PCM), in which the solute cavity is built as an envelope of spheres centered on atoms or atomic groups with appropriate radii. In particular, we used the integral equation formalism (IEFPCM) variant as implemented in Gaussian 09 [17].

Synthesis:

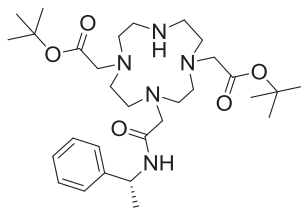
(R)-2-bromo-N-(1-phenylethyl)acetamide



R-(+)-1-phenylethylamine (9.0g, 74.3 mmol) was dissolved in 300 ml of a mixture of water/chloroform 1:1. Bromoacetyl bromide (9.7mL, 111.0 mmol) in chloroform and an aqueous solution of K_2CO_3 (3M) were each added simultaneously dropwise to the stirred solution at room temperature over a two hour period while maintaining the pH between 6-7. The mixture was stirred an additional 2 hours at room temperature. The chloroform layer was separated and washed once with saturated aqueous $NaHCO_3$ solution and twice with water. The organic layer was dried over Na_2SO_4 and the solvent was evaporated under reduced pressure. The crude product was recrystallized from hot carbon tetrachloride and the product was isolated by filtration as white crystals (15.0 g, 75%).

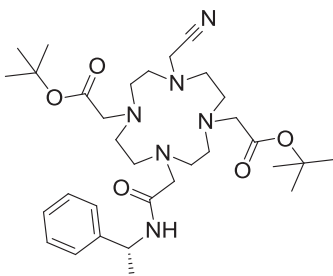
^1H NMR (CDCl₃, 300 MHz), δ : 7.31-7.18 (m, 5H, Ar-H), 6.69 (br. s, 1H, NH), 5.02 (dq, $J=6.9$ and 7.5 Hz, 1H, CHCH₃), 3.78 (dd, $J=17.4$ Hz, 2H, Br-CH₂CO), 1.45 (d, $J=6.9$ Hz, 3H, CHCH₃). **^{13}C NMR (CDCl₃, 75 MHz)**, δ : 164.5 (CO), 142.3 (Ar-C_q), 128.7, 127.5, 126.0, 49.5 (CHCH₃), 29.2 (BrCH₂), 21.6 (CH₃). **Mass spectrometry (ESI)**: calculated for C₁₀H₁₃BrNO⁺ [M+H]⁺: 242.0; Found 242.0.

(R)-di-tert-butyl 2,2'-(4-(2-oxo-2-((1-phenylethyl)amino)ethyl)-1,4,7,10-tetraazacyclododecane-1,7-diyl)diacetate (2)



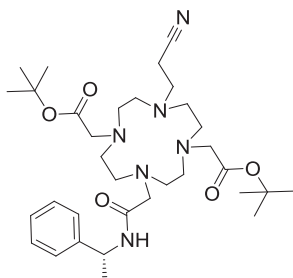
DO2A-bis(tert-butyl ester) **1** (6.0 g, 15.0 mmol) was dissolved in 150mL of a mixture of water dioxane 1:1. The pH was adjusted to 8 before adding Bromoacetyl-R-Methylbenzylamine (3.6 g, 1.05 mmol) in one portion. The pH was kept between 7 and 8 until the starting materials could no longer be observed by TLC. The product was then extracted into dichloromethane, washed with water and dried over Na₂SO₄. Removal of the solvents yielded the crude product which was recrystallized from ethyl acetate to yield **2** as white crystals (7.5 g, 89 %).

^1H NMR (CDCl₃, 30 MHz), δ : 7.51 (d, $J=7.5$ Hz, 1H, NH), 7.34-7.20 (m, 5H, Ar-H), 5.04 (dq, $J=6.9$ and 7.5 Hz, 1H, CHCH₃), 3.32-3.06 (m, 6H, 3CH₂COO), 2.94 (br. s, 4H), 2.84-2.65 (br. m, 12H), 1.48 (d, $J=6.9$ Hz, 3H, CHCH₃), 1.37 (br. s, 18H, 2 C(CH₃)₃). **^{13}C NMR (CDCl₃, 75 MHz)**, δ : 170.2 (CO₂^tBu), 170.2 (CONH), 143.3 (Ar-C_q), 128.7 (Ar-CH), 127.6 (Ar-CH), 126.6 (Ar-CH), 81.7 (C(CH₃)₃), 57.7, 54.6, 54.3, 52.0, 49.2, 49.2, 47.3, 28.12 (C(CH₃)₃), 21.7 (CHCH₃). **HRMS (ESI)**: calculated for C₃₀H₅₂N₅O₅⁺ [M+H]⁺: 562.3962; Found 562.3960.

(R)-di-tert-butyl 2,2'-(4-(cyanomethyl)-10-(2-oxo-2-((1-phenylethyl)amino)ethyl)-1,4,7,10-tetraazacyclododecane-1,7-diyl)diacetate (3a)

A solution of **2** (1.2 g, 2.1 mmol), bromoacetonitrile (0.15 mL, 2.1 mmol) and Cs_2CO_3 (1.5 g, 4.5 mmol) in 40 mL DMF was stirred at room temperature for overnight. The reaction was monitored by TLC. After completion, the reaction mixture was diluted with water and extracted with dichloromethane. The organic layer was dried over Na_2SO_4 before evaporating under reduced pressure and the brownish residue was used for the next step without further purification (1.25 g, 97 %).

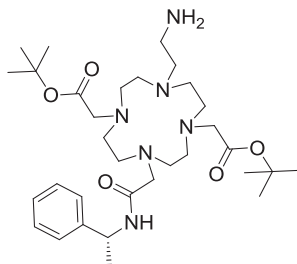
$^1\text{H NMR}$ (CDCl_3 , 300 MHz), δ : 8.20 (d, $J=7.8$ Hz, 1H, NH), 7.27-7.16 (m, 5H, Ar-H), 5.16 (dq, $J=6.9$ and 7.5 Hz, 1H, CHCH_3), 3.32 (dd, $J=17.7$ Hz, CH_2 , CH_2CN), 3.03-2.89 (m, 6H, $3\text{CH}_2\text{CO}$), 2.73-2.56 (m, 12H), 2.49-2.35 (m, 4H), 1.43 (d, 3H, CH_3 , $J=6.9$ Hz), 1.37 (s, 18H, $2\text{C}(\text{CH}_3)_3$). **$^{13}\text{C NMR}$ (CDCl_3 , 75 MHz)**, δ : 170.6 (CONH), 170.2 (2CO), 143.0 (Ar- C_q), 128.3, 127.1, 126.4, 114.8 (CN), 80.8 ($\text{C}(\text{CH}_3)_3$), 58.3, 55.9, 54.6, 52.4, 52.3, 51.5, 47.4 (CH), 42.9 (CH_2CN), 28.0 ($\text{C}(\text{CH}_3)_3$), 20.6 (CHCH_3). **LRMS (ESI)**: calculated for $\text{C}_{32}\text{H}_{53}\text{N}_6\text{O}_5^+$ $[\text{M}+\text{H}]^+$: 601.4; Found 600.4.

(R)-di-tert-butyl 2,2'-(4-(2-cyanoethyl)-10-(2-oxo-2-((1-phenylethyl)amino)ethyl)-1,4,7,10-tetraazacyclododecane-1,7-diyl)diacetate (3b)

A solution of **2** (4.0 g, 7.8 mmol), triethylamine (1.6 g, 15.6 mmol) and acrylonitrile (0.8 g, 15.6 mmol) in 50 mL Methanol was stirred at room temperature for 24 h. The reaction was monitored by TLC. After completion, the solvent was evaporated under reduced pressure and the crude product was purified using flash column chromatography (silica gel, 5 % MeOH in CH₂Cl₂, *R_f* = 0.55) to give **3b** as transparent gum (3.5 g, 79 %).

¹H NMR (CDCl₃, 300 MHz), δ: 8.23 (d, *J*=8.1 Hz, NH), 7.35 (d, *J*=6.9 Hz, 2H, Ar-H), 7.16-7.05 (m, 3H, Ar-H), 5.12 (dq, *J*=6.6 and 7.2 Hz, 1H, CHCH₃), 3.06-2.90 (m, 6H), 2.63-2.40 (m, 18H), 2.45 (t, *J*=6.6 Hz, 2H, CH₂CN), 1.45 (d, *J*=6.9 Hz, 3H, CHCH₃), 1.37 (s, 18H, C(CH₃)₃). **¹³C NMR (CDCl₃, 75 MHz)**, δ: 170.8 (CONH), 170.2 (2CO), 142.9 (Ar-C_q), 128.2 (Ar-CH), 126.9 (Ar-CH), 126.4 (Ar-CH), 118.8 (CN), 80.6 (C(CH₃)₃), 58.7, 54.2, 55.6, 53.0, 52.5, 51.8, 50.8, 47.6 (CHCH₃), 27.9 (C(CH₃)₃), 20.7 (CHCH₃), 15.4 (CH₂CN). **HRMS (ESI)**: calculated for C₃₃H₅₅N₆O₅⁺ [M+H⁺]: 615.4228; Found 615.4222.

(R)-di-tert-butyl 2,2'-(4-(2-aminoethyl)-10-(2-oxo-2-((1-phenylethyl)amino)ethyl)-1,4,7,10-tetraazacyclododecane-1,7-diyl)diacetate (4a)

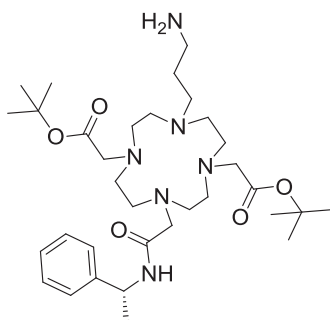


A solution of **3a** (0.9g, 1.5 mmol), Ra-Ni (1g) and H₂ (35 psi) in 7N NH₃/Methanol (40mL) was stirred at room temperature in Parr-apparatus for 6 h. The reaction was monitored by mass spectrometry. After completion, the reaction mixture was filtered through celite[®]. The filtrate was evaporated under reduced pressure and the residue was used in the next step without purification (0.74 g of yellow oil).

¹H NMR (CDCl₃, 300 MHz), δ: 7.25-7.11 (m, 5H, Ar-H), 5.05 (dq, *J*=6 Hz, 1H, CHCH₃), 3.20-2.26 (overlapping m, 26H), 1.41 (d, *J*=9 Hz, 3H, CHCH₃), 1.33 (s, 18H, C(CH₃)₃). **¹³C NMR (CDCl₃, 75 MHz)**, δ: 171.0 (CO), 170.1 (CO), 142.8 (Ar-C_q), 128.1 (Ar-CH), 127.9 (Ar-CH), 126.1 (Ar-CH), 76.4

($2\text{C}(\text{CH}_3)_3$), 58.6, 55.4, 55.4, 54.3, 53.2, 52.3, 51.7, 47.5 (CHCH_3), 39.1 (CH_2NH_2), 27.7 ($2\text{C}(\text{CH}_3)_3$), 20.7 (CHCH_3). **HRMS (ESI)**: calculated for $\text{C}_{32}\text{H}_{57}\text{N}_6\text{O}_5^+$ [$\text{M}+\text{H}^+$]: 605.4384; Found 605.4387.

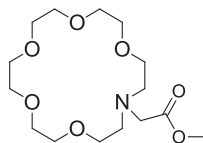
(R)-di-tert-butyl 2,2'-(4-(3-aminopropyl)-10-(2-oxo-2-((1-phenylethyl)amino)ethyl)-1,4,7,10-tetraazacyclododecane-1,7-diyl)diacetate (4b)



4b was prepared as according to the same procedure as used for **3b** (0.39 g, 0.6 mmol) to yield the crude as yellow solid (0.25 g, 63%, yellow solid) which was used without purification for the next step.

^1H NMR (CDCl_3 , 300 MHz), δ : 7.45-7.06 (m, 5H, Ar-H), 4.97 (dq, $J=6.9$ Hz, 1H, CHCH_3), 3.59-2.1 (overlapping m, 28H), 1.50 (d, $J=7.2$ Hz, 3H, CHCH_3), 1.38 (s, 18H, $\text{C}(\text{CH}_3)_3$). **^{13}C NMR (CDCl_3 , 75 MHz)**, δ : 171.1 (2CO), 169.8 (CONH), 144.5 (Ar-Cq), 128.0 (Ar-CH), 126.3 (Ar-CH), 126.1 (Ar-CH), 81.6 ($2\text{C}(\text{CH}_3)_3$), 58.3, 56.2, 50.27, 50.0, 49.4, 49.3, 38.6 (CH_2NH_2), 29.4 ($\text{CH}_2\text{CH}_2\text{NH}_2$), 27.9 ($\text{CH}_2(\text{CH}_2)_2\text{NH}_2$), 27.9 and 27.8 ($2\text{C}(\text{CH}_3)_3$), 22.3 (CHCH_3). **HRMS (ESI)**: calculated for $\text{C}_{33}\text{H}_{59}\text{N}_6\text{O}_5^+$ [$\text{M}+\text{H}^+$]: 619.4541; Found 619.4542.

Benzyl 2-(1,4,7,10,13-pentaoxa-16-azacyclooctadecan-16-yl)acetate (5)

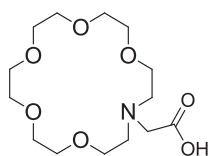


1-aza-18-crown-6-ether (0.45 g, 1.73 mmol) was dissolved in acetonitrile together with K_2CO_3 (0.5g, 3.6 mmol) and methyl bromoacetate (0.28 mL, 1.9 mmol). The reaction mixture was heated at 60°C for overnight. The inorganic impurities were removed by filtration and the

solvent was evaporated under reduced pressure. The crude product was purified by flash chromatography to give **5** as pale yellow oil (0.67g, 95 %).

$^1\text{H NMR}$ (CDCl_3 , 300 MHz), δ : 3.55 (s, 3H, CH_3), 3.53-3.45 (m, 20H, 10CH_2), 3.37 (s, 2H, CH_2CO), 2.78 (t, $J=5.4$ Hz, 4H, $2\text{CH}_2\text{N}$). **$^{13}\text{C NMR}$ (CDCl_3 , 75 MHz)**, δ : 172.0 (CO), 70.1, 69.8, 69.1, 55.2 (CH_2CO), 54.1 ($2\text{CH}_2\text{N}$), 51.1 (CH_3). **HRMS (ESI)**: calculated for $\text{C}_{15}\text{H}_{29}\text{NO}_7\text{Na}^+$ $[\text{M}+\text{Na}]^+$: 358.1836; Found 358.1836.

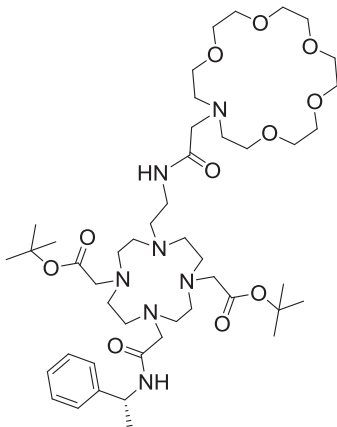
2-(1,4,7,10,13-pentaoxa-16-azacyclooctadecan-16-yl)acetic acid (**6**)



0.59g of **5** was dissolved in ethanol (15 mL) and 10 mL of aqueous solution of NaOH 2N was added. The reaction mixture was heated at reflux for overnight. The solvents were evaporated under reduced pressure to give the crude which product which was purified by flash chromatography to afford a colorless hygroscopic foam (0.2 g, 85%).

$^1\text{H NMR}$ (MeOD , 300 MHz), δ : 4.18 (s, CH_2CO), 3.86-3.79 (m, 4H, 2CH_2 , $2\text{CH}_2\text{CH}_2\text{N}$), 3.67-3.61 (m, 16H), 3.51-3.44 (m, 4H, $2\text{CH}_2\text{-N}$). **$^{13}\text{C NMR}$ (MeOD , 75 MHz)**, δ : 170.4 (CO), 71.3, 71.2, 70.9, 67.0, 56.3 (2NCH_2), 54.4 (CH_2CO). **HRMS (ESI)**: calculated for $\text{C}_{14}\text{H}_{27}\text{NO}_7\text{Na}^+$ $[\text{M}+\text{Na}]^+$: 344.1679; Found 344.1680.

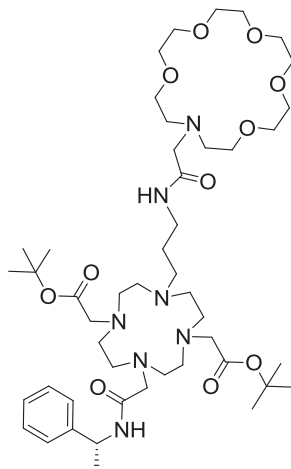
(R)-di-tert-butyl 2,2'-(4-(2-(2-(1,4,7,10,13-pentaoxa-16-azacyclooctadecan-16-yl)acetamido)ethyl)-10-(2-oxo-2-((1-phenylethyl)amino)ethyl)-1,4,7,10-tetraazacyclododecane-1,7-diyl)diacetate (7a)



4a (0.53g, 0.87 mmol) was added to a stirred solution of **6** (0.30 g, 0.94 mmol) and HBTU (0.66g, 1.75 mmol) in dry DMF (20ml) at room temperature. After stirring at room temperature overnight, the DMF was evaporated and the residue was taken up with dichloromethane (40 ml) and the resulting precipitate removed by filtration. Water was added and the two layers were separated. The aqueous layer was extracted with dichloromethane twice. The organic layer was washed with water, dried over Na_2SO_4 and then evaporated to give a brown gum which was purified on column chromatography (silica gel, 2% MeOH/ CH_2Cl_2) to give a yellow oil (0.49 g, 62%).

^1H NMR (CDCl_3 , 300 MHz), δ : 7.25-7.10 (m, 5H, Ar-H), 4.91 (dq, $J=6.9$ Hz, 1H, CHCH_3), 3.60-1.20 (overlapping m, 52H), 1.43-1.32 (overlapping m, 21H, CHCH_3 & $2\text{C}(\text{CH}_3)_3$). **^{13}C NMR (CDCl_3 , 75 MHz)**, δ : 173.1, 172.7, 172.1, 171.3, 170.2, 143.5 (Ar- C_q), 128.3, 126.8, 125.8, 82.63, 82.4 ($2\text{C}(\text{CH}_3)_3$), 68.7, 68.6, 68.3, 68.2, 67.9, 67.8, 66.6, 58.1, 56.79, 56.4, 56.2, 54.0, 53.9, 52.7, 50.1 (b), 48.9, 35.4, 27.7 ($\text{C}(\text{CH}_3)_3$), 27.6 ($\text{C}(\text{CH}_3)_3$), 21.7 (CHCH_3). **HRMS (ESI)**: calculated for $\text{C}_{46}\text{H}_{82}\text{N}_7\text{O}_{11}^+$ [$\text{M}+\text{H}^+$]: 908.6066; Found 908.6061.

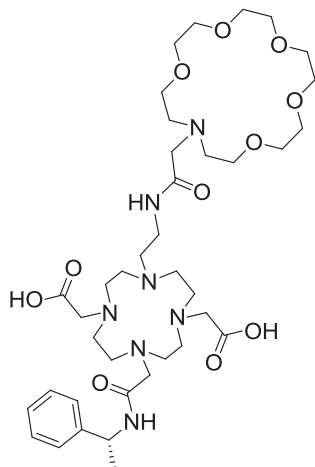
(R)-di-tert-butyl 2,2'-(4-(3-(2-(1,4,7,10,13-pentaoxa-16-azacyclooctadecan-16-yl)acetamido)propyl)-10-(2-oxo-2-((1-phenylethyl)amino)ethyl)-1,4,7,10-tetraazacyclododecane-1,7-diyl)diacetate (7b)



This compound was synthesized according to the same procedure for **7a**. Reaction of **6** (0.34g, 1.06 mmol) with the amine **4b** (0.65 g, 1.06 mmol) in the presence of HBTU (0.80, 2.10 mmol) afforded 0.62 g (64% yield) of yellow oil after purification by HPLC.

¹H NMR (CDCl₃, 300 MHz): δ 7.27-7.08 (m, 5H, ArH), 4.98-4.85 (m, 1H, CHCH₃), 3.66-2.45 (overlapping m, 52H), 1.91-1.75 (m, 2H, CH₂CH₂NH₂), 1.41-1.33 (overlapping m, 21H, CH₃CH and C(CH₃)₃). **¹³C NMR (CDCl₃, 75 MHz),** δ: 170.1, 169.1, 162.5, 143.5, 128.8, 127.0, 126.0, 81.8 (C(CH₃)₃), 70.1, 69.7, 68.9, 68.5, 68.4, 68.1, 66.8, 58.2, 56.3, 55.9, 55.2, 54.3, 53.7, 51.6, 50.6, 49.5, 49.1, 47.6, 36.7, 31.3, 28.0, 22.18 (CHCH₃). **LRMS (ESI):** calculated for C₄₇H₈₄N₇O₁₁⁺ [M+H]⁺: 922.6; Found 922.6.

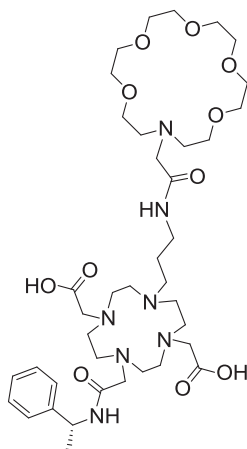
(R)-2,2'-(4-(2-(2-(1,4,7,10,13-pentaoxa-16-azacyclooctadecan-16-yl)acetamido)ethyl)-10-(2-oxo-2-((1-phenylethyl)amino)ethyl)-1,4,7,10-tetraazacyclododecane-1,7-diyl)diacetic acid (L⁵)



7a (0.32 g, 0.35 mmol) was dissolved in formic acid and stirred at 60°C overnight. The complete removal of the ^tBu protecting groups was monitored by mass spectrometry, and the excess formic acid was evaporated under reduced pressure. The crude residue was dissolved in 10% CH₃CN in water and filtered through a 0.45 μm filter. The pH was adjusted to 2-3 and the product was purified by HPLC and then lyophilized to isolate a white hygroscopic solid (0.15 g, 54%).

¹H NMR (D₂O, 300 MHz), δ: 7.38-7.20 (m, 5H, Ar-H), 4.93 (q, *J*=6.9 Hz, 1H, CHCH₃), 4.07 (s, 2H), 3.83-3.07 (overlapping m, 48H), 2.94 (br. s, 6H), 2.73 (t, *J*=6.3 Hz, 2H, CH₂CH₂NHCO), 1.41 (d, *J*=6.9 Hz, 3H, CHCH₃). **¹³C NMR (D₂O, 75 MHz)**, δ: 170.8, 169.4, 169.3, 1688, 165.3, 143.9 (Ar-C_q), 128.9, 127.4, 125.9, 69.7, 69.6, 69.5, 69.4, 63.7, 56.8, 55.2, 54.3, 51.8, 51.6, 50.8, 49.1, 47.8, 47.6, 36.2 (CH₂NHCO), 21.6 (CHCH₃). **HRMS (ESI)**: calculated for C₃₈H₆₇N₇O₁₁²⁺ [M+2H]²⁺: 398,7444; Found 398,7446.

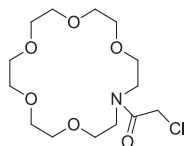
(R)-2,2'-(4-(3-(2-(1,4,7,10,13-pentaoxa-16-azacyclooctadecan-16-yl)acetamido)propyl)-10-(2-oxo-2-((1-phenylethyl)amino)ethyl)-1,4,7,10-tetraazacyclododecane-1,7-diyl)diacetic acid (L⁶)



Deprotection of compound **7b** (0.45g, 0.49 mmol) was carried out following a similar protocol used for the preparation of **L⁵** and afforded 0.22 mg of ligand **L⁶** as white hygroscopic solid.

¹H RMN (D₂O, 300 MHz), δ : 7.37-7.22 (m, 5H, Ar-H), 4.87 (q, $J=6.9$ Hz, 1H, CHCH₃), 4.05 (s, 2H), 3.78-2.90 (overlapping m, 48H), 2.56 (br. s, 2H, CH₂(CH₂)₂NHCO), 1.69 (quint, $J=6.9$ Hz, 2H, CH₂CH₂NHCO), 1.38 (d, $J=6.9$ Hz, 3H, CHCH₃). **¹³C RMN (D₂O, 75 MHz)**, δ : 170.3, 169.8, 168.9, 164.9, 143.8, 128.8, 127.3, 125.8, 69.7, 69.6, 69.4, 69.3, 63.6, 56.6, 55.0, 54.0, 51.5, 51.2, 50.7, 49.8, 49.3, 49.2, 48.8, 48.0, 47.8, 37.2, 24.8, 21.3. **HRMS (ESI)**: calculated for C₃₉H₆₇N₇O₁₁⁺ [M-H⁺]: 808.4815; Found 808.4832.

2-chloro-1-(1,4,7,10,13-pentaoxa-16-azacyclooctadecan-16-yl)ethanone (8)

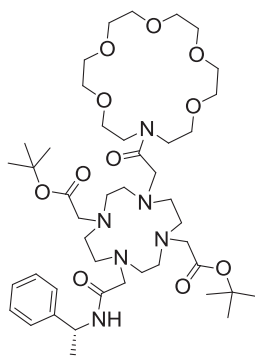


A solution of chloroacetyl chloride (0.3 ml, 3.8 mmol) in chloroform (20 ml) was added dropwise to a stirred solution of triethylamine (1.5 ml, 11.2 mmol) and 1-aza-18-crown-6-ether (1 g, 3.8 mmol) in chloroform (50 ml) at -10 °C. The reaction mixture was stirred for additional 6h at room temperature. The organic layer was then washed with water (50 ml), an aqueous solution of 1N HCl and brine. The organic phase was dried over Na₂SO₄ and the solvent was

evaporated under reduced pressure to afford a pale yellow residue which was purified by column chromatography (silica-gel, 4% MeOH/CH₂Cl₂) to give **8** (1.3 g, quantitative yield) as a pale yellow oil.

¹H NMR (CDCl₃, 300 MHz), δ: 3.92 (s, 2H, CH₂Cl), 3.71-3.51 (m, 24H). **¹³C NMR (CDCl₃, 75 MHz)**, δ: 167.1 (CO), 70.8, 70.4, 70.3, 70.3, 70.2, 70.0, 69.2, 69.0, 49.9 (CH₂N), 47.2 (CH₂N), 26.9 (CH₂Cl). **HRMS (ESI)**: calculated for C₁₄H₂₆ClNO₆Na⁺ [M+Na]⁺: 362.1340; Found 362.1343.

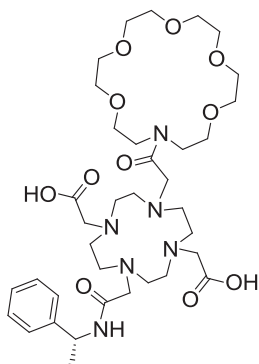
(R)-di-tert-butyl 2,2'-(4-(2-oxo-2-((1-phenylethyl)amino)ethyl)-10-(2-oxo-2-(1,4,7,10,13-pentaoxa-16-azacyclooctadecan-16-yl)ethyl)-1,4,7,10-tetraazacyclododecane-1,7-diyl)diacetate (9)



A solution of **8** (0.82 g, 2.14 mmol), **2** (1.20g, 2.14 mmol) and K₂CO₃ (0.65 g, 4.7 mmol) in 40 mL DMF was stirred at 50 °C for 24 h. The reaction was monitored by TLC. After completion, salt was removed by filtration and the solvent was evaporated. The residue was taken up with CH₂Cl₂ (100 ml) and washed twice with water. The organic layer was dried over Na₂SO₄ and evaporated under reduced pressure to afford pale yellow oil (1.49 g, 72%). The product was used in the next step without further purification.

¹H NMR (CDCl₃, 300 MHz): 7.41-7.27 (m, 5H, Ar-H), 4.87 (dq, *J*=6.9 Hz, 1H, CHCH₃), 3.81-3.02 (m, 46H), 1.42 (d, *J*=7.5 Hz, 3H, CHCH₃). **¹³C NMR (CDCl₃, 75 MHz)**: 171.3, 171.2, 169.7, 169.6, 168, 143.9, 128.8, 127.4, 125.8, 69.8, 69.76, 69.5, 68.6, 68.4, 56.8, 56.6, 54.1, 52.6, 51.7, 51.2, 51.0, 49.5, 48.3, 47.9, 47.7, 47.3, 46.4, 21.4. **HRMS (ESI)**: calculated for C₄₄H₇₆N₆O₁₁Na [M+Na]⁺: 887.5464; Found 887.5467.

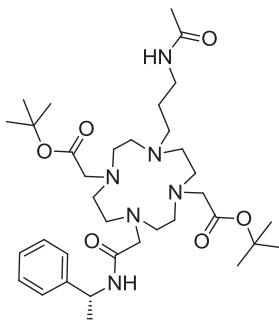
(R)-2,2'-(4-(2-oxo-2-((1-phenylethyl)amino)ethyl)-10-(2-oxo-2-(1,4,7,10,13-pentaoxa-16-azacyclooctadecan-16-yl)ethyl)-1,4,7,10-tetraazacyclododecane-1,7-diyl)diacetic acid (L**⁷)**



Deprotection of compound **9** (0.68g, 0.78mmol) was carried out following a similar protocol used for the preparation of **L**⁵ and afforded the ligand **L**⁷ as white solid (0.28 g, 48%).

¹H NMR (D₂O, 300 MHz), δ : 7.41-7.27 (m, 5H, Ar-H), 4.88 (q, $J=6.9$ Hz, 1H, CHCH₃), 3.79-3.02 (overlapping m, 48H), 1.42 (d, $J=6.9$ Hz, 3H, CHCH₃). **¹³C NMR (D₂O, 75 MHz)**, δ : 171.3, 171.2, 169.7, 169.6, 168.4, 143.9, 128.8, 127.4, 125.8, 69.75, 69.6, 69.5, 68.6, 68.5, 56.8, 56.6, 54.1, 52.6, 51.7, 51.6, 51.2, 51.0, 49.5, 48.4, 47.9, 47.7, 47.3, 46.4, 21.42. **HRMS (ESI)**: calculated for C₃₆H₆₀N₆O₁₁⁺ [M-H⁺]: 751,4236; Found 751,4231.

(R)-di-tert-butyl 2,2'-(4-(3-acetamidopropyl)-10-(2-oxo-2-((1-phenylethyl)amino)ethyl)-1,4,7,10-tetraazacyclododecane-1,7-diyl)diacetate (10**)**

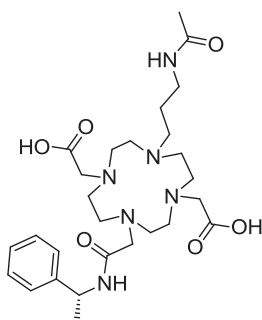


Acetyl chloride (93 μ l, 1.3 mmol) was dissolved in dry CH₂Cl₂ and added dropwise to a stirred mixture of **4b** (0.81g, 1.3 mmol) and triethylamine (0.73ml, 5.2mmol) in dry CH₂Cl₂ at room temperature. After completion of addition, the reaction was stirred for further 1 hour and water was added. The organic layer was separated and washed twice with water, dried over

Na₂SO₄. The solvent was removed under reduced pressure to dryness (0.71 g, 82%). The title compound was used for next step without further purification.

¹H NMR (CDCl₃, 500 MHz), δ: 8.27 (d, *J*=8.5 Hz, 1H, NH), 7.24 (m, 5H, Ar-H), 5.11 (dq, *J*=6.5 Hz, 1H, CHCH₃), 3.25 (m, 2H), 3.99 (m, 6H), 2.70 (m, 8H), 2.43 (overlapping m, 10H), 1.89 (s, 3H, CH₃CO), 1.53 (quint, *J*=6.5 Hz, 2H, CH₂CH₂NHCO), 1.45 (d, *J*=6.5 Hz, 3H, CHCH₃), 1.38 (s, 18H, 2C(CH₃)₃). **¹³C NMR (CDCl₃, 125 MHz)**, δ: 170.8 (CO), 170.3 (CO), 170.1 (CO), 143.1 (Ar-C_q) 128.4, 127.1, 126.5, 80.9 (C(CH₃)₃), 58.8 (3 NCH₂CO), 55.6, 54.4, 53.4, 53.3, 52.4, 51.9, 47.9 (CHCH₃), 38.1 (CH₂NHCO), 28.1 (2C(CH₃)₃), 26.2 (CH₂CH₂NHCO), 23.0 (CH₃CO), 21.4 (CHCH₃). **HRMS (ESI)**: calculated for C₃₆H₆₀N₆O₁₁ [M+H]⁺: 661.4647; Found 661.4648.

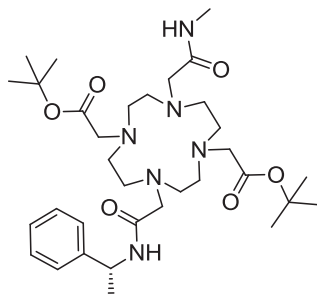
(R)-2,2'-(4-(3-acetamidopropyl)-10-(2-oxo-2-((1-phenylethyl)amino)ethyl)-1,4,7,10-tetraazacyclododecane-1,7-diyl)diacetic acid (L¹⁰)



Deprotection of compound **10** (0.41 g, 0.62 mmol) was carried out following a similar protocol used for the preparation of **L⁵**. Except that the crude was purified using column chromatography on neutral alumina (30% H₂O/CH₃CN) to give the ligand **L¹⁰** as white solid (0.26 g, 75%).

¹H NMR (D₂O, 500 MHz), δ: 7.39-7.34 (m, 4H, Ar-H), 7.31-7.27 (dd, *J*=7.0 Hz, 1H, Ar-H), 4.89 (q, *J*=7.5 Hz, 1H, CHCH₃), 3.75-3.54 (m, 6H), 3.33 (br. s, 8H), 3.13 (m, 4H), 2.96 (br. s, 6H), 2.64 (br. s, 2H, CH₂(CH₂)₂NHCO), 1.96 (s, 3H, CH₃CO), 1.70 (quint, *J*=6.0 Hz, 2H, CH₂CH₂NHCO), 1.41 (d, *J*=7.5 Hz, 3H, CHCH₃). **¹³C NMR (D₂O, 125 MHz)**, δ: 174.1, 170.5, 170.1, 143.8, 128.6, 127.4, 125.8, 56.5 (br), 54.1, 51.4 (br), 51.1 (br), 50.7 (br), 49.9, 49.5 (CHCH₃), 48.5 (br), 48.1 (br), 37.1 (CH₂NHCO), 24.5 (CH₂CH₂CH₂), 21.9 (COCH₃), 21.3 (CHCH₃). **LRMS (ESI)**: calculated for C₃₆H₆₀N₆O₁₁ [M+H]⁺: 549.3400; Found 549,3395.

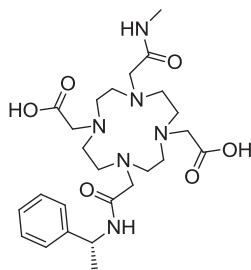
(R)-di-tert-butyl 2,2'-(4-(2-(methylamino)-2-oxoethyl)-10-(2-oxo-2-((1-phenylethyl)amino)ethyl)-1,4,7,10-tetraazacyclododecane-1,7-diyl)diacetate (11)



A solution of **2** (0.8 g, 1.43 mmol), 2-chloro-N-methylacetamide (0.15 g, 1.42 mmol) and Na₂CO₃ (0.32 g, 2.99 mmol) in CH₃CN was stirred under reflux overnight. Inorganic salts were removed by filtration, solvent was removed under reduced pressure and the product was purified using column chromatography on silica, (10% MeOH/CH₂Cl₂) to give a pale yellow oily material (0.787 g, 87%).

¹H NMR (CDCl₃, 500 MHz), δ: 7.4 (d, *J*=7.5 Hz, 2H, Ar-H), 7.29 (dd, *J*=7.0, 2H, Ar-H), 7.20 (dd, *J*=7.5 Hz, 1H, Ar-H), 5.02 (dq, *J*=6.5 Hz, 1H, CHCH₃), 4.27 (br. s, 2H), 3.90 (br. s, 2H), 3.50-3.26 (br. m, 10H), 3.08 (br. s, 2H), 2.89-2.84 (m, 8H), 2.77 (d, *J*=4.0 Hz, 3H, CH₃NH), 1.52 (d, *J*=6.0 Hz, 3H, CHCH₃), 1.44 (br. s, 18H, 2C(CH₃)₃). **¹³C NMR (CDCl₃, 125 MHz)**, δ: 169.8, 168.9, 166.1, 143.7 (C(CH₃)₃), 128.4, 127.0, 126.2, 81.9, 55.9, 55.1, 53.1 (br), 52.8 (br), 49.6 (CHCH₃), 49.1, 48.4, 28.1 (C(CH₃)₃), 25.8 (CH₃NH), 22.5 (CHCH₃). **HRMS (ESI)**: calculated for C₃₆H₆₀N₆O₁₁ [M+H]⁺: 633.4334; Found 633.4341.

(R)-2,2'-(4-(2-(methylamino)-2-oxoethyl)-10-(2-oxo-2-((1-phenylethyl)amino)ethyl)-1,4,7,10-tetraazacyclododecane-1,7-diyl)diacetic acid (L¹¹)



Deprotection of **11** (0.68 g, 0.68 mmol) was carried out following a similar protocol used for the preparation of **L¹⁰** and afforded the ligand **L¹¹** as white solid (0.40 g, 71%).

^1H NMR (D_2O , 500 MHz): 7.39-7.34 (m, 4H, Ar-H), 7.29-7.27 (m, 1H, Ar-H), 4.94 (q, $J=6.5$ Hz, 1H, CHCH_3), 3.78 (s, 2H), 3.63-3.3 (overlapping m, 14H), 3.16-2.83 (overlapping m, 8H), 2.58 (s, 2H), 1.42 (d, $J=7.5$ Hz, 3H, CHCH_3). **^{13}C NMR (D_2O , 125 MHz):** 172.8, 171.3, 169.4, 169.2, 143.9, 128.9, 127.4, 125.9, 56.9, 56.2, 56.0, 54.6, 51.8, 51.6, 50.8, 50.5, 49.4, 48.4, 48.3, 48.1, 25.9 (NHCH₃), 21.4 (CHCH₃). **HRMS (ESI):** calculated for $\text{C}_{36}\text{H}_{60}\text{N}_6\text{O}_{11}$ [M+H]⁺: 521.3082; Found 521.3086.

2.7. References

1. Yew DT, Chan WY, Luo CB, Zheng DR, Yu MC: **Neurotransmitters and neuropeptides in the developing human central nervous system - A review.** *Biological Signals and Receptors* 1999, **8**(3):149-159.
2. Meldrum BS: **Glutamate as a neurotransmitter in the brain: Review of physiology and pathology.** *Journal of Nutrition* 2000, **130**(4):1007S-1015S.
3. Werner F-M, Covenas R: **Classical Neurotransmitters and Neuropeptides Involved in Major Depression: a Review.** *International Journal of Neuroscience* 2010, **120**(7):455-470.
4. Fillenz M: **In vivo neurochemical monitoring and the study of behaviour.** *Neuroscience and Biobehavioral Reviews* 2005, **29**(6):949-962.
5. Tao JM, Perdew JP, Staroverov VN, Scuseria GE: **Climbing the density functional ladder: Nonempirical meta-generalized gradient approximation designed for molecules and solids.** *Physical Review Letters* 2003, **91**(14).
6. Fratiglioni L, Winblad B, von Strauss E: **Prevention of Alzheimer's disease and dementia. Major findings from the Kungsholmen project.** *Physiology & Behavior* 2007, **92**(1-2):98-104.
7. Dolg M, Stoll H, Savin A, Preuss H: **ENERGY-ADJUSTED PSEUDOPOTENTIALS FOR THE RARE-EARTH ELEMENTS.** *Theoretica Chimica Acta* 1989, **75**(3):173-194.
8. Platas-Iglesias C: **The Solution Structure and Dynamics of MRI Probes Based on Lanthanide(III) DOTA as Investigated by DFT and NMR Spectroscopy.** *European Journal of Inorganic Chemistry* 2012(12):2023-2033.
9. Carlos Platas-Iglesias, Adrian Roca-Sabio, Martin Regueiro-Figueroa, David Esteban-Gomez, Andres de Blas, Rodriguez-Blas T: **Applications of Density Functional Theory (DFT) to Investigate the Structural, Spectroscopic and Magnetic Properties of Lanthanide(III) Complexes** *Current Inorganic Chemistry* 2011(1):91-116.
10. Perry M, Li Q, Kennedy RT: **Review of recent advances in analytical techniques for the determination of neurotransmitters.** *Analytica Chimica Acta* 2009, **653**(1):1-22.
11. Crespi F: **Wireless in vivo voltammetric measurements of neurotransmitters in freely behaving rats.** *Biosensors & Bioelectronics* 2010, **25**(11):2425-2430.
12. Matzneller P, Brunner M: **Recent advances in clinical microdialysis.** *Trac-Trends in Analytical Chemistry* 2011, **30**(9):1497-1504.
13. Darvesh AS, Carroll RT, Geldenhuys WJ, Gudelsky GA, Klein J, Meshul CK, Van der Schyf CJ: **In vivo brain microdialysis: advances in neuropsychopharmacology and drug discovery.** *Expert Opinion on Drug Discovery* 2011, **6**(2):109-127.
14. Lovtsevich NV, Davydova LA: **Microdialysis and neuromonitoring.** *Anesteziologiya i Reanimatologiya* 2008(2):85-88.
15. Engelborghs S, DeDeyn PP: **The neurochemistry of Alzheimer's disease.** *Acta Neurol Belg* 1997, **97**(2):67-84.
16. Gautschi OP, Seule M, Cadosch D, Land M, Fournier JY, Hildebrandt G: **Cerebral microdialysis Possibilities and limits.** *Anesthesiologie Intensivmedizin Notfallmedizin Schmerztherapie* 2009, **44**(4):268-274.
17. Tomasi J, Mennucci B, Cammi R: **Quantum mechanical continuum solvation models.** *Chem Rev* 2005, **105**(8):2999-3093.
18. Shapiro MG, Westmeyer GG, Romero PA, Szablowski JO, Kuster B, Shah A, Otey CR, Langer R, Arnold FH, Jasanoff A: **Directed evolution of a magnetic resonance imaging contrast agent for noninvasive imaging of dopamine.** *Nat Biotechnol* 2010, **28**(3):264-U120.

19. Mammen M, Choi SK, Whitesides GM: **Polyvalent interactions in biological systems: Implications for design and use of multivalent ligands and inhibitors.** *Angewandte Chemie-International Edition* 1998, **37**(20):2755-2794.
20. Chung MK, Lee SJ, Waters ML, Gagne MR: **Self-Assembled Multi-Component Catenanes: The Effect of Multivalency and Cooperativity on Structure and Stability.** *Journal of the American Chemical Society* 2012, **134**(28):11430-11443.
21. Zimmer L, Luxen A: **PET radiotracers for molecular imaging in the brain: Past, present and future.** *NeuroImage* 2012, **61**(2):363-370.
22. Kim SG, Ahn KH: **Novel artificial receptors for alkylammonium ions with remarkable selectivity and affinity.** *Chemistry-a European Journal* 2000, **6**(18):3399-3403.
23. Arena G, Casnati A, Contino A, Lombardo GG, Sciotto D, Ungaro R: **Water-soluble calixarene hosts that specifically recognize the trimethylammonium group or the benzene ring of aromatic ammonium cations: A combined (1)H NMR, calorimetric, and molecular mechanics investigation.** *Chemistry-a European Journal* 1999, **5**(2):738-744.
24. Cram DJ: **PREORGANIZATION - FROM SOLVENTS TO SPHERANDS.** *Angewandte Chemie-International Edition in English* 1986, **25**(12):1039-1057.
25. Imai H, Misawa K, Munakata H, Uemori Y: **Water-soluble zinc porphyrins as artificial receptors for amino acids.** *Chemical & Pharmaceutical Bulletin* 2008, **56**(10):1470-1472.
26. Steed JW, Gale PA: **Supramolecular Chemistry: From Molecules to Nanomaterials:** Wiley; 2012.
27. Bretonniere Y, Cann MJ, Parker D, Slater R: **Ratiometric probes for hydrogencarbonate analysis in intracellular or extracellular environments using europium luminescence.** *Chemical Communications* 2002(17):1930-1931.
28. Polasek M, Kotek J, Hermann P, Cisarova I, Binnemans K, Lukes I: **Lanthanide(III) Complexes of Pyridine-N-Oxide Analogues of DOTA in Solution and in the Solid State. A Near Kind of Isomerism in Complexes of DOTA-like Ligands.** *Inorganic Chemistry* 2009, **48**(2):466-475.
29. Regueiro-Figueroa M, Djanashvili K, Esteban-Gomez D, Chauvin T, Toth E, de Blas A, Rodriguez-Blas T, Platas-Iglesias C: **Molecular Recognition of Sialic Acid by Lanthanide(III) Complexes through Cooperative Two-Site Binding.** *Inorganic Chemistry* 2010, **49**(9):4212-4223.
30. Parker D: **Excitement in f block : structure, dynamics and function of nine-coordinate chiral lanthanide complexes in aqueous media.** *Chemical Society Reviews* 2004, **33**(3):156-165.
31. Parker D, Yu JH: **A pH-insensitive, ratiometric chemosensor for citrate using europium luminescence.** *Chemical Communications* 2005(25):3141-3143.
32. Dickins RS, Parker D, Bruce JI, Tozer DJ: **Correlation of optical and NMR spectral information with coordination variation for axially symmetric macrocyclic Eu(III) and Yb(III) complexes: axial donor polarisability determines ligand field and cation donor preference.** *Dalton Transactions* 2003(7):1264-1271.
33. Cantrill SJ, Fulton DA, Heiss AM, Pease AR, Stoddart JF, White AJP, Williams DJ: **Molecular Meccano, Part 60 - The influence of macrocyclic polyether constitution upon ammonium ion/crown ether recognition processes.** *Chemistry-a European Journal* 2000, **6**(12):2274-2287.
34. Adair C, Woods M, Zhao P, Pasha A, Winter PM, Lanza GM, Athey P, Sherry AD, Kiefer GE: **Spectral properties of a bifunctional PARACEST europium chelate: an intermediate for targeted imaging applications.** *Contrast Media & Molecular Imaging* 2007, **2**(1):55-58.
35. Kovacs Z, Sherry AD: **pH-controlled selective protection of polyaza macrocycles.** *Synthesis-Stuttgart* 1997(7):759-&.
36. Stezowski JJ, Hoard JL: **HEAVY-METAL IONOPHORES - CORRELATIONS AMONG STRUCTURAL PARAMETERS OF COMPLEXED NONPEPTIDE POLYAMINO ACIDS.** *Israel Journal of Chemistry* 1984, **24**(4):323-334.

37. Bianchi A, Calabi L, Giorgi C, Losi P, Mariani P, Paoli P, Rossi P, Valtancoli B, Virtuani M: **Thermodynamic and structural properties of Gd³⁺ complexes with functionalized macrocyclic ligands based upon 1,4,7,10-tetraazacyclododecane.** *Journal of the Chemical Society-Dalton Transactions* 2000(5):697-705.
38. Dickins RS, Parker D, deSousa AS, Williams JAG: **Closely diffusing O-H, amide N-H and methylene C-H oscillators quench the excited state of europium complexes in solution.** *Chemical Communications* 1996(6):697-698.
39. Beeby A, Clarkson IM, Dickins RS, Faulkner S, Parker D, Royle L, de Sousa AS, Williams JAG, Woods M: **Non-radiative deactivation of the excited states of europium, terbium and ytterbium complexes by proximate energy-matched OH, NH and CH oscillators: an improved luminescence method for establishing solution hydration states.** *Journal of the Chemical Society-Perkin Transactions 2* 1999(3):493-503.
40. Dunand FA, Borel A, Merbach AE: **How does internal motion influence the relaxation of the water protons in Ln(III)DOTA-like complexes?** *Journal of the American Chemical Society* 2002, **124**(4):710-716.
41. Powell DH, NiDhubhghaill OM, Pubanz D, Helm L, Lebedev YS, Schlaepfer W, Merbach AE: **Structural and dynamic parameters obtained from O-17 NMR, EPR, and NMRD studies of monomeric and dimeric Gd³⁺ complexes of interest in magnetic resonance imaging: An integrated and theoretically self consistent approach.** *J Am Chem Soc* 1996, **118**(39):9333-9346.
42. Plush SE, Gunnlaugsson T: **Luminescent sensing of dicarboxylates in water by a bismacrocyclic dinuclear Eu(III) conjugate.** *Organic Letters* 2007, **9**(10):1919-1922.
43. Merbach AE, Toth E: **The Chemistry of Contrast Agents in Medical Magnetic Resonance Imaging:** Wiley: New York; 2001.
44. Spirlet MR, Rebizant J, Desreux JF, Loncin MF: **CRYSTAL AND MOLECULAR-STRUCTURE OF SODIUM AQUO(1,4,7,10-TETRAAZACYCLODODECANE-1,4,7,10-TETRAACETATO)EUROPATE(III) TETRAHYDRATE, NA+(EUDOTA.H₂O)-.4H₂O, AND ITS RELEVANCE TO NMR-STUDIES OF THE CONFORMATIONAL BEHAVIOR OF THE LANTHANIDE COMPLEXES FORMED BY THE MACROCYCLIC LIGAND DOTA.** *Inorganic Chemistry* 1984, **23**(3):359-363.
45. Raitsimring AM, Astashkin AV, Baute D, Goldfarb D, Caravan P: **W-band O-17 pulsed electron nuclear double resonance study of gadolinium complexes with water.** *Journal of Physical Chemistry A* 2004, **108**(35):7318-7323.
46. Ruloff R, Toth E, Scopelliti R, Tripier R, Handel H, Merbach AE: **Accelerating water exchange for Gd-III chelates by steric compression around the water binding site.** *Chemical Communications* 2002(22):2630-2631.
47. Fu X-Q, Hang T, Ye Q, Xiong R-g: **Synthesis, structure and dielectric deuterated effect of a novel organic-inorganic hybrid compound.** *Inorganic Chemistry Communications* 2011, **14**(1):281-284.
48. Martell AE, Motekaitis RJ: **THE DETERMINATION AND USE OF STABILITY CONSTANTS;** 1988.
49. Dunand FA, Dickins RS, Parker D, Merbach AE: **Towards rational design of fast water-exchanging Gd(dota-like) contrast agents? Importance of the M/m ratio.** *Chemistry-a European Journal* 2001, **7**(23):5160-5167.
50. Caravan P, Ellison JJ, McMurry TJ, Lauffer RB: **Gadolinium(III) chelates as MRI contrast agents: Structure, dynamics, and applications.** *Chem Rev* 1999, **99**(9):2293-2352.
51. Aime S, Botta M, Ermondi G: **NMR-STUDY OF SOLUTION STRUCTURES AND DYNAMICS OF LANTHANIDE(III) COMPLEXES OF DOTA.** *Inorganic Chemistry* 1992, **31**(21):4291-4299.
52. Vedernikov AI, Ushakov EN, Efremova AA, Kuz'mina LG, Moiseeva AA, Lobova NA, Churakov AV, Strelenko YA, Alfimov MV, Howard JAK *et al*: **Synthesis, Structure, and Properties of Supramolecular Charge-Transfer Complexes between Bis(18-crown-6)stilbene and**

- Ammonioalkyl Derivatives of 4,4'-Bipyridine and 2,7-Diazapyrene.** *Journal of Organic Chemistry* 2011, **76**(16):6768-6779.
53. P. Gans A, Sabatini A, Vacca: **Investigation of equilibria in solution. Determination of equilibrium constants with the HYPERQUAD suite of programs.** *Talanta* 1966, **43**:1739-1753.
54. R. M. Smith, R. J. Motekaitis, Martell AE: **NIST Standard Reference Database.** 1997.
55. Hugi AD, Helm L, Merbach AE: **HIGH-PRESSURE NMR KINETICS .23. WATER EXCHANGE ON HEXAAQUAVANADIUM(III) - A VARIABLE-TEMPERATURE AND VARIABLE-PRESSURE O-17-NMR STUDY AT 1.4 AND 4.7 TESLA.** *Helvetica Chimica Acta* 1985, **68**(2):508-521.
56. Corsi DM, Platas-Iglesias C, van Bekkum H, Peters JA: **Determination of paramagnetic lanthanide(III) concentrations from bulk magnetic susceptibility shifts in NMR spectra.** *Magnetic Resonance in Chemistry* 2001, **39**(11):723-726.
57. Aime S, Botta M, Fasano M, Crich SG, Terreno E: **Gd(III) complexes as contrast agents for magnetic resonance imaging: A proton relaxation enhancement study of the interaction with human serum albumin.** *Journal of Biological Inorganic Chemistry* 1996, **1**(4):312-319.
58. Bertini I, Luchinat C, Aime S: **NMR of paramagnetic substances.** *Coordination Chemistry Reviews* 1996, **150**:R7-+.
59. Delaglio F, Grzesiek S, Vuister GW, Zhu G, Pfeifer J, Bax A: **NMRPIPE - A MULTIDIMENSIONAL SPECTRAL PROCESSING SYSTEM BASED ON UNIX PIPES.** *Journal of Biomolecular Nmr* 1995, **6**(3):277-293.
60. Vranken WF, Boucher W, Stevens TJ, Fogh RH, Pajon A, Llinas P, Ulrich EL, Markley JL, Ionides J, Laue ED: **The CCPN data model for NMR spectroscopy: Development of a software pipeline.** *Proteins-Structure Function and Bioinformatics* 2005, **59**(4):687-696.
61. Esteban-Gómez D, de Blas A, Rodríguez-Blas T, Helm L, Platas-Iglesias C: **Hyperfine Coupling Constants on Inner-Sphere Water Molecules of GdIII-Based MRI Contrast Agents.** *Chemphyschem* 2012, **13**(16):3640-3650.

3

Attempts to Improve the Ligand Design for Neurotransmitters Detection

CHAPTER 3: ATTEMPTS TO IMPROVE THE LIGAND DESIGN FOR NEUROTRANSMITTERS

DETECTION	126
3.1. DESIGN OF THE COMPLEXES	128
3.2. SYNTHESIS OF THE COMPLEXES	132
3.2.1.Synthesis of Ligand L ⁸	132
3.2.2.Synthesis of ligand L ⁹	133
3.3. RESULTS AND DISCUSSION	136
3.3.1.Photophysical characterization	136
3.3.1.1. Luminescence emission of EuL ⁸	136
3.3.1.2. Near-infrared emission of YbL ⁸ and NdL ⁸	137
3.3.2. ¹⁷ O NMR measurements	140
3.3.3.Binding Assays	144
3.3.3.1. Relaxometric titrations of GdL ⁸ and GdL ⁹	144
3.3.3.2. Luminescence emission of EuL ⁸	147
3.3.3.3. Near-infrared emission of NdL ⁸ and YbL ⁸	149
3.4. CONCLUSIONS	163
3.5. EXPERIMENTAL PROCEDURES AND MATERIALS	165
3.6. REFERENCES	181

3.1 Design of the complexes

Our findings described in the previous chapter demonstrated the proof of principle and showed the promise of the synthesized contrast agents for use in MR imaging of neurotransmitters. Nevertheless, the non-selectivity of these probes let a significant room for improvements. In this respect, we report in this chapter our efforts aimed at further improving the design. We have focused on introducing structural changes to make the design more reliable through improving the binding affinity and selectivity. Thus, while designing the new systems, two main objectives were pursued: i) incorporation of chromophores adapted to sensitize lanthanide luminescence and ii) increasing the sensitivity of binding through changing the monoaza-crown ether moiety. We sought to proceed step by step thus to tune one feature at once and examine the effect of each change in comparison to the previous complexes GdL⁵ and GdL⁶ in terms of MRI contrast and/or optical properties and their responsiveness to neurotransmitters.

Luminescence sensitization of visible emitting Eu³⁺ and near-infrared emitting Yb³⁺ and Nd³⁺.

Ratiometric approaches offer the most effective way to observe and quantify changes in analyte concentration [1, 2]. To take advantage from the ratiometric response displayed with the previous complexes in chapter 2, we sought to improve it further by introducing a more suitable antenna to develop responsive ratiometric optical probes. In particular, we focused on the benzophenone chromophore. Benzophenone (BP) is one of the most extensively studied photosensitizers [3]. It has been previously demonstrated that upon excitation of the $\pi-\pi^*$ transition band, Eu³⁺ luminescence can be sensitized. Due to its relatively high triplet excitation energy, and high triplet quantum yield, BP is photoexcited by a relatively long wavelength light and can transfer its triplet energy to other molecules (triplet energy transfer: TET) [4-7].

The outcome of such design is shown in figure 3.1. Para-substituted benzophenone containing complexes have been reported:

- 1) To display absorption bands at lower energies than the corresponding ortho- or meta-substituted benzophenones. This was ascribed to the increase of the electronic delocalization across the amide group.

- 2) To emit efficiently as compared to ortho- and meta-substituted benzophenone. For instance, the quantum yield of the Eu^{3+} para-benzophenone-^tBu-DO3A complex is 20 times higher than that of the ortho-substituted analogue [6].

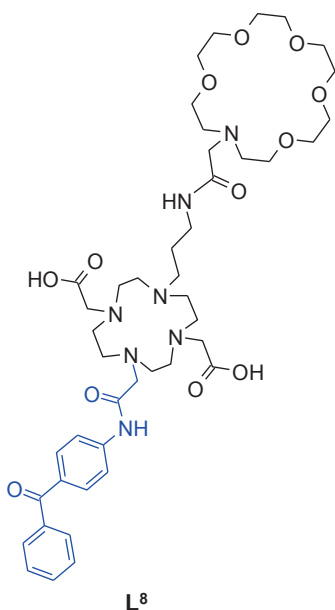
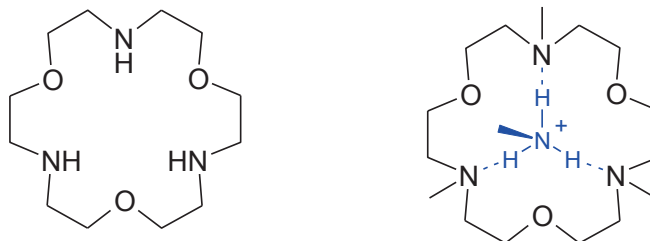


Figure 3.1: Benzophenone-containing ligand L^8 . The benzophenone moiety is known to promote sensitization of lanthanide luminescence.

Enhancement of the binding affinity. One of the aspects that might limit the efficiency of the ditopic complexes LnL^{5-6} is the relatively weak interaction between the NH_3^+ and the monoaza-crown ether. Regardless of its strength, monoaza-crown ethers have manifold selectivity for potassium (K^+) over NH_3^+ [8]. K^+ (similarly to Ca^{2+} and Mg^{2+}) occurs in significant quantity in extracellular fluid and is closely linked to the release of transmitters [9]. Thus, there is a need to have a more potent crown ether that enables binding of ammonium selectively with respect to K^+ .

The 4,10,16-triaza-18-crown-6 ether, with alternating nitrogen and oxygen atoms in the ring, was employed for this purpose (figure 3.2). The arrangement of the three nitrogens in the triaza-crown matches the symmetry axis of a primary ammonium cation thus enabling the formation of three $\text{N}^{\cdots}\text{H}-\text{N}$ hydrogen bonds. $\text{N}-\text{H}^{\cdots}\text{N}$ hydrogen bonding is known to be stronger than $\text{N}-\text{H}^{\cdots}\text{O}$ [10] and it provides a sufficient number of binding sites for ammonium ions, but

fewer for K^+ ions compared to monoaza-18-crown-6 (Figure 3.2). As a consequence, the selectivity for NH_4^+ over K^+ is significantly higher and the stability of the ammonium complexes increases for the triaza-crown. For instance, the triaza-18-crown-6 will complex the organic ammonium $CH_3-NH_3^+$ ion about 30 times more strongly than the monoaza-18-crown-6 analogue, whilst the affinity towards K^+ ion drops considerably [11] (table 3.1).



4,10,16-triaza-18-crown-6

Figure 3.2: Structure of 4,10,16-triaza-18-crown-6 and the binding scheme of the ammonium ion to the 4,10,16-trimethyl triaza-crown ether. The pKa values of the trimethyl triaza-crown are 10.23, 7.53 and 5.42 in aqueous solution at 25°C [11].

Table 3.1: Stability constants K_s for the binding of cationic substrates by monoaza-, diaza- and triaza-crown ether macrocycles [11].

Macrocycle	K^+	$CH_3-NH_3^+$	$Ph-(CH_2)_2NH_3^+$
18-crown- O_6	170000	2100	1500
18-crown- O_4N_2	12500	2200	2000
18-crown- O_3N_3	6000*	65000*	50000*

*Solvent: methanol:water 9:1, 25°C (NMe₄Br 0.1M)

4,10,16-triaza-18-crown-6 was first reported by Lehn and coworkers¹ and was later used as a key building block for binding DNA conjugates [12, 13] and in ditopic hosts for dual binding of amino acid zwitterions [14-16] (figure 3.3).

¹ J.-M. Lehn, United States Patent No. 3,888,887, June 10, 1975

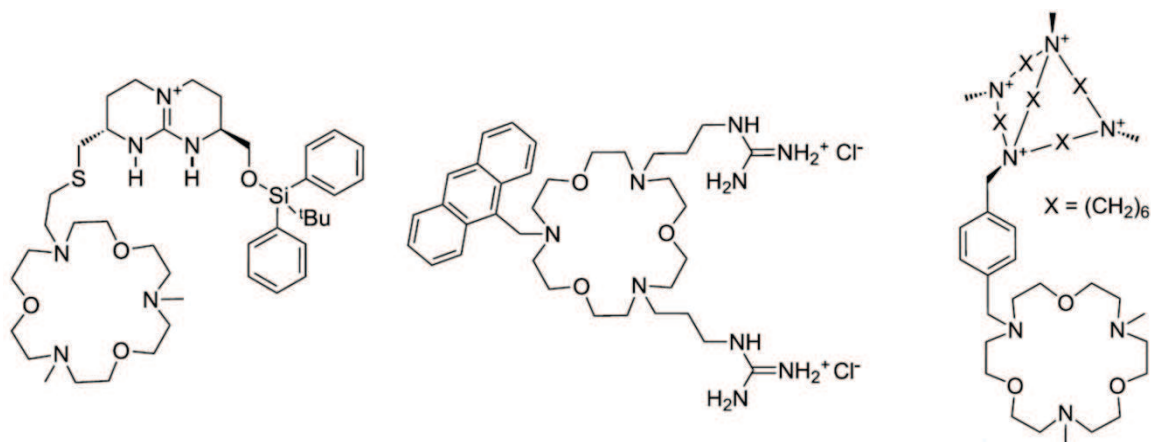


Figure 3.3: Left: Chiral bicyclic guanidinium aza-crown receptor for amino acid zwitterions [14]. Middle: Receptor for amino acids containing a triaza-crown connected (i) to two charged guanidinium groups which interact with carboxylates, and (ii) to the luminescent anthracene moiety. Upon ammonium ion binding the quenching of the anthracene emission by PET is intercepted leading to an emission increase [15]. Right: Ditopic receptor for GABA. The triaza-crown is connected to a positively charged polyammonium macrocycle for CO_2^- binding [16].

Based on these literature data, we have decided to incorporate a triaza-crown structure in our ligand design, as illustrated in figure 3.4.

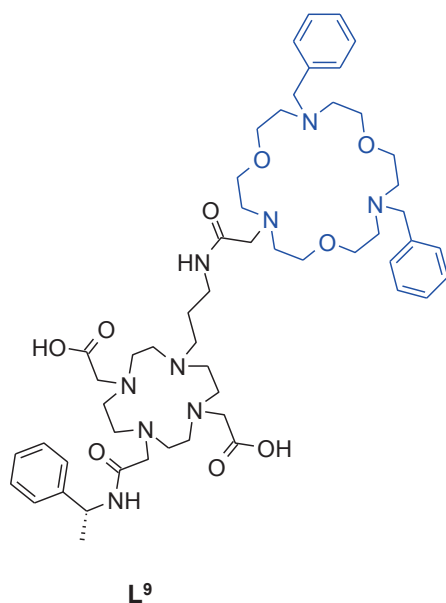


Figure 3.4: Chemical structure of triaza-crown-containing ligand L⁹.

3.2. Synthesis of the complexes

3.2.1. Synthesis of Ligand L⁸:

Para-benzophenone-chloroacetamide was prepared from the commercially available 2-aminobenzophenone by acetylation with chloroacetyl chloride (according to a reported procedure [17]). The monoacetamide was used for mono-N-functionalization of ^tBu-DO2A to yield the intermediate **12** (figure 3.5). Functionalization of the fourth NH group in the cyclen ring *via* reductive amination with N-Cbz protected 3-aminopropanal, followed with Cbz protecting group removal afforded the amine **13**.

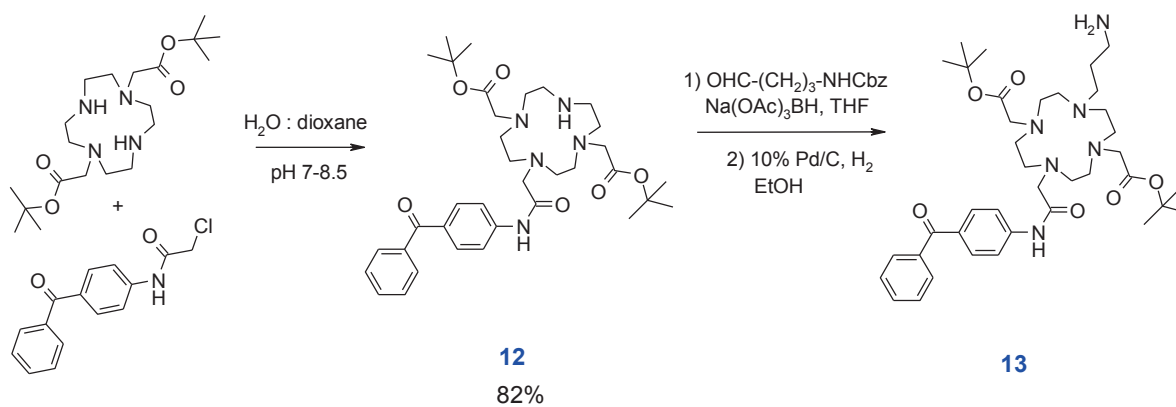


Figure 3.5

Amine **13** was coupled with monoaza-crown carboxylic acid **6** (see chapter 2) under standard conditions using HBTU as the coupling agent, followed by the removal of tert-Butyl groups to give the ligand L⁸.

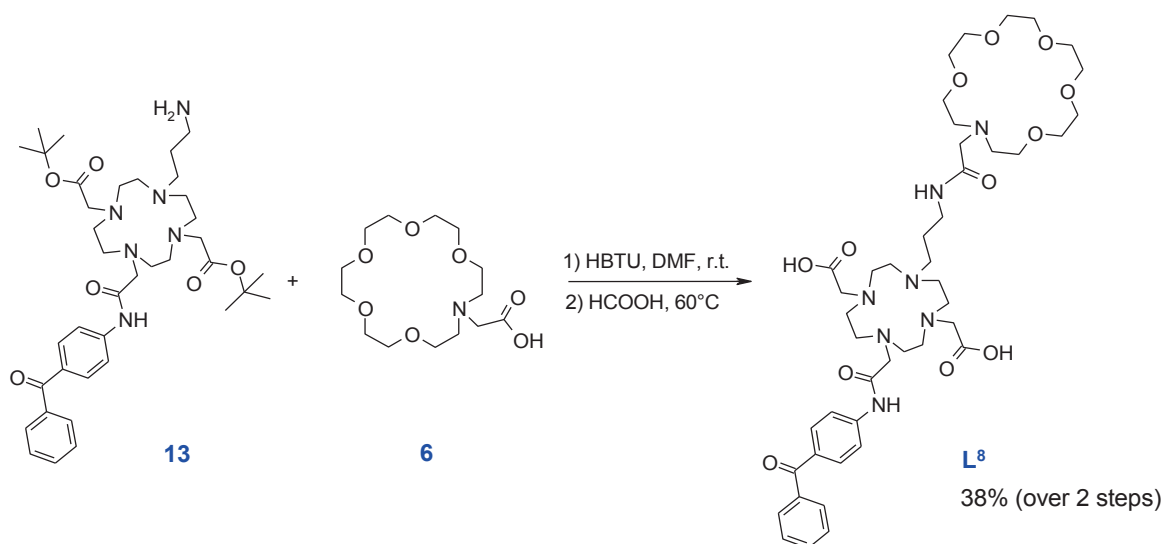


Figure 3.6

3.2.2. Synthesis of ligand L⁹

Ligand L⁹ was synthesized by coupling two building blocks as illustrated in the following figure:

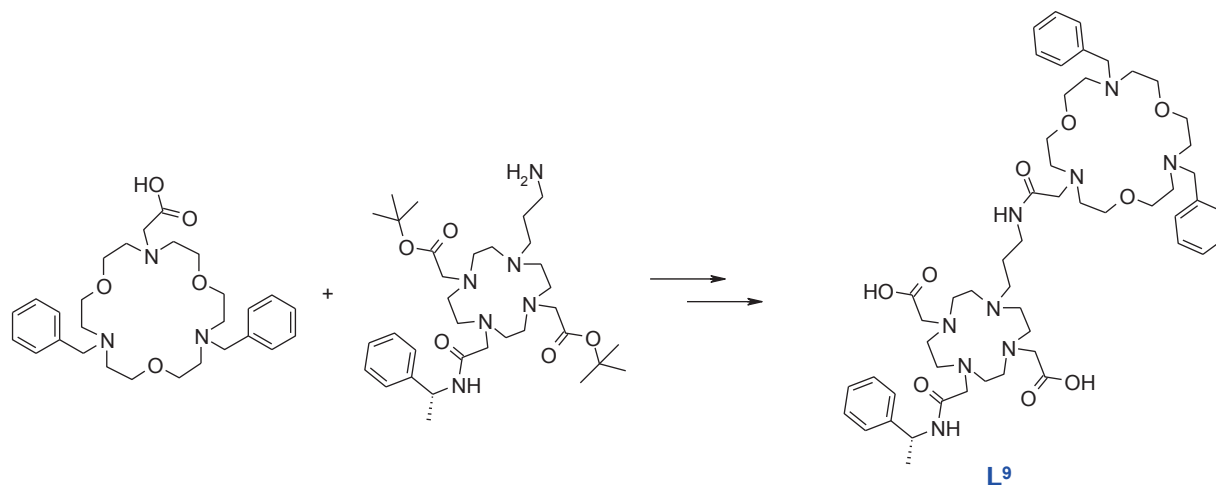


Figure 3.7

The 4,10,16-triaza-18-crown-6 required for the synthesis of the carboxylic acid precursor is not commercially available. Thus, we initially attempted to synthesize it using a slightly modified synthetic pathway of the literature method [12]. The synthetic route is illustrated in figure 3.8 and involved employing the commercially available compound **14** as starting material that was treated with benzoic anhydride and subsequently mesylated to give building block **16**. Treatment of **16** with glycine methylester gave the dibenzoyl diamide **17**. Selective reduction of dibenzoyl diamide **17** was attempted using some of the methods described in the literature using i) silanes in the presence of zinc catalysts [18, 19], ii) borane (BH₃ in THF) [20] and B₂H₆ (formed *in situ* from NaBH₄ and BF₃–Et₂O in dry THF) [21]. The desired reduction could occur only in the latter conditions, but reduction of the methyl ester took place as well.

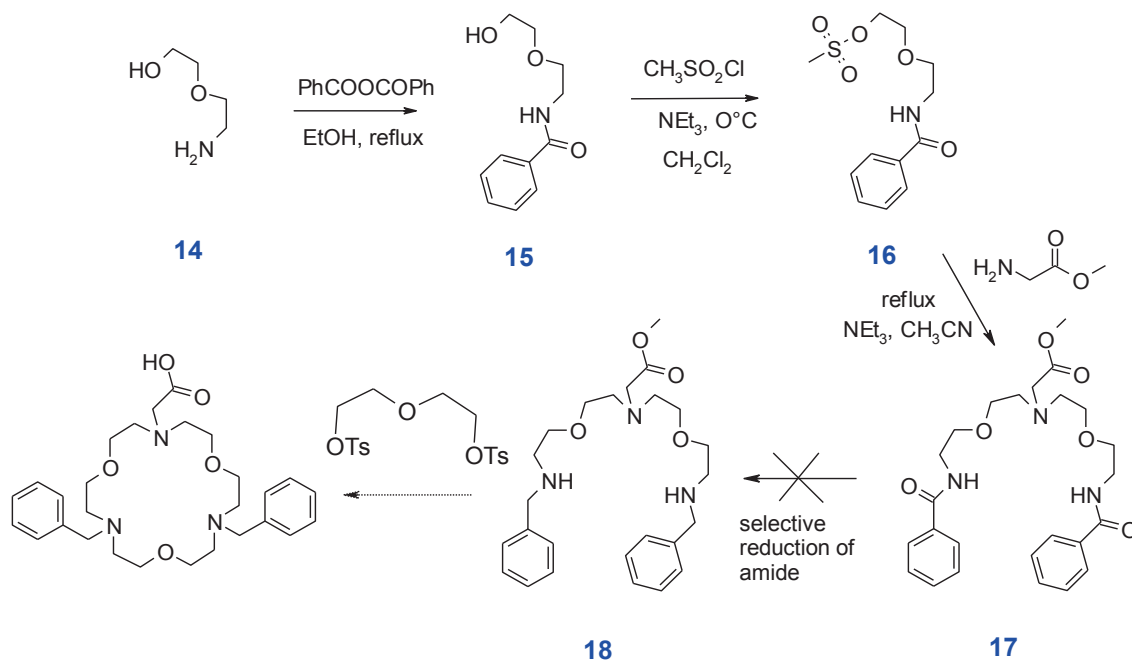


Figure 3.8

An alternative synthetic route, as shown in figure 3.9, was chosen where the treatment of **16** with ethanoamine (instead of glycine methyl ester) afforded dibenzoyl diamide **19**. Reduction using LiAlH₄ of this diamide led to the corresponding diamine **20**, a suitable intermediate for a macrocyclization reaction. Treatment of diamines with diethyleneglycol ditosylate (as previously reported [13]) did not work in our case. Instead, it was reacted with diglycol chloride to form the macrocycle **21**, followed by reduction using LiAlH₄ to give **22**. Finally, Jones oxidation of the compound **22** yielded the desired building block carboxylic acid **23**.

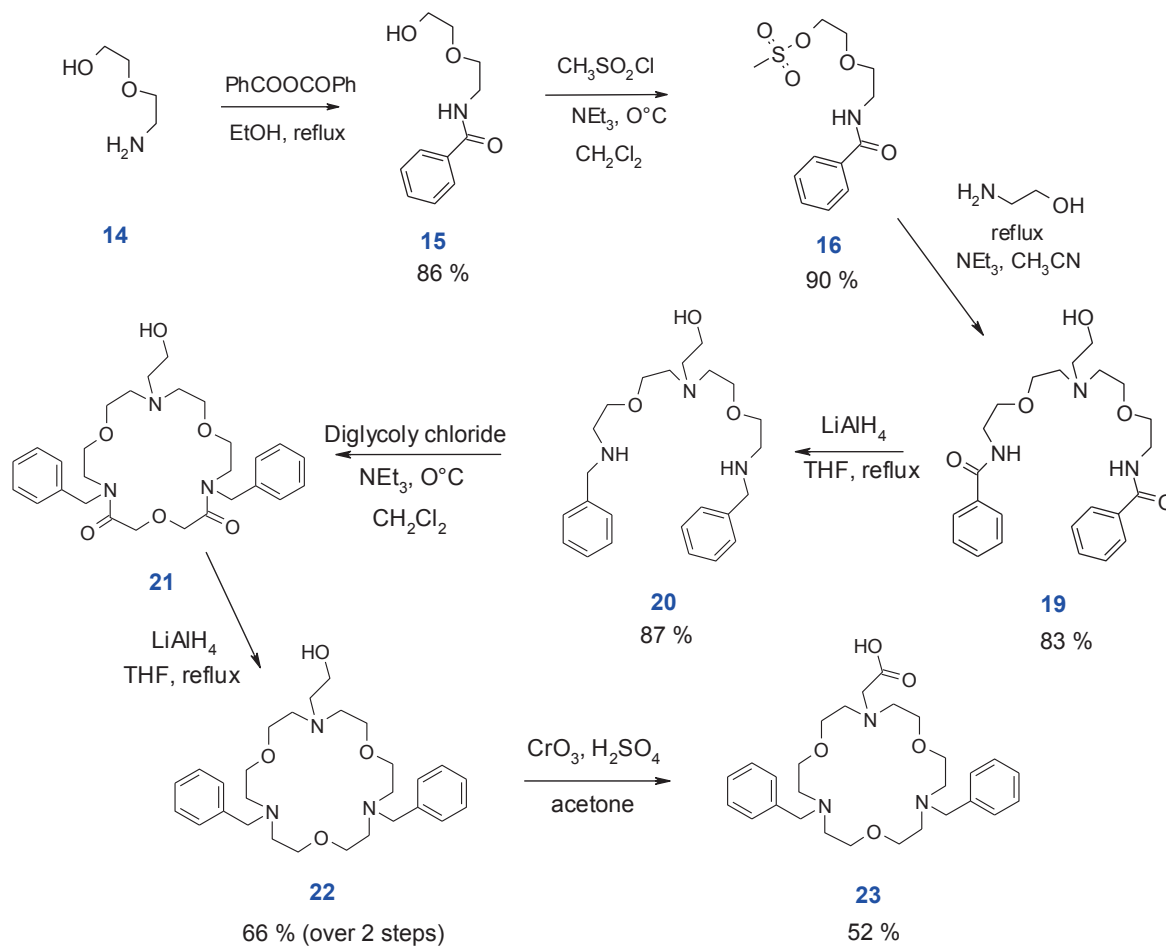


Figure 3.9

Precursor **2** (used for the synthesis of **L**⁵⁻⁶) was used in a reductive amination reaction with benzyl (3-oxopropyl)carbamate, followed by removal of the Cbz protecting group by means of catalytic hydrogenolysis to afford the free amine **25** (figure 3.10).

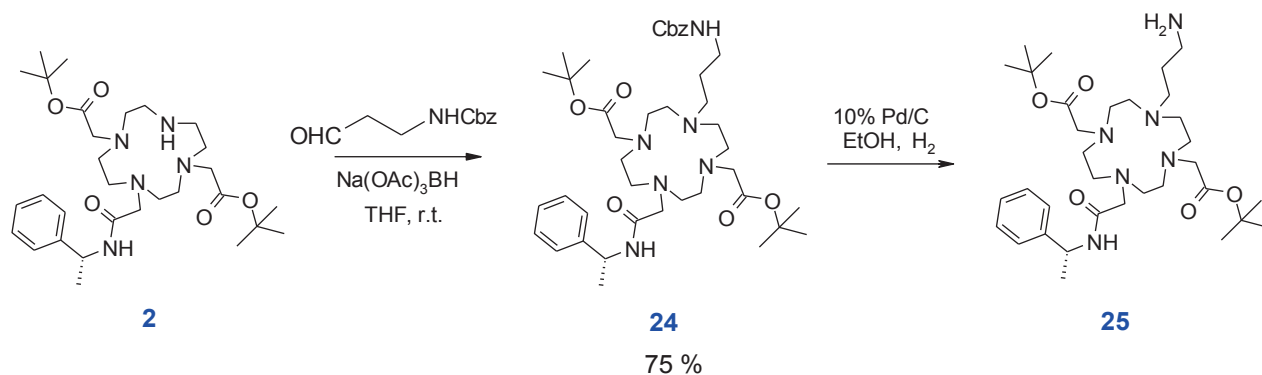


Figure 3.10

Finally, crown ether carboxylic acid **23** was coupled with the free amine-DO2A **25** using standard amide coupling conditions and the tert-butyl protecting groups were readily removed using formic acid to give ligand **L⁹** (figure 3.11).

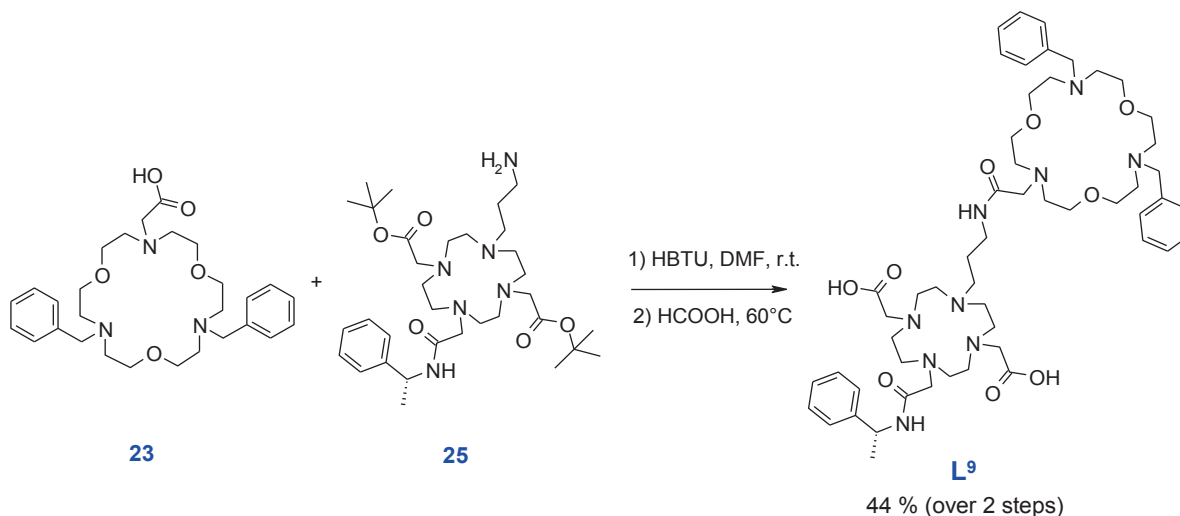


Figure 3.11

Complexation. Ligands **L⁸⁻⁹** were loaded with Ln^{3+} using excess of lanthanide chloride salts ($\text{LnCl}_3 \cdot 6\text{H}_2\text{O}$) in water and the pH was kept at 6-7 during the complexation. To remove the excess of Ln^{3+} , all complexes were purified over neutral alumina by eluting with $\text{CH}_3\text{CN}:\text{H}_2\text{O}$.

3.3. Results and discussion

3.3.1 Photophysical characterization

3.3.1.1. Luminescence emission of EuL^8

The emission and excitation spectra of the EuL^8 complex are displayed in figure 3.12. The absorption spectrum of the EuL^8 complex showed a broad band with a maximum at ca. 300 nm, corresponding to the $\pi-\pi^*$ transition of the benzophenone. Upon excitation at this wavelength, the characteristic line-like emission band at 592, 617, 651 and 698 nm for the deactivation of $^5\text{D}_4 \rightarrow ^7\text{F}_j$ ($j = 1, 2, 3, 4$) of Eu^{3+} appears. By fixing the emission at 617 nm, the excitation spectrum was recorded. The Eu^{3+} luminescence emission and the good superimposition of the absorption and excitation spectra prove unambiguously that the triplet state T_1 of the benzophenone is capable of sensitising the excited states of Eu^{3+} .

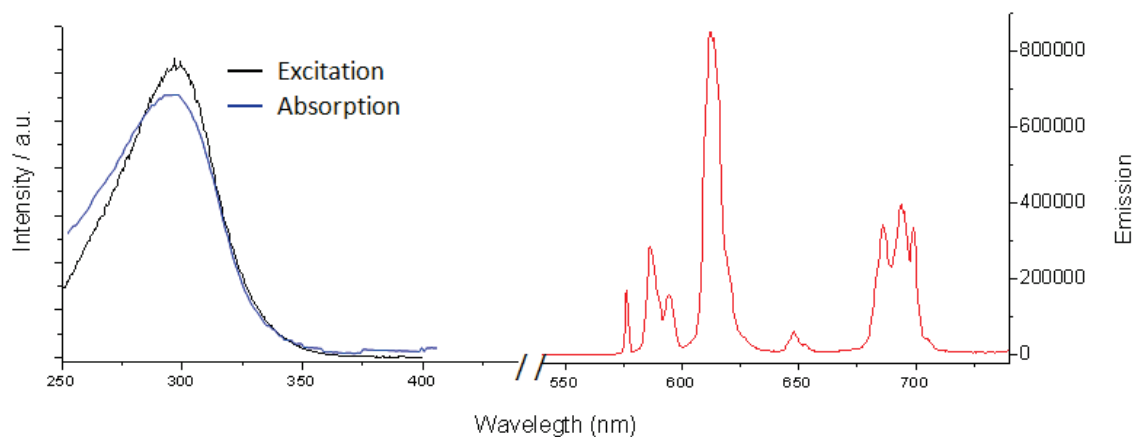


Figure 3.12: Emission and excitation spectra of 50 μM EuL^8 buffered solution (λ_{ex} 300 nm, λ_{em} 617, 25°C).

3.3.1.2. Near-infrared emission of YbL^8 and NdL^8 .

In seeking to extend the applicability of the L^8 complexes as emissive probes, we prepared the Yb^{3+} and Nd^{3+} analogues to investigate the properties and utility of the benzophenone chromophore as a sensitizer of near-infrared luminescence in the case of Yb^{3+} and Nd^{3+} . In order to assess the position of the triplet state of the ligand, the Gd^{3+} complex has been also prepared and investigated. Indeed, with this metal ion, no energy transfer from the chromophore to the lanthanide ion can occur because the Gd^{3+} electronic levels are too high in energy to accept a transfer from the singlet and/or triplet state of the benzophenone. All the NIR luminescence measurements have been performed with the help of Svetlana Eliseeva in the group of Stéphane Petoud.

Figure 3.13 shows the absorption spectra of GdL^8 , YbL^8 and NdL^8 in H_2O . They exhibited a strong absorption peak at about 300 nm, corresponding to the $\pi-\pi^*$ absorption of the benzophenone. Figure 3.14 shows the phosphorescence spectrum of GdL^8 in H_2O , when excited at 300 nm. Figures 3.15 and 3.16 depict the emission and excitation spectra of YbL^8 and NdL^8 , respectively in H_2O . Luminescence lifetimes were determined under excitation at 355 nm while the signal was detected in the near-infrared range (850-1450 nm). The measured lifetimes along with quantum yields are reported in table 3.2.

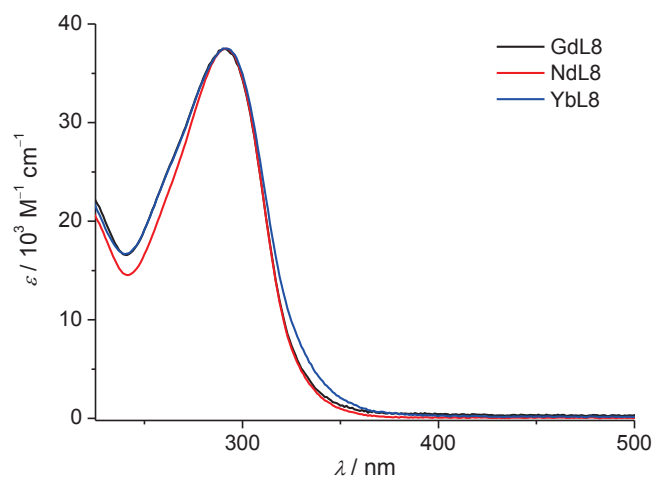


Figure 3.13. Absorption spectra of LnL^8 complexes (100 μM , HEPES buffer, room temperature).

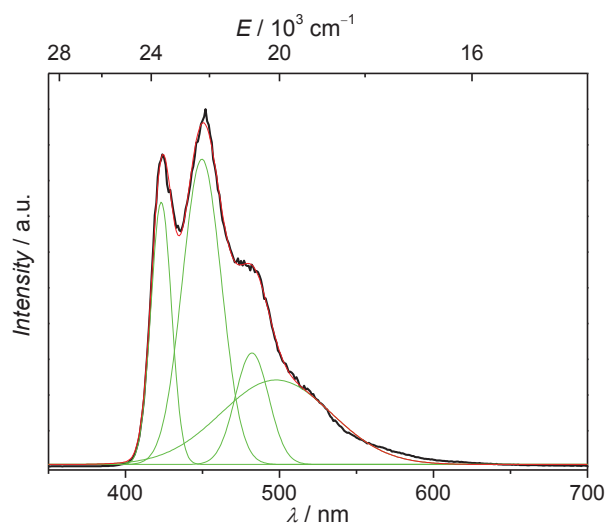


Figure 3.14. Phosphorescence spectrum of GdL^8 (time delay 50 μs) under excitation at 300 nm at 77K.

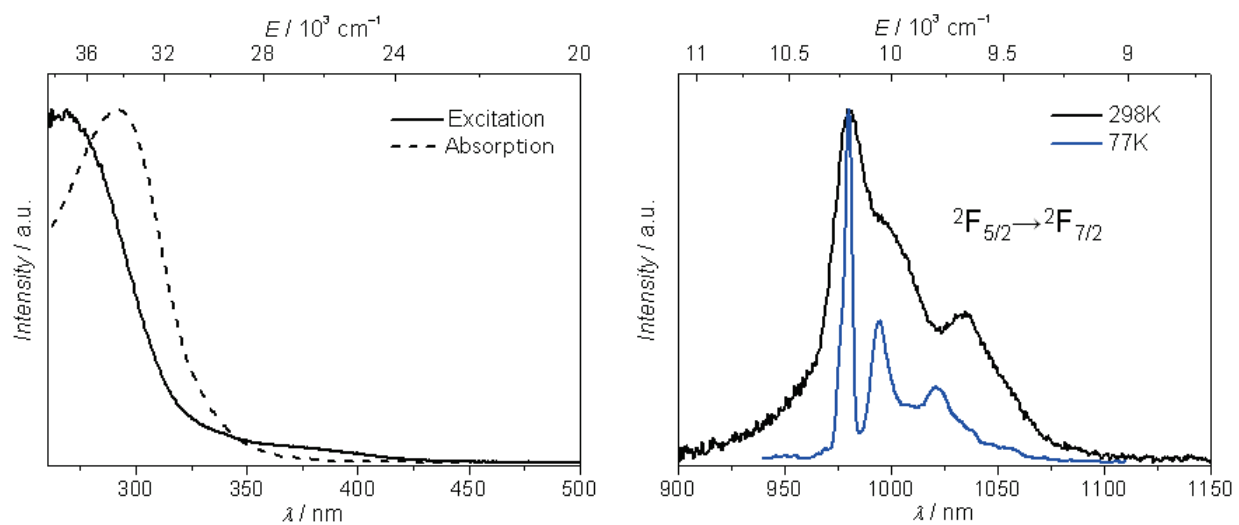


Figure 3.15. (Left) Excitation ($\lambda_{em} = 980$ nm) and (right) emission ($\lambda_{ex} = 300$ nm) spectra of YbL^8 complex in HEPES buffer.

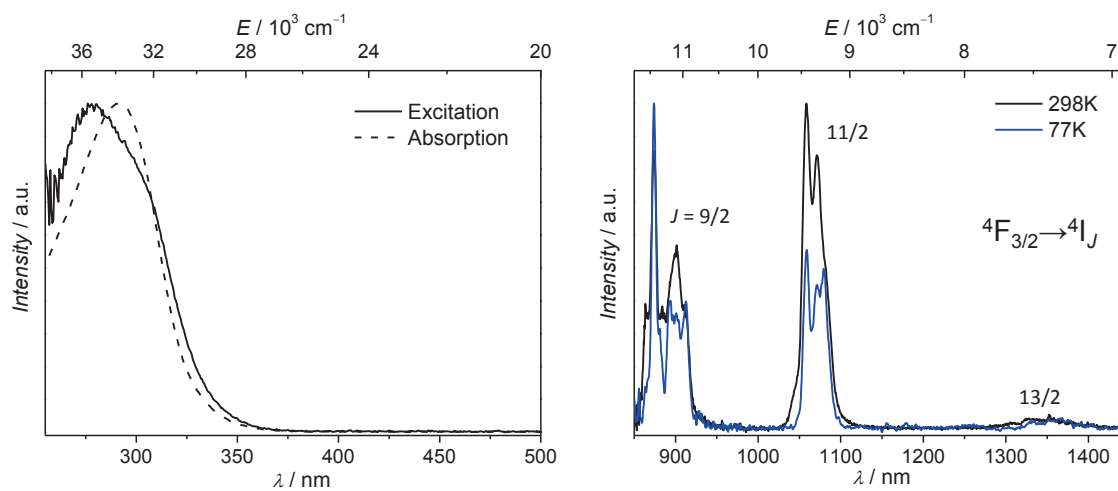


Figure 3.16. (Left) Excitation ($\lambda_{em} = 1064$ nm) and (right) emission ($\lambda_{ex} = 300$ nm) spectra of NdL^8 complex in HEPES buffer.

Table 3.2. Photophysical parameters of LnL⁸ complexes in HEPES buffer under ligand excitation.^a

Compound	τ_{obs}	$Q_{\text{Ln}}^{\text{L}} / \%$
YbL ⁸	2.28(2) μs (68%)	$4.9(2) \cdot 10^{-3}$
	0.69(1) μs (32%) < τ > = 2.08	
NdL ⁸	92.4(5) ns	$1.84(3) \cdot 10^{-2}$

^a Data for 295 K unless otherwise stated. Standard deviation (2σ) between parentheses; estimated relative errors: τ_{obs} , $\pm 2\%$; Q_{Ln}^{L} , $\pm 10\%$.

Absorption spectra are similar for all lanthanides demonstrating a broad band due to $\pi \rightarrow \pi^*$ ligand transitions in the range 250-350 nm with maximum at 290-292 nm ($\epsilon = 37\,400\text{-}37\,500\text{ M}^{-1}\text{ cm}^{-1}$). Absorption spectrum of YbL⁸ shows a slight broadening of the band towards lower energy.

Position of the triplet state of the ligand determined from the phosphorescence spectrum of GdL⁸ (0-0 transition) was found to be at $23\,640\text{ cm}^{-1}$ (423 nm). This value is similar to that of benzophenone, $24\,070\text{ cm}^{-1}$ [22].

Upon ligand excitation, YbL⁸ and NdL⁸ show characteristic emission in the NIR range. The quantum yields in general are comparable with the values for other DOTA complexes in aqueous solutions [23]. However, it should be mentioned that the quantum yield of YbL⁸ is lower than that of NdL⁸, which might be a result of existing photoelectron transfer from monoaza-18-crown-6 moiety in the case of the former, as discussed later in this chapter.

The luminescence decay is monoexponential in the case the of NdL⁸, while biexponential behavior was observed for YbL⁸ which might be due to the presence of different isomers in solution [24].

3.3.2. ¹⁷O NMR measurements

In order to assess the parameters describing water exchange and rotational dynamics on GdL⁸ and GdL⁹, we have performed a variable temperature ¹⁷O NMR study on aqueous solutions of

these Gd^{3+} complexes. Figure 3.17 shows the measured temperature dependency of the reduced ^{17}O chemical shifts ($\Delta\omega_r$), and transverse ($1/T_{2r}$) and longitudinal ($1/T_{1r}$) relaxation rates. For complexes GdL^{8-9} , the transverse ^{17}O relaxation rates, $1/T_{2r}$, increase with decreasing temperature at higher temperatures, indicating here that these complexes are in the fast exchange regime. At lower temperatures, the transverse relaxation rates turn into an intermediate and in particular for the GdL^8 complex, to a slow exchange regime. The reduced chemical shifts follow the same trend.

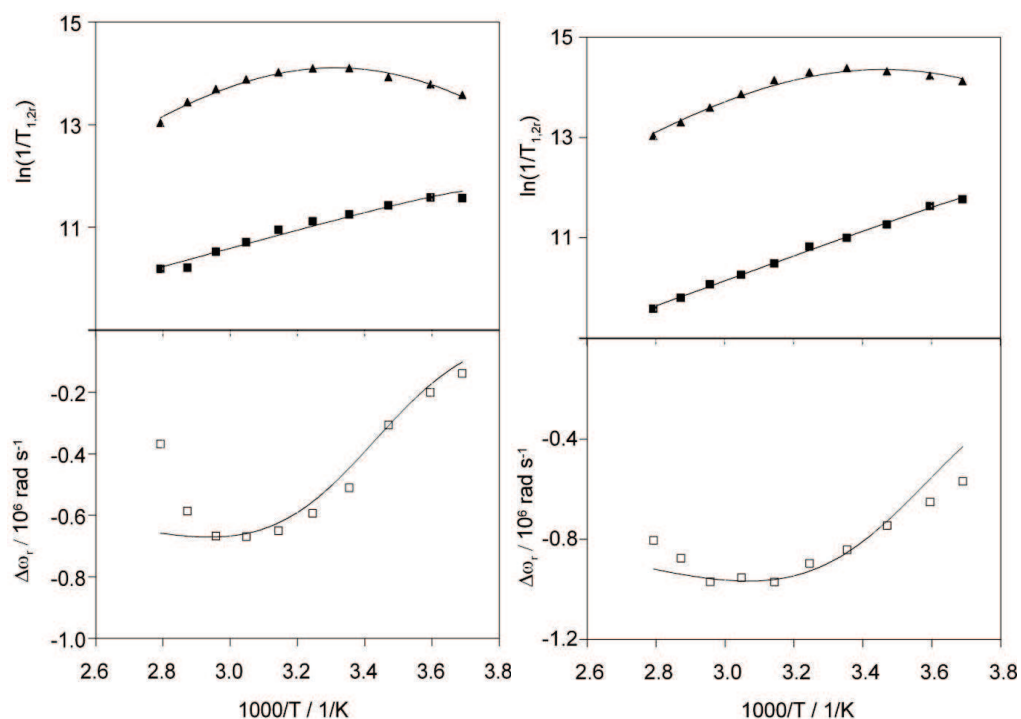


Figure 3.17: Temperature dependence of the reduced transverse ^{17}O relaxation rates, $1/T_{2r}$ (\blacktriangle), $1/T_{1r}$ (\blacksquare) and the reduced ^{17}O chemical shifts, $\Delta\omega_r$ (\square) for GdL^8 (left) and GdL^9 (right). The curves represent the fit to the experimental data points as explained in the text.

One inner sphere water molecule has been supposed for both complexes, based on analogy to structurally similar systems, in particular those studied in Chapter 2. In the slow exchange regime, the reduced transverse relaxation rates are directly determined by the water exchange rate. In the fast exchange regime, on the other hand, the reduced transverse relaxation rate is defined by the transverse relaxation rate of the bound water oxygen, $1/T_{2m}$, which is in turn influenced by the water exchange rate, k_{ex} , the longitudinal electronic relaxation rate, $1/T_{1e}$,

and the scalar coupling constant, A/\hbar . The reduced ^{17}O chemical shifts are determined by A/\hbar . Transverse ^{17}O relaxation is governed by the scalar relaxation mechanism, thus contains no information on the rotational motion of the system. In contrast to $1/T_{2r}$, the longitudinal ^{17}O relaxation rates, $1/T_{1r}$, are determined by dipole-dipole and quadrupolar relaxation mechanisms, both related to rotation. The dipolar term depends on the Gd^{3+} -water oxygen distance, r_{GdO} , while the quadrupolar term is influenced by the quadrupolar coupling constant, $\chi(1+\eta^2/3)^{1/2}$. The analysis of the experimental ^{17}O NMR data for both systems was performed according to the traditional Solomon-Bloembergen-Morgan theory. The theoretical equations used in the data analysis are shown in the Appendix. All parameters obtained from the fits are shown in Table 3.3.

In the fitting procedure, r_{GdO} has been fixed to 2.50 Å, based on available crystal structures [25, 26] and recent ESEEM results [27]. The quadrupolar coupling constant, $\chi(1+\eta^2/3)^{1/2}$, has been set to the value for pure water, 7.58 MHz. The following parameters have been adjusted: the water exchange rate, k_{ex}^{298} , the activation entropy, ΔS^\ddagger , the activation enthalpy for water exchange, ΔH^\ddagger , the scalar coupling constant, A/\hbar , the rotational correlation time (τ_{R}^{298}) and its activation energy, E_{R} , and the parameters characterizing the electron spin relaxation, such as the correlation time for the modulation of the zero-field-splitting, τ_{v}^{298} , and its activation energy, E_{v} , and the mean-square zero-field-splitting energy, Δ^2 . The empirical constant describing the outer sphere contribution to the ^{17}O chemical shift, C_{os} , was also fitted and gave reasonable values. E_{v} was fixed to 1 kJ/mol, otherwise small negative values were obtained.

For GdL^8 and GdL^9 , both partially in the fast water exchange regime, the reduced chemical shifts and, consequently the scalar coupling constant calculated, give a direct indication of the hydration state of the complexes. For GdL^9 , the chemical shifts and thus the scalar coupling constant clearly evidence one inner sphere water molecule. For GdL^8 , the reduced chemical shifts, and correspondingly the scalar coupling constant, are slightly lower than what we would expect for a complex with one inner sphere water molecule. It can be the consequence of an increased steric demand of the bulky benzophenone moiety which somewhat restricts the water access to the lanthanide ion. The same steric restriction might be also responsible for the

considerably slower water exchange on GdL^8 with respect to GdL^9 or GdL^6 , which have analogous structures with a different crown ether and/or a different chromophore moiety. The water exchange rate for GdL^9 is similar to that for GdL^6 and it is about three times higher than that for GdDOTA. This, as discussed in Chapter 2, is directly related to the structure of the complexes. The faster exchange is likely the consequence of the coordination of the amide function which is relatively far and therefore induces more constraints around the water binding site. Higher steric constraint is known to lead to faster water exchange in dissociatively activated water exchange processes [28]. We should note that the mechanism of the water exchange has not been directly assessed (it would be possible by variable pressure measurements, not done here). The calculated activation entropies are close to zero indicating an interchange water exchange process; however, we should be aware of the large errors associated to the activation entropies which make unreliable any conclusion drawn from these data on the mechanism of water exchange.

Table 3.3: Parameters obtained from the fitting of the transverse and longitudinal ^{17}O NMR relaxation rates and chemical shifts as a function of temperature at 11.7 T. The analogous parameters for GdL^6 and GdDOTA are also shown for comparison.

	GdL^8	GdL^9	$\text{GdL}^{6\text{a}}$	GdDOTA^{b}
$k_{\text{ex}}^{298} (10^6 \text{s}^{-1})$	5.1(3)	11.8(6)	13.0	<u>4.1</u>
$\Delta H^\ddagger (\text{kJ}\cdot\text{mol}^{-1})$	35.0(5)	31.5(6)	33.3	<u>49.8</u>
$\Delta S^\ddagger (\text{J}\cdot\text{mol}^{-1}\cdot\text{K}^{-1})$	+1(2)	-3(5)	+4	+48.5
$\tau_{\text{R}}^{298} (\text{ps})$	440(20)	360(15)	292	77
$E_{\text{R}} (\text{kJ}\cdot\text{mol}^{-1})$	15.0(2)	20.7(2)	17.6	16.1
$\tau_{\text{V}}^{298} (\text{ps})^{\text{c}}$	4.8(0.2)	3.0(1)	2.0	11
$\Delta^2 (10^{20} \text{s}^{-1})$	0.891(5)	0.69(6)	0.36	0.16
$A/\hbar (10^6 \text{rad}\cdot\text{s}^{-1})$	-2.9(1)	-3.6(1)	-3.7	-3.7
C_{os}	0.0	0.10(5)	0.21	0.21

a) Chapter 2.

b) from D. H Powell, O. M. Ni Dhubhghaill, D. Pubanz, L. Helm, Y. S. Lebedev, W. Schlaepfer, A. E. Merbach, *J. Am. Chem. Soc.* **1996**, *118*, 9333-9346.

The rotational correlation times obtained in the fit are relatively long as compared to that of GdDOTA, which reflects the bigger size of the complexes studied here. GdL⁸ has a particularly long τ_R ²⁹⁸ as compared to GdL⁶ which can be attributed to the bulkiness of the benzophenone group.

3.3.3. Binding Assays

3.3.3.1. Relaxometric titrations of GdL⁸ and GdL⁹

The relaxivities of GdL⁸ and GdL⁹ were measured to be 6.7 and 8.8, mM⁻¹s⁻¹ respectively at 300MHz and 37°C. The higher relaxivity of GdL⁹ in comparison to 7.8 mM⁻¹s⁻¹ for GdL⁶ might be due to the larger size of the benzyl substituted triaza-crown ether.

It was noticed that the aqueous solution of the GdL⁹ complex was subject to a slow but steady decrease of relaxivity over time (days) if not well sealed from air and maintained at -20°C, such decrease was also observed for all the other responsive complexes, but to a lower extent. This can be explained by the uptake of carbon dioxide from air and the subsequent coordination of hydrogencarbonate to the complex (see below). Therefore, samples used for titrations were prepared prior to use and were kept closed to reduce contact with air.

Relaxometric titrations of GdL⁸⁻⁹ were undertaken at 300 MHz and 37°C to measure the change of r_1 as a function of added neurotransmitter and HCO₃⁻. Figures 3.17 and 3.18 depict the relaxometric titration curves of GdL⁸ and GdL⁹, respectively, with acetylcholine, GABA, aspartate, glutamine, glycine and hydrogen carbonate. The fitted values of the dissociation constants (K_d) for 1:1 complex formation are reported in Table 3.3.

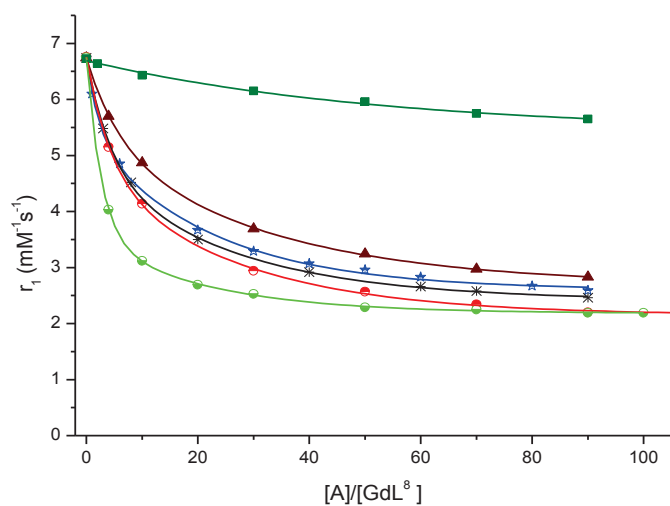


Figure 3.17: ^1H NMR relaxometric titrations of GdL^8 with Ach (■), GABA (▲), Asp (★), Glu (✱), Gly (●) and hydrogen carbonate (●) at 300 MHz, 37°C in D_2O and pD7.8 (HEPES 25mM).

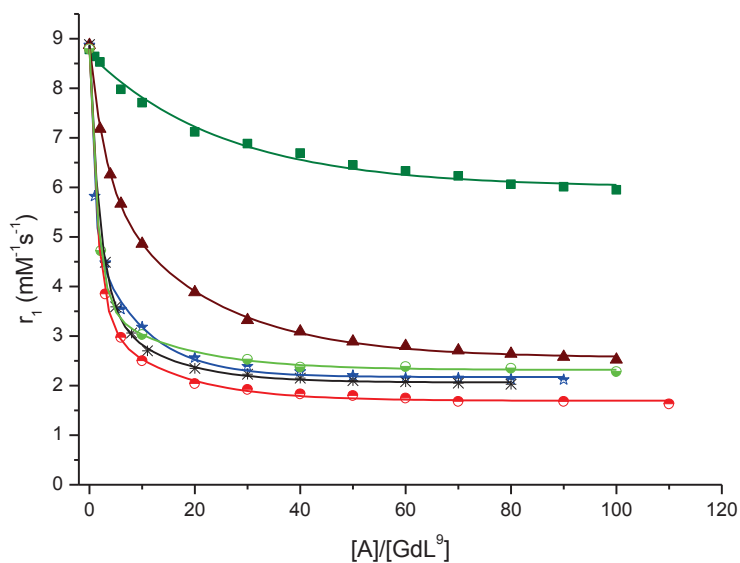


Figure 3.18: ^1H NMR relaxometric titrations of GdL^9 with Ach (■), GABA (▲), hydrogen carbonate (●), Asp (★), Glu (✱) and Gly (●) at 300 MHz, 37°C in D_2O and pD7.8 (HEPES 25mM).

Table 3.3: Dissociation constants and the percentages of the observed change in relaxivity upon interaction of GdL^{8,9} complexes with neurotransmitters and HCO₃⁻, in D₂O at 300MHz, 37°C and pD 7.8. Data for GdL⁶ are shown for comparison.

	GdL ⁶		GdL ⁸		GdL ⁹	
	K _d (mM)	r _{1p} (%)	K _d (mM)	r _{1p} (%)	K _d (mM)	r _{1p} (%)
Glycine	5.6*	74*	12.4	75	2.9	82
Glutamate	9.1	69	12.4	70	3.2	79
GABA	8.0*	67*	28.1	70	10.1	77
Aspartate	-	-	14.0	67	2.9	75
HCO ₃ ²⁻	-	-	4.3	69	2.3	74
HPO ₄ ⁻	-	0	-	12	-	19

*Values are obtained from titrations done in H₂O at 60 MHz (chapter 2).

The examination of the relaxometric titration curves and the resulting data shown in Table 3.3 reveals some apparent trends:

- Concerning the binding of acetylcholine and GABA in comparison to the α -amino acid neurotransmitters, the behavior of GdL⁸⁻⁹ is similar GdL⁶. Namely, the binding of GABA is less important than that of the other neurotransmitters, while acetylcholine binds even to a lesser extent to these complexes.
- GdL⁸ has gained notable affinity towards HCO₃⁻ ($K_d = 14.7$ mM was obtained for GdL⁵). In contrast, its binding affinity towards neurotransmitters has considerably decreased (as compared to GdL⁶), though the overall decrease of relaxivity did not change significantly. So, on the overall, the introduction of the benzophenone led to a loss of selectivity for neurotransmitters over carbonate.
- There is a small change in relaxivity induced by hydrogen phosphate in the case of GdL⁸ and GdL⁹ (table 3.3), while GdL⁶ was not sensitive to hydrogen phosphate at all. This change, however, remains insignificant.
- The most noteworthy trend is the increased affinity of GdL⁹ for α -amino acid neurotransmitters, in comparison to the monoaza-containing complex, GdL⁶, as it can be seen from table 3.3. Figure 3.19 below further illustrates this through the example of glutamate.

- GdL⁹ containing the triaza crown ether has an increased affinity to neurotransmitters, however also to bicarbonate. Overall, it remains non-selective to neurotransmitters, despite what was expected.

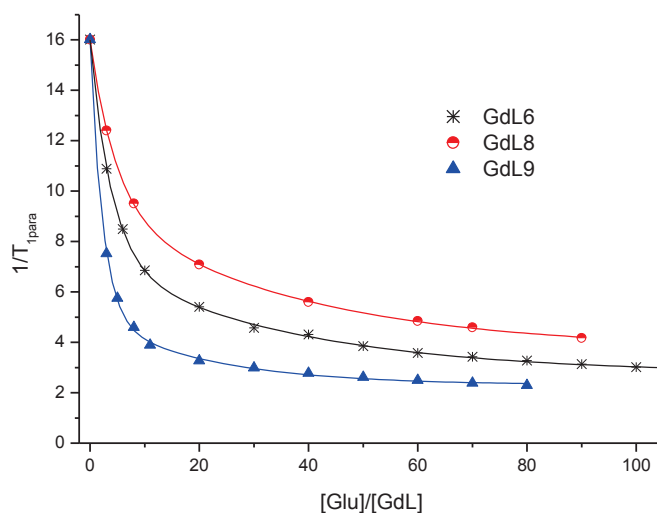


Figure 3.19: Comparative curves showing the $1/T_1$ responses of GdL^{6,8-9} to glutamate. It clearly demonstrates the enhanced sensitivity of GdL⁹ to glutamate (300 MHz, 37°C in D₂O and pD7.8, HEPES 25mM).

3.3.3.2. Luminescence emission of EuL⁸

In order to examine the ability of EuL⁸ to function as luminescent sensor for neurotransmitters and its eventual capability to provide a ratiometric optical response to these biomarkers, similar to the one observed with EuL⁵, we have recorded the emission spectra in the presence of different concentrations of neurotransmitters, as well as HCO₃⁻ or HPO₄⁻. Figure 3.20 represents the change of the emission intensity at 610 nm upon excitation at 300 nm, while figure 3.21 reports the full emission spectra recorded in the absence and in the presence of 30, 50 and 70 equivalents of glycine as an example.

From these figures, it is obvious that the emission change of EuL⁸ upon binding glycine is less substantial than the one induced by EuL⁵ in presence of glutamate, reported in chapter 2. Consequently, the efficiency of the ratiometric response has considerably been diminished. Moreover, EuL⁸ displayed high selectivity for carbonate over neurotransmitters, which is consistent with what was demonstrated by the relaxometric experiments.

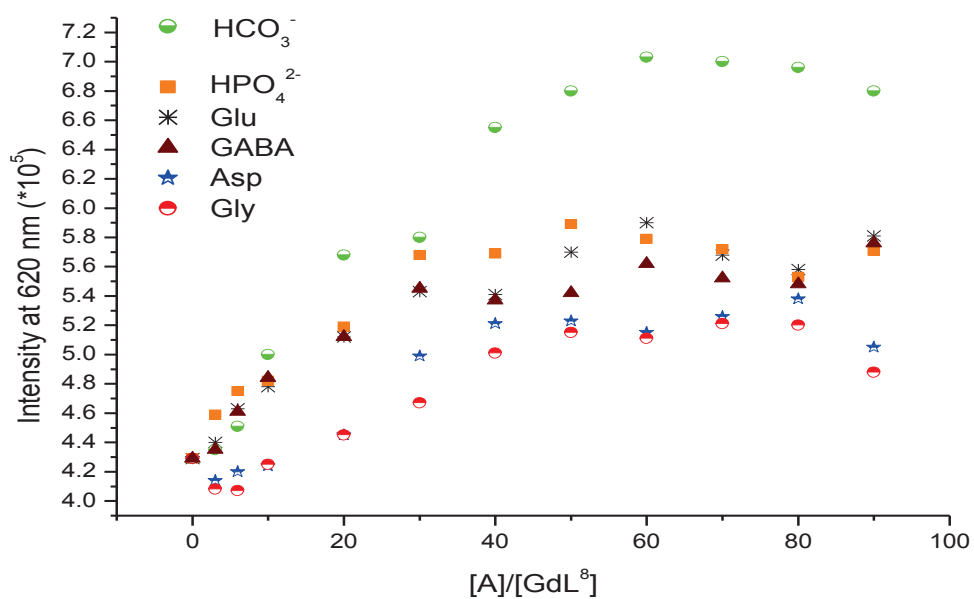


Figure 3.20: Luminescence intensity at 620 nm of aqueous EuL^8 solution (50 μM) upon its titration with bicarbonate, phosphate, glutamate, GABA, Aspartate and glycine; excitation at 300 nm.

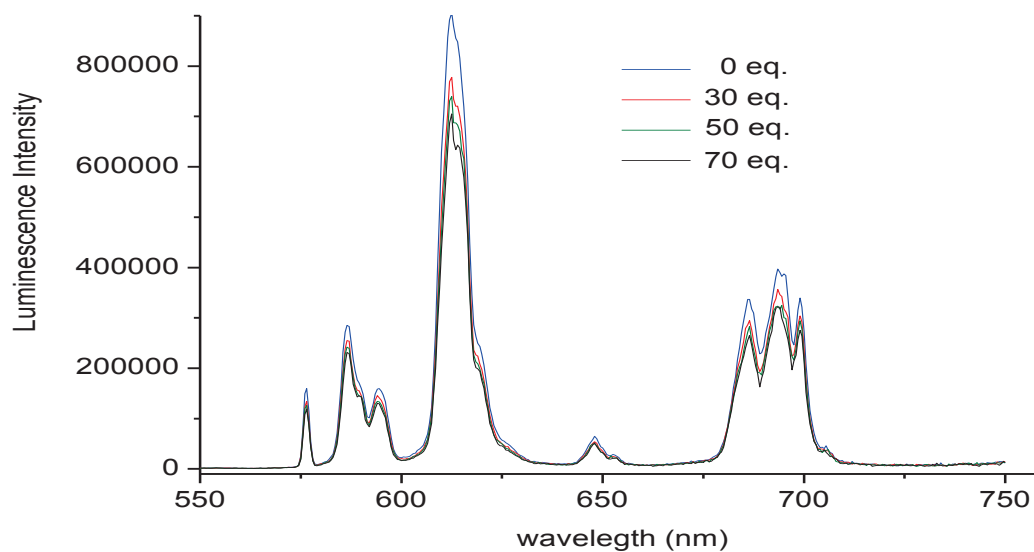


Figure 3.21: Europium emission spectral changes for EuL^8 with added glycine (50 μM complex, 25mM HEPES, pH 7.4, λ_{ex} 300 nm).

In this case, we did not assess the changes of hydration state by luminescence measurements. However, according to the results from luminescence studies of the EuL^{5-6} complexes, we assume that q is diminished upon formation of ternary complexes with EuL^8 . Consequently, the relaxivity changes observed for the interaction of the neurotransmitters with GdL^8 is also the result of the decreasing hydration number.

3.3.3.3. Near-infrared emission of NdL^8 and YbL^8

Absorption and luminescence spectroscopies were also used to estimate the ability of different neurotransmitters to interact with the NIR emitting NdL^8 and YbL^8 . The main effect was expected to occur for emission spectra since the elimination of high-energy O-H vibrations of water molecules from the coordination sphere of lanthanide ion should result in the increase of luminescence intensity. For comparison, we also studied the effect of K^+ which is known to interact with the crown ether moiety. The following figures show the results of the titration of YbL^8 and NdL^8 with potassium, glycine, glutamate, acetylcholine and hydrogen carbonate.

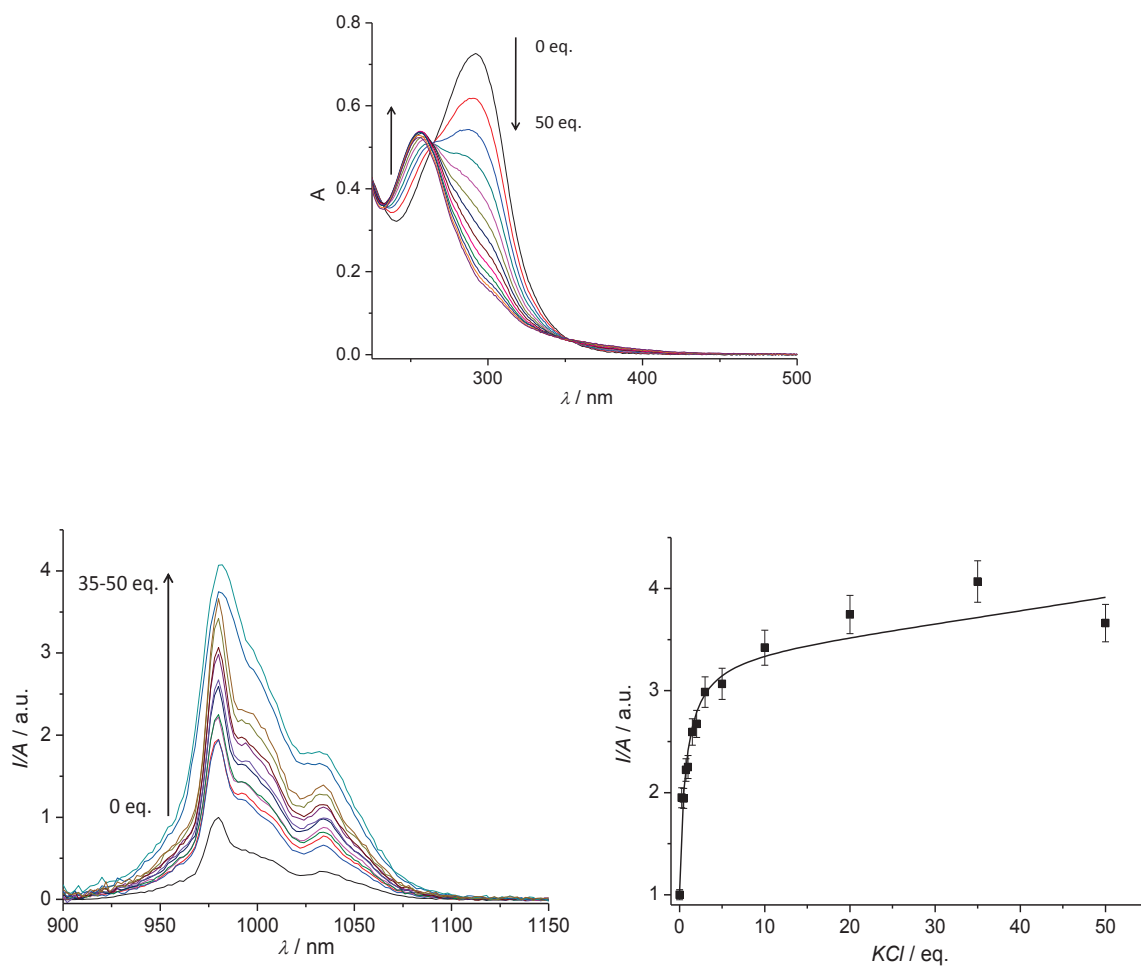
Titration of YbL⁸ with K⁺

Figure 3.22: Variation of absorption (top), emission spectra (bottom left, $\lambda_{\text{ex}} = 300 \text{ nm}$) and corrected luminescence intensity, I/A (bottom, right, at 980 nm , ${}^2F_{5/2} \rightarrow {}^2F_{7/2}$ transition) of YbL⁸ upon titration with KCl (100 μM complex, room temperature).

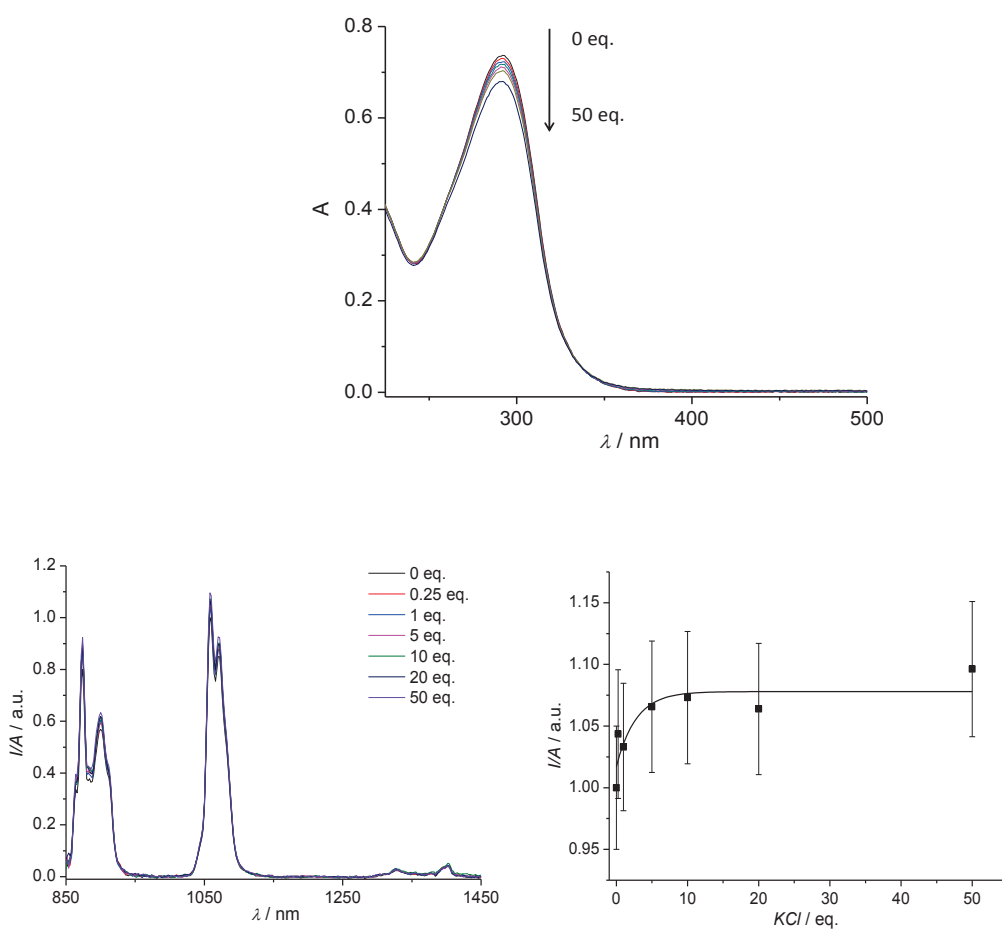
Titration of NdL⁸ with K⁺

Figure 3.23: Variation of absorption (top), emission spectra (bottom left, $\lambda_{\text{ex}} = 300$ nm) and corrected luminescence intensity, I/A (bottom, right, at 1058 nm, ${}^4F_{3/2} \rightarrow {}^4I_{11/2}$ transition) of NdL⁸ upon titration with KCl (100 μM complex, room temperature).

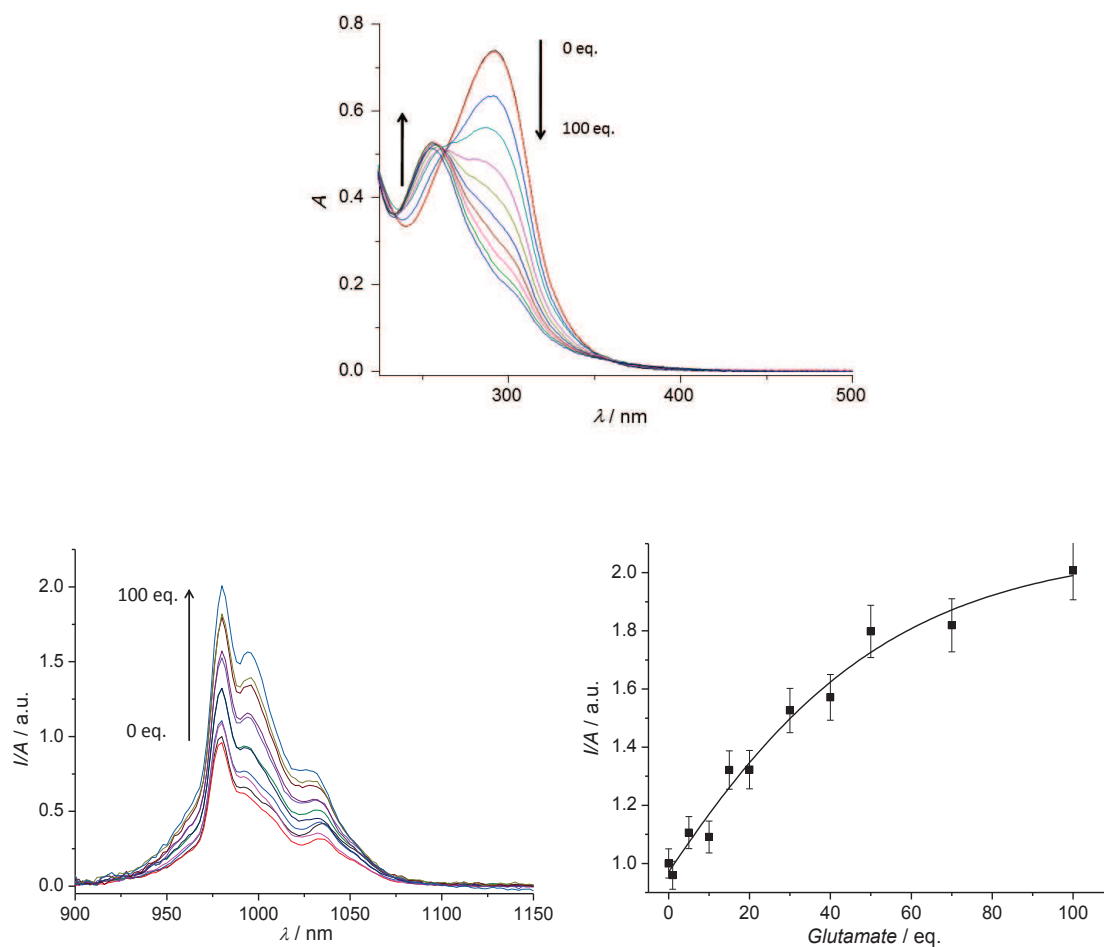
Titration of YbL⁸ with glutamate

Figure 3.24: Variation of absorption (top), emission spectra (bottom left, $\lambda_{\text{ex}} = 300 \text{ nm}$) and corrected luminescence intensity, I/A (bottom, right, at 980 nm , ${}^2F_{5/2} \rightarrow {}^2F_{7/2}$ transition) of YbL⁸ upon titration with **glutamate** ($100 \mu\text{M}$ complex, room temperature).

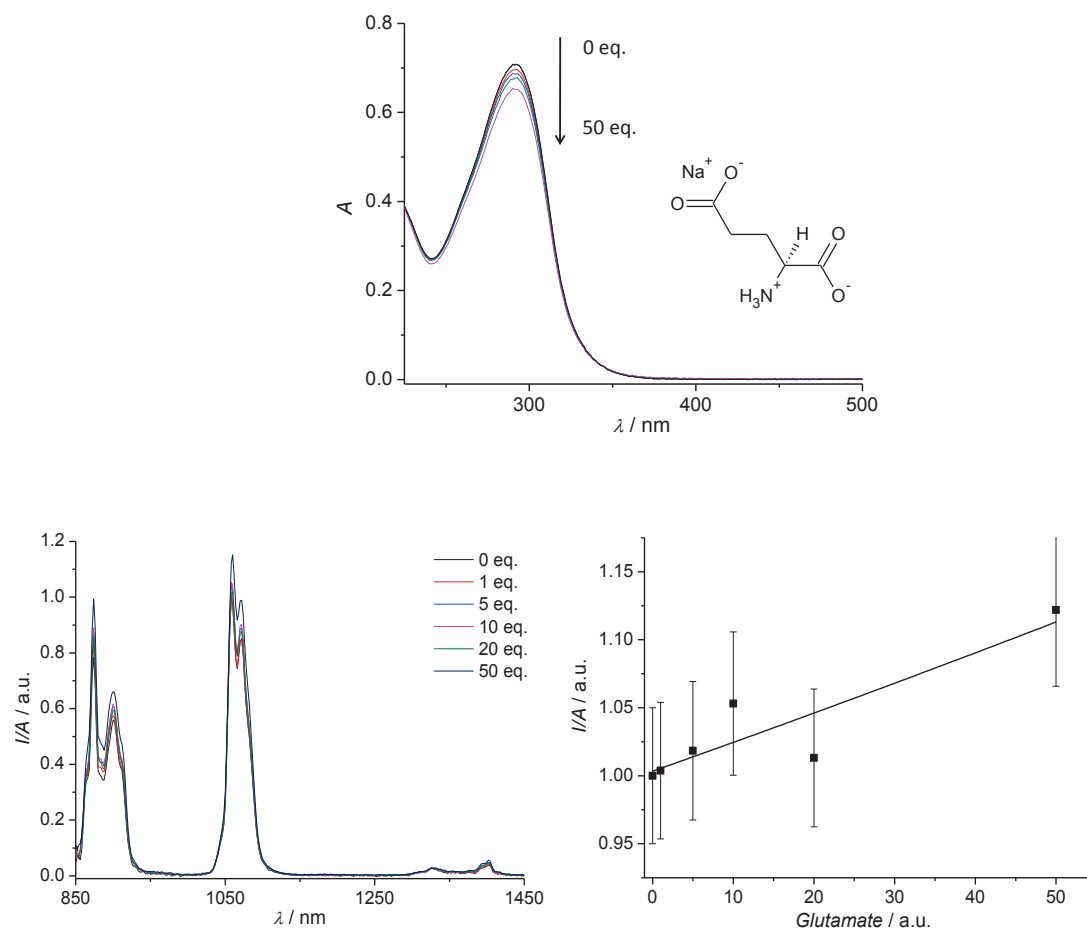
Titration of NdL⁸ with glutamate

Figure 3.25: Variation of absorption (top), emission spectra (bottom left, $\lambda_{\text{ex}} = 300 \text{ nm}$) and corrected luminescence intensity, I/A (bottom, right, at 1058 nm, ${}^4F_{3/2} \rightarrow {}^4I_{11/2}$ transition) of NdL⁸ upon titration with **glutamate** (100 μM complex, room temperature).

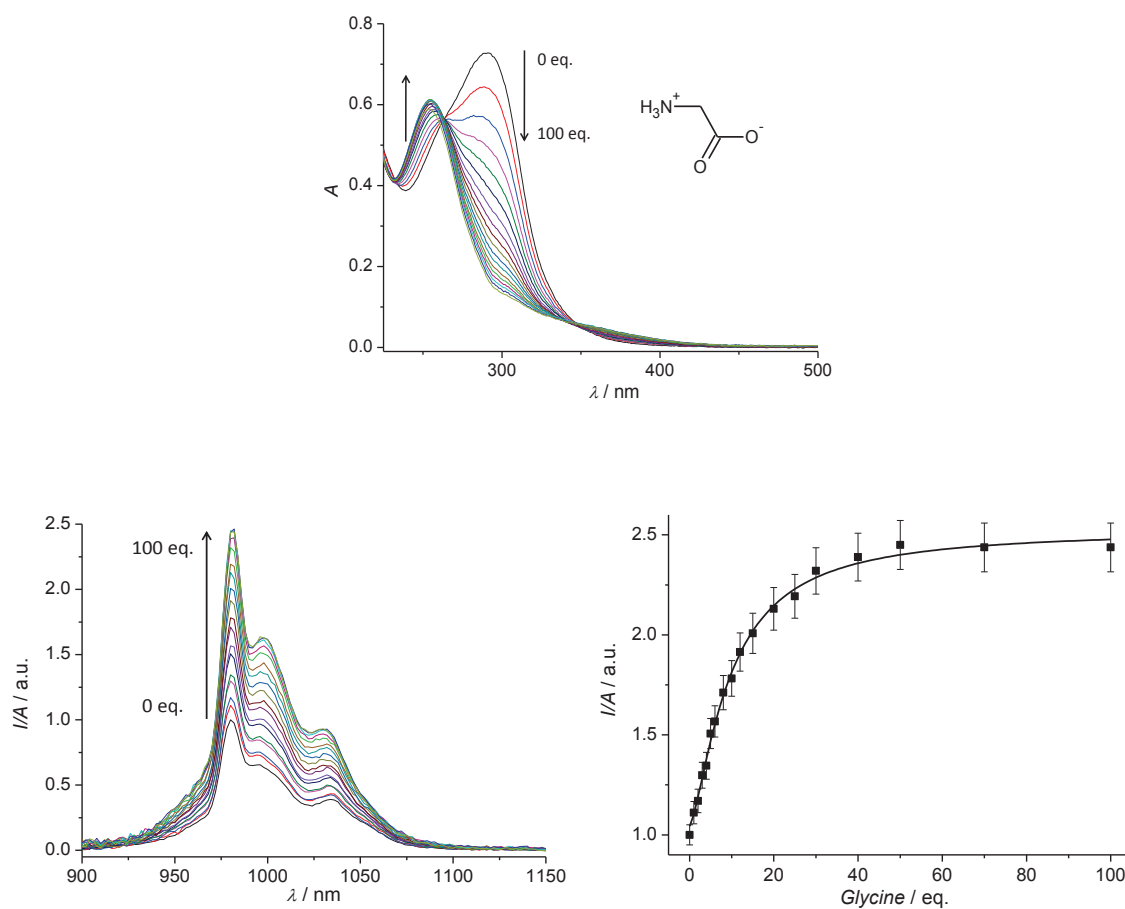
Titration of YbL⁸ with glycine

Figure 3.26: Variation of absorption (top), emission spectra (bottom left, $\lambda_{\text{ex}} = 300 \text{ nm}$) and corrected luminescence intensity, I/A (bottom, right, at 980 nm , ${}^2\text{F}_{5/2} \rightarrow {}^2\text{F}_{7/2}$ transition) of YbL⁸ upon titration with glycine ($100 \mu\text{M}$ complex, room temperature).

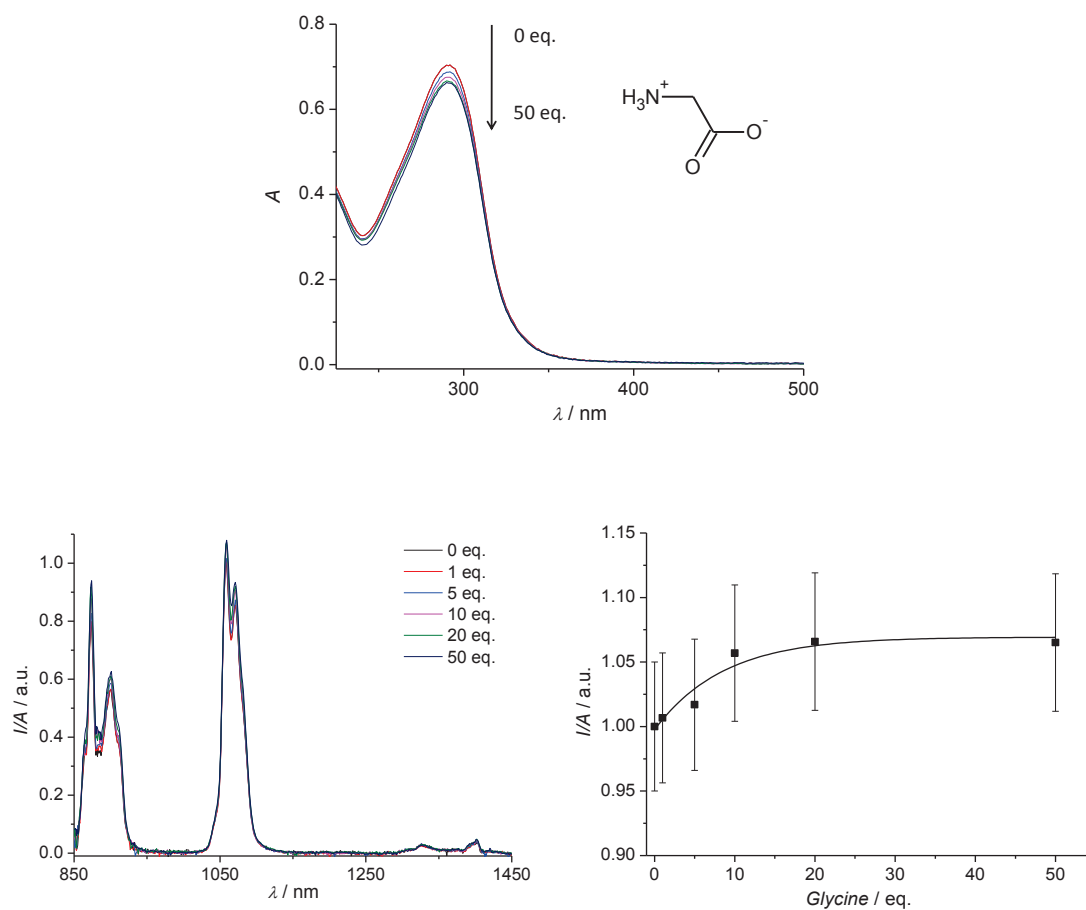
Titration of NdL⁸ with glycine

Figure 3.27: Variation of absorption (top), emission spectra (bottom left, $\lambda_{\text{ex}} = 300$ nm) and corrected luminescence intensity, I/A (bottom, right, at 1058 nm, ${}^4F_{3/2} \rightarrow {}^4I_{11/2}$ transition) of NdL⁸ upon titration with **glycine** (100 μM complex, room temperature).

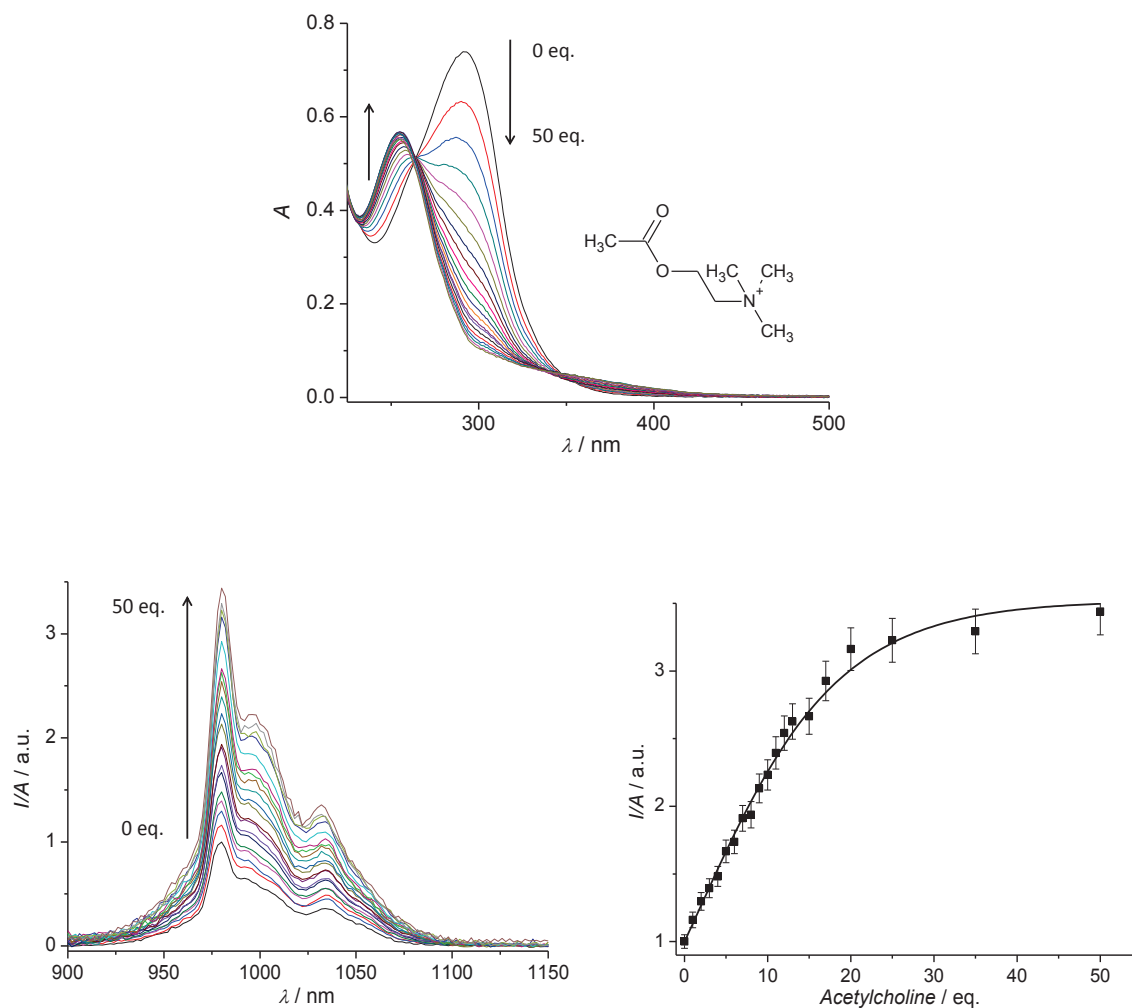
Titration of YbL⁸ with acetylcholine

Figure 3.28: Variation of absorption (top), emission spectra (bottom left, $\lambda_{\text{ex}} = 300 \text{ nm}$) and corrected luminescence intensity, I/A (bottom, right, at 980 nm , ${}^2F_{5/2} \rightarrow {}^2F_{7/2}$ transition) of YbL⁸ upon titration with acetylcholine ($100 \mu\text{M}$ complex, room temperature).

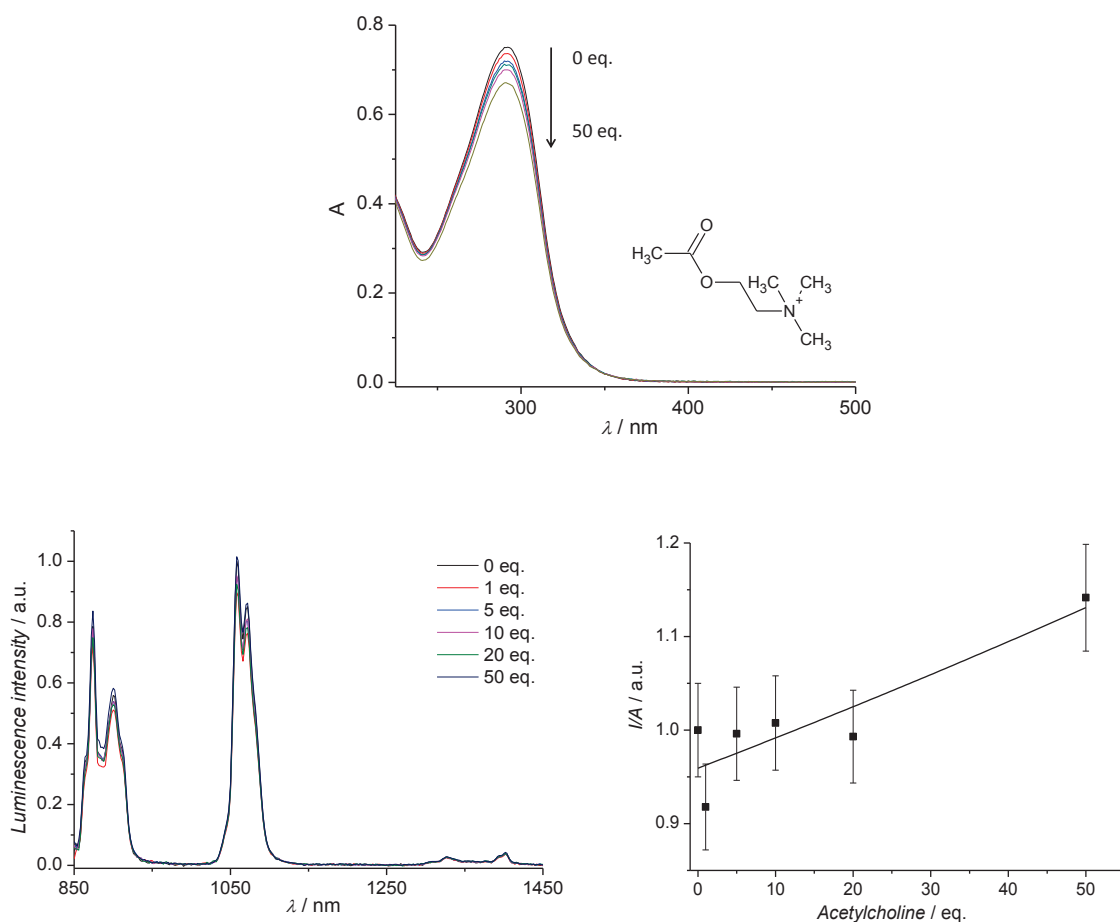
Titration of NdL⁸ with acetylcholine

Figure 3.29: Variation of absorption (top), emission spectra (bottom left, $\lambda_{\text{ex}} = 300 \text{ nm}$) and corrected luminescence intensity, I/A (bottom, right, at 1058 nm, ${}^4F_{3/2} \rightarrow {}^4I_{11/2}$ transition) of NdL⁸ upon titration with **acetylcholine** (100 μM complex, room temperature).

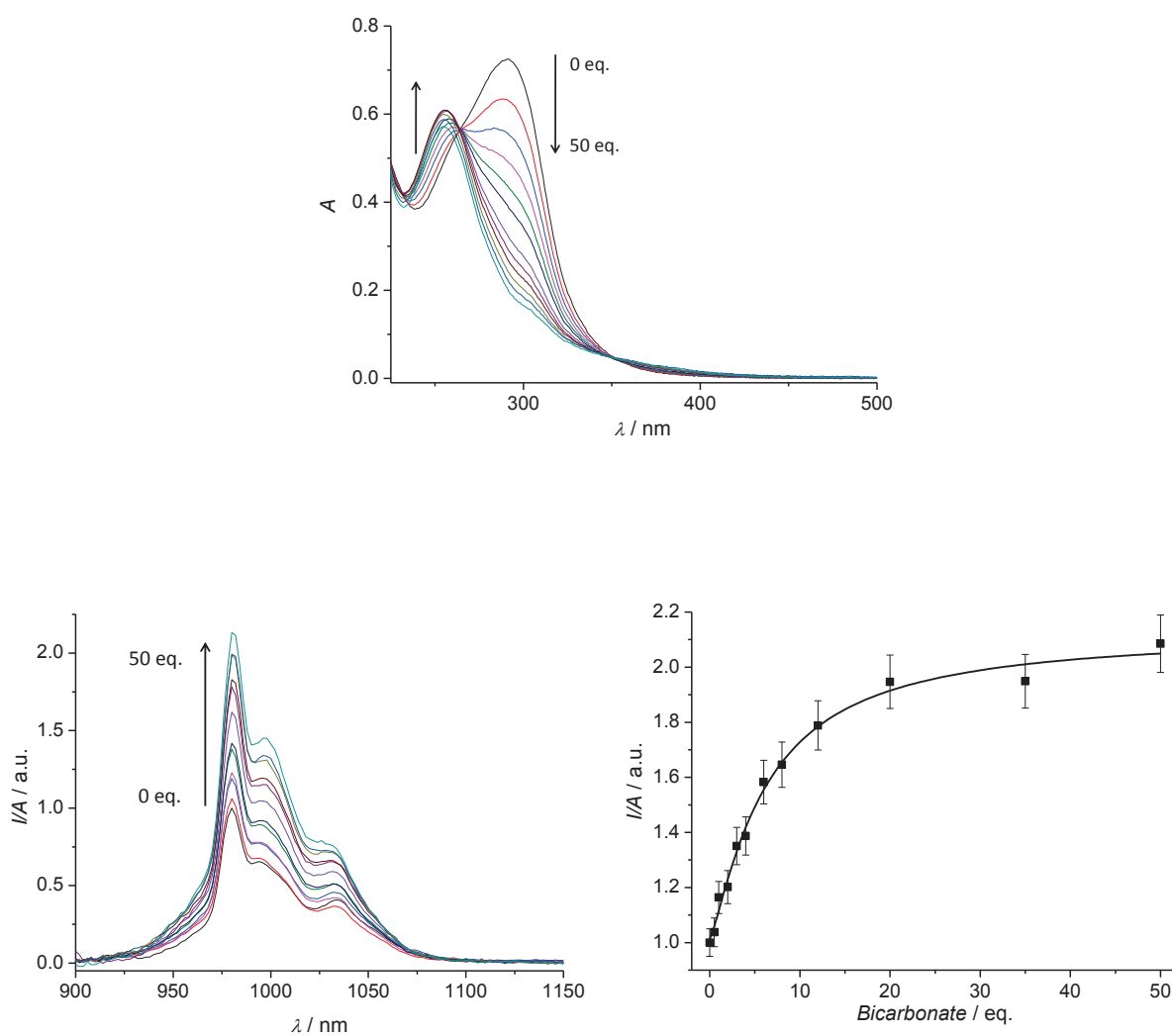
Titration of YbL^8 with hydrogen carbonate

Figure 3.30: Variation of absorption (top), emission spectra (bottom left, $\lambda_{\text{ex}} = 300 \text{ nm}$) and corrected luminescence intensity, I/A (bottom, right, at 980 nm , ${}^2\text{F}_{5/2} \rightarrow {}^2\text{F}_{7/2}$ transition) of YbL^8 upon titration with hydrogen carbonate ($42.6 \mu\text{M}$ complex, room temperature).

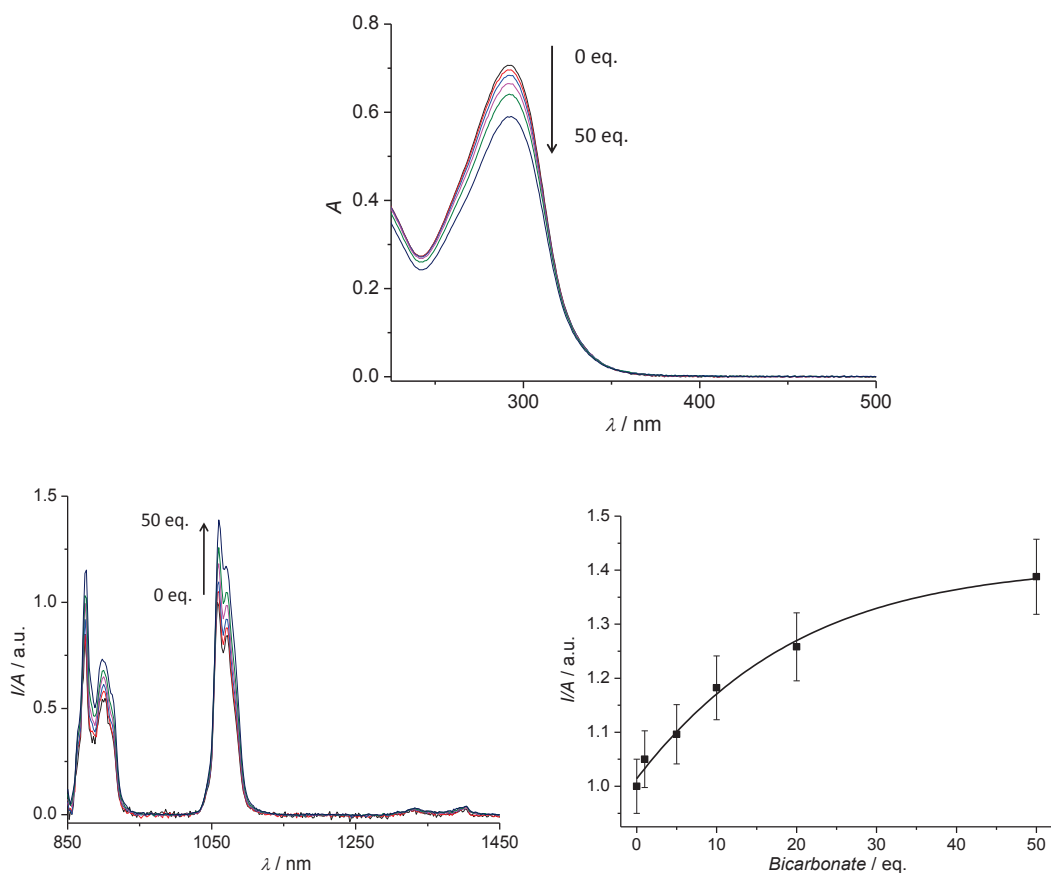
Titration of NdL⁸ with hydrogen carbonate

Figure 3.31: Variation of absorption (top), emission spectra (bottom left, $\lambda_{\text{ex}} = 300 \text{ nm}$) and corrected luminescence intensity, I/A (bottom, right, at 1058 nm , ${}^4F_{3/2} \rightarrow {}^4I_{11/2}$ transition) of NdL⁸ upon titration with **hydrogen carbonate** ($42.6 \mu\text{M}$ complex, room temperature).

YbL⁸ demonstrated a significant blue shift in the absorption spectra ($\sim 40 \text{ nm}$, figure 3.22) upon titration with KCl. The emission intensity of YbL⁸ is decreasing following the trend in the absorption spectra; however, the global efficiency is still increasing. In contrast to YbL⁸, NdL⁸ exhibited no significant variations both in absorption and emission when titrated with K⁺ (figure 3.23). We have tested that the addition of K⁺ does not affect the relaxivity of GdL⁸. A possible explanation for the observed changes in the K⁺/YbL⁸ system might be that the electron-rich

crowns ether is likely participating in a photoinduced electron transfer (PET) process [29, 30], suggesting that an intramolecular charge transfer occurs from the nitrogen lone pair of the monoaza-18-crown-6 moiety to Yb^{3+} . Yb^{3+} can be relatively easily reduced to Yb^{2+} which makes possible an electron transfer involving this lanthanide ion. Photo-induced electron transfer (PET) might occur over a distance of 10 Å [31]. The interaction of the K^+ ion with the *N*-atom lone pair quenches the photo-induced electron transfer (PET) as illustrated in the following figure:

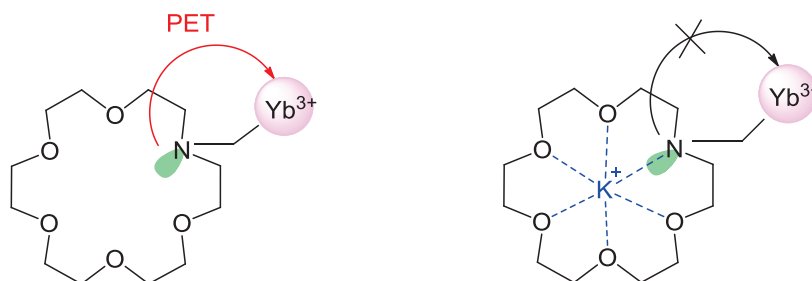


Figure 3.32: Left: Model of the photo-induced electron transfer (PET) of the amine lone pair to the Yb^{3+} ion. Right: Model of the potassium complexation involving the lone pair to prevent PET.

Nd^{3+} is not capable of showing any redox activity preventing any PET process. Assuming that the photo-induced electron transfer (PET) is responsible for the changes observed for YbL^8 upon K^+ titration, it is understandable that NdL^8 behaves differently towards the K^+ ion.

Upon titration with Glu, Gly and Ach, YbL^8 demonstrates similar results as with the K^+ ion, i.e. a blue shift in the absorption spectra (figures 3.24, 3.26 and 3.28). Emission intensity of YbL^8 is decreasing following the trend in absorption spectra; however, the global efficiency is increasing by 2-, 2.4- and 3.2-times for glutamate, glycine and acetylcholine, respectively. This enhancement of emission intensity is most likely due to the decrease in hydration number, although the quenching of the photoinduced electron transfer (PET) process upon interaction of neurotransmitters can also contribute to the increased emission intensity.

Addition of sodium bicarbonate to YbL^8 has the similar effect as the organic neurotransmitters: a blue shift in absorption spectra and an increase of the global emission intensity by ~2-fold (figure 3.30).

Dissociation constants for the interaction of YbL⁸ with glutamate, glycine, acetylcholine, hydrogen carbonate and K⁺ ions were estimated from the variation of the absorption spectra and are reported in table 3.4 (the fits using the SPECFIT program are shown in the appendix).

Table 3.4. Dissociation constants estimated from the absorption spectra for the interaction of YbL⁸ with neurotransmitters and small ions.

Analyte	Dissociation constant, K_d / mM
Glutamate	1.91(3)
Glycine	0.35 (2)
Acetylcholine	$9.1(3) \times 10^{-5}$ ^a
HCO ³⁻	0.180 (3)
K ⁺	0.0219 (3)

a: for acetylcholine, the dissociation constant refers to the dissociation of the species 1:2 YbL⁸(ACh)₂. The fit of the absorbance data was unacceptably bad when only a 1:1 species was supposed.

Intriguingly, the positively charged ACh appears to cause the largest enhancement of luminescence intensity of YbL⁸. Moreover, the fit of the absorbance data was not possible with the assumption of a single 1:1 species, and when 1:1 and 1:2 (YbL⁸:ACh) species have been assumed, the fit resulted in a unreasonably low value for the 1:1 species. Therefore, we report the dissociation constant of the 1:2 (YbL⁸:ACh) species in Table 3.4. ACh apparently is not binding extensively to the metal ion according to what was proved by the relaxometric titrations and, therefore, the emission enhancement and the absorbance changes cannot be related to a substantial change in the initial hydration state. In addition, tertiary ammoniums do not interact with 18-crown-6 ethers [32]. Thus one could speculate that the ammonium group of ACh is involved in a π -interaction with benzophenone. Interactions of cations, especially protonated tertiary amines, with aromatic residues are of considerable importance in biological recognition [33]. Previous studies have shown that ammonium cation- π interactions at the acetylcholine binding sites of the nicotinic receptor (nAChR) are significant for receptor activation with acetylcholine [34-36].

We should note that for the neurotransmitter- or hydrogencarbonate- LnL^8 ternary complexes, considerably higher (about one order of magnitude) dissociation constants from the relaxometric measurements for GdL^8 than from the absorbance data for YbL^8 . At this point, it is difficult to rationalize this difference. One obvious factor to consider is the different size of the two lanthanide ions, Gd^{3+} being larger than Yb^{3+} . Consequently, Yb^{3+} has a higher effective charge which can result in a higher stability of the ternary complexes. Indeed, even if the crown ether participates actively in the binding, the major governing force is the electrostatic effect between the positive charge of the lanthanide ion and the negative charge of the carboxylate function. One should not forget either that for YbL^8 , the dissociation constants are calculated from the absorbance data which reflects the response of the benzophenone moiety, therefore these results are less directly dependent on the ditopic binding of the neurotransmitters to the lanthanide ion and to the crown ether.

Contrary to these binding results on YbL^8 , NdL^8 demonstrated very different behavior. Variations in emission spectra of NdL^8 upon titrations are negligible, irregular and lie within experimental errors (5-10%) as shown in figures 3.23, 3.25, 3.27, 3.29 and 3.31. Only in the case of addition of sodium bicarbonate to the NdL^8 solution, we observe an emission increase of ~ 1.4 -times (figure 3.31). Given that the NdL^8 complex can not exhibit any electronic transfer involving the metal, this small change might be a result of the partial replacement of the water molecule bound to Nd^{3+} ion by the bicarbonate anion.

In overall, all these results show that the luminescence response of these complexes to different neurotransmitters, anions and cations is very variable as a function of the used lanthanide ion. It appears that the origin of the observed emission enhancement is various and is depending on the nature of added neurotransmitter or anion/cation. The emission enhancement observed with YbL^8 in the presence of Glu and Gly is likely due (i) to the quenching of a PET process involving the metal ion and (ii) to a diminution in hydration number. On the contrary, acetylcholine seems to induce none of those processes but it might be involved in π -interaction with the chromophore benzophenone. In the case of NdL^8 , the effect of removal of O-H vibrations of H_2O from the inner coordination sphere might be compensated

by the presence of C-H vibrations in the neurotransmitter molecules which also have non-negligible impact on luminescence quenching of NIR-emitting ions, as it has been observed previously [37].

More important, the non-sensitivity of NdL⁸ to neurotransmitters in contrast to YbL⁸ provides the possibility for ratiometric analysis that is independent of probe concentration. Such ratiometric approach involves using a mixture of Nd³⁺/Yb³⁺ complexes and monitoring the intensity ratio of their respective emission bands [38-40].

3.4. Conclusions:

In summary, it was possible to design and synthesize two new neurotransmitter responsive probes, for the purpose of improving both the optical properties and the binding affinity.

First, we have designed a benzophenone-containing complex that allowed not only sensitising the luminescence of the visible-emitting Eu³⁺ ion, but also that of the NIR emitting Yb³⁺ and Nd³⁺ ions. The Yb³⁺ analogue acts as a very sensitive near-infrared emitting luminescent probe responsive to neurotransmitters. The mechanism by which the luminescence emission is modulated has not yet been fully elucidated. It seems that the diminution of the hydration number upon neurotransmitter binding is not the only responsible parameter. We hypothesized that a photo-induced electron transfer occurs from the crown ether moiety to the redox-active Yb³⁺ ion, which is not operational in the case of Nd³⁺. The quenching of this photo-induced electron transfer upon neurotransmitter binding also contributes to the observed photophysical changes. From the luminescence results combined with the relaxometric data on the Gd³⁺ analogue, it appeared that the binding affinity of the LnL⁸ chelates towards neurotransmitters has decreased, in comparison to the previous complexes described in chapter 2. Additionally, these complexes were found to be much more selective towards bicarbonate.

In a parallel approach, we have introduced in our ligand design a triazacrown ether having an intrinsically better selectivity for the complexation of primary ammonium cations over K⁺. The objective of creating a probe endowed with higher sensitivity for neurotransmitters has been

achieved; however, the selectivity of GdL^9 to neurotransmitters over bicarbonate is not yet sufficient.

3.5. Experimental procedures and materials

All commercial reagents and solvents were used as received from the suppliers unless otherwise indicated. Tetrahydrofuran (THF) was freshly distilled from the sodium complex of benzophenone before use.

Analytical ^1H and ^{13}C NMR spectra were recorded on a Bruker Avance III 300 MHz spectrometer operating at 300.17 and 75.48 MHz, for ^1H and ^{13}C , respectively. All experiments were performed at 25 °C.

Chromatographic methods: Flash column chromatography was performed using flash silica gel 60 (70-230 mesh ASTM). Analytical thin layer chromatography (TLC) was performed on aluminum sheet silica gel plates with silica gel 60 F254 (Merck). The compounds were visualized by UV254 light and/or developed with dragendorff stain. Purification using reversed phase HPLC was on a Varian PrepStar Instrument, Australia, equipped with PrepStar SD-1 pump heads. UV absorbance was measured using a ProStar 335 photodiode array detector at 214 nm and 254 nm. This detector is equipped with a dual-path length flow cell which enables measurement of absorption of analytical and preparative samples without changing the flow cell. Reversed-phase analytical HPLC was performed in a stainless steel Chromsep (length 250 mm, internal diameter 4.6 mm, outside diameter 3/8 inch and particle size 8 μm) C18 column and preparative HPLC was performed in a stainless steel Chromsep (length 250 mm, internal diameter 41.4 mm, outside diameter 2 inch and particle size 8 μm) C18 column (Varian, Advanced Chromatographic Solutions).

Electrospray ionization mass spectrometry (ESI-MS) spectra were performed on an SL 1100 system (Agilent) with ion trap detection in the positive and negative ion modes. FT-ICR-MS were performed on a Bruker FT-ICR Apex II spectrometer Agilent (Germany).

^{17}O NMR Measurements. Variable temperature ^{17}O NMR measurements on aqueous solution of the Gd^{3+} complexes were obtained on a Bruker Avance 500 (11.75 T, 67.8 MHz) spectrometer. The temperature was calculated according to a previous calibration with ethylene glycol and MeOH [41]. Acidified water (HClO_4 , $\text{pH}\sim 4$) was used as an external reference. Longitudinal ^{17}O relaxation times T_1 were measured by the inversion-recovery pulse

sequence[42], and the transverse relaxation times (T_2) were obtained by the Carr-Purcell-Meiboom-Gill spin-echo technique [43]. Analysis of the ^{17}O NMR experimental data was performed with the Scientist[®] software. To eliminate the susceptibility corrections to the chemical shift [44], the samples were placed in a glass sphere fixed in a 10 mm NMR tube. For sufficient accuracy, at least 20 mM concentration of the Gd^{3+} complex has been used. To improve sensitivity, the amount of ^{17}O was enriched by adding H_2^{17}O (10% H_2^{17}O , CortecNet) to achieve approximately 1% ^{17}O content in the sample.

Luminescence measurements on EuL⁸. For luminescence emission titration of **EuL⁸**, 50 μM complex aqueous solution was introduced as triplicate (for each neurotransmitter) in a 96-well plate. Neurotransmitters and HCO_3^- were added stepwise to each well and the plate was shaken for 30 seconds. The luminescence was measured shortly at 610 nm in a microplate reader.

Photophysical measurements on YbL⁸ and NdL⁸. 100 μM solutions in HEPES buffer were used. Absorption spectra were measured on a UVICON XL spectrophotometer from Secomam using quartz Suprasil cells (Hellma[®] 115F-QS, bandpass 0.2 cm). For collecting luminescence data samples were placed into 2.4 mm i.d. quartz capillaries or quartz Suprasil cells. Emission and excitation spectra were measured on a Horiba-Jobin-Yvon Fluorolog 3 spectrofluorimeter equipped with visible (220-800 nm, a photon-counting unit R928P) and NIR (800-1600 nm, a DSS-IGA020L Jobin-Yvon solid-state InGaAs detector cooled to 77 K) detectors. All spectra were corrected for the instrumental functions. Luminescence lifetimes were determined under excitation at 355 nm provided by a YG 980 Quantel Nd:YAG laser while the signal was detected in the near-infrared range (950-1450 nm, a photon-counting unit H10330-45 from Hamamatsu). The output signal from the detectors was then fed to a Tektronix TDS 754C 500MHz bandpass digital oscilloscope and then transferred to a PC for treatment with Origin 8[®]. Lifetimes are averages of at least three independent measurements. Quantum yields in the NIR were determined with a Fluorolog 3 spectrofluorimeter according to a comparative method with Nd^{3+} tropolonate ($Q = 0.21\%$ in DMSO under excitation at 340 nm) using an integration sphere (GMP SA). Each sample was measured several times under slightly different experimental conditions. Estimated experimental error for quantum yields determination is 10 %.

Neurotransmitter Binding Studies. Ternary complex formation with neurotransmitters was assessed by performing relaxometric titrations at 37°C on a Stellar SMARTracer Fast Field Cycling NMR relaxometer at 37 °C (60 MHz) or on a Bruker AvanceIII 300 MHz spectrometer. The pH was maintained by a 25 mM HEPES buffer. A HEPES buffered solution of the neurotransmitter was added stepwise to the 1-2 mM GdL complex solutions of up to at least 100 equivalents. The concentration of the Gd³⁺ solutions was determined by bulk magnetic susceptibility method (BMS) using *tert*-butanol enriched samples [42]. The dissociation constants were determined according to the following equations where the paramagnetic relaxation rate $1/T_{1para}$ is the sum of the contributions originating from the free GdL complex and the GdL-analyte adduct (GdLA). The $1/T_{1para}$ values measured as a function of the analyte (neurotransmitter) concentrations have been fitted to the equations below:

$$1/T_{1para} = \left(r_1^{GdLA} \times Z + (c_{GdL} - Z) \times r_1^{GdL} \right) \times 1000$$

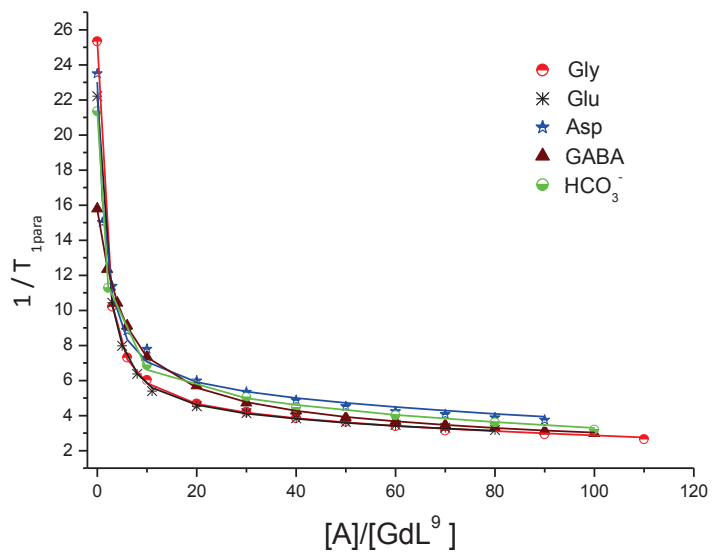
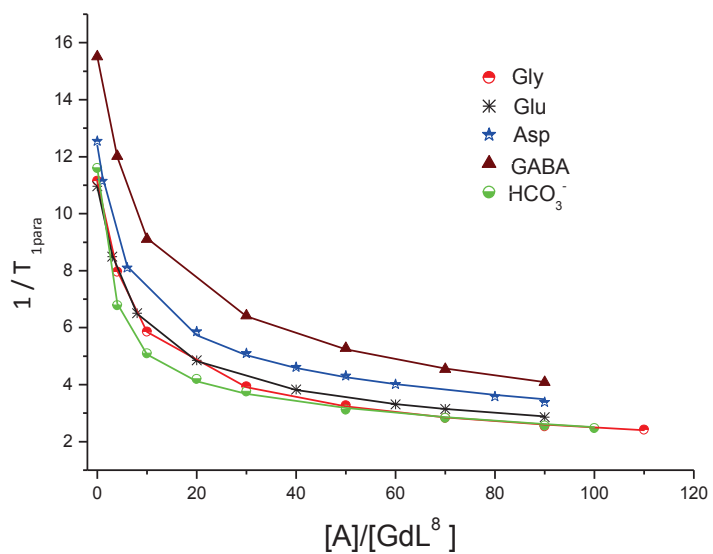
Where

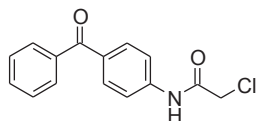
$$Z = \frac{\left(K_d + c_{GdL} + c_A \right) + \sqrt{\left(K_d + c_{GdL} + c_A \right)^2 - 4(c_A \times c_{GdL})}}{2}$$

The dissociation constant is defined as:

$$K_d = \frac{[A] \times [GdL]}{[GdLA]}$$

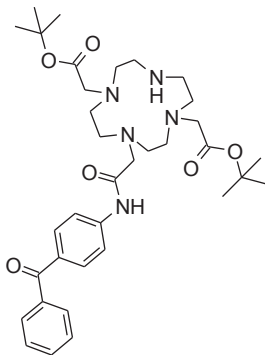
where r_1^{GdL} and r_1^{GdLA} are the relaxivities of the free complex and the fully bound complex, respectively. K_d is the dissociation constant, C_{GdL} and C_{CA} represent the concentrations of both GdL and analyte. Both K_d and r_1^{GdLA} have been obtained through a two parameter fitting of the relaxation rate data measured at various analyte concentrations. Representative fits are shown below for GdL⁸ and GdL⁹.



Synthesis:**N-(2-Benzoyl-phenyl)-2-chloro-acetamide**

To a stirred solution of 4-aminobenzophenone (5.0 g, 18.3 mmol) and triethylamine (5.30 mL, 27.4 mmol) in dry CH₂Cl₂ was slowly added over 30 minutes 2-chloroacetyl chloride (2.21 mL, 27.8 mmol) in dry CH₂Cl₂. After 24 hours the organic phase was washed with hydrochloric acid, water and dried over Na₂SO₄. Removal of the solvent yielded a dark purple oil (7.28 g) which was purified using column chromatography (hexane:ethyl acetate) and recrystallised from hot hexane: ethyl acetate to obtain orange crystals (4.38 g, 63%).

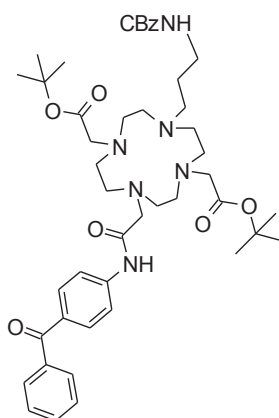
¹H NMR (CDCl₃, 300 MHz), δ: 8.39 (s, 1H, NH), 7.88-7.47 (m, 9H, Ar-H), 4.06 (s, 2H, CH₂). ¹³C NMR (CDCl₃, 75 MHz), δ: 195.5 (CO), 163.7 (COCH₂), 140.7 (Cq), 137.6 (Cq), 133.9 (Cq), 132.4, 131.5, 129.9, 128.3, 119.1, 29.3 (CH₂Cl). Mass Spectrometry (ESI): calculated for C₁₅H₁₃ClNO₂⁺ [M+H]⁺: 274.1; Found 274.1 .

di-tert-butyl 2,2'-(4-(2-((4-benzoylphenyl)amino)-2-oxoethyl)-1,4,7,10-tetraazacyclododecane-1,7-diyl)diacetate (12)

DO2A-^tBu **1** (7.78g, 19.4 mmol) was dissolved in a mixture of water/dioxane 1:1. The pH was adjusted to 8 before adding Benzophenone chloroacetamide (5.32 g, 19.4 mmol) in one portion. The pH was kept between 7 and 8 until the starting materials could no longer be observed by TLC. The product was then extracted into dichloromethane, washed with water and dried over Na₂SO₄. Removal of the solvents yielded the crude product which was recrystallized from hot hexane-ethyl acetate to yield the **12** as white crystals (10.1 g, 82%).

^1H NMR (CDCl_3 , 300 MHz), δ : 10.25 (s, 1H, NH), 7.96-7.41 (m, 9H, Ar-H), 3.53 (s, 2H, CH_2CONH), 3.30 (s, 4H, $2\text{CH}_2\text{COO}$), 3.08 (s, 4H), 2.92 (s, 4H), 2.84 (s, 8H), 1.38 (s, 18H, $\text{C}(\text{CH}_3)_3$). **^{13}C NMR (CDCl_3 , 75 MHz), δ :** 195.4 (CO), 170.3 (2COO), 142.2 (Cq), 137.7 (Cq), 132.6 (Cq), 132.1, 131.5, 129.7, 128.1, 128.0, 118.6, 81.7 ($\text{C}(\text{CH}_3)_3$), 57.4, 55.5, 54.6, 52.2, 49.5, 47.1, 28.0 ($\text{C}(\text{CH}_3)_3$). **HRMS (ESI):** calculated for $\text{C}_{35}\text{H}_{52}\text{N}_5\text{O}_6^+$ $[\text{M}+\text{H}]^+$: 638.3912; Found 638.3913.

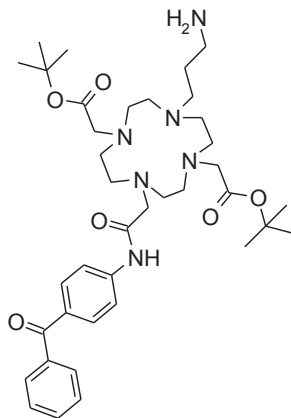
di-tert-butyl 2,2'-(4-(2-((4-benzoylphenyl)amino)-2-oxoethyl)-10-(3-(((benzyloxy)carbonyl)amino)propyl)-1,4,7,10-tetraazacyclododecane-1,7-diyl)diacetate



A solution of **12** (8.77 g, 13.7 mmol) and 3-[(Benzyloxycarbonyl)amino]propionaldehyde (7.12 g, 34.4 mmol) in dry THF was stirred at room temperature over 4 Å molecular sieves for 2 hours. Sodium triacetoxyborohydride (7.29 g, 34.4 mmol) was added and the mixture was stirred for further 24 hours. Sieves were removed by filtration and the filtrate was concentrated under reduced pressure. The resulting oil was triturated several times with hexane to remove the excess of reduced aldehyde and filtered to afford the desired compound as a yellow solid (9.8 g, 86%).

^1H NMR (CDCl_3 , 300 MHz), δ : 7.85-7.34 (m, 9H, Ar-H), 7.23 (s, 5H, Ar-H of Cbz), 4.99 (s, 2H, CH_2Ph), 3.20 (s, 2H), 3.07 (s, 4H), 2.81 (s, 2H), 2.69 (s, 6H), 2.51 (s, 8H), 1.90 (s, 2H), 1.59-1.64 (m, 2H, $\text{CH}_2\text{CH}_2\text{NHCO}$), 1.30 (s, 18H, $\text{C}(\text{CH}_3)_3$). **HRMS (ESI):** calculated for $\text{C}_{46}\text{H}_{64}\text{N}_6\text{O}_8\text{Na}^+$ $[\text{M}+\text{Na}]^+$: 851.4678; Found 851.4676.

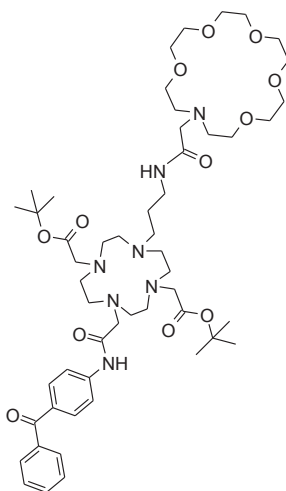
di-tert-butyl 2,2'-(4-(3-aminopropyl)-10-(2-((4-benzoylphenyl)amino)-2-oxoethyl)-1,4,7,10-tetraazacyclododecane-1,7-diyl)diacetate (13)



10% Pd/C (1.8 g) was added to a solution of the above Cbz-protected compound (9.11g, 10.9 mmol) in ethanol. The resulting mixture was stirred at room temperature under 1 atm of H₂ for overnight. The reaction was then filtered over celite® to remove the palladium catalyst and the solvent was removed by rotary evaporation. The residue was dissolved in CH₂Cl₂ and washed three times with water. The organic layer was dried over Na₂SO₄ and then evaporated to yield 7.64 g of a yellow powder, which was used for the next step without further purification.

HRMS (ESI): calculated for C₃₈H₅₉N₆O₆⁺ [M+H]⁺: 695.4490; Found 695.4492.

di-tert-butyl 2,2'-(4-(3-(2-(1,4,7,10,13-pentaoxa-16-azacyclooctadecan-16-yl)acetamido)propyl)-10-(2-((4-benzoylphenyl)amino)-2-oxoethyl)-1,4,7,10-tetraazacyclododecane-1,7-diyl)diacetate

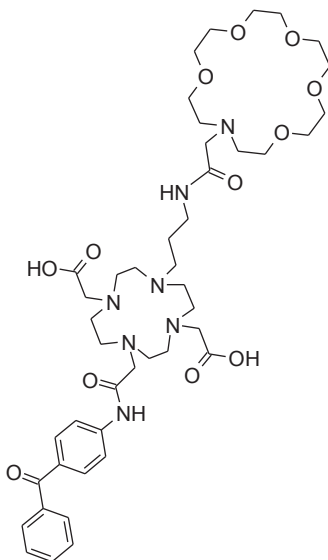


The crude of compound **13** (0.63 g, 0.91 mmol) was added to a stirred solution of **6** (0.29 g, 0.91 mmol) and HBTU (0.69 g, 1.81 mmol) in dry 20 mL of DMF at room temperature. After stirring at room temperature overnight, the DMF was evaporated and the residue was taken up with a mixture of CH₂Cl₂:H₂O. The aqueous layer was separated and extracted twice with CH₂Cl₂. The organic layer was washed dried over Na₂SO₄ and then evaporated to give a brown gum which was purified on column chromatography (silica gel, 3% MeOH/CH₂Cl₂) to give a yellow solid (0.57 g, 62%).

¹H NMR (CDCl₃, 300 MHz), δ: 7.78-6.74 (m, 6H, Ar-H), 7.56 (t, *J*=7.2 Hz, 1H, Ar-H), 7.46 (t, *J*=7.5, 2H, Ar-H), 3.74-3.30 (overlapping m, 36H), 2.98-2.63 (m, 16H), 2.00 (br. s, 2H), 1.43 (18H, C(CH₃)₃). **¹³C NMR (CDCl₃, 75 MHz)**, δ: 195.5, 169.8, 169.5, 142.3 (Ar-C_q), 137.7 (Ar-C_q), 132.2, 131.9, 131.2, 129.6, 128.1, 118.6, 81.7 (C(CH₃)₃), 70.3, 70.1, 69.8, 69.3, 68.2, 66.8, 56.7, 56.7, 56.1, 55.4, 53.5, 51.7, 50.2, 49.6, 47.2, 36.5 (CH₂CH₂NHCO), 27.9 (C(CH₃)₃), 23.5 (CH₂CH₂NHCO).

HRMS (ESI): calculated for C₅₂H₈₄N₇O₁₂⁺ [M+H]⁺: 998.6172; Found 998.6200.

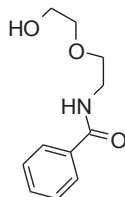
2,2'-(4-(3-(2-(1,4,7,10,13-pentaoxa-16-azacyclooctadecan-16-yl)acetamido)propyl)-10-(2-((4-benzoylphenyl)amino)-2-oxoethyl)-1,4,7,10-tetraazacyclododecane-1,7-diyl)diacetic acid (L⁸)



The above compound (1.1 g, 1.10 mmol) was dissolved in formic acid and stirred at 60°C overnight. The complete removal of the ^tBu protecting groups was monitored by mass spectrometry, and the excess of formic acid was evaporated under reduced pressure. The crude residue was dissolved in 10% CH₃CN in water and filtered through a 0.45 μm filter. The pH was adjusted to 2-3 and the product was purified by HPLC and then lyophilized to isolate a white hygroscopic solid (0.6 g, 61%).

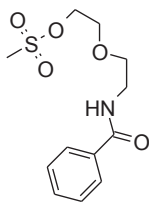
¹H NMR (D₂O, 300 MHz), δ: 7.80-7.57 (m, 7H, Ar-H), 7.59 (m, 2H, Ar-H), 3.96 (s, 2H), 3.90 (s, 4H), 3.75 (m, 4H), 3.66-3.63 (overlapping m, 20H), 3.52-3.50 (m, 6H), 3.44-3.40 (m, 4H), 3.26-2.97 (m, 10 H), 2.66 (m, 2H, CH₂(CH₂)₂NHCO), 1.76-1.67 (m, 2H, CH₂CH₂NHCO). **¹³C NMR (D₂O, 75 MHz)**, δ: 201.3, 173.5, 173.2, 172.3, 167.7, 145.5, 139.6, 136.1, 134.7, 134.4, 132.9, 131.4, 121.9, 72.6, 72.5, 72.3, 72.2, 66.5, 59.6, 57.9, 57.7, 54.4, 54.1, 53.6, 52.5, 51.0, 50.9, 40.2, 31.1, 28.5. **HRMS (ESI)**: calculated for C₄₄H₆₇N₇O₁₂Na⁺ [M+Na]⁺: 908.4740; Found 908.4739.

N-(2-(2-hydroxyethoxy)ethyl)benzamide (15)



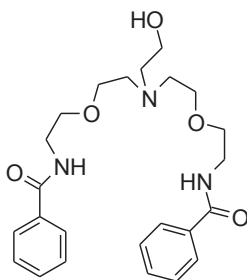
Benzoic anhydride (20 g, 88 mmol) was slowly added to 2-(2-aminoethoxy)ethanol (8.8 mL, 88mol) in ethanol at 0°C. This mixture was refluxed for 2 days and monitored with TLC. The mixture was evaporated under reduced pressure, and the residue was dissolved in 400 mL of 5% aqueous sodium carbonate and was extracted 2 times CH₂Cl₂. The CH₂Cl₂ layer were dried over anhydrous sodium sulfate, filtered, and evaporated under reduced pressure to give **15** as colorless oil (15.8 g, 86%).

¹H NMR (CDCl₃, 300 MHz), δ: 7.81-7.75 (m, 2H, Ar-H), 7.49-7.36 (m, 3H, Ar-H), 7.00 (s, 1H, NH), 3.77-3.69 (m, 2H, CH₂OH), 3.67-3.62 (overlapping m, 4H, CH₂NH and CH₂O), 3.60-3.55 (m, 2H, CH₂CH₂OH). **¹³C NMR (CDCl₃, 75 MHz)**, δ: 167.7 (CO), 134.3, 131.4, 128.4, 126.9, 72.2 (CH₂CH₂OH), 69.8 (CH₂O), 61.6 (CH₂OH), 39.7 (CH₂NH).

2-(2-benzamidoethoxy)ethyl methanesulfonate (16)

Methanesulfonyl chloride (7.1 mL, 91 mmol) was added dropwise to a solution of **15** (15.8g, 76 mmol) and triethylamine (21.1 mL, 151 mmol) in dry CH₂Cl₂ while keeping the temperature below 0°C. After completion of addition, the mixture was stirred further 2 hours at room temperature. Water was added to quench the reaction and the two layers were separated. The organic layer was washed twice with an aqueous solution 1N HCl and once with water, dried over Na₂SO₄ and the solvent removed under reduced pressure. The oily residue was triturated in hexane to yield a white precipitate (19.5g, 90%).

¹H NMR (CDCl₃, 300 MHz), δ: 7.83-7.78 (m, 2H, Ar-H), 7.51-7.39 (m, 3H, Ar-H), 6.83 (s, 1H, NH), 4.39-4.35 (m, 2H, CH₂OMs), 3.77-3.73 (m, 2H, CH₂CH₂OMs), 3.67 (br. s, 4H, CH₂NH and CH₂O), 2.99 (s, 3H, CH₃). **¹³C NMR (CDCl₃, 75 MHz)**, δ: 167.5 (CO), 134.2, 131.4, 128.4, 126.9, 69.8 (CH₂OMs), 68.7 (CH₂O), 68.6 (CH₂O), 39.5 (CH₂NH), 37.6 (CH₃). **LRMS (ESI)**: calculated for C₁₂H₁₈NO₅S⁺ [M+H]⁺: 288.1; Found 287.9.

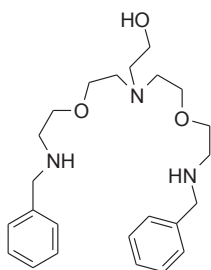
N,N'-((((2-hydroxyethyl)azanediyl)bis(ethane-2,1-diyl))bis(oxy))bis(ethane-2,1-diyl) dibenzamide (19)

Compound **16** (5g, 17.4 mmol), ethanolamine (0.53 mL, 8.7 mmol) and triethylamine (9.7 mL, 69.6 mmol) in acetonitrile was refluxed for 24 hours. The solvent was removed under reduced pressure and the residue was dissolved in 5% Na₂CO₃ aqueous solution and extracted with CH₂Cl₂ twice. The organic layer was dried over Na₂SO₄ and the solvent removed under reduced

pressure. The crude was purified by Chromatography on alumina (2% MeOH/CH₂Cl₂) to give 3.1 g of pale yellow oil (83%).

¹H NMR (CDCl₃, 300 MHz), δ: 7.76-7.72 (m, 4H, Ar-H), 7.37-7.24 (m, 8H, Ar-H & 2NH), 6.83 (s, 1H, NH), 3.49-3.44 (m, 8H, 2CH₂O & 2CH₂NHCO), 3.40-3.36 (m, 6H, 2CH₂O & CH₂OH), 3.65 (t, *J*=5.4 Hz, 4H, 2CH₂CH₂N), 2.59 (t, *J*=5.4 Hz, 2H, CH₂CH₂OH). **¹³C NMR (CDCl₃, 75 MHz)**, δ: 167.3 (CO), 134.2, 131.0, 128.1, 126.8, 69.4 (2CH₂O), 69.2 (2CH₂O), 58.6 (CH₂OH), 55.7 (CH₂CH₂OH), 54.1 (2CH₂N), 39.5 (2CH₂NHCO). **HRMS (ESI)**: calculated for C₂₄H₃₄N₃O₅⁺ [M+H]⁺: 444.2493; Found 444.2497.

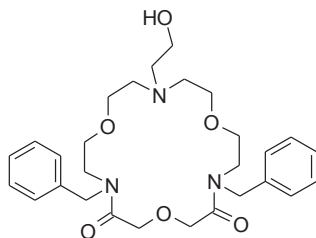
2-(bis(2-(2-(benzylamino)ethoxy)ethyl)amino)ethanol (20)



Compound **19** (9.38g, 21.1mmol) was slowly added as a solution in dry THF to a stirred suspension of LiAlH₄ (5.7 g, 63.4 mmol) in dry THF. The reaction was stirred overnight at reflux temperature and was allowed to cool to room temperature. The excess of LiAlH₄ was neutralised by adding cautiously 15 ml of water followed by 1N NaOH aq. Solution (15 mL). Na₂SO₄ was added and the mixture was stirred for an additional 2 hours, filtered and the solvent removed. The residue was taken up with ether and the precipitate was filtered off. The solvent was evaporated to give 7.1 g of colorless oil (87%) which was used for the next step without any further purification.

¹H NMR (CDCl₃, 300 MHz), δ: 7.28-7.10 (m, 10H, Ar-H), 3.71 (s, 4H, 2CH₂Ph), 3.46 (t, *J*=5.7 Hz, 4H, 2CH₂O), 3.44-3.37 (overlapping m, 6H, 2CH₂O & CH₂OH), 2.72-2.63 (m, 8H, 4CH₂N), 2.59 (t, *J*=5.1 Hz, 2H, CH₂CH₂OH). **¹³C NMR (CDCl₃, 75 MHz)**, δ: 140.1, 128.2, 128.0, 126.7, 70.24 (2CH₂O), 69.3 (2CH₂O), 59.2 (CH₂OH), 56.8 (CH₂CH₂OH), 54.1 (2CH₂N), 53.7 (2CH₂Ph), 39.5 (2CH₂NH). **HRMS (ESI)**: calculated for C₂₄H₃₈N₃O₃⁺ [M+H]⁺: 416.2907; Found 416.2908.

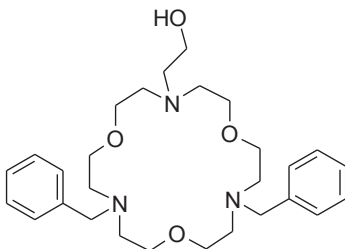
4,16-dibenzyl-10-(2-hydroxyethyl)-1,7,13-trioxa-4,10,16-triazacyclooctadecane-3,17-dione (21)



Diglycolyl chloride (1.72mL, 14.4 mmol) and **20** (6g,14.4 mmol) each dissolved in dry CH₂Cl₂ (150mL), were placed in dropping funnels, and over a period of 8 hours were simultaneously dripped into a stirred solution of triethylamine (11.5 mL, 82 mmol) in 500 mL of dry CH₂Cl₂ at 0°C under an inert atmosphere. After completion of addition, the mixture was stirred for further 2 hours at room temperature and the reaction was quenched with 5% Na₂CO₃ aq. solution. The aqueous layer was separated and extracted twice with CH₂Cl₂. The combined organic layers were dried over Na₂SO₄ and evaporated under reduced pressure to give the product which was used for next step without further purification.

¹H NMR (CDCl₃, 300 MHz), δ: 7.39-7.02 (m, 10H), 4.64-3.18 (m, 6H), 4.64-3.18 (overlapping m, 16H), 2.72-2.49 (overlapping m, 6H). **HRMS (ESI)**: calculated for C₂₈H₄₀N₃O₆⁺ [M+H]⁺: 514.2911; Found 514.2910.

2-(10,16-dibenzyl-1,7,13-trioxa-4,10,16-triazacyclooctadecan-4-yl)ethanol (22)

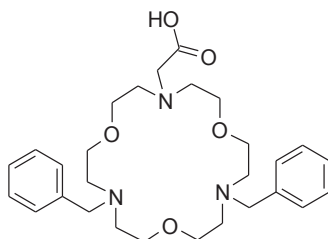


Compound **21** (6.70g, 13.1 mmol) was slowly added as a solution in dry CH₂Cl₂ to a stirred suspension of LiAlH₄ (1.48 g, 63.4 mmol) in THF. The reaction was stirred overnight at reflux temperature and was allowed to cool to room temperature. The excess of lithium aluminium

hydride was neutralised by adding cautiously 5 ml of water. Na_2SO_4 was added and the mixture was stirred for an additional 2 hours, filtered and the solvent removed. The residue was purified by flash chromatography on alumina ($\text{CH}_2\text{Cl}_2 \rightarrow \text{CH}_2\text{Cl}_2/\text{AcOEt}$ 1:1) to give 4.3g of the title compound as light yellow oil (66.3 % over two steps).

$^1\text{H NMR}$ (CDCl_3 , 300 MHz), δ : 7.30-7.09 (m, 10H, Ar-H), 3.57 (s, 4H, $2\text{CH}_2\text{Ph}$), 3.53-3.38 (m, 14H), 2.77-2.60 (m, 12H), 2.57 (t, $J=5.1$ Hz, $\text{CH}_2\text{CH}_2\text{OH}$). $^{13}\text{C NMR}$ (CDCl_3 , 75 MHz), δ : 139.5, 128.6, 128.0, 126.7, 69.8, 69.7, 59.7, 59.2, 56.8, 54.8, 53.8, 53.7. **HRMS (ESI)**: calculated for $\text{C}_{28}\text{H}_{44}\text{N}_3\text{O}_4^+$ $[\text{M}+\text{H}]^+$: 486.3326; Found 486.3323.

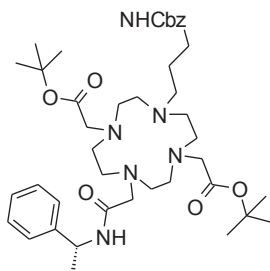
2-(10,16-dibenzyl-1,7,13-trioxa-4,10,16-triazacyclooctadecan-4-yl)acetic acid (**23**)



A solution of chromium trioxide (0.29 g, 2.96 mmol) in 6 mL of 1.5M solution of H_2SO_4 was maintained between 5-10°C while a solution of **22** (0.36 g, 0.74 mmol) in acetone was added slowly. The mixture was stirred overnight at room temperature. The solvent was removed and the crude compound was purified by HPLC to give a pale green solid (0.19 g, 52%).

$^1\text{H NMR}$ (D_2O , 500 MHz), δ : 7.54-7.46 (m, 10H, Ar-H), 4.43 (s, 4H, $2\text{CH}_2\text{Ph}$), 3.93-3.80 (br. m, 14H, $6\text{CH}_2\text{O}$ & CH_2COO), 3.55 (br. s, 4H), 3.46 (br. s, 8H). $^{13}\text{C NMR}$ (D_2O , 125 MHz), δ : 170.5, 131.8, 130.5, 129.4, 127.7, 64.2, 63.7, 57.2, 55.3, 55.1, 52.4, 52.1. **HRMS (ESI)**: calculated for $\text{C}_{28}\text{H}_{42}\text{N}_3\text{O}_5^+$ $[\text{M}+\text{H}^+]$: 500.3118; Found 500.3113.

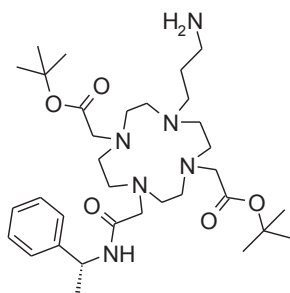
(R)-di-tert-butyl 2,2'-(4-(3-(((benzyloxy)carbonyl)amino)propyl)-10-(2-oxo-2-((1-phenylethyl)amino)ethyl)-1,4,7,10-tetraazacyclododecane-1,7-diyl)diacetate (24)



A solution of **2** (2.08 g, 3.70 mmol) and 3-[[Benzyloxycarbonyl]amino]propionaldehyde (1.5 g, 3.70 mmol) in dry THF was stirred at room temperature over 4 Å molecular sieves for 2 hours. Sodium triacetoxyborohydride (1.57 g, 7.41 mmol) was added and the mixture was stirred for further 24 hours. Sieves were removed by filtration and the filtrate was concentrated under reduced pressure. The resulting oil was triturated several times with hexane to remove the excess of reduced aldehyde and filtered to afford **24** as a yellow solid (2.1 g, 75%).

HRMS (ESI): calculated for $C_{39}H_{67}N_7O_{11}^+$ [$M+H^+$]: 753.4909; Found 753.4902.

(R)-di-tert-butyl 2,2'-(4-(3-aminopropyl)-10-(2-oxo-2-((1-phenylethyl)amino)ethyl)-1,4,7,10-tetraazacyclododecane-1,7-diyl)diacetate (25)

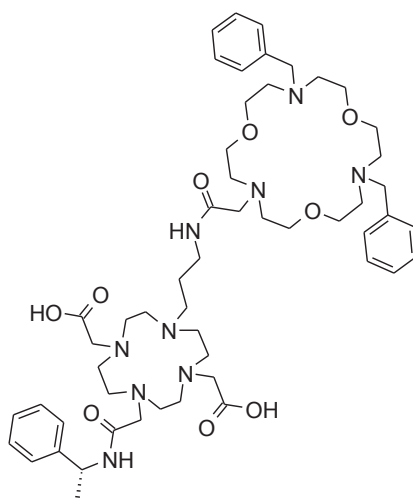


10% Pd/C (0.3 g) was added to a solution of **24** (2.0 g, 2.66 mmol) in ethanol. The resulting mixture was stirred at room temperature under 1 atm of H_2 for overnight. The reaction was then filtered over celite® to remove the palladium catalyst and the solvent was removed by

rotary evaporation. The residue was dissolved in CH_2Cl_2 and the precipitate was removed by filtration. The organic layer was dried over Na_2SO_4 and then evaporated to give 1.5 g of a yellow powder, which was used for the next step without further purification.

$^1\text{H NMR}$ (CDCl_3 , 300 MHz), δ : 7.42-7.33 (m, 2H, Ar-H), 7.20 (t, $J=7.2$ Hz, 2H, Ar-H), 7.11 (t, $J=7.2$ Hz, 1H, Ar-H), 4.97 (dq, $J=6.9$ Hz, 1H, CHCH_3), 3.59-2.10 (overlapping m, 28H), 1.50 (d, $J=7.2$ Hz, 3H, CHCH_3), 1.38 (s, 18H, $\text{C}(\text{CH}_3)_3$). $^{13}\text{C NMR}$ (CDCl_3 , 75 MHz), δ : 171.1 (2CO), 169.8 (CONH), 144.5 (Ar-Cq), 128.0 (Ar-CH), 126.3 (Ar-CH), 126.1 (Ar-CH), 81.6 ($2\text{C}(\text{CH}_3)_3$), 58.3, 56.2, 50.27, 50.0, 49.4, 49.3, 38.6 (CH_2NH_2), 29.4 ($\text{CH}_2\text{CH}_2\text{NH}_2$), 27.9 ($\text{CH}_2(\text{CH}_2)_2\text{NH}_2$), 27.8 ($2\text{C}(\text{CH}_3)_3$), 22.3 (CHCH_3). **HRMS (ESI)**: calculated for $\text{C}_{33}\text{H}_{59}\text{N}_6\text{O}_5^+$ $[\text{M}+\text{H}]^+$: 619.4541; Found 619.4542.

(R)-2,2'-(4-(3-(2-(10,16-dibenzyl-1,7,13-trioxa-4,10,16-triazacyclooctadecan-4-yl)acetamido)propyl)-10-(2-oxo-2-((1-phenylethyl)amino)ethyl)-1,4,7,10-tetraazacyclododecane-1,7-diyl)diacetic acid (L^9)



Compound **25** (0.28 g, 0.46 mmol) was added to a stirred solution of **23** (0.32 g, 0.46 mmol) and HBTU (0.35 g, 0.92 mmol) in dry 20 mL of DMF at room temperature. After stirring at room temperature overnight, the DMF was evaporated and the residue was taken up with a mixture of $\text{CH}_2\text{Cl}_2:\text{H}_2\text{O}$. The aqueous layer was separated and extracted twice with CH_2Cl_2 . The organic layer was washed dried over Na_2SO_4 and then evaporated to give the crude that, without further purification, was deprotected following a similar protocol used for the preparation of L^8 and it afforded of L^9 as a white solid (0.26 g, 38%) after purification by HPLC.

^1H NMR (D_2O , 300 MHz), δ : 7.52-7.43 (m, 9H, Ar-H), 7.41-7.25 (m, 6H, Ar-H), 4.89 (q, $J=7.2$ Hz, 1H, CHCH_3), 4.24 (br. s, 4H), 3.70 (overlapping m, 16H), 3.27 (overlapping m, 24H), 2.87 (br. s, 10H), 2.60-2.43 (m, 2H, $\text{CH}_2(\text{CH}_2)_2\text{NHCO}$), 1.65 (br. s, 2H, $\text{CH}_2\text{CH}_2\text{NHCO}$), 1.40 (d, $J=7.2$ Hz, 3H, CH_3CH). **^{13}C NMR (D_2O , 125 MHz), δ :** 170.2, 165.0, 143.7 (Ar- C_q), 131.6, 130.5, 129.4, 128.9, 127.9, 127.4, 125.9, 64.5, 64.4, 63.7, 57.4, 56.6, 56.5, 54.8, 54.3, 54.0, 52.7, 52.4, 51.5, 51.2, 50.6, 49.9, 49.3, 48.3, 48.1, 48.00, 37.5 ($\text{CH}_2\text{CH}_2\text{NHCO}$), 24.9 ($\text{CH}_2\text{CH}_2\text{NHCO}$), 21.23 (CH_3). **LRMS (ESI):** calculated for $\text{C}_{53}\text{H}_{82}\text{N}_9\text{O}_9^+$ $[\text{M}+\text{H}]^+$: 988.6235; Found 988,6230.

3.6. References:

- Bretonniere Y, Cann MJ, Parker D, Slater R: **Ratiometric probes for hydrogencarbonate analysis in intracellular or extracellular environments using europium luminescence.** *Chem Commun* 2002(17):1930-1931.
- Parker D, Yu JH: **A pH-insensitive, ratiometric chemosensor for citrate using europium luminescence.** *Chem Commun* 2005(25):3141-3143.
- Palit DK: **Photophysics and excited state relaxation dynamics of p-hydroxy and p-amino-substituted benzophenones: a review.** *Research on Chemical Intermediates* 2005, **31**(1-3):205-225.
- Shiraishi Y, Koizumi H, Hirai T: **Photosensitized oxygenation of sulfides within an amphiphilic dendrimer containing a benzophenone core.** *Journal of Physical Chemistry B* 2005, **109**(18):8580-8586.
- Rodriguez-Ubis JC, Alonso MT, Juanes O, Sedano R, Brunet E: **The discovery of a simple ligand based on acetophenone bearing excellent quantum yields for the excitation of Eu³⁺ and Tb³⁺.** *Journal of Luminescence* 1998, **79**(2):121-125.
- Wilkinson AJ, Maffeo D, Beeby A, Foster CE, Williams JAG: **Sensitization of Europium(III) luminescence by benzophenone-containing ligands: Regioisomers, rearrangements and chelate ring size, and their influence on quantum yields.** *Inorganic Chemistry* 2007, **46**(22):9438-9449.
- Beeby A, Bushby LM, Maffeo D, Williams JAG: **Intramolecular sensitisation of lanthanide(III) luminescence by acetophenone-containing ligands: the critical effect of para-substituents and solvent.** *J Chem Soc-Dalton Trans* 2002(1):48-54.
- Izatt RM, Terry RE, Nelson DP, Chan Y, Eatough DJ, Bradshaw JS, Hansen LD, Christensen JJ: **CALORIMETRIC TITRATION STUDY OF INTERACTION OF SOME UNIVALENT AND BIVALENT-CATIONS WITH BENZO-15-CROWN-5, 18-CROWN-6, DIBENZO-24-CROWN-8, AND DIBENZO-27-CROWN-9 IN METHANOL-WATER SOLVENTS, AT 25 DEGREESC AND MU = 0.1.** *J Am Chem Soc* 1976, **98**(24):7626-7630.
- Chen KC, Nicholson C: **Spatial buffering of potassium ions in brain extracellular space.** *Biophys J* 2000, **78**(6):2776-2797.
- Steed JW, Gale PA: **Supramolecular Chemistry: From Molecules to Nanomaterials:** Wiley; 2012.
- Lehn JM, Vierling P: **18 -N303 AZA-OXA MACROCYCLE - SELECTIVE RECEPTOR UNIT FOR PRIMARY AMMONIUM CATIONS.** *Tetrahedron Letters* 1980, **21**(14):1323-1326.
- Vogel S, Rohr K, Dahl O, Wengel J: **Synthesis of an asymmetrically substituted AZA crown ether as metal and amino acid binding site in DNA conjugates.** *Nucleosides Nucleotides & Nucleic Acids* 2003, **22**(5-8):1039-1040.
- Vogel S, Rohr K, Dahl O, Wengel J: **A substituted triaza crown ether as a binding site in DNA conjugates.** *Chem Commun* 2003(8):1006-1007.
- Sasaki S, Hashizume A, Citterio D, Fujii E, Suzuki K: **Fluororeceptor for zwitterionic form amino acids in aqueous methanol solution.** *Tetrahedron Letters* 2002, **43**(40):7243-7245.
- Schmidtchen FP: **TETAZAC - A NOVEL ARTIFICIAL RECEPTOR FOR BINDING OMEGA-AMINO CARBOXYLATES.** *Journal of Organic Chemistry* 1986, **51**(26):5161-5168.
- Metzger A, Gloe K, Stephan H, Schmidtchen FP: **Molecular recognition and phase transfer of underivatized amino acids by a foldable artificial host.** *Journal of Organic Chemistry* 1996, **61**(6):2051-2055.
- Torrens A, Mas J, Port A, Castrillo JA, Sanfeliu O, Guitart X, Dordal A, Romero G, Fisas MA, Sanchez E *et al*: **Synthesis of new benzoxazinone derivatives as neuropeptide Y5 antagonists for the treatment of obesity.** *Journal of Medicinal Chemistry* 2005, **48**(6):2080-2092.

18. Das S, Addis D, Junge K, Beller M: **Zinc-Catalyzed Chemoselective Reduction of Tertiary and Secondary Amides to Amines**. *Chemistry-a European Journal* 2011, **17**(43):12186-12192.
19. Das S, Addis D, Zhou S, Junge K, Beller M: **Zinc-Catalyzed Reduction of Amides: Unprecedented Selectivity and Functional Group Tolerance**. *J Am Chem Soc* 2010, **132**(6):1770-+.
20. Roeske RW, Weigl FL, Prasad KU, Thompson RM: **SELECTIVE REDUCTION OF AMIDE CARBONYL GROUP IN DIPEPTIDES BY BORANE**. *Journal of Organic Chemistry* 1976, **41**(7):1260-1261.
21. Gunnlaugsson T, Gunaratne HQN, Nieuwenhuyzen M, Leonard JP: **Synthesis of functionalised macrocyclic compounds as Na⁺ and K⁺ receptors: a mild and high yielding nitration in water of mono and bis 2-methoxyaniline functionalised crown ethers**. *Journal of the Chemical Society-Perkin Transactions 1* 2002(17):1954-1962.
22. Shiraishi Y, Furubayashi Y, Nishimura G, Hirai T: **Sensitized luminescence properties of dinuclear lanthanide macrocyclic complexes bearing a benzophenone antenna**. *Journal of Luminescence* 2007, **127**(2):623-632.
23. Mewis RE, Archibald SJ: **Biomedical applications of macrocyclic ligand complexes**. *Coord Chem Rev* 2010, **254**(15-16):1686-1712.
24. Aime S, Botta M, Fasano M, Marques MPM, Geraldes C, Pubanz D, Merbach AE: **Conformational and coordination equilibria on DOTA complexes of lanthanide metal ions in aqueous solution studied by H-1-NMR spectroscopy**. *Inorganic Chemistry* 1997, **36**(10):2059-2068.
25. Spirlet MR, Rebizant J, Desreux JF, Loncin MF: **CRYSTAL AND MOLECULAR-STRUCTURE OF SODIUM AQUO(1,4,7,10-TETRAAZACYCLODODECANE-1,4,7,10-TETRAACETATO)EUROPATE(III) TETRAHYDRATE, NA+(EUDOTA.H2O).4H2O, AND ITS RELEVANCE TO NMR-STUDIES OF THE CONFORMATIONAL BEHAVIOR OF THE LANTHANIDE COMPLEXES FORMED BY THE MACROCYCLIC LIGAND DOTA**. *Inorganic Chemistry* 1984, **23**(3):359-363.
26. Stezowski JJ, Hoard JL: **HEAVY-METAL IONOPHORES - CORRELATIONS AMONG STRUCTURAL PARAMETERS OF COMPLEXED NONPEPTIDE POLYAMINO ACIDS**. *Israel Journal of Chemistry* 1984, **24**(4):323-334.
27. Raitsimring AM, Astashkin AV, Baute D, Goldfarb D, Caravan P: **W-band O-17 pulsed electron nuclear double resonance study of gadolinium complexes with water**. *Journal of Physical Chemistry A* 2004, **108**(35):7318-7323.
28. Ruloff R, Toth E, Scopelliti R, Tripier R, Handel H, Merbach AE: **Accelerating water exchange for Gd-III chelates by steric compression around the water binding site**. *Chem Commun* 2002(22):2630-2631.
29. Kubo K, Ishige R, Kubo J, Sakurai T: **Synthesis and complexation behavior of N-(1-naphthylmethyl)-1,4,7,10,13-pentaoxa-16-azacyclooctadecane**. *Talanta* 1999, **48**(1):181-187.
30. Ji HF, Dabestani R, Brown GM, Hettich RL: **Spacer length effect on the photoinduced electron transfer fluorescent probe for alkali metal ions**. *Photochemistry and Photobiology* 1999, **69**(5):513-516.
31. Kubo K, Ishige R, Kato N, Yamamoto E, Sakurai T: **Synthesis and complexation behavior of N,N'-bis(1-naphthylmethyl)-1,4,10,13-tetraoxa-7,16-diazacyclo-octadecane**. *Heterocycles* 1997, **45**(12):2365-2379.
32. Spath A, Konig B: **Molecular recognition of organic ammonium ions in solution using synthetic receptors**. *Beilstein journal of organic chemistry* 2010, **6**:32.
33. Meyer EA, Castellano RK, Diederich F: **Interactions with aromatic rings in chemical and biological recognition**. *Angewandte Chemie-International Edition* 2003, **42**(11):1210-1250.
34. Kryger G, Silman I, Sussman JL: **Three-dimensional structure of a complex of E2020 with acetylcholinesterase from *Torpedo californica***. *Journal of Physiology-Paris* 1998, **92**(3-4):191-194.

35. Kryger G, Silman I, Sussman JL: **Structure of acetylcholinesterase complexed with E2020 (Aricept (R)): implications for the design of new anti-Alzheimer drugs.** *Structure with Folding & Design* 1999, **7**(3):297-307.
36. Sussman JL, Harel M, Frolow F, Oefner C, Goldman A, Toker L, Silman I: **ATOMIC-STRUCTURE OF ACETYLCHOLINESTERASE FROM TORPEDO-CALIFORNICA - A PROTOTYPIC ACETYLCHOLINE-BINDING PROTEIN.** *Science* 1991, **253**(5022):872-879.
37. Comby S, Bünzli J-CG: **Chapter 235 Lanthanide Near-Infrared Luminescence in Molecular Probes and Devices.** 2007, **37**:217-470.
38. Poole RA, Kielar F, Richardson SL, Stenson PA, Parker D: **A ratiometric and non-enzymatic luminescence assay for uric acid: differential quenching of lanthanide excited states by anti-oxidants.** *Chem Commun* 2006(39):4084-4086.
39. Tremblay MS, Halim M, Sames D: **Cocktails of Tb³⁺ and Eu³⁺ complexes: A general platform for the design of ratiometric optical probes.** *J Am Chem Soc* 2007, **129**(24):7570-7577.
40. Montgomery CP, Murray BS, New EJ, Pal R, Parker D: **Cell-Penetrating Metal Complex Optical Probes: Targeted and Responsive Systems Based on Lanthanide Luminescence.** *Accounts Chem Res* 2009, **42**(7):925-937.
41. Hugi AD, Helm L, Merbach AE: **HIGH-PRESSURE NMR KINETICS .23. WATER EXCHANGE ON HEXAAQUAVANADIUM(III) - A VARIABLE-TEMPERATURE AND VARIABLE-PRESSURE O-17-NMR STUDY AT 1.4 AND 4.7 TESLA.** *Helvetica Chimica Acta* 1985, **68**(2):508-521.
42. Corsi DM, Platas-Iglesias C, van Bekkum H, Peters JA: **Determination of paramagnetic lanthanide(III) concentrations from bulk magnetic susceptibility shifts in NMR spectra.** *Magnetic Resonance in Chemistry* 2001, **39**(11):723-726.
43. Aime S, Botta M, Fasano M, Crich SG, Terreno E: **Gd(III) complexes as contrast agents for magnetic resonance imaging: A proton relaxation enhancement study of the interaction with human serum albumin.** *Journal of Biological Inorganic Chemistry* 1996, **1**(4):312-319.
44. Bertini I, Luchinat C, Aime S: **NMR of paramagnetic substances.** *Coord Chem Rev* 1996, **150**:R7-+.

4

Attempts to Synthesize L¹⁻⁴

CHAPTER 4. ATTEMPTS TO SYNTHESIZE L¹⁻⁴	184
4.1. ATTEMPTS TO SYNTHESIZE L¹⁻²	186
4.1.1. Coupling via amid-bond formation	186
4.1.2. Coupling via alkylation.....	189
4.1.3. Coupling via reductive amination.....	190
a) Preparation of aldehyde by deprotection of acetal:	192
b) Preparation of aldehyde by reduction of nitrile:.....	193
c) Preparation of aldehyde by oxidation of alkene:.....	194
d) Preparation of aldehyde by Swern oxidation:	195
4.2. ATTEMPTS TO SYNTHESIZE LIGANDS L³⁻⁴	195
4.2.1. Coupling <i>via</i> alkylation	195
4.2.2. Coupling via reductive amination.....	196
a) Preparation of aldehyde by deprotection of acetal:	197
b) Preparation of aldehyde by reduction of Weinreb amide:	197
SUMMARY AND CONCLUSIONS	199

Herein, are described briefly some of the synthetic pathways that have been attempted to prepare the ligands L¹⁻⁴ (see Chapter 2). Several types of reactions were explored in order to couple the two macrocycles, cyclen and monoaza-crown moieties.

4.1 Attempts to synthesize L¹⁻²

4.1.1. Coupling via amid-bond formation

The first approach was conducted according to the figure 4.1. It consisted of synthesizing an N-alkylamine lariat crown-ether moiety which should be coupled to the cyclen-based carboxylic acid using various coupling conditions.

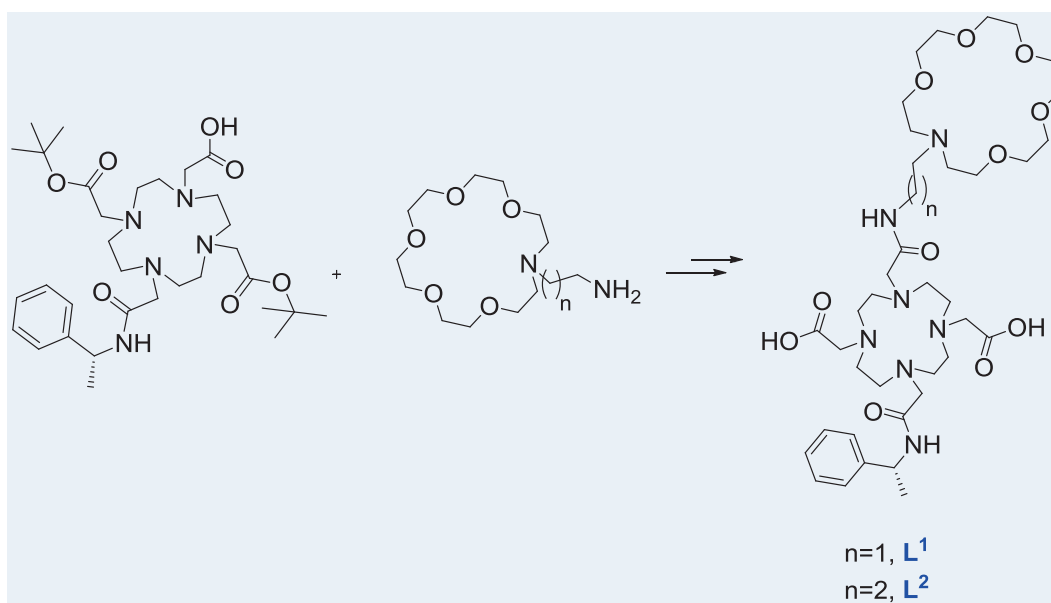


Figure 4.1. Synthetic approach for L¹⁻²

The carboxylic acid moiety was synthesized in 6 steps (figure 4.2). The synthesis started from the cyclen which was functionalized to get the *trans*-bis(*tert*-Bu)-DO2A ester **1**. Monoalkylation of **1** was carried out using 2-chloro-N-(1-phenylethyl)acetamide to form the molecule **2**. Finally, alkylation of **2** using benzyl bromoacetate, followed by removal of the benzyl group by means of catalytic hydrogenolysis leads to a mixture of acid **27** and corresponding methyl ester. Only the methyl ester is obtained if the hydrogenolysis is prolonged.

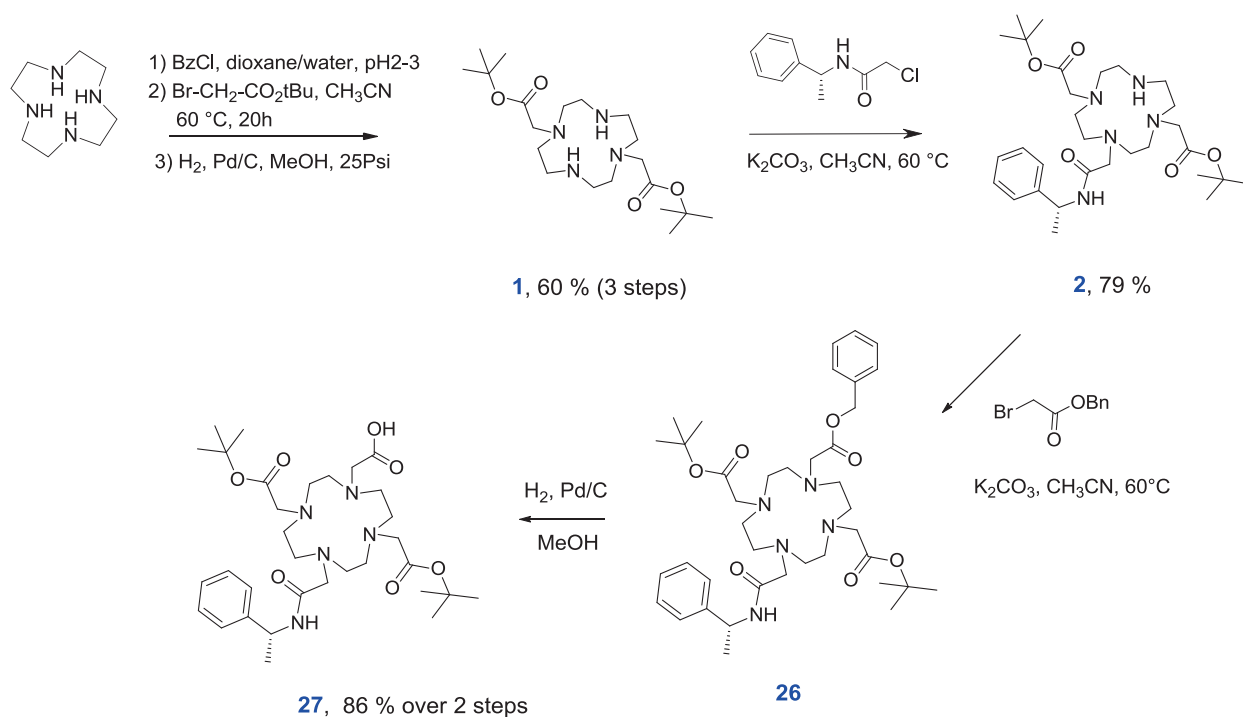


Figure 4.2

On the other hand, N-alkylamine lariat crown ether moieties were synthesized from 1-aza-18-crown-6-ether by the reaction with the N-Cbz protected 2-bromopropylamine and 3-bromopropylamine to get the intermediate **28** and **29**, respectively (figure 4.3). The next step involved removal of the Cbz protecting group. Since the conversion to the amines was not complete, another pathway was tried to synthesize the lariats **30** and **31**.

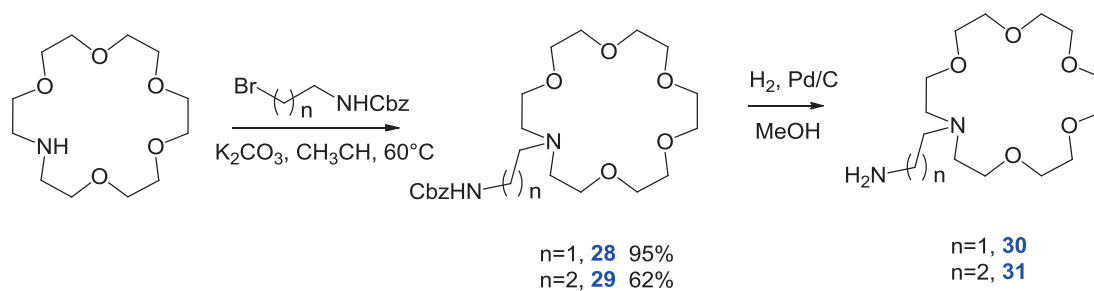


Figure 4.3

This new synthetic pathway included the synthesis of the nitriles **32** and **33** which were reduced to the corresponding free amines **34** and **35** by hydrogenolysis using Raney-Ni catalyst (figure 4.4).

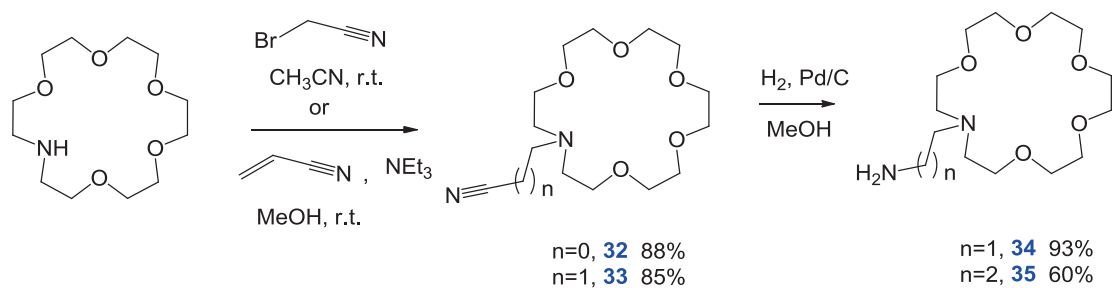


Figure 4.4

Attempts to carry out the coupling between amines **34**, **35** and the acid **27** were unsuccessful (figure 4.5). HOBt/EDCI and HBTU were used as coupling reagents; however, only starting materials could be detected by mass spectrometry and TLC.

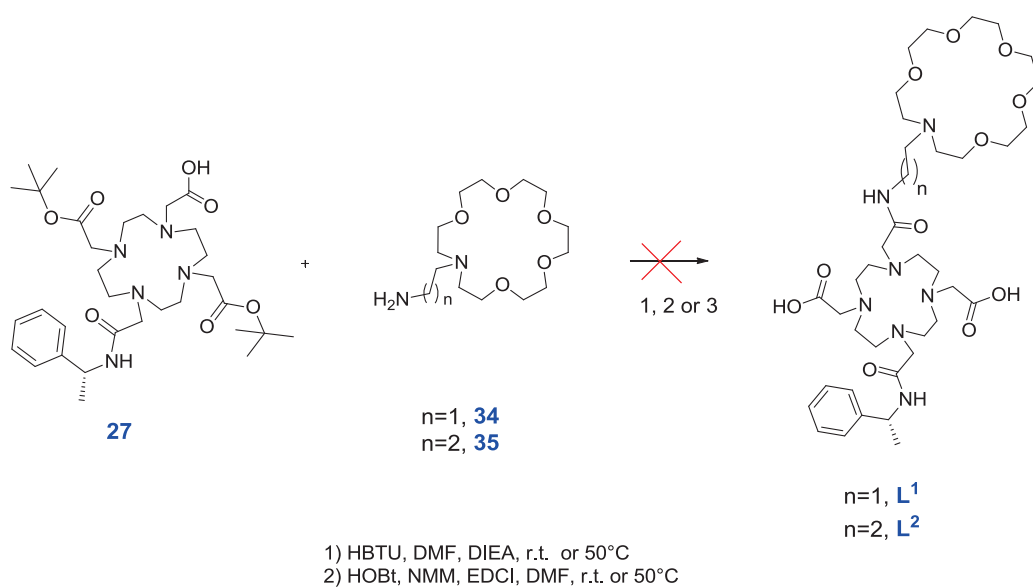


Figure 4.5

Additionally, acid **27** was reacted with ethyl chloroformate to form the mixed anhydride **36**. No reaction took place when the anhydride was treated with the amines **34** (figure 4.6).

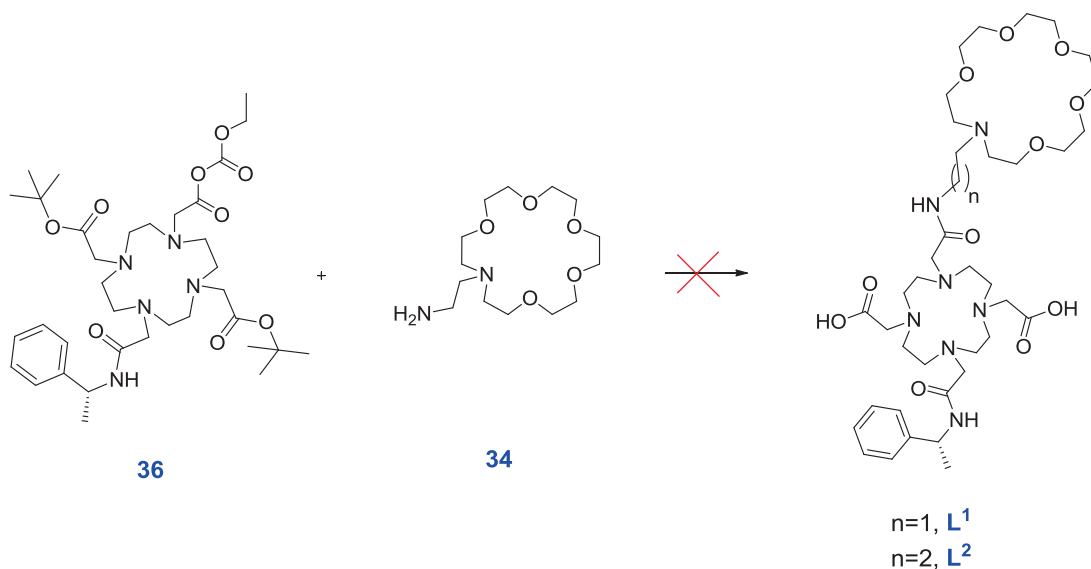


Figure 4.6

4.1.2. Coupling via alkylation

Since the coupling of the two macrocyclic moieties via amide-bond formation was unsuccessful, another synthetic route was chosen. It consisted of synthesizing the whole linker on the monoaza-crown, before attaching it to the cyclen moiety. For this purpose, the free amine crown ether was converted to a halo-acetamide and was subsequently used in an alkylation reaction with the DO3A-monoamide **2** as illustrated in the following figure:

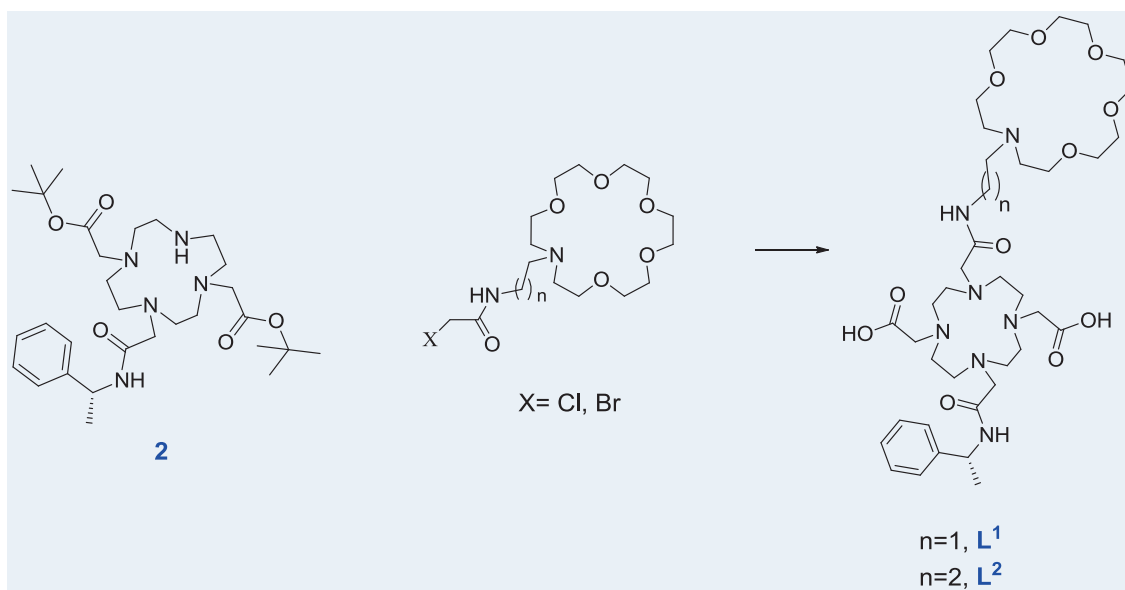
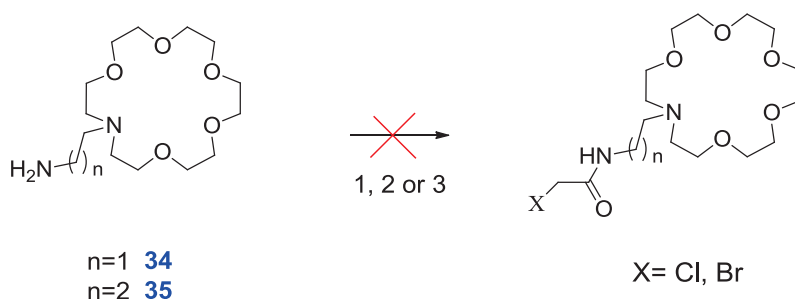


Figure 4.7

The precursor **2** was synthesized as previously reported in chapter 2, figure 2.10.

Various reaction conditions regarding the number of added equivalents of bromoacetyl bromide (or chloroacetyl chloride) and the reaction temperature (0 to -20 °C) were attempted. However, acetylation of amine crown ethers **34** and **35** with bromoacetyl bromide or chloroacetyl chloride resulted in very low yields of desired products (figure 4.8). In addition, coupling the amines **34** and **35** with bromoacetic acid (in the presence of HBTU/DIPEA) could not be achieved; only starting materials were detected.



- 1) BrCH₂COBr, H₂O/CH₂Cl₂ pH = 6-7, K₂CO₃ (or NEt₃)
- 2) BrCH₂COOH, PyPoB, DCC, DMF
- 3) BrCH₂COOH, HBTU, DIEA, DMF

Figure 4.8

4.1.3. Coupling via reductive amination

Similarly to the previous synthetic route described in 4.1.2, building the whole linker on the cyclen moiety **2** and then coupling to the monoaza-crown was attempted. The linker is containing an aldehyde group which will allow attaching the monoaza-crown ether via reductive amination, as described in the following figure:

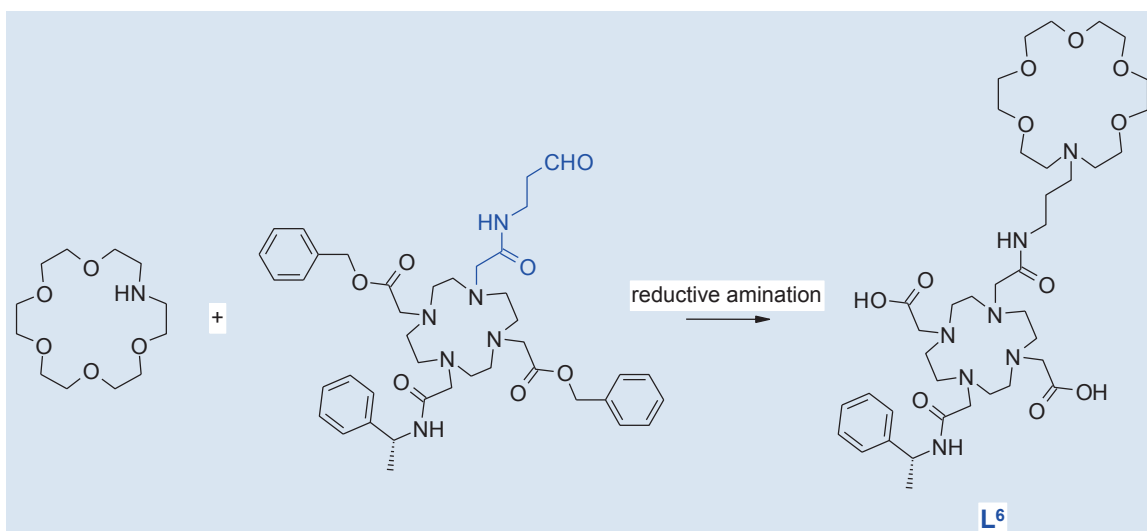


Figure 4.9

Figure 4.10 shows the different precursors that have been synthesized in order to convert them to aldehyde prior to the coupling with monoaza-crown moiety. Accordingly, we attempted to obtain the aldehyde-containing moiety by:

- Deprotection of acetal **36** under acidic conditions.
- Reduction of nitrile **37** to aldehyde using diisobutylaluminum hydride (DIBAL-H)
- Conversion of alkene **38** to the aldehyde with the ozonolysis.
- Swern oxidation of alcohol **39**.

Since the *tert*-Bu esters are labile under some of the used reaction conditions, Cbz protecting groups were used instead (figure 4.10).

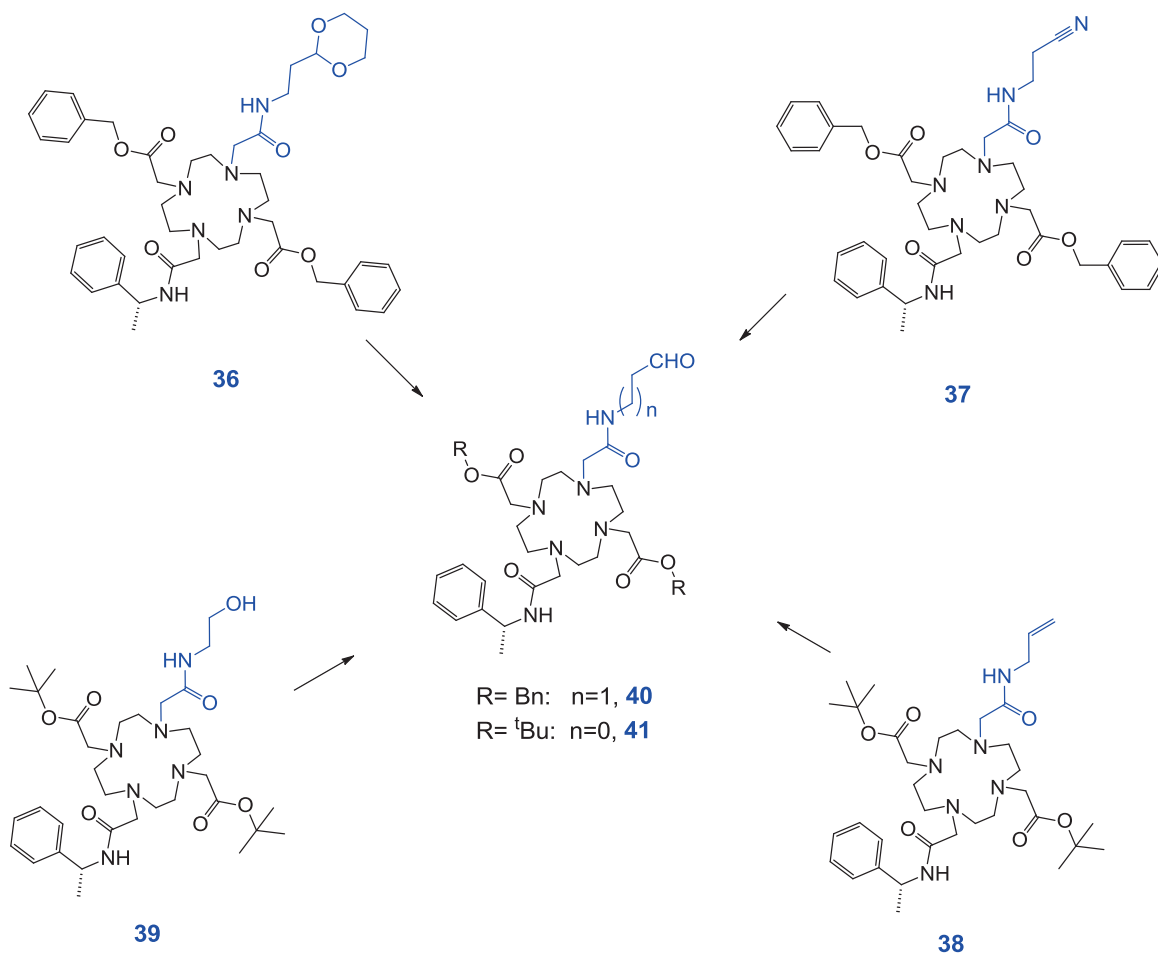


Figure 4.10

a) Preparation of aldehyde by deprotection of acetal:

Figure 4.11 shows the synthetic route used to prepare the acetal-containing moiety **36**.

The acetal-amine **42** was obtained from commercially available corresponding bromide in two steps: the sodium phthalimide was first *N*-alkylated with bromoethyl dioxane to give the corresponding *N*-ethylphthalimide dioxane, which was then deprotected under basic conditions using hydrazine.

Compound **43** was obtained from cyclen over 2 steps. The alkylation with bromomethyl ester gave the ester **44**, which was subsequently deprotected under basic conditions to afford the corresponding carboxylic acid **45**. This was coupled with the acetalamine **42** to afford the acetal-containing precursor **36**. Treatment with hydrogen peroxide did not result in removal of

the acetal protecting group since only the starting material was observed. Using harsh acidic conditions, we obtained a mixture of unidentifiable products.

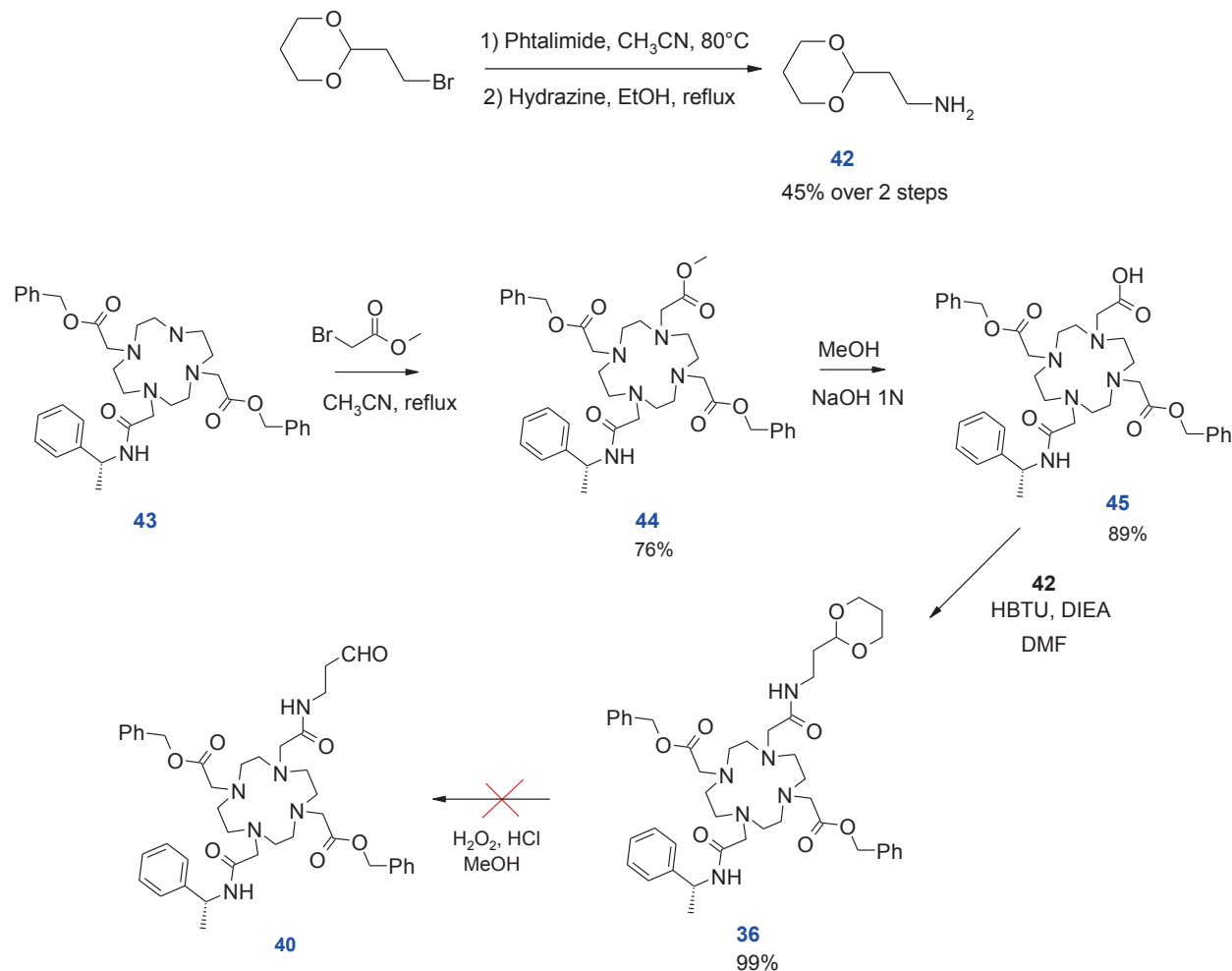


Figure 4.11

b) Preparation of aldehyde by reduction of nitrile:

The synthetic route used to prepare the nitrile-containing moiety **37** is illustrated in figure 4.12. Firstly, 3-amino-propionitrile was reacted with bromoacetyl bromide to get the linker **46**, which was then used to functionalize the previously made intermediate **45** to give **37**. Attempts to convert the nitrile group to aldehyde, using DIBAL-H, led to a mixture of unidentifiable compounds.

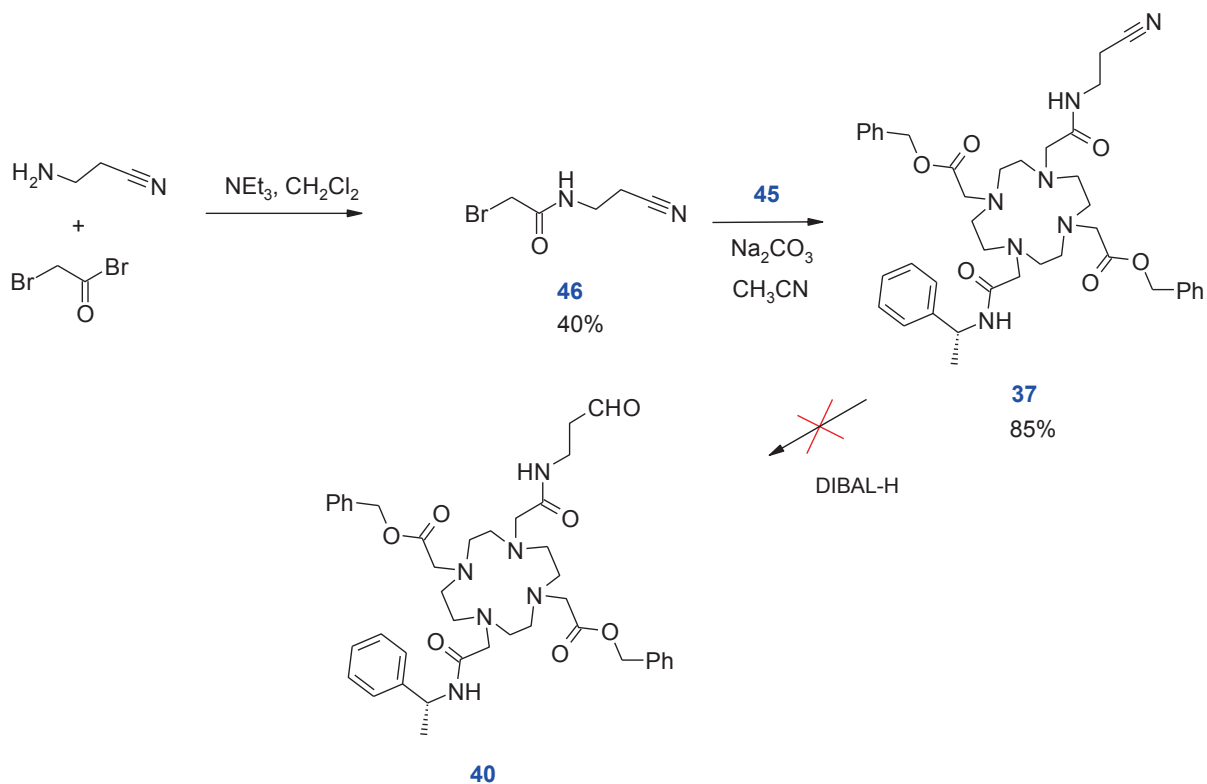


Figure 4.12

c) Preparation of aldehyde by oxidation of alkene:

The alkene-containing precursor **38** was synthesized over one step from the acid **27**, which underwent a coupling reaction with allylamine (figure 4.13). Oxidation of the alkene by ozonolysis was not successful and it appeared that the starting material was subject to decomposition.

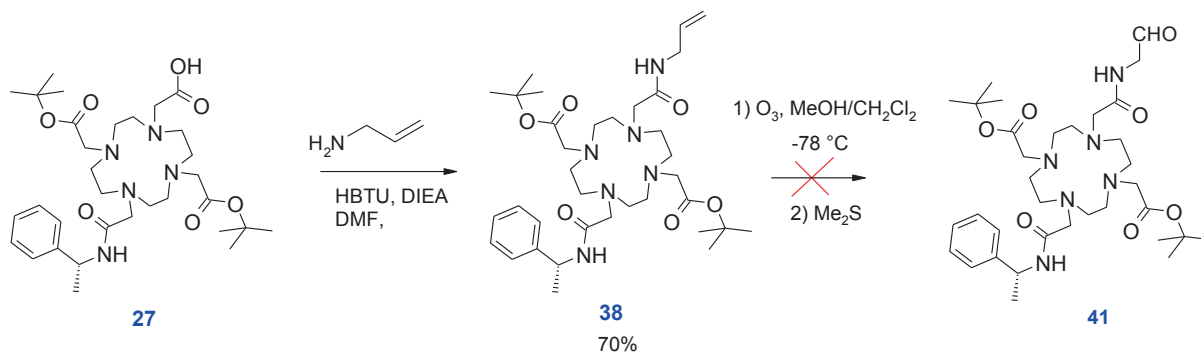


Figure 4.13

d) Preparation of aldehyde by Swern oxidation:

Similarly to **38**, alcohol-containing precursor **39** was prepared from the acid **27** by coupling reaction with the commercially available 2-benzyloxy ethanamine, followed by removal of benzyl protecting group *via* hydrogenolysis (figure 4.14). Next, the Swern oxidation was attempted on the alcohol **39**, giving rise to unidentifiable products.

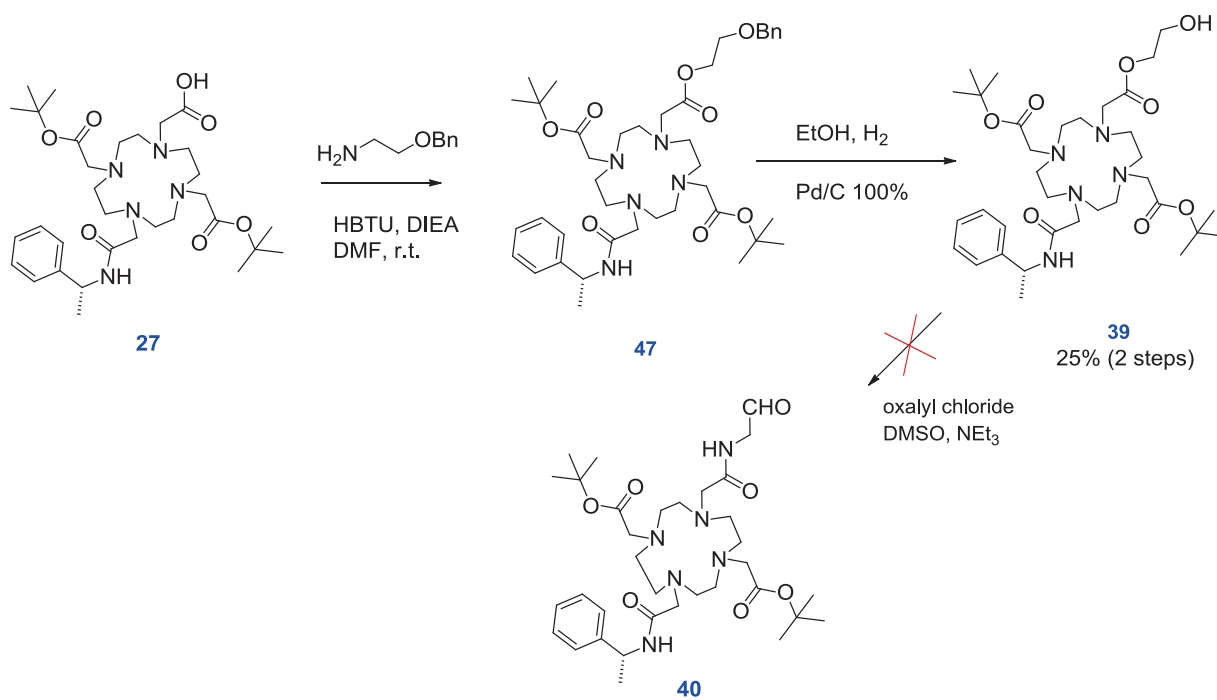


Figure 4.14

4.2 Attempts to synthesize ligands L³⁻⁴

For the synthesis of ligands L³⁻⁴, strategies similar to those described above were used. They involved the coupling via alkylation and reductive amination of the two macrocycles.

4.2.1. Coupling *via* alkylation

The synthesis consisted of functionalizing the monoazacrown with a simple chloroalkyl arm, which could then be used to alkylate the cyclen moiety, as seen in figure 4.16. Although the reaction was performed in a very concentrated media to favour the alkylation of cyclen moiety,

mass spectrometry showed that the chloroalkyl-crowns **48** and **49** were subject to intracyclisation to give the tetrammonium products **50** and **51**, respectively. It should be noted that the reactions with excess of the chloroalkyl-crown were excluded due to the high cost of the commercially available monoaza-crown ether.

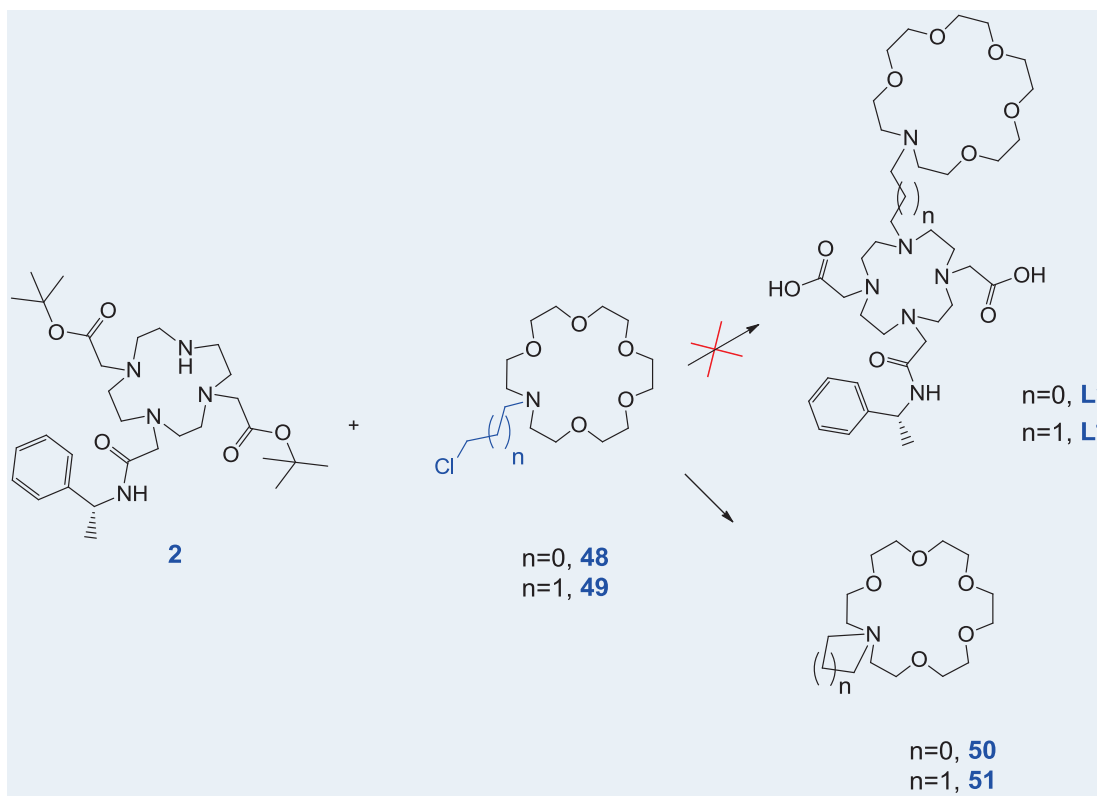


Figure 4.16

4.2.2. Coupling via reductive amination

The synthetic route shown in figure 4.17 was attempted to achieve coupling of the two macrocycles via reductive amination.

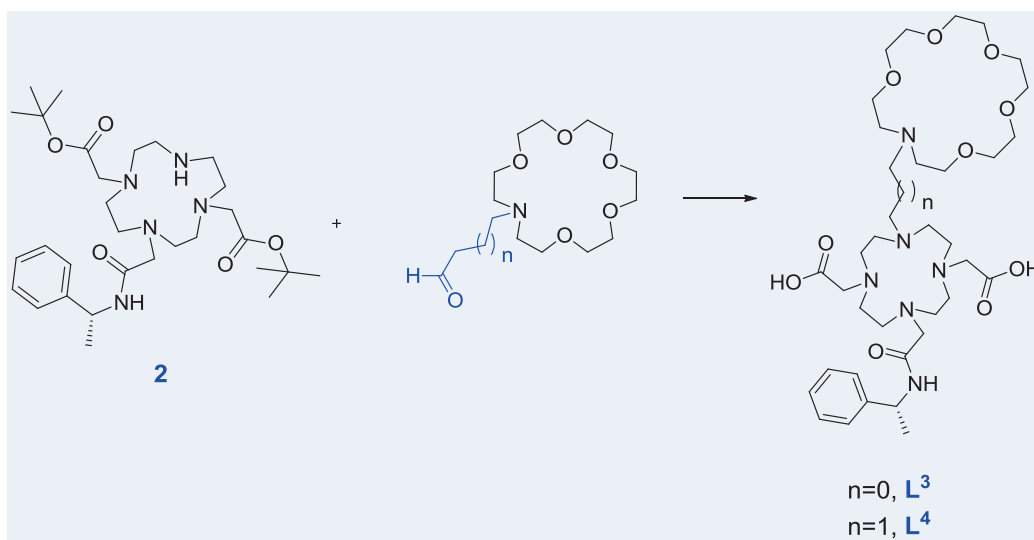


Figure 4.17

In order to prepare the aldehyde-containing crown, two pathways were explored:

a) Preparation of aldehyde by deprotection of acetal:

N-Alkylation of monoaza-crown with bromoethyl dioxane afforded the acetal-containing intermediate **52**. Subsequent treatment with hydrogen peroxide in the presence of hydrogen chloride (2N) led to an incomplete conversion. Moreover, when the reaction is done in a more acidic media, the appearance of unidentifiable products was observed.

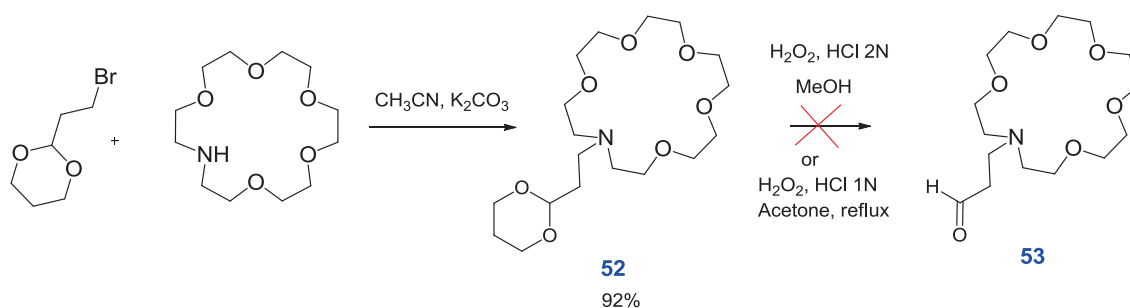


Figure 4.18

b) Preparation of aldehyde by reduction of Weinreb amide:

Synthesis of the aldehyde-containing aza-crown ether was also attempted utilizing the Weinreb method. The advantage of this method over other reduction methods would be avoiding the

common problem of over-addition of the reducing agent and hence the undesired formation of alcohol. The adopted synthetic route is illustrated in figure 4.19. Nitrile **33** was prepared as described above (section 4.1.1, figure 4.4). Hydrolysis under harsh basic conditions (HCl 6N) led to the corresponding carboxylic acid **54**, which was then reacted with the commercially available N,O-dimethylhydroxylamine hydrochloride to form the Weinreb amide **55**. However, the subsequent treatment of this amide with lithium aluminium hydride did not lead to the desired aldehyde.

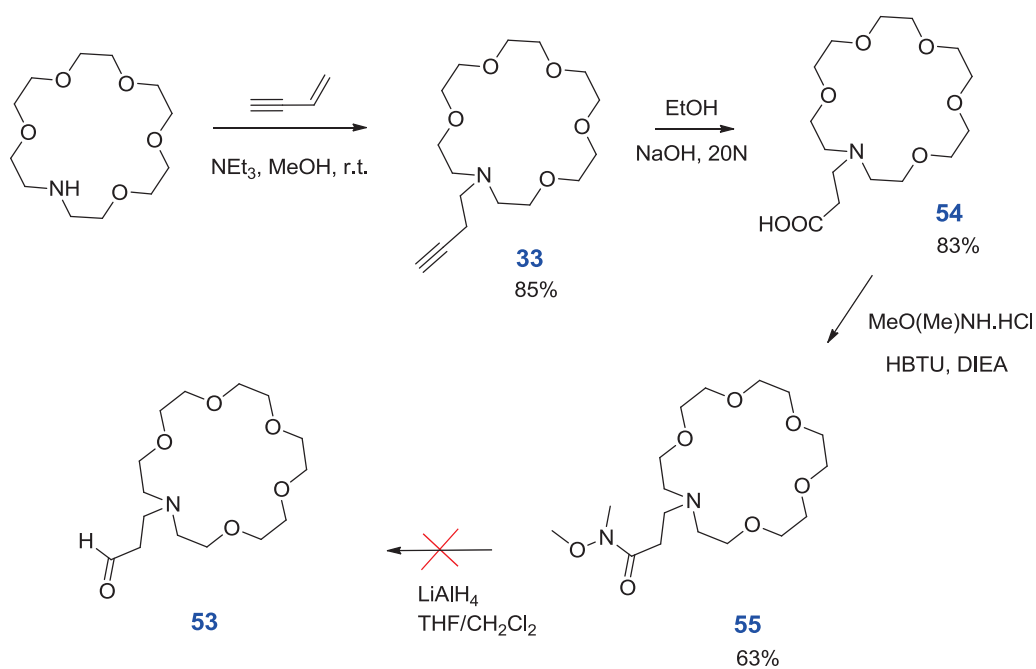


Figure 4.19

General conclusions

The work presented in this thesis aimed at developing lanthanide-based, responsive contrast agents for sensing neurotransmitters by MR imaging. The general design approach was based on modulating the proton relaxivity *via* the modulation of the hydration number of the contrast agents by neurotransmitters binding. We have specifically targeted amino acid neurotransmitters, which are zwitterionic in nature, having a deprotonated, negatively charged carboxylate and a protonated, positively charged ammonium group that can both serve as potential binding sites. Accordingly, the molecular design focused on a divalent binding approach that enables the contrast agents to simultaneously form two interactions with neurotransmitters. Such dual-binding approach has a clear advantage over monovalent binding.

The first part of this study, described in chapter 2, involved the synthesis of three chelators L^{5-7} , and the physico-chemical characterization of their Gd^{3+} complexes including their relaxometric properties. These ligands are based on cyclen derivatives to chelate the paramagnetic Ln^{3+} ion and were designed to be coordinatively unsaturated to host the carboxylate group of the neurotransmitters. They were conjugated to a monoaza-crown ether which serves as binding site for the ammonium group.

The potentiometric titrations performed on the three ligands allowed determining four protonation constants for the unit that chelates the lanthanide ion. Additional protonation was found to occur on the nitrogen of the monoaza-crown in the case of the ligands L^{5-6} . This implies that the nitrogen of the monoaza-crown is unprotonated at physiological pH, and therefore is more prone to interact with the ammonium ion.

The ^{17}O NMR study evidenced fast water exchange for the GdL^{5-6} complexes, with an exchange rate considerably higher than that on GdL^7 . GdL^{5-6} have remarkably high relaxivities, with $r_1=6.1$ and $7.7 \text{ mM}^{-1}\text{s}^{-1}$, respectively, while GdL^7 exhibits a relaxivity of $4.4 \text{ mM}^{-1}\text{s}^{-1}$ (20 MHz and 37°C). Despite the high relaxivities, the hydration number was determined to be one for all the three complexes, as demonstrated by ^{17}O NMR on the Gd^{3+} - and by luminescence lifetime measurements on the Eu^{3+} - and Tb^{3+} -analogues. The change of T_1 relaxation rate upon addition

of neurotransmitters evidenced the ability of the complexes GdL^{5-6} to trigger an MRI turn-off response. On the contrary, the complex GdL^7 was not responsive to all investigated neurotransmitters. The dissociation constants for the interaction between the amino acid neurotransmitters and the responsive Gd^{3+} complexes have been estimated from the relaxometric titration curves to be in the range of 5-20 mM. Additionally, GdL^5 and GdL^6 were found to respond to the same extent to bicarbonate, a predominant ion in the extracellular physiological fluids. Measurement of the luminescence lifetimes of the Tb^{3+} complex demonstrated that the formation of ternary complexes with neurotransmitters implies a decrease in hydration number, which is in agreement with the relaxometric studies. Attractively, the complexes EuL^{5-6} have shown a ratiometric luminescence response, which might be valuable for the subsequent measurements of neurotransmitter levels both in *in vitro* and *in vivo* assays.

Computational studies performed on the ternary GdL^5 -Glycine complex showed that the dual-binding to the glycine is indeed sterically feasible. In order to prove experimentally that the interaction between the monoaza-crown and the ammonium group of neurotransmitter takes place, solution NMR studies were carried out on a diamagnetic analogue, YL^5 . In the presence of glutamate, the peaks of the crown ether in ^{13}C - ^1H 2D HSQC spectrum were subject to a strong shift, which might be an indication that the interaction with the ammonium group takes place. Further investigations in this direction are needed to confirm that interaction.

Chapter 3 dealt with the development of two new chelators whose design was meant to improve the optical properties of the probes and their affinity towards neurotransmitters. To optimize the optical properties for potential use in bimodal imaging, we have designed ligand L^8 , which is structurally similar to L^6 except that p-aminobenzophenone was introduced as luminescence sensitizer to the cyclen backbone. The complex GdL^8 exhibited a relaxivity of $6.7 \text{ mM}^{-1}\text{s}^{-1}$, in comparison to $7.7 \text{ mM}^{-1}\text{s}^{-1}$ for GdL^6 . According to the ^{17}O NMR studies, GdL^8 has relatively fast water exchange. It was possible to demonstrate that the benzophenone chromophore sensitizes the Eu^{3+} emission in the visible range and the Yb^{3+} and Nd^{3+} emission in the near-infrared. Interaction with neurotransmitters led to remarkable changes of the

luminescence emission intensity of EuL^8 and YbL^8 , while NdL^8 remained unaffected. The analysis of the luminescence titrations of the complex YbL^8 with neurotransmitters pointed towards a possible photoinduced electron transfer (PET) process occurring from the electron-rich triaza-crown to the redox active Yb^{3+} ion, which is not possible for NdL^8 . Quenching this PET process upon binding of amino acid neurotransmitters seems to contribute to the observed change of luminescence emission intensity. On the other hand, the relaxometric properties of GdL^8 are also altered by neurotransmitter binding; GdL^8 turned out to have more affinity towards the bicarbonate ion, while the affinity towards neurotransmitters has diminished. This was reflected in the higher dissociation constants of the ternary complexes formed with GdL^8 in comparison those with GdL^6 . In addition, the non-sensitivity of NdL^8 to neurotransmitters in contrast to YbL^8 provides the possibility for ratiometric analysis that is independent of probe concentration, by using a cocktail of the two lanthanide complexes.

Finally, to improve the binding affinity to neurotransmitters, a triaza-crown ether having much better affinity and selectivity towards the ammonium group has been introduced in replacement of the monoaza-crown in the ligand L^6 . ^{17}O NMR studies showed that similarly to GdL^6 and GdL^8 , the complex GdL^9 has a high water exchange rate. The relaxivity of GdL^9 was found to be $8.8 \text{ mM}^{-1}\text{s}^{-1}$, in comparison to $7.7 \text{ mM}^{-1}\text{s}^{-1}$ for GdL^6 (20 MHz and 37°C). The relaxometric titration studies with neurotransmitters evidenced that the presence of the new crown ether considerably improves the affinity towards neurotransmitters; the dissociation constants were estimated to be about 2-3 mM.

In overall, these Gd^{3+} and luminescent lanthanide complexes present promising relaxometric and optical responses, respectively, to zwitterionic neurotransmitters. These studies also demonstrated the necessity for a dual-binding approach. Nevertheless, the efficiency of the systems needs to be further improved, mainly by suppressing competitive binding of the bicarbonate ion. For optical detection, a more suitable antenna that enables improved sensitization of NIR-emitting lanthanides should be included.

Appendix

APPENDIX	200
A.1. Most common neurotransmitters, their functions and the disorders associated with their dysfunctions.....	204
A.2. Reported concentration of some neurotransmitters.....	205
A.3. ^1H & ^{13}C NMR spectra of L ⁵⁻¹¹ and ^1H NMR spectra of EuL ⁵⁻⁸	206
A.4. Equations used for the fits of ^{17}O NMR and ^1H NMRD Data.....	215
A.5. SPECFIT data (absorption titrations of YbL ⁸).....	220

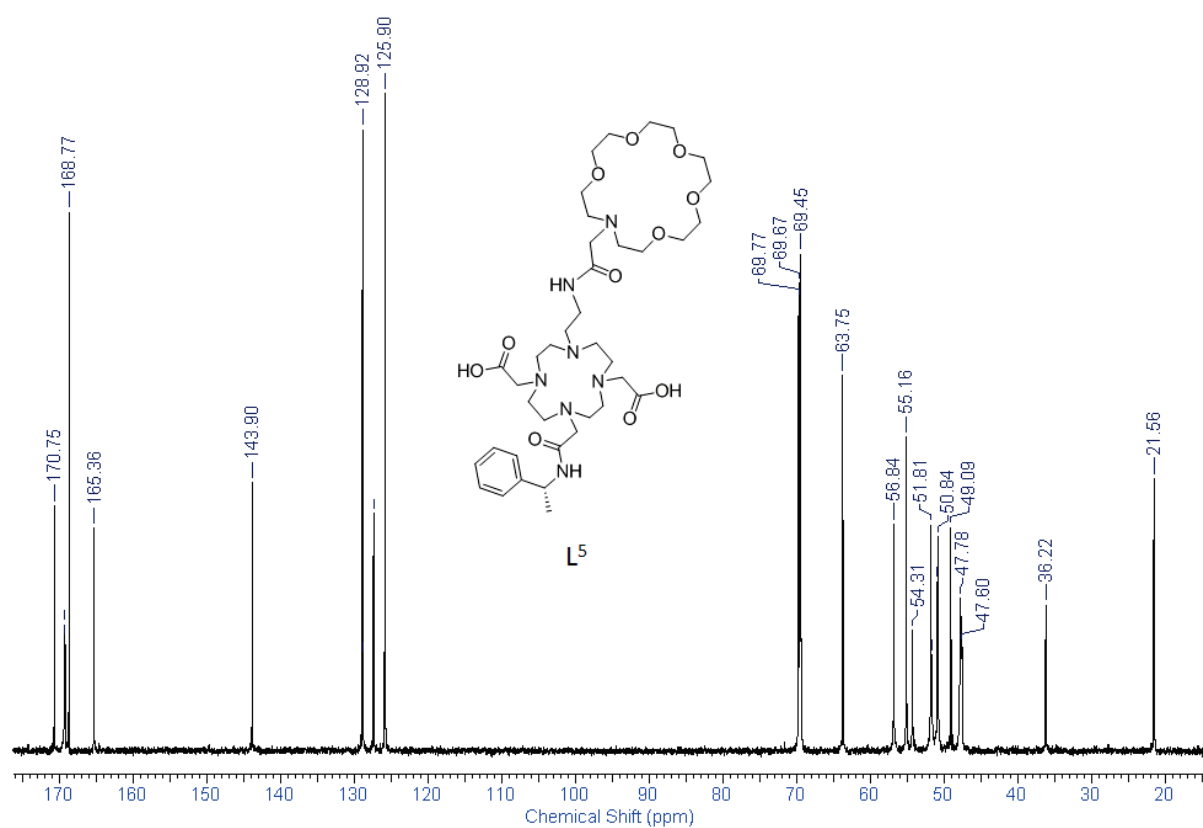
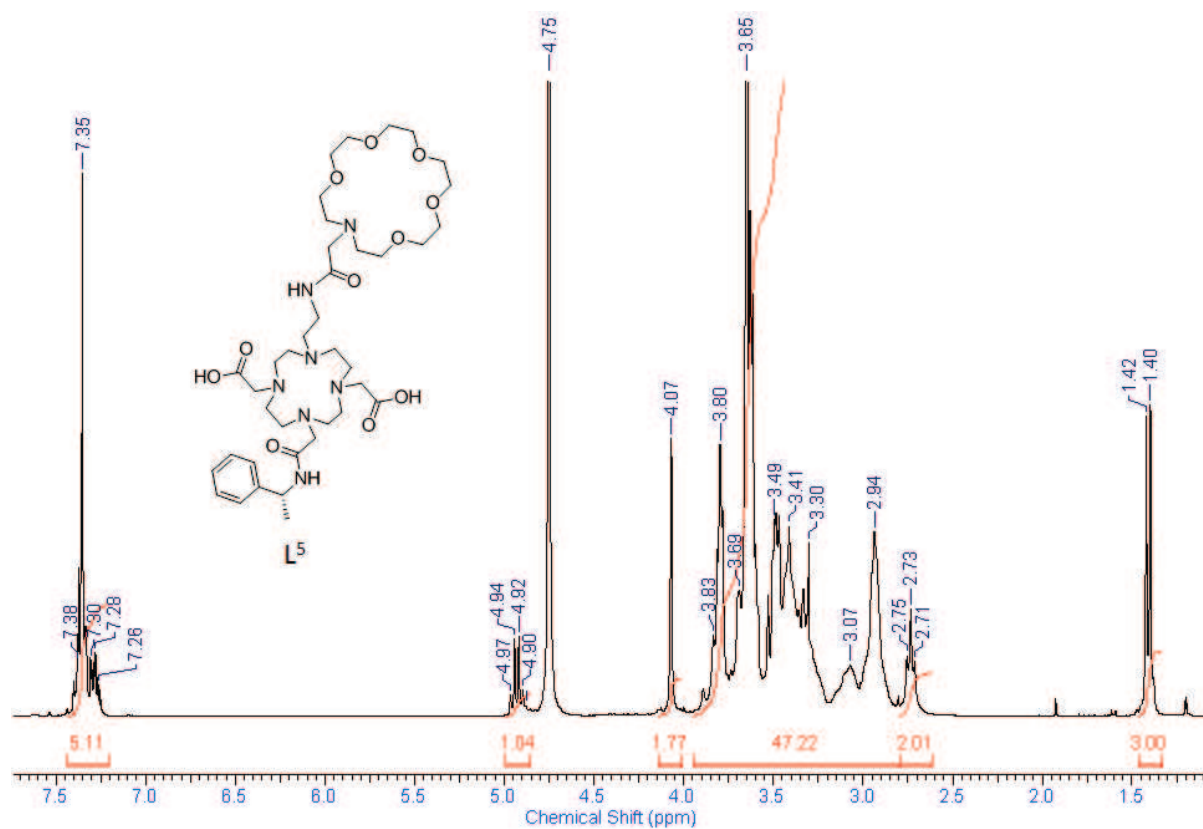
A.1. Most common neurotransmitters, their functions and the disorders associated with their dysfunctions.

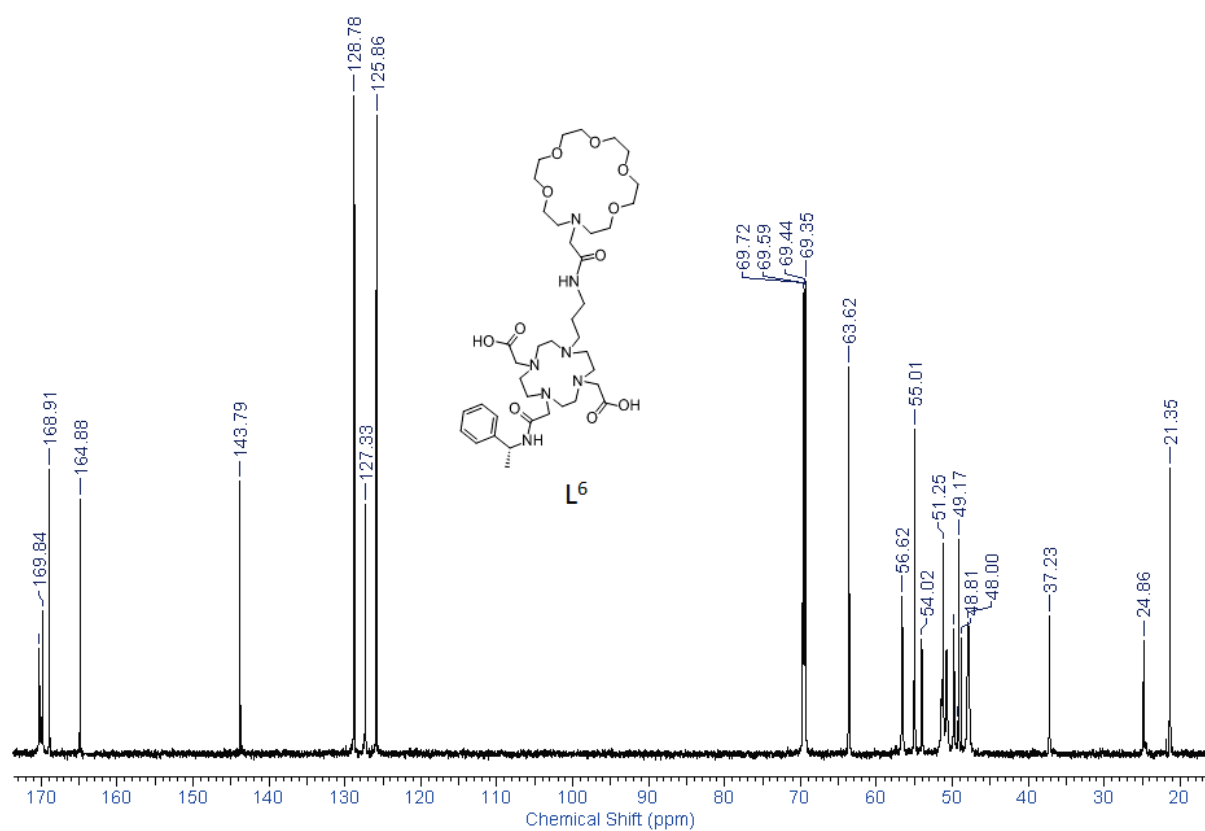
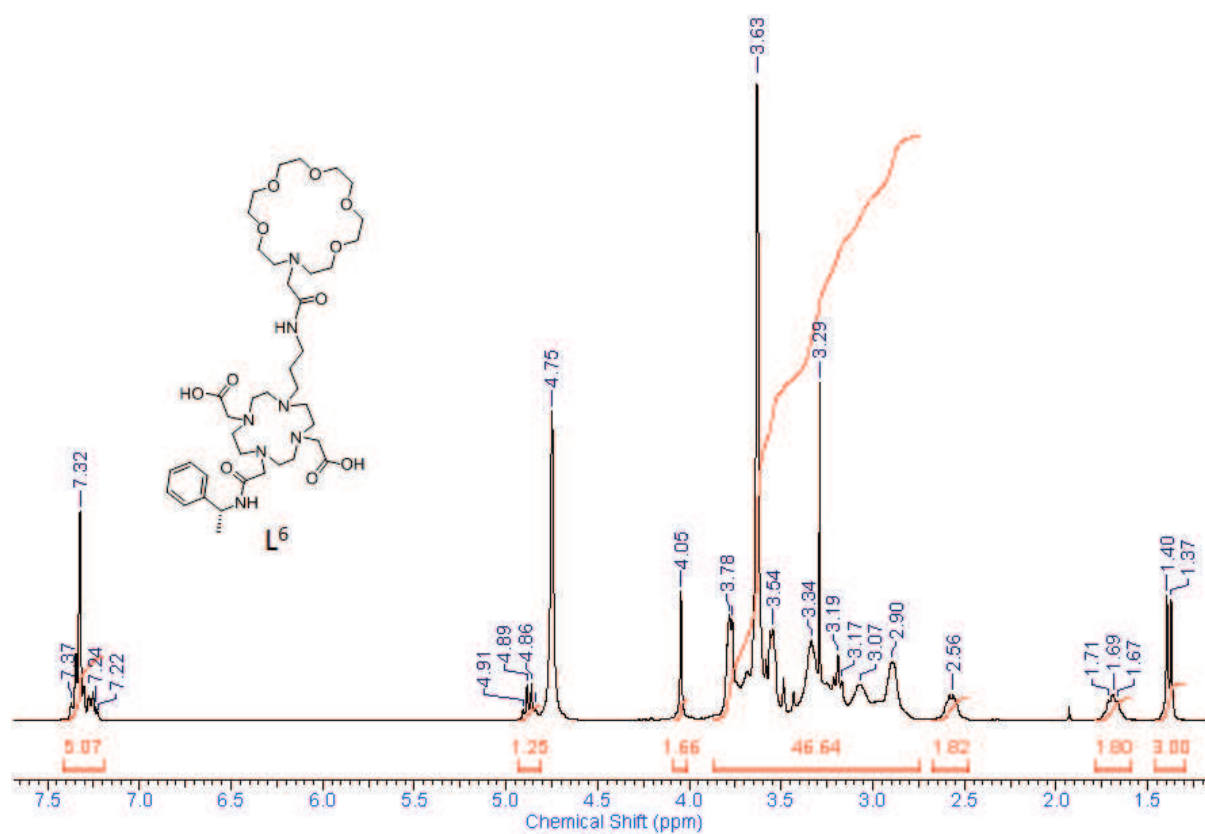
Neurotransmitter	Function	Disorder
Acetylcholine (mostly excitatory)	wakefulness, attentiveness, anger, aggression, sexuality, thirst...	Alzheimer's disease is associated with a lack of acetylcholine in certain regions of the brain.
Amino-acids :		
GABA (inhibitory)	motor control, vision, anxiety and many other cortical functions.	- Epilepsy - Huntington's disease.
Glutamate (excitatory)	Learning and memory	-Alzheimer's disease (memory malfunctions). - Lou Gehrig's disease (excessive glutamate production)
Bioactive amines:		
Dopamine (Inhibitory)	controlling movement and posture. It also modulates mood, Positive reinforcement and dependency	- muscle rigidity (Parkinson's disease) - schizophrenia - anxiety disorder
Norepinephrine	attentiveness, emotions, sleeping, dreaming, and learning.	mood disorders such as manic depression.
Serotonin	regulating body temperature, sleep, mood, appetite, and pain.	Depression, suicide, and aggressiveness appear to involve certain imbalances in serotonin

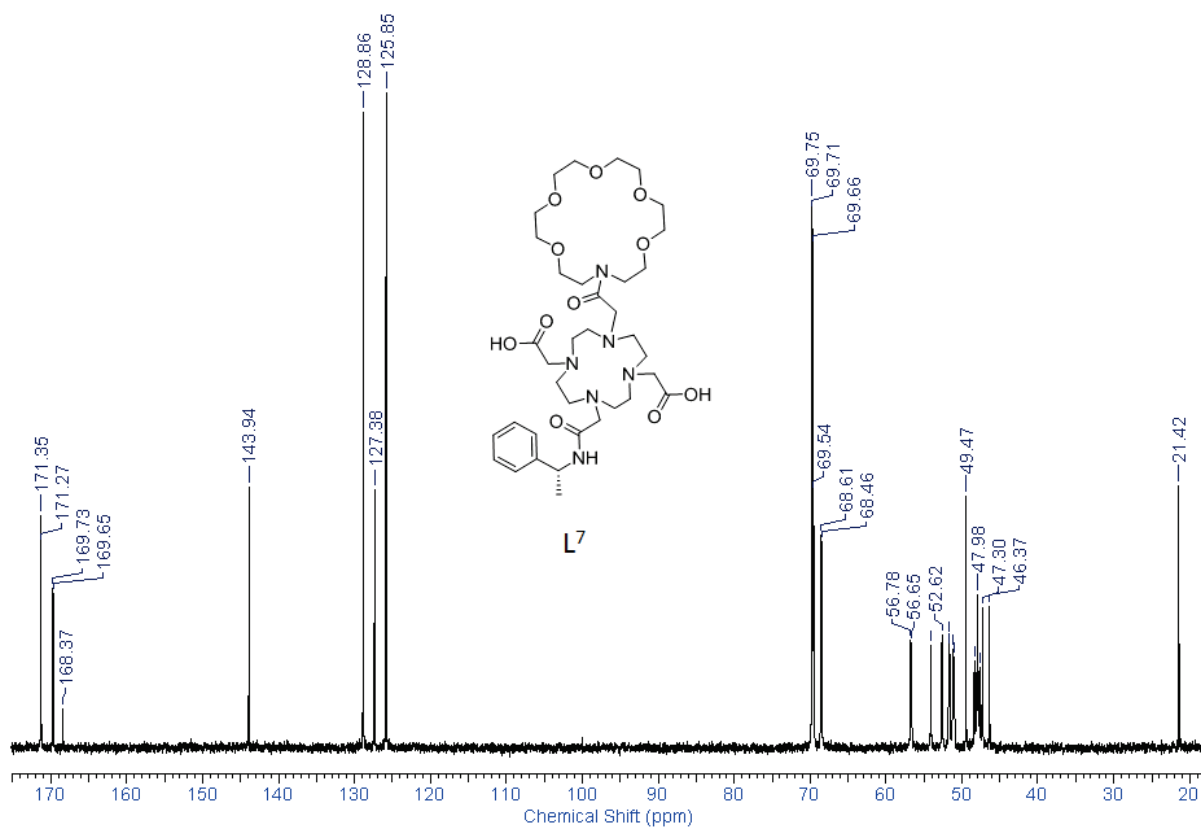
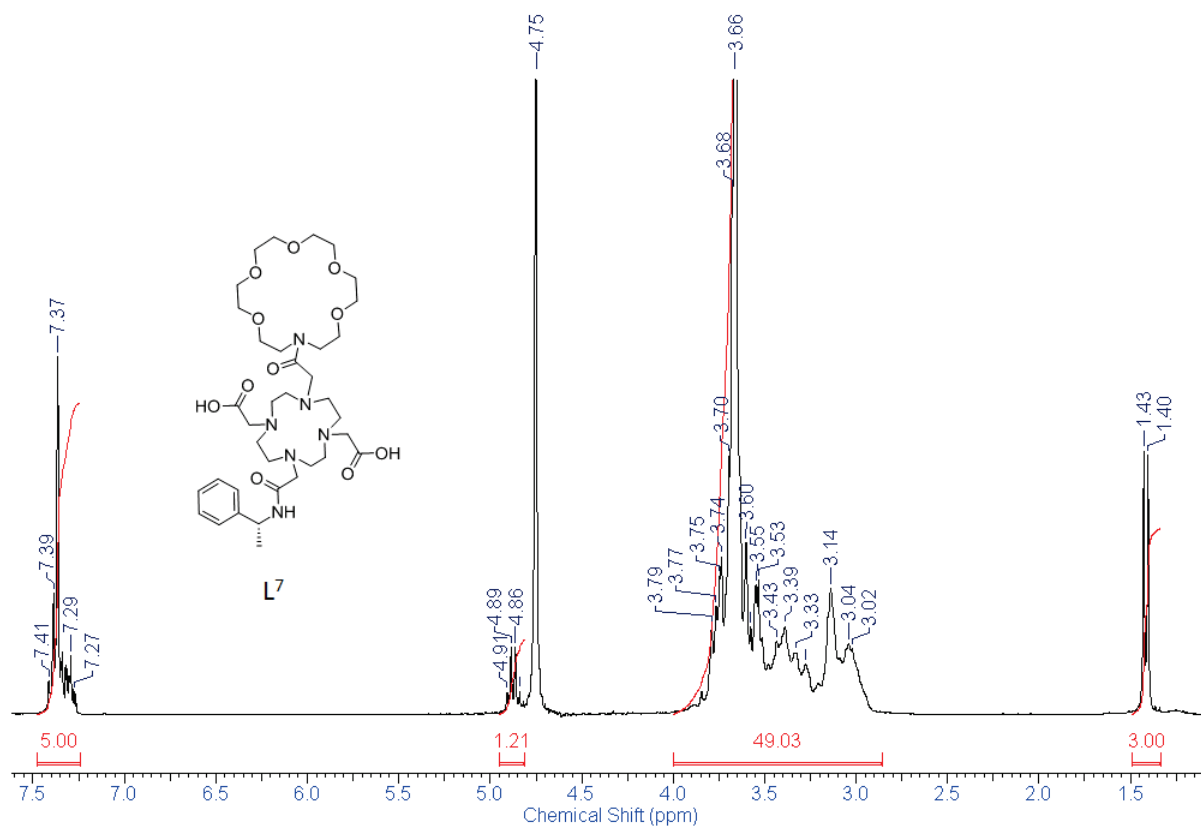
A.2. Reported concentration of some neurotransmitters

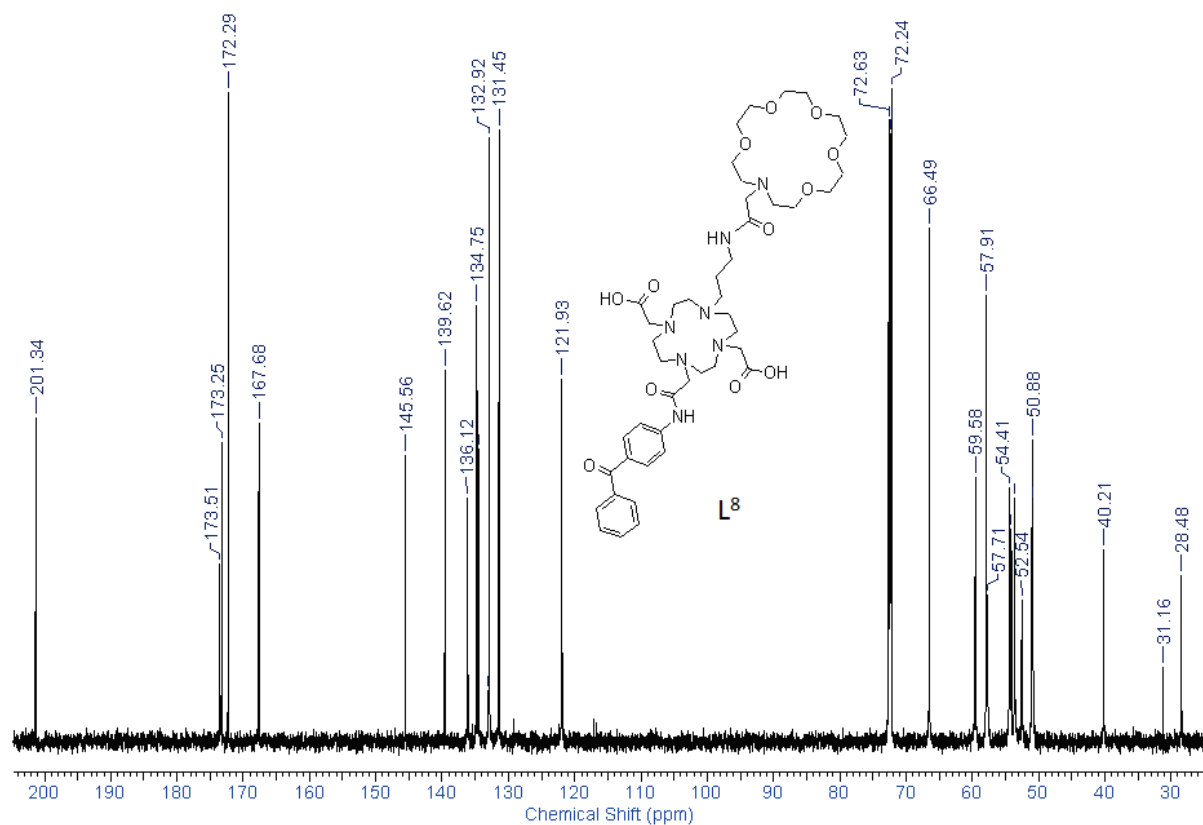
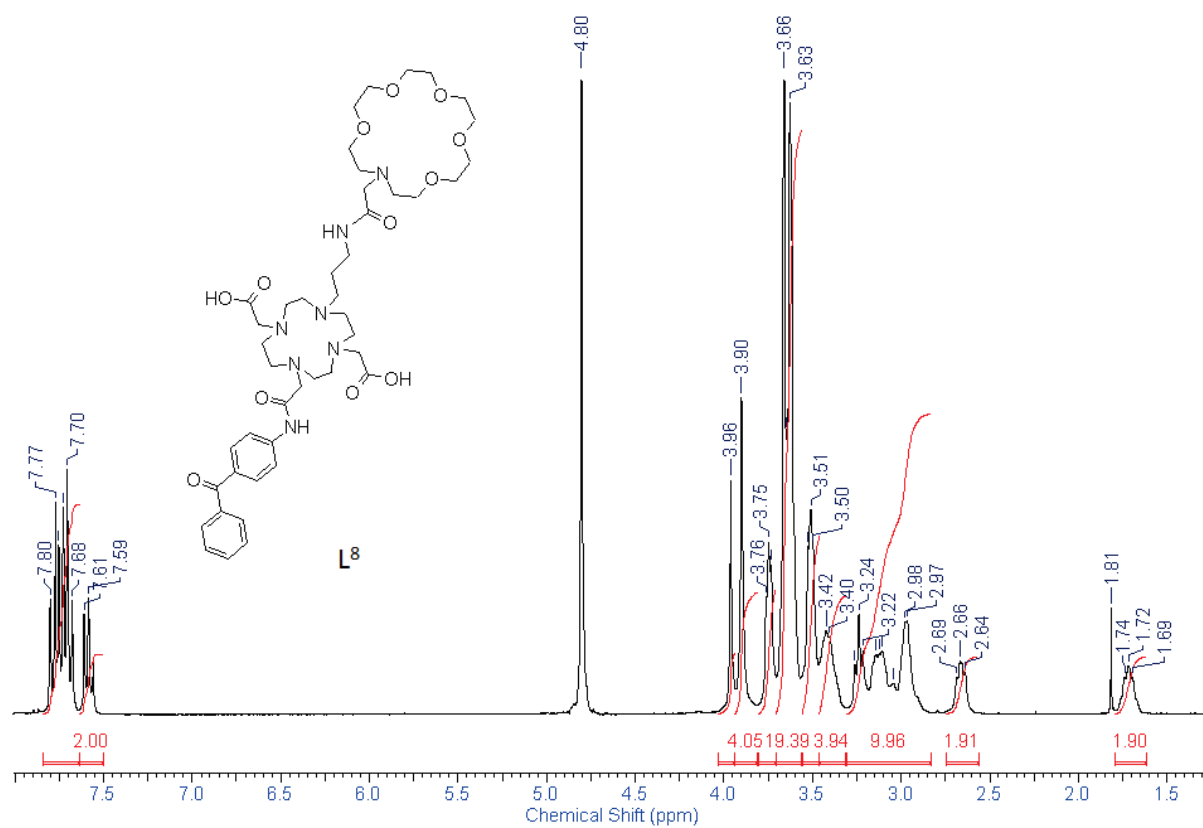
Transmitter	Conc	Method	Region	Reference	Species
Glutamine	246 – 572 μM	Microdialysis/ HPLC/LIF	Medial preoptic, Right frontal	Anderson 1999 Richards 2003	Rat Human
Glutamate	39.5 – 47.86 μM	LIF	Medial preoptic, Left frontal	Anderson 1999 Richards 2003	Rat Human
GABA	1.17 - 4.4 μM	LIF	Left frontal Medial, preoptic area	Richards 2003 Anderson 1999	Human Rat
Aspartate	8.9 – 11.59 μM	Microdialysis/ HPLC/EC,LIF	Medial preoptic area Left frontal	Anderson 1999 Richards 2003	Rat Human
Glycine	31.3 - 65.17 μM	EC, LIF	Medial preoptic area Left frontal	Anderson 1999 Richards 2003	Rat Human
Acetyl Choline	10.3 - 420 nM	MS, ECS	PFC	Zhang 2007 Gessa 1995	Monkey Cat

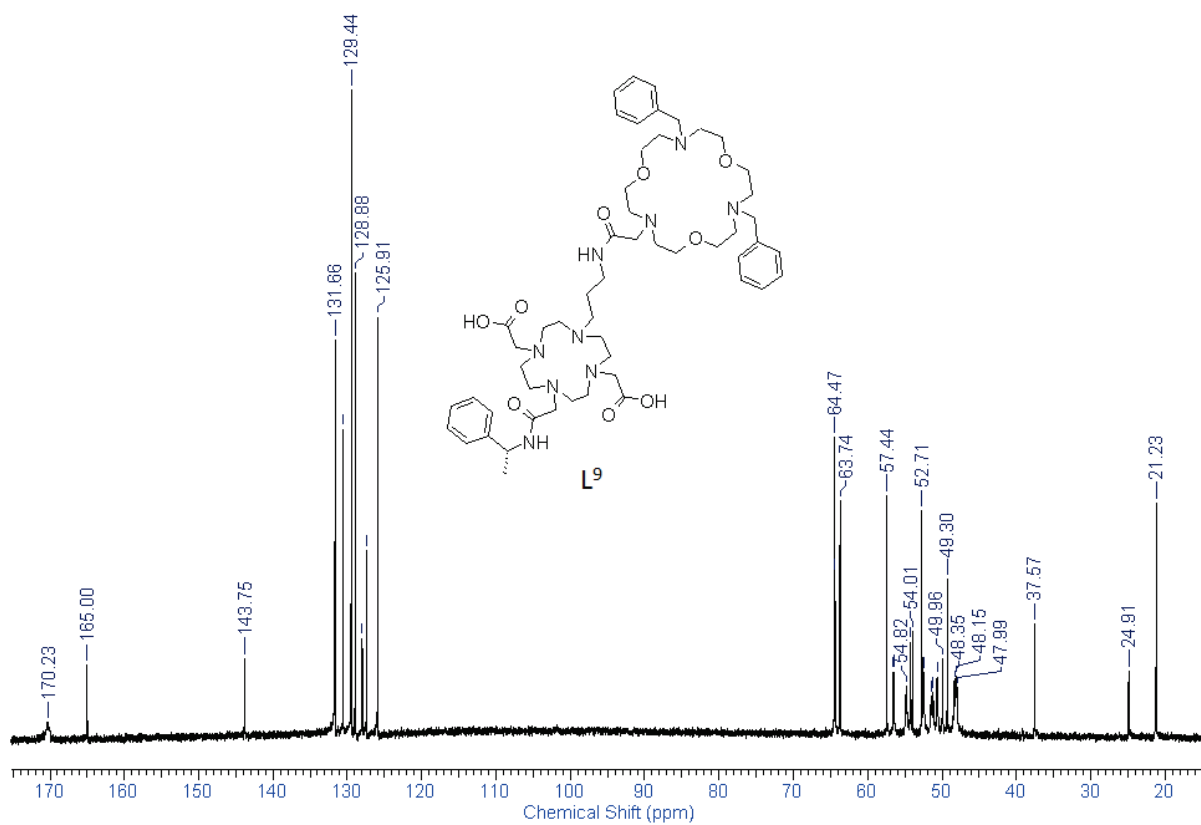
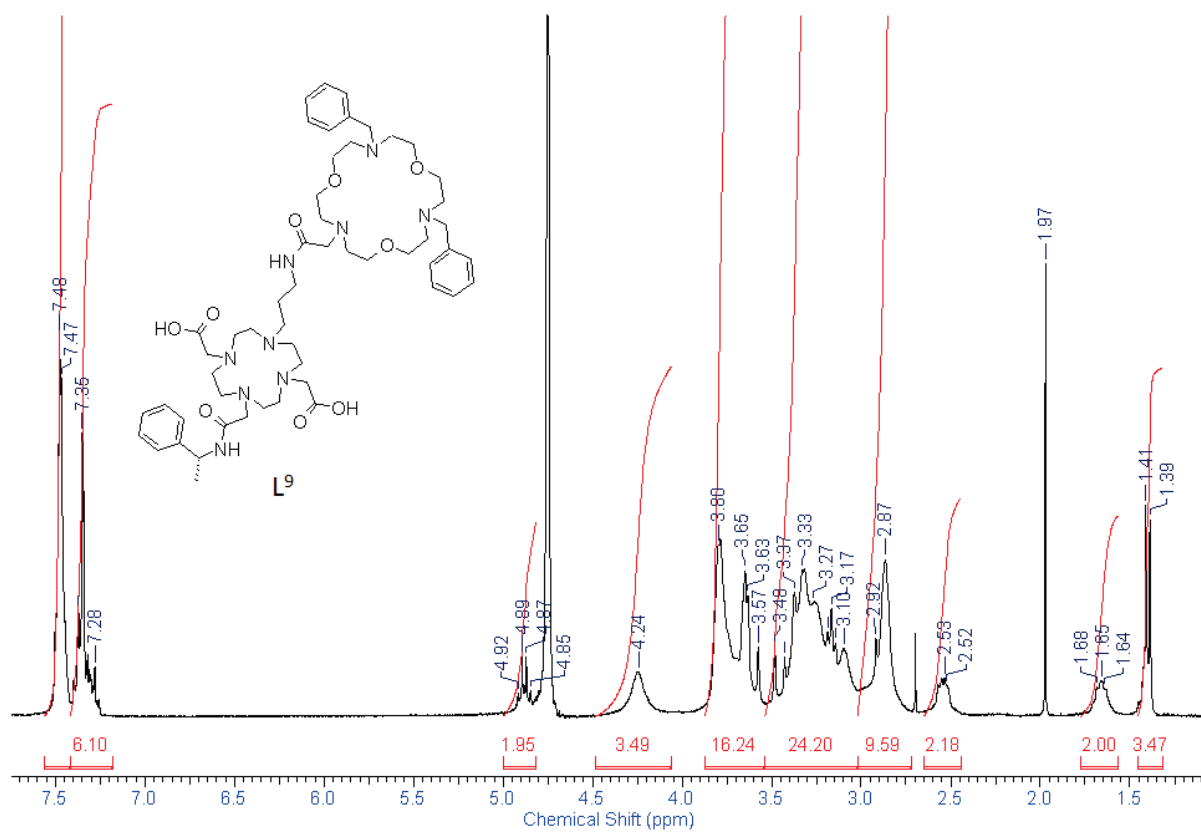
Transmitter	Conc	Method	Region	Reference	Species
Tyrosine	17.9 μM	LIF	Medial preoptic area	Anderson 1999	Rat
L-DOPA	475 – 505 nM	EC	Hypothalamus, medulla	Goldstein 1991	Rat
Dopamine	9.6 – 30.3 nM	MS,EC	Straitum, PFC	Nakahara 1988, Zhang 2007	Rat, Monkey
Noradrenaline	7.4 – 95 nM	EC	Medulla, hypothalamus	John 1998, Goldstein 1991	Rat
Adrenaline	5 - 65 nM	EC	Medulla, hypothalamus	John 1998 Marsedn 1987	Rat

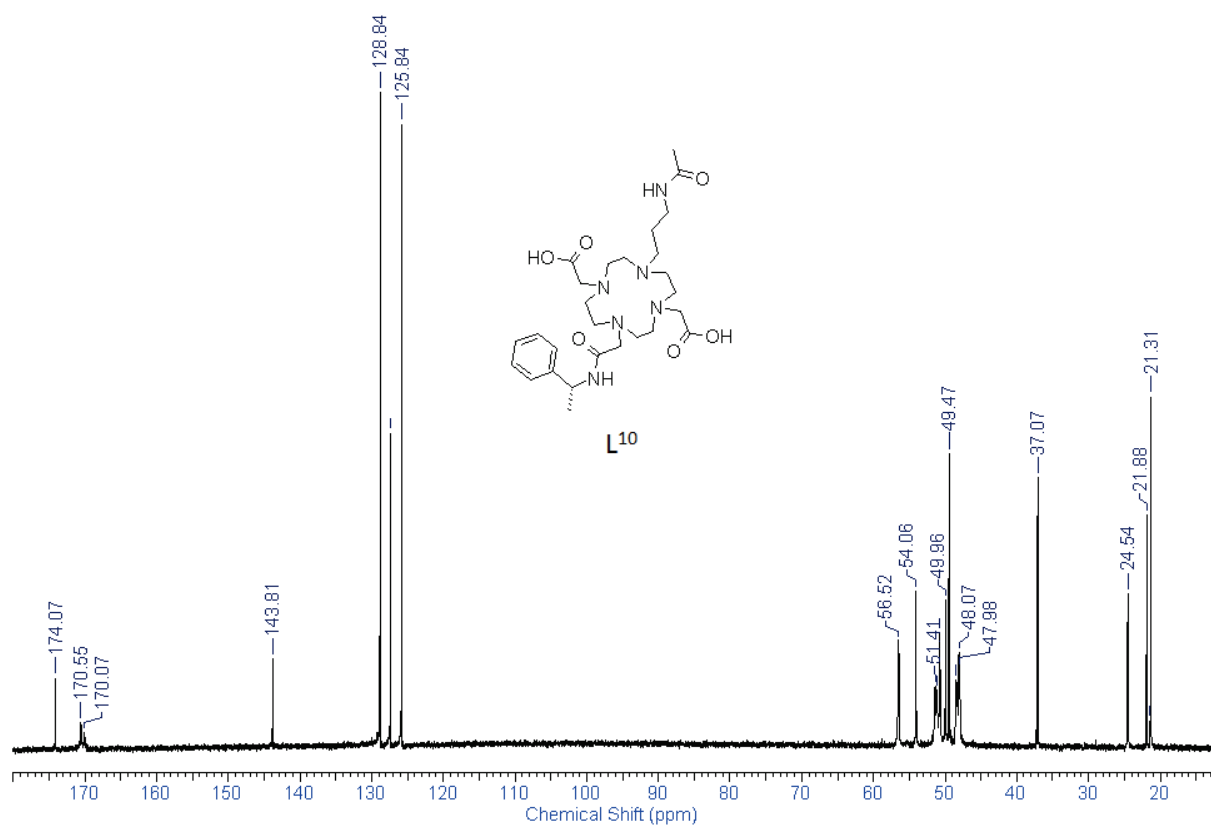
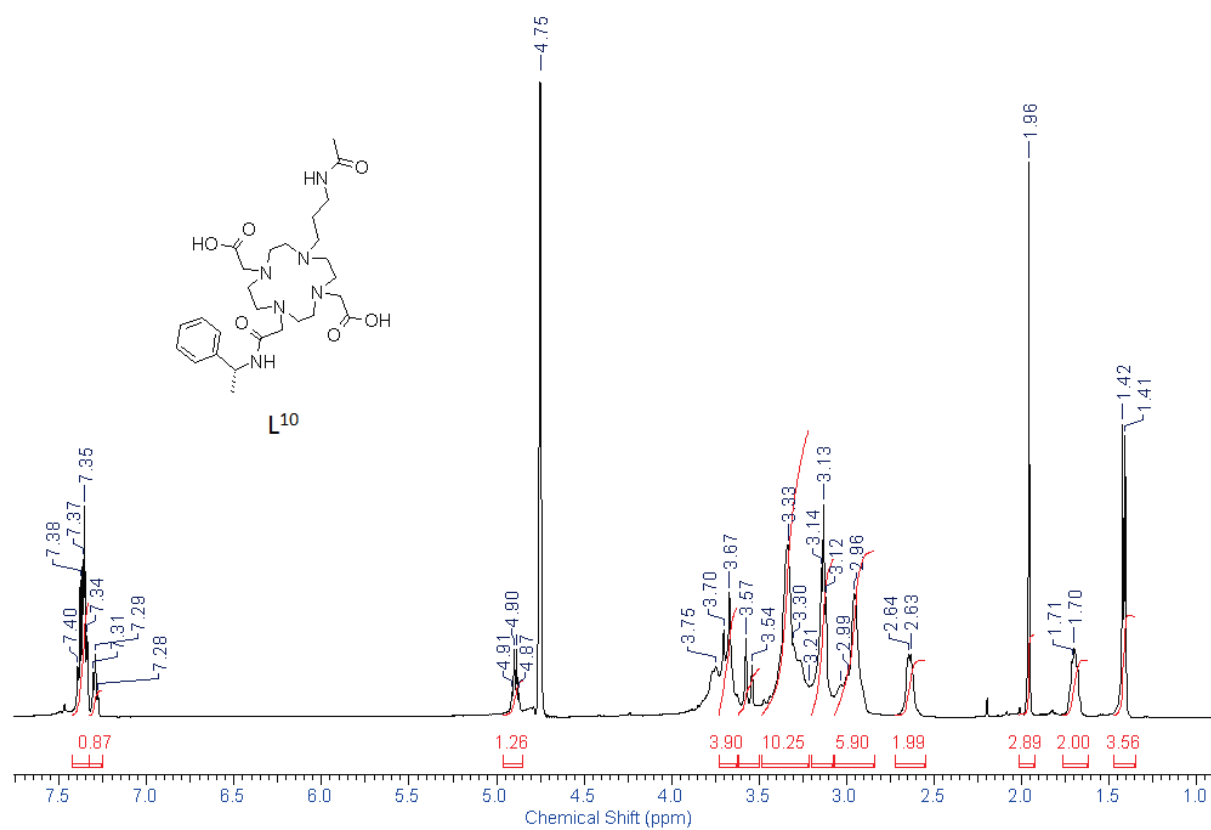
A.3. ^1H & ^{13}C NMR spectra of L^{5-11} and EuL^{5-8} 

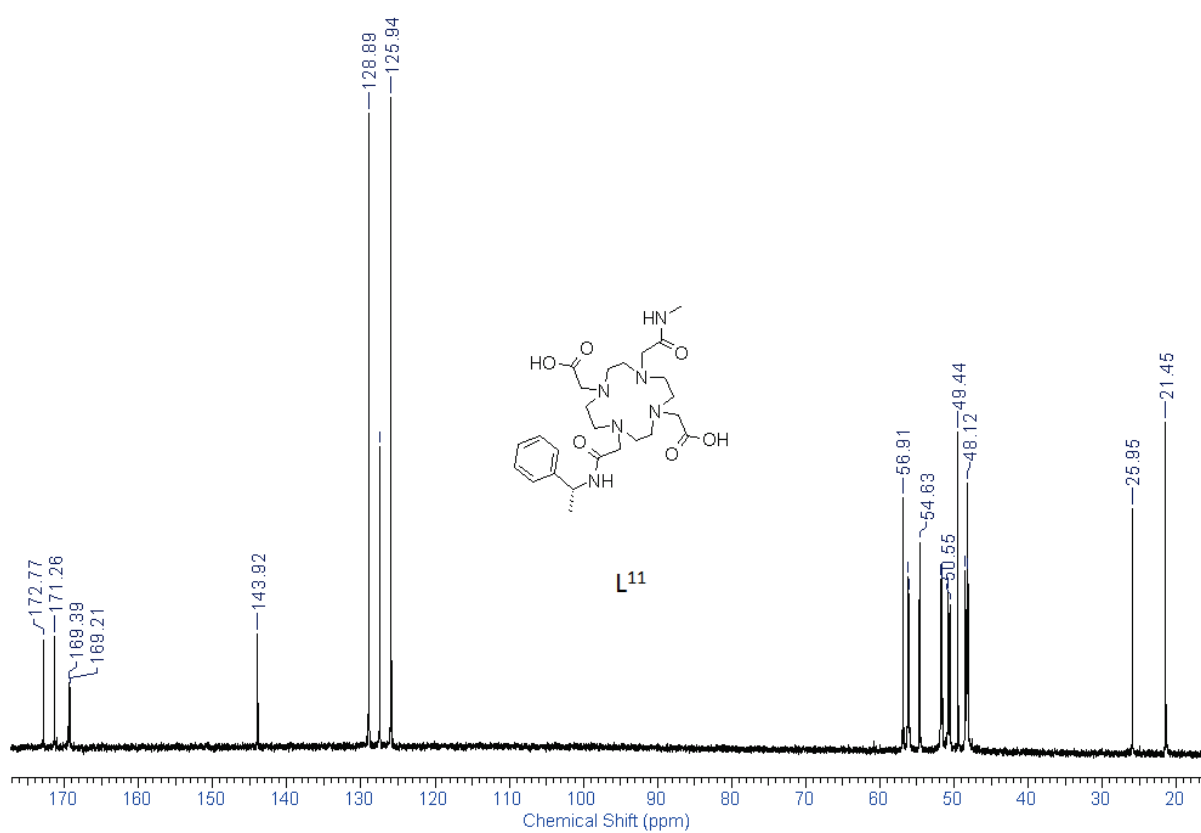
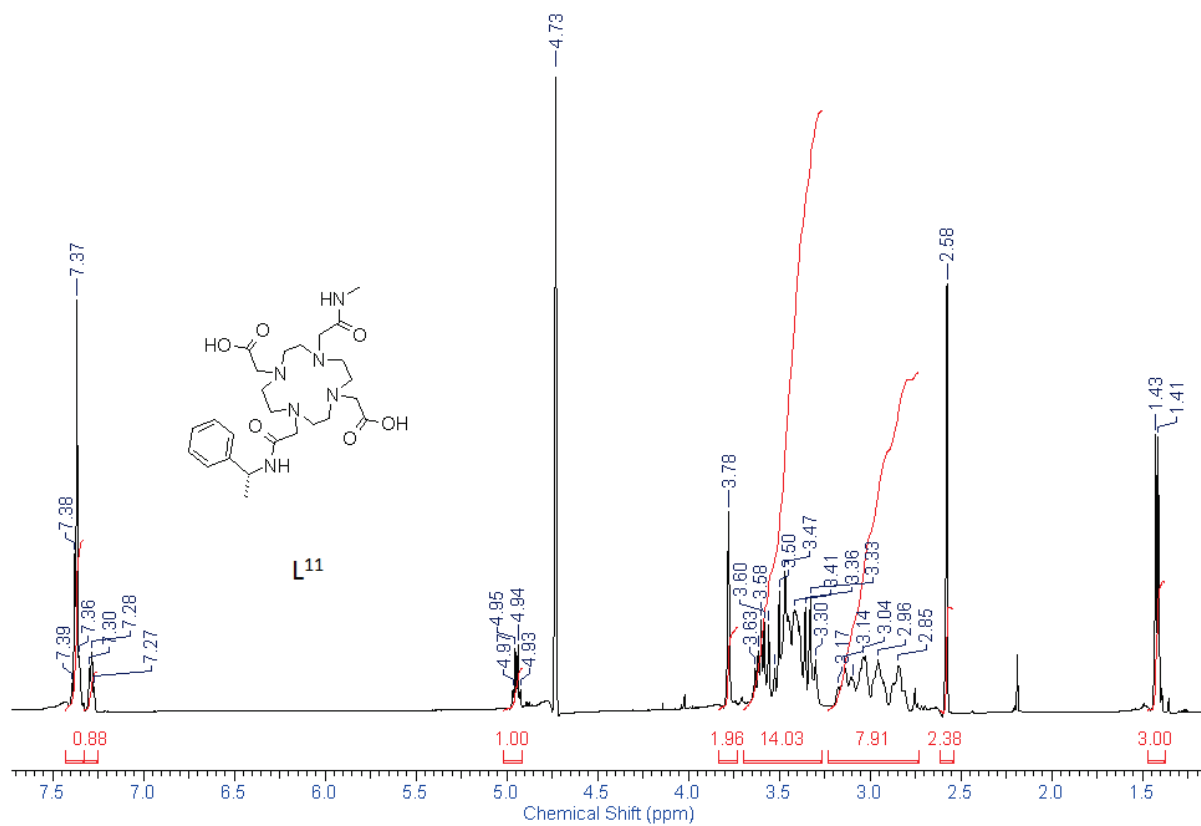


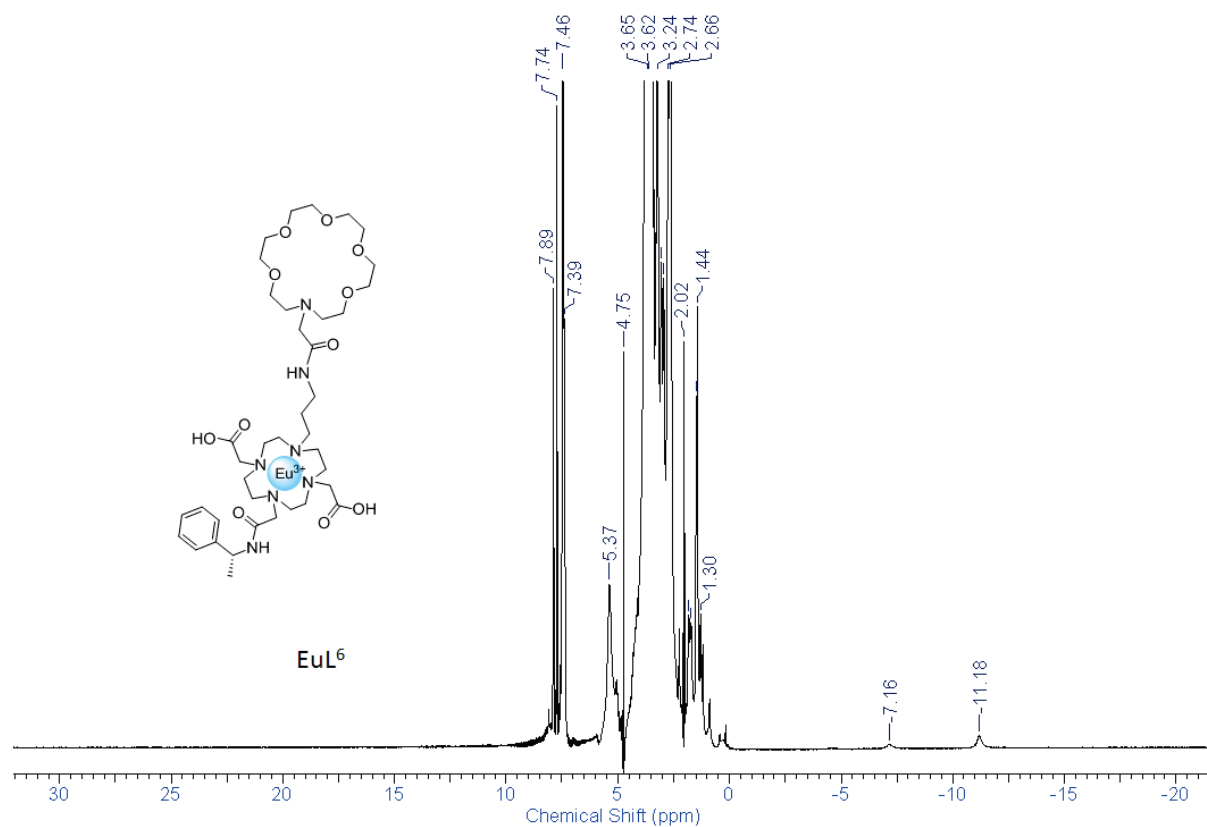
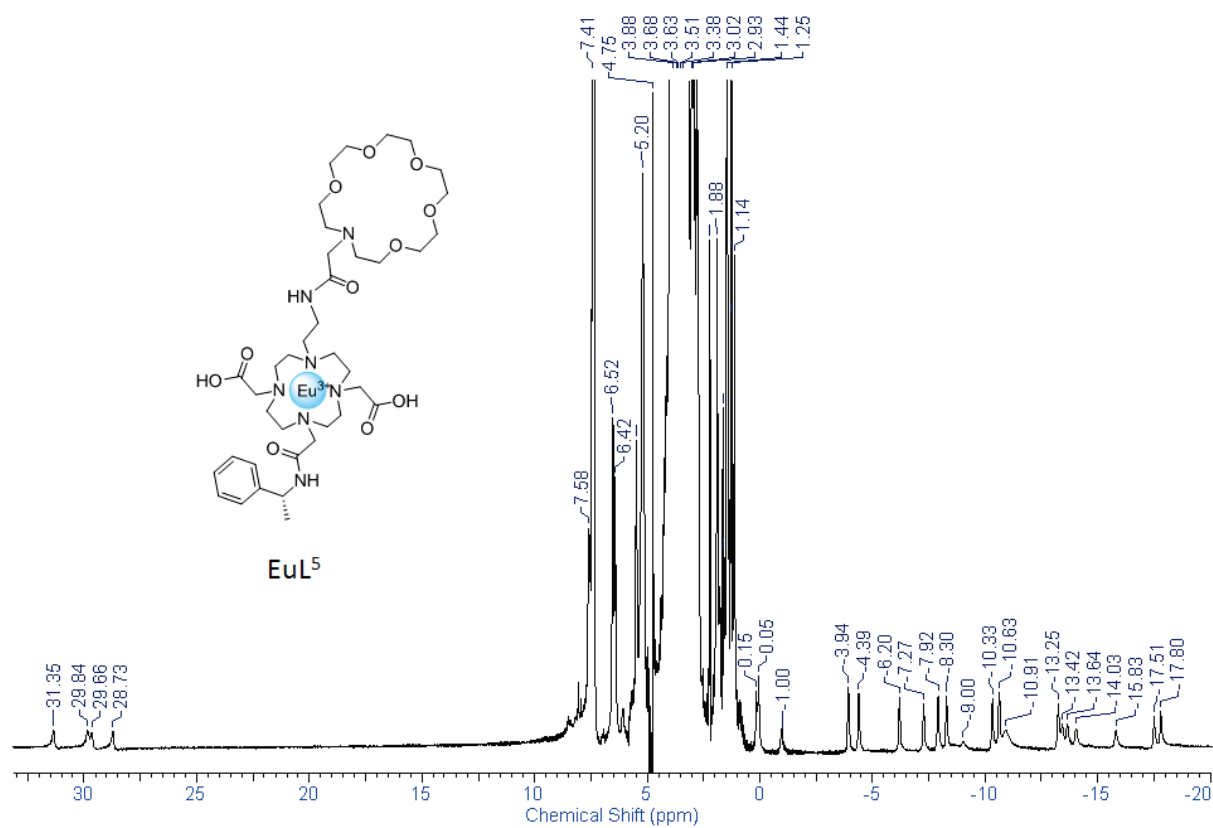


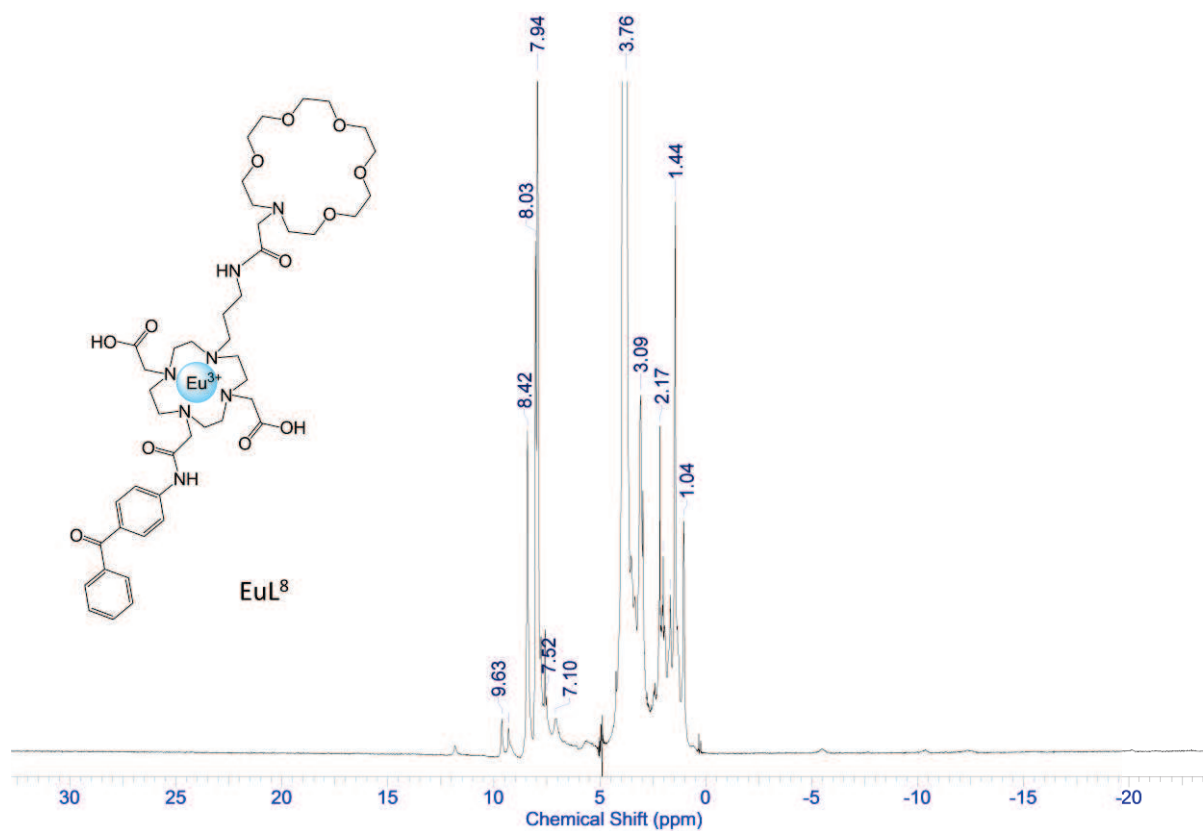
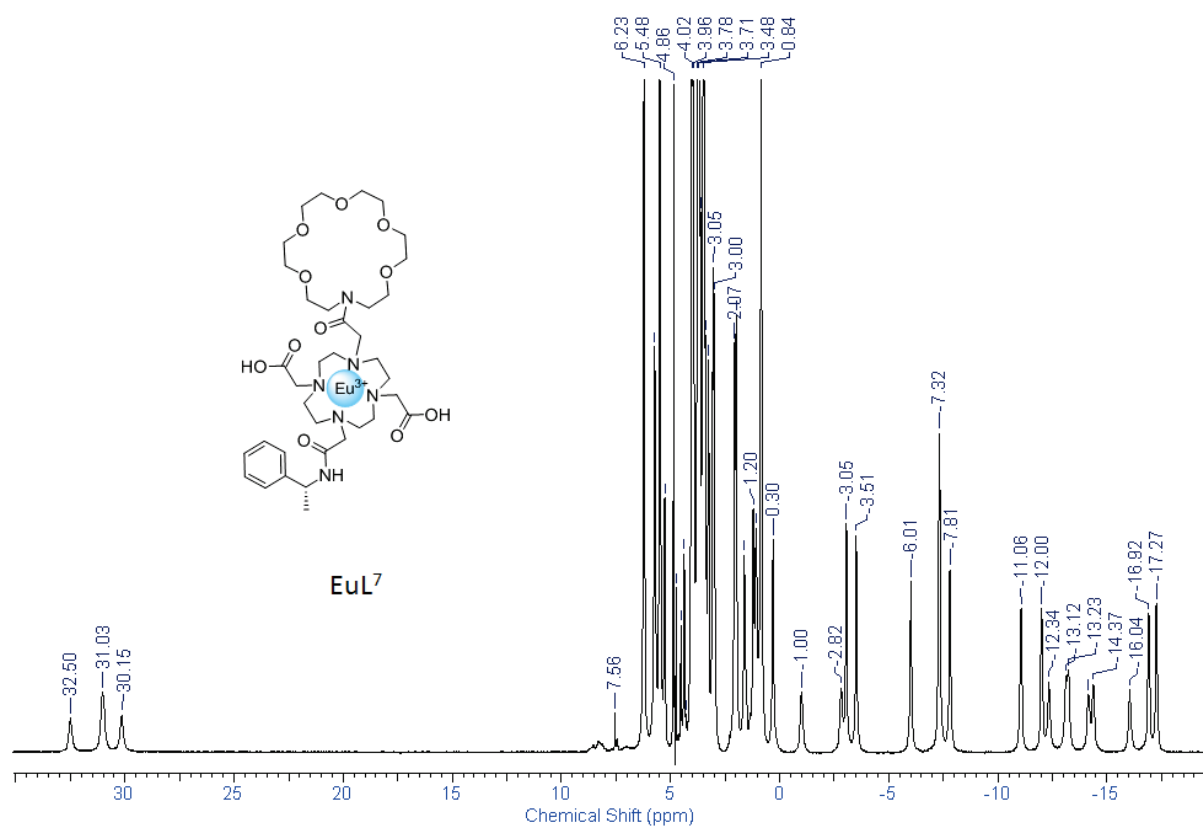












A.4. Equations used for the fits of ^{17}O NMR and ^1H NMRD Data

^{17}O NMR spectroscopy

From the measured ^{17}O NMR relaxation rates and angular frequencies of the paramagnetic solutions, $1/T_1$, $1/T_2$ and ω , and from the acidified water reference, $1/T_{1A}$, $1/T_{2A}$ and ω_A , it is possible to calculate the reduced relaxation rates and chemical shifts, $1/T_{1r}$, $1/T_{2r}$ and $\Delta\omega_r$ (Eq. 1-3), where $1/T_{1m}$, $1/T_{2m}$ are the relaxation rates of the bound water and $\Delta\omega_m$ is the chemical shift difference between bound and bulk water, τ_m is the mean residence time or the inverse of the water exchange rate k_{ex} and P_m is the mole fraction of the bound water [1,2]

$$\frac{1}{T_{1r}} = \frac{1}{P_m} \left[\frac{1}{T_1} - \frac{1}{T_{1A}} \right] = \frac{1}{T_{1m} + \tau_m} + \frac{1}{T_{1os}} \quad (1)$$

$$\frac{1}{T_{2r}} = \frac{1}{P_m} \left[\frac{1}{T_2} - \frac{1}{T_{2A}} \right] = \frac{1}{\tau_m} \frac{T_{2m}^{-2} + \tau_m^{-1} T_{2m}^{-1} + \Delta\omega_m^2}{(\tau_m^{-1} + T_{2m}^{-1})^2 + \Delta\omega_m^2} + \frac{1}{T_{2os}} \quad (2)$$

$$\Delta\omega_r = \frac{1}{P_m} (\omega - \omega_A) = \frac{\Delta\omega_m}{(1 + \tau_m T_{2m}^{-1})^2 + \tau_m^2 \Delta\omega_m^2} + \Delta\omega_{os} \quad (3)$$

The outer sphere contributions to the ^{17}O relaxation rates $1/T_{1os}$ and $1/T_{2os}$ can be neglected according to previous studies [3]. Therefore, Eqs. 1-2 can be further simplified into Eqs. 4-5:

$$\frac{1}{T_{1r}} = \frac{1}{T_{1m} + \tau_m} \quad (4)$$

$$\frac{1}{T_{2r}} = \frac{1}{T_{2m} + \tau_m} \quad (5)$$

The exchange rate is assumed to be described by the Eyring equation (Eq 6), where ΔS^\ddagger and ΔH^\ddagger are the entropy and enthalpy of activation for the water exchange process, and k_{ex}^{298} is the exchange rate at 298.15 K. R is the usual gas constant whereas h and k_B are the Planck and Boltzmann constants, respectively:

$$\frac{1}{\tau_m} = k_{ex} = \frac{k_B T}{h} \exp \left\{ \frac{\Delta S^\ddagger}{R} - \frac{\Delta H^\ddagger}{RT} \right\} = \frac{k_{ex}^{298} T}{298.15} \exp \left\{ \frac{\Delta H^\ddagger}{R} \left(\frac{1}{298.15} - \frac{1}{T} \right) \right\} \quad (6)$$

In the transverse relaxation the scalar contribution, $1/T_{2sc}$, is the most important Eq. 7. $1/\tau_{s1}$ is the sum of the exchange rate constant and the electron spin relaxation rate.

$$\frac{1}{T_{2m}} \cong \frac{1}{T_{2sc}} = \frac{S(S+1)}{3} \left(\frac{A}{\hbar} \right)^2 \left(\tau_{s1} + \frac{\tau_{s2}}{1 + \omega_S^2 \tau_{s2}^2} \right) \quad (7)$$

$$\frac{1}{\tau_{s1}} = \frac{1}{\tau_m} + \frac{1}{T_{1e}} \quad (7b)$$

The ^{17}O longitudinal relaxation rates in Gd^{III} solutions are the sum of the contributions of the dipole-dipole (dd) and quadrupolar (q) mechanisms as expressed by Eq. 10-12 for non-extreme narrowing conditions, where γ_s is the electron and γ_I is the nuclear gyromagnetic ratio ($\gamma_s = 1.76 \times 10^{11} \text{ rad s}^{-1} \text{ T}^{-1}$, $\gamma_I = -3.626 \times 10^7 \text{ rad s}^{-1} \text{ T}^{-1}$), r_{GdO} is the effective distance between the electron charge and the ^{17}O nucleus, I is the nuclear spin (5/2 for ^{17}O), χ is the quadrupolar coupling constant and η is an asymmetry parameter :

$$\frac{1}{T_{1m}} = \frac{1}{T_{1dd}} + \frac{1}{T_{1q}} \quad (8)$$

with:

$$\frac{1}{T_{1dd}} = \frac{2}{15} \left(\frac{\mu_0}{4\pi} \right)^2 \frac{\hbar^2 \gamma_I^2 \gamma_S^2}{r_{GdO}^6} S(S+1) \times [3J(\omega_I; \tau_{d1}) + 7J(\omega_S; \tau_{d2})] \quad (9)$$

$$\frac{1}{T_{1q}} = \frac{3\pi^2}{10} \frac{2I+3}{I^2(2I-1)} \chi^2 (1 + \eta^2/3) \times [0.2J_1(\omega_I) + 0.8J_2(\omega_I)] \quad (10)$$

In Eq. 3, the chemical shift of the bound water molecule, $\Delta\omega_m$, depends on the hyperfine interaction between the Gd^{III} electron spin and the ^{17}O nucleus and is directly proportional to the scalar coupling constant, A/\hbar , as expressed in Eq. 11.[4]

The isotopic Landé g factor is equal to 2.0 for the Gd^{III} , B represents the magnetic field, and k_B is the Boltzmann constant.

$$\Delta\omega_m = \frac{g_L \mu_B S(S+1) B}{3k_B T} \frac{A}{\hbar} \quad (11)$$

The outer sphere term of the chemical shift was found proportional to $\Delta\omega_m$, through an empirical constant C_{os} . [5]

$$\Delta\omega_{os} = C_{os} \Delta\omega_m \quad (12)$$

¹H NMRD relaxivity

The measured longitudinal proton relaxation rate, R_1^{obs} is the sum of a paramagnetic and a diamagnetic contribution as expressed in Eq. 13, where r_l is the proton relaxivity:

$$R_1^{obs} = R_1^d + R_1^p = R_1^d + r_l C_{Gd} \quad (13)$$

The relaxivity can be divided into terms of inner and outer sphere, as follows:

$$r_l = r_{lis} + r_{los} \quad (14)$$

The inner sphere term is obtained in Eq. 15, where q is the number of inner sphere water molecules [6].

$$r_{lis} = \frac{1}{1000} \times \frac{q}{55.55} \times \frac{1}{T_{1m}^H + \tau_m} \quad (15)$$

The longitudinal relaxation rate of inner sphere protons, $1/T_{1m}^H$ is expressed by Eq. 16, where r_{GdH} is the effective distance between the electron charge and the ¹H nucleus, ω_l is the proton resonance frequency and ω_s is the Larmor frequency of the Gd^{III} electron spin.

$$\frac{1}{T_{1m}^H} = \frac{2}{15} \left(\frac{\mu_0}{4\pi} \right)^2 \frac{\hbar^2 \gamma_l^2 \gamma_s^2}{r_{GdH}^6} S(S+1) \times [3J(\omega_l; \tau_{d1}) + 7J(\omega_s; \tau_{d2})] \quad (16)$$

$$\frac{1}{\tau_{di}} = \frac{1}{\tau_m} + \frac{1}{\tau} + \frac{1}{T_{ie}} \quad (17)$$

The longitudinal and transverse electronic relaxation rates, $1/T_{1e}$ and $1/T_{2e}$ are expressed by Eq. 18-19, where τ_v is the electronic correlation time for the modulation of the zero-field-splitting interaction, E_v the corresponding activation energy and Δ^2 is the mean square zero-field-splitting energy. We assumed a simple exponential dependence of τ_v versus $1/T$ as written in Eq. 20.

$$\left(\frac{1}{T_{1e}}\right)^{ZFS} = \frac{1}{25} \Delta^2 \tau_v \{4S(S+1) - 3\} \left(\frac{1}{1 + \omega_S^2 \tau_v^2} + \frac{4}{1 + 4\omega_S^2 \tau_v^2} \right) \quad (18)$$

$$\left(\frac{1}{T_{2e}}\right)^{ZFS} = \Delta^2 \tau_v \left(\frac{5.26}{1 + 0.372\omega_S^2 \tau_v^2} + \frac{7.18}{1 + 1.24\omega_S \tau_v} \right) \quad (19)$$

$$\tau_v = \tau_v^{298} \exp\left\{ \frac{E_v}{R} \left(\frac{1}{T} - \frac{1}{298.15} \right) \right\} \quad (20)$$

The outer-sphere contribution can be described by Eq. 21 where N_A is the Avogadro constant, and J_{os} is its associated spectral density function [7,8].

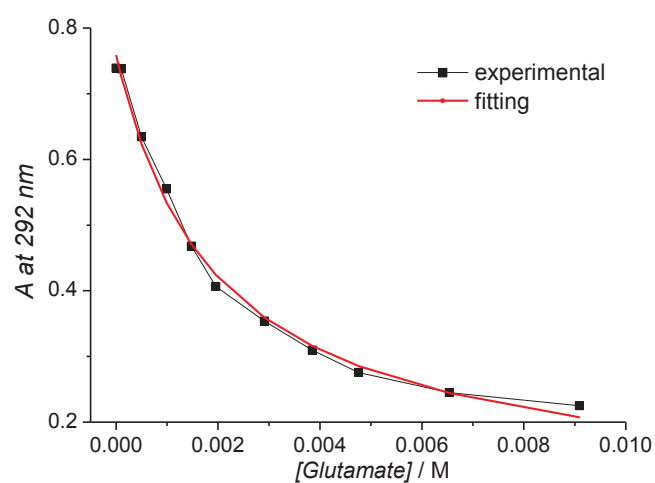
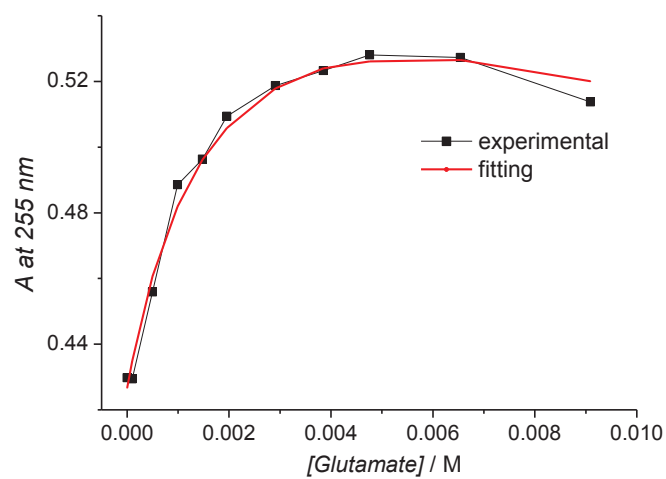
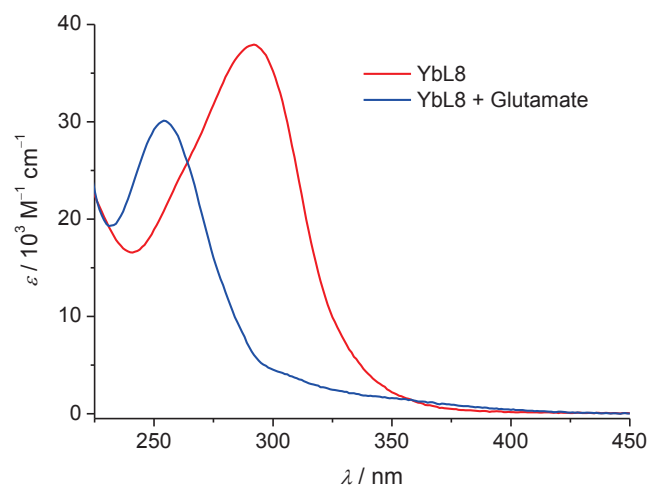
$$r_{1os} = \frac{32N_A\pi}{405} \left(\frac{\mu_0}{4\pi}\right)^2 \frac{\hbar^2 \gamma_S^2 \gamma_I^2}{a_{GdH} D_{GdH}} S(S+1) [3J_{os}(\omega_I, T_{1e}) + 7J_{os}(\omega_S, T_{2e})] \quad (21)$$

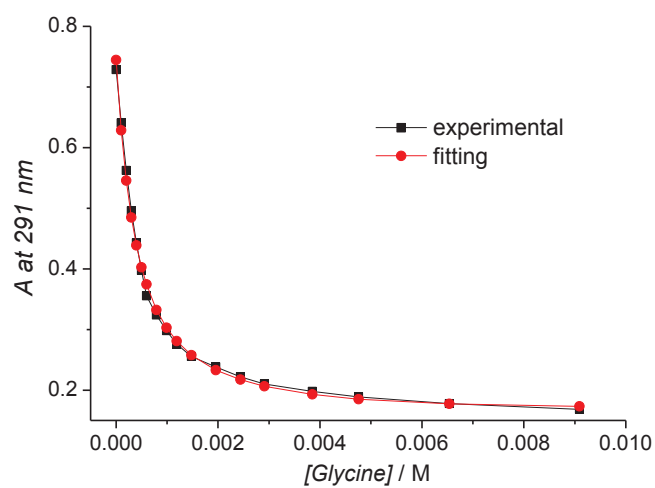
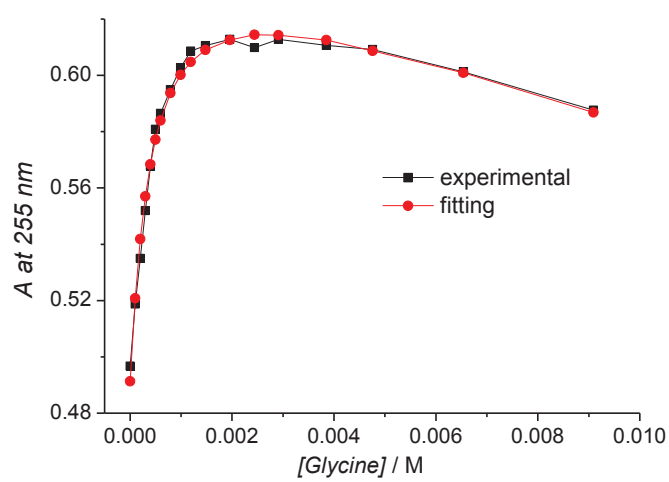
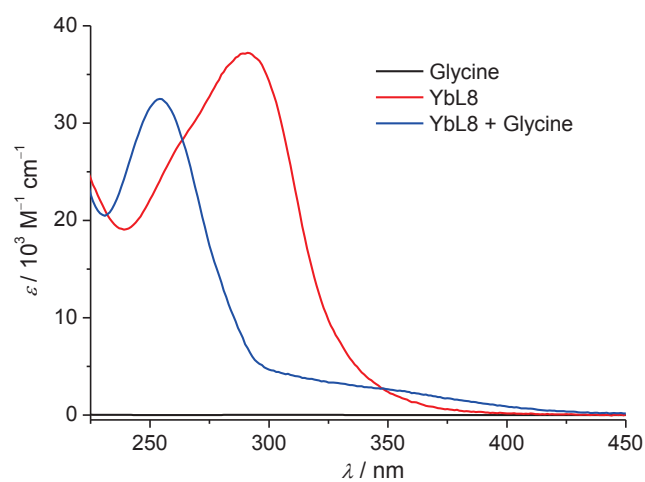
$$J_{os}(\omega, T_{je}) = Re \left[\frac{1 + \frac{1}{4} \left(i\omega\tau_{GdH} + \frac{\tau_{GdH}}{T_{je}} \right)^{1/2}}{1 + \left(i\omega\tau_{GdH} + \frac{\tau_{GdH}}{T_{je}} \right)^{1/2} + \frac{4}{9} \left(i\omega\tau_{GdH} + \frac{\tau_{GdH}}{T_{je}} \right) + \frac{1}{9} \left(i\omega\tau_{GdH} + \frac{\tau_{GdH}}{T_{je}} \right)^{3/2}} \right] \quad j = 1, 2 \quad (22)$$

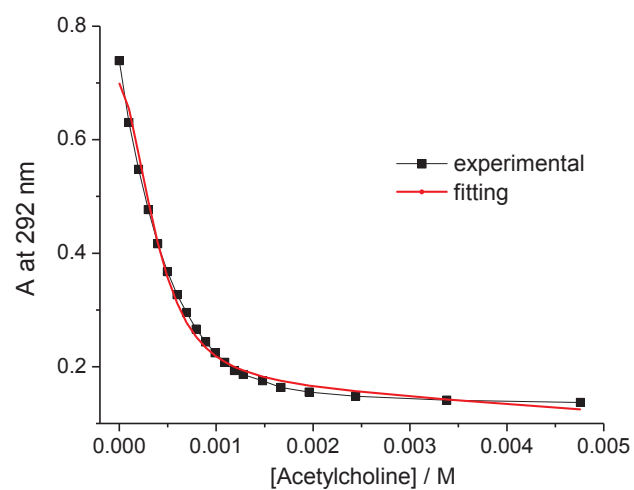
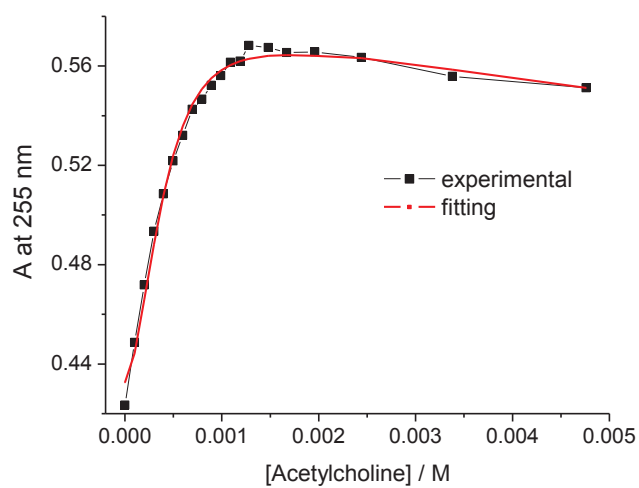
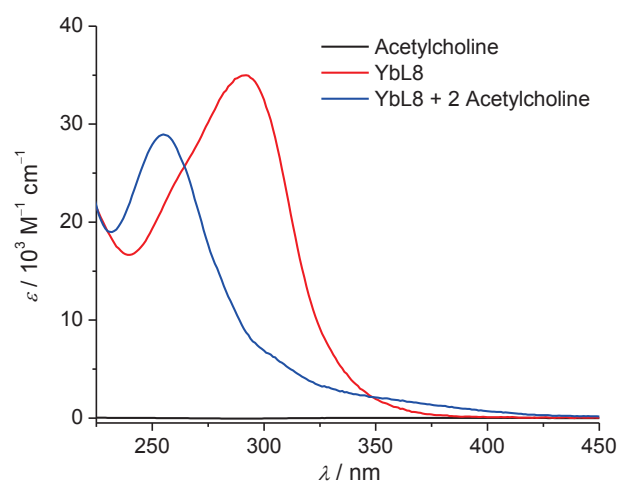
The diffusion coefficient for the diffusion of a water proton away from a Gd^{III} complex, D_{GdH} , is assumed to obey an exponential law versus the inverse of the temperature, with an activation energy E_{GdH} , as given in Eq. 23. D_{GdH}^{298} is the diffusion coefficient at 298.15 K.

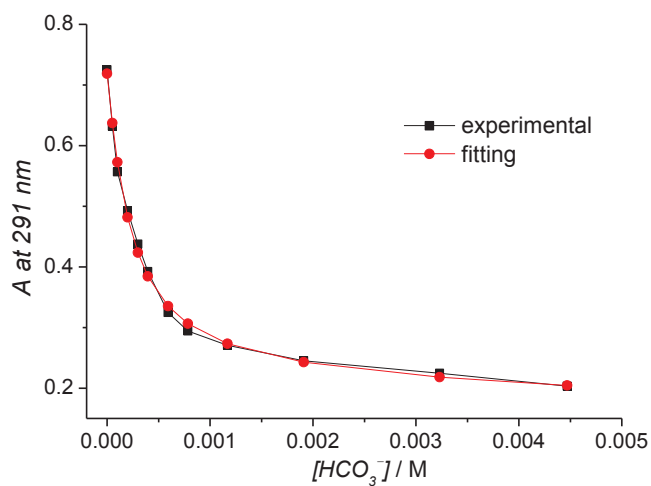
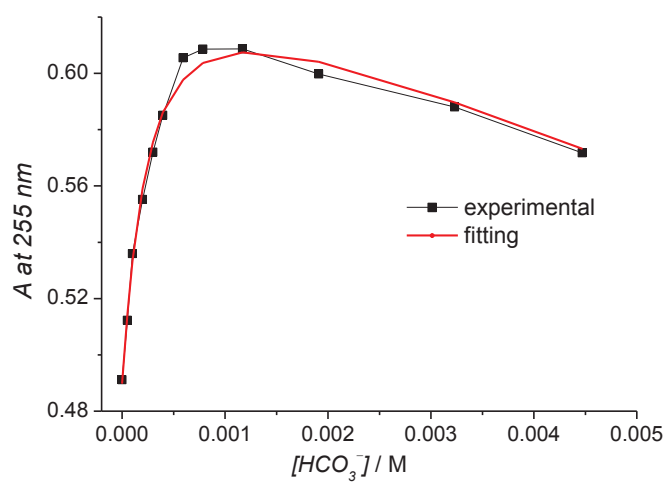
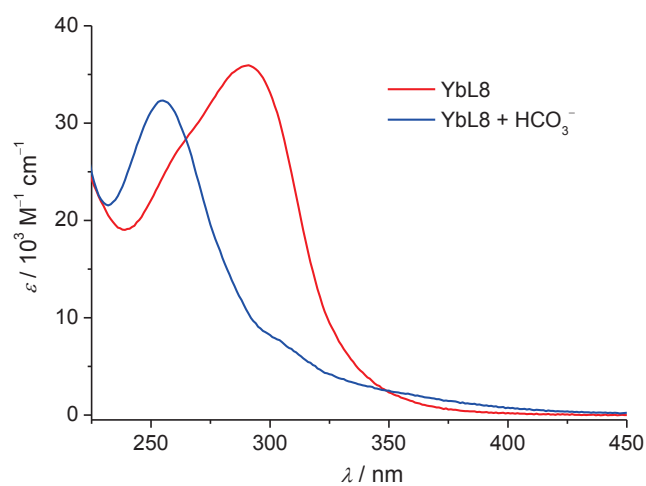
$$D_{\text{GdH}} = D_{\text{GdH}}^{298} \exp \left\{ \frac{E_{\text{GdH}}}{R} \left(\frac{1}{298.15} - \frac{1}{T} \right) \right\} \quad (23)$$

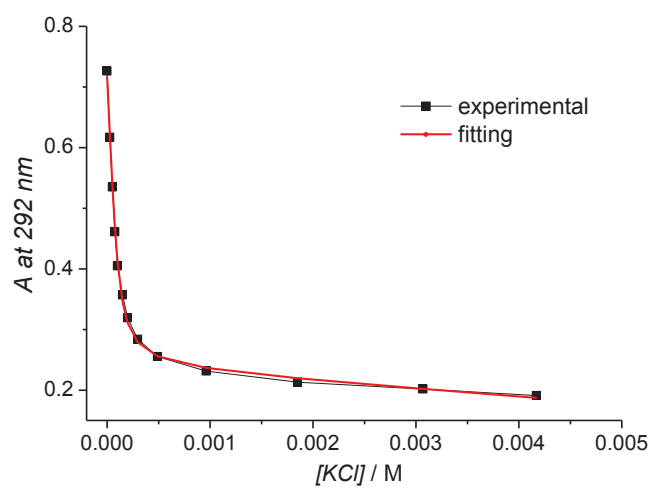
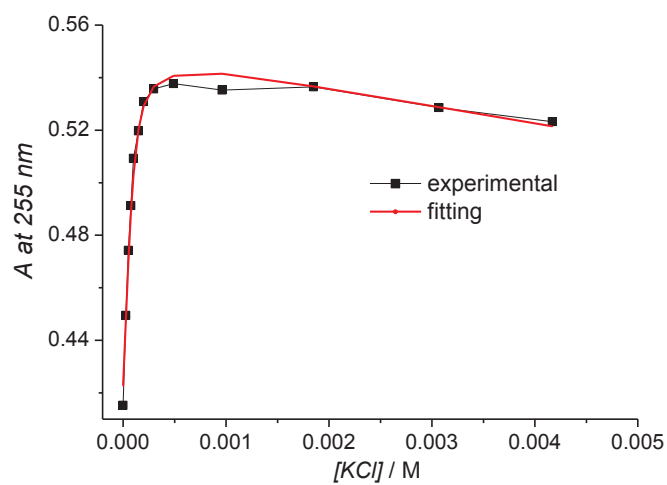
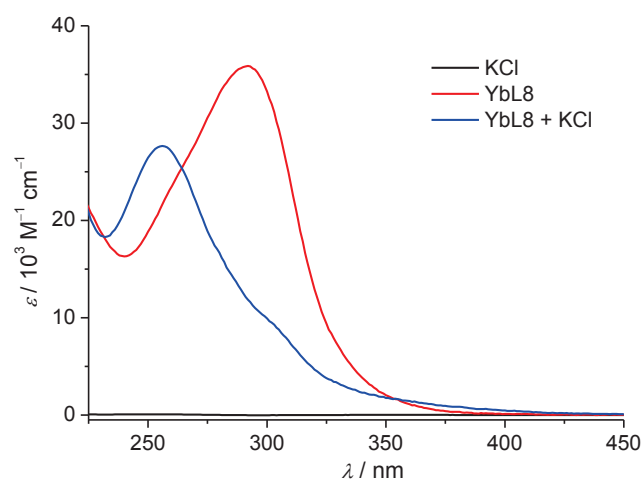
- [1] T. J. Swift, R. E. Connick, *J.Chem.Phys.* **1962**, *37*, 2, 307.
- [2] J. R. Zimmermann, W. E. Brittain, *Journal of Physical Chemistry*, **1957**, *61*, 1328.
- [3] K. Micskei, L. Helm, E. Brücher, A. E. Merbach, *Inorganic Chemistry* **1993**, *32*, 3844.
- [4] H. G. Brittain, J. F. Desreux, *Inorg.Chem.* **1984**, *23*, 4459.
- [5] G. González, D. H. Powell, V. Tissières, A. E. Merbach, *Journal of Physical Chemistry* **1994**, *98*, 53.
- [6] Z. Luz, S. Meiboom, *J. Chem. Phys.* **1964**, *40*, 2686.
- [7] J. H. Freed, *J.Chem.Phys.* **1978**, *68*, 4034.
- [8] S. H. Koenig, R. D. I. Brown, *Progress in NMR Spectroscopy* **1991**, *22*, 487.

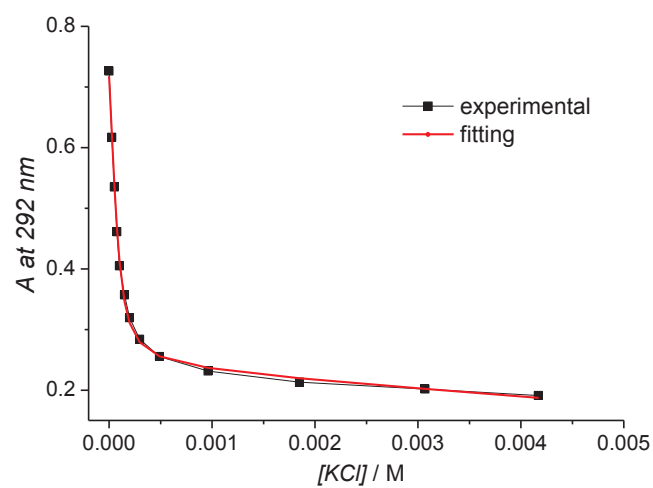
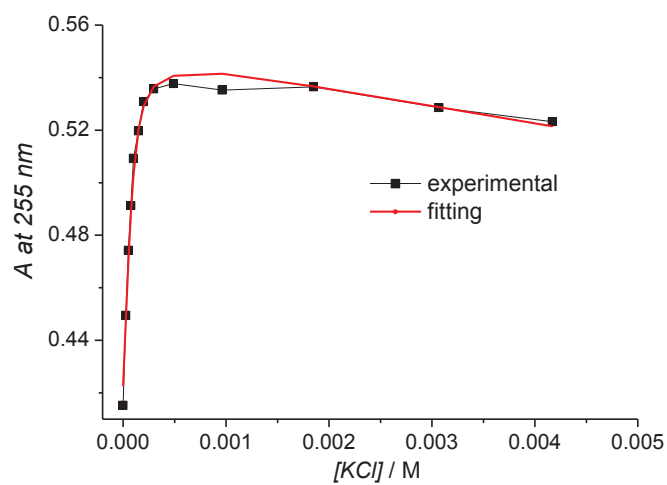
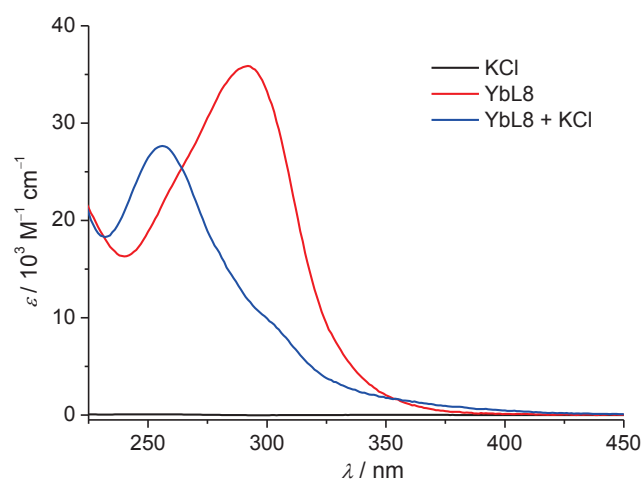
A.5. SPECFIT data (absorption titrations of YbL⁸)











Résumé français

Grâce à son excellente résolution spatiale et temporelle, l'imagerie par résonance magnétique (IRM) a pris une importance considérable parmi les techniques d'imagerie biomédicale et de diagnostic. Cette technique non invasive permet d'observer avec une précision de l'ordre du millimètre les tissus biologiques du corps humain. Elle est basée sur le phénomène de la résonance magnétique nucléaire des noyaux d'atomes d'hydrogène. Ce sont en particulier les protons de l'eau qui sont détectés et qui génèrent le contraste, étant donné que l'eau est le principal constituant des tissus biologiques. Le contraste des images peut être remarquablement accentué grâce à l'utilisation d'agents de contraste paramagnétiques, des complexes de gadolinium essentiellement, qui accélèrent la relaxation des protons de l'eau dans leur environnement. Ces agents sont principalement des agents T_1 et ont au moins une molécule d'eau coordonnée au centre métallique et qui est en échange permanent avec les molécules d'eau environnantes, permettant ainsi la propagation de l'effet paramagnétique et donc la diminution du temps de relaxation de l'ensemble des protons.

Lors de la conception de nouveaux agents de contraste, les efforts se concentrent souvent sur l'amélioration de l'efficacité de l'agent. Cette efficacité, définie comme étant la capacité à augmenter la vitesse de relaxation des spins nucléaires environnants par unité de concentration du complexe, est nommée relaxivité et est définie par l'équation suivante :

$$\frac{1}{T_{1,obs}} = \frac{1}{T_{1,d}} + r_1[Gd^{3+}]$$

où $1/T_{1,obs}$ représente la vitesse de relaxation observée et $1/T_{1,d}$ est la vitesse de relaxation diamagnétique qui correspond à la vitesse de relaxation du solvant en absence de l'agent paramagnétique. La relaxivité se situe autour de $4 \text{ mM}^{-1}\text{s}^{-1}$ à 20 MHz (0,5 T) pour les agents de contraste commerciaux.

La relaxivité peut être modulée principalement par les variations du nombre de molécules d'eau coordonnée aux lanthanides, de la vitesse d'échange de ce(s) molécule(s) d'eau avec le

solvant ou du temps de corrélation rotationnel, temps qui caractérise la rotation du complexe sur lui-même.

Ces dernières années ont vu l'émergence d'une nouvelle génération d'agents de contraste, plus spécifiques, pour l'imagerie moléculaire. En particulier, les agents dits « intelligents », ont pour but la visualisation, de façon non-invasive et en temps réel, des changements de facteurs impliqués dans divers processus biologiques ou pathologiques, tels que la concentration en métal, le pH ou l'activité enzymatique. Ces sondes « intelligentes » doivent reporter l'évènement moléculaire visé, en apportant une réponse magnétique via des changements dans la relaxivité du complexe de Gd^{3+} .

D'autre part, l'imagerie bimodale IRM/optique offre l'avantage de combiner l'excellente résolution de l'IRM à la haute sensibilité de l'imagerie optique pour un même agent chélateur. La chimie de coordination des lanthanides se trouve au cœur de cette approche, grâce à leurs excellentes propriétés magnétiques et optiques, d'autant plus que leur similarité chimique permet la substitution d'un Ln^{3+} par un autre sans modifier les propriétés intrinsèques des complexes. Comme cela a été dit précédemment, les complexes de Gd^{3+} sont les plus couramment utilisés en tant qu'agents de contraste pour l'IRM, alors que d'autres lanthanides(III) luminescents sont utilisés pour l'imagerie optique. En effet, certains lanthanides sont capables d'émettre dans le visible ou dans le proche infrarouge. L'imagerie dans le proche infrarouge a l'avantage d'être compatible avec les applications biologiques et il est donc toujours préférable de développer des agents luminescents émettant dans cette région plutôt que dans le visible.

Dans ce travail, nous nous sommes intéressés à la synthèse de complexes de lanthanides sensibles aux neurotransmetteurs (NTs) ainsi qu'à leur caractérisation *in vitro* en vue d'une application en IRM et en imagerie optique. Etant donné l'importance des neurotransmetteurs et leur implication dans les fonctions cognitives et comportementales, leur détection non-invasive *in vivo* est d'un intérêt crucial pour la compréhension de celles-ci.

Dans une première partie de ce travail, une première série de complexes de Ln^{3+} a été développée. Leur conception a été réalisée de manière à donner une réponse de type T_1 en

présence des NTs. Nous avons ciblé essentiellement les neurotransmetteurs aminoacides : l'acide γ -aminobutyrique (GABA), glycine, glutamate et aspartate. Ils constituent le groupe majeur au niveau du système nerveux central et se trouvent à des concentrations de l'ordre de micro- au millimolaire, plus faciles à détecter par l'IRM. De plus, ils ont la caractéristique structurale d'être zwitterioniques, ce qui en fait des cibles intéressantes pour la construction de récepteurs ditopiques. C'est donc dans cette optique qu'ont été conçus les complexes macrocycliques LnL⁵⁻⁷ présentés dans le schéma 1. Ces complexes possèdent deux sous-unités macrocycliques destinées à former une interaction bivalente avec les NTs ; d'une part entre le carboxylate du NT et le complexe de Ln³⁺ positivement chargé et d'autre part entre la fonction amine du NT et le monoaza-éther couronne. Ce dernier est connu pour sa capacité à complexer l'ion ammonium primaire en ancrant le groupe -NH_3^+ dans sa cavité circulaire par trois liaisons hydrogène $^+\text{N-H}\dots\text{X}$ (X = O, N).

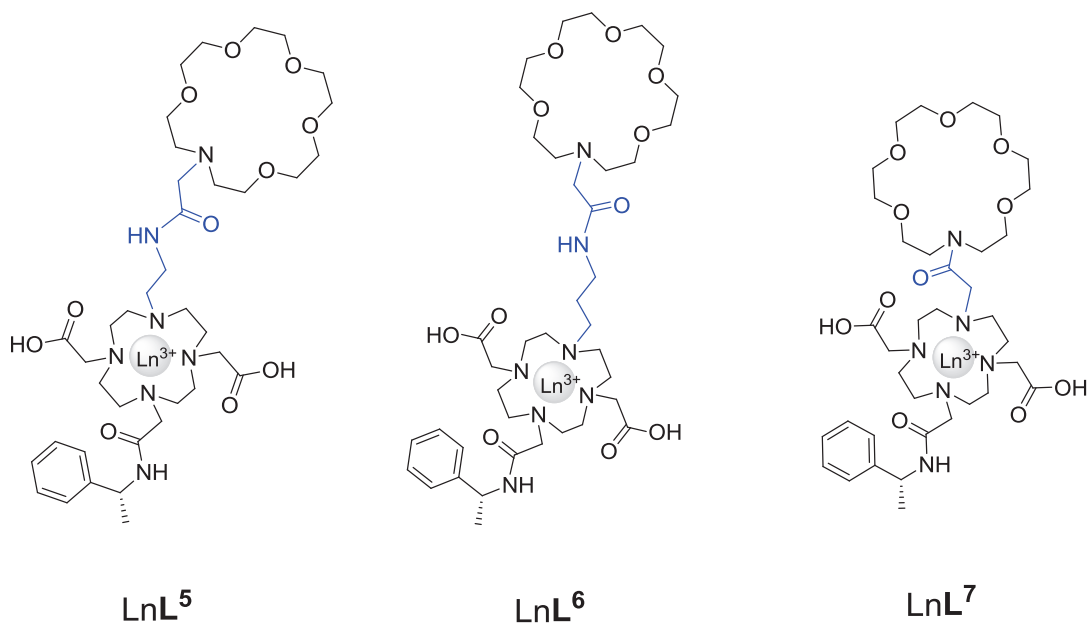


Schéma 1

Le concept général de détection est basé sur le fait que dans un état initial, un certain nombre de molécules d'eau se trouvent liées directement à l'ion lanthanide du complexe étudié. L'interaction d'un NT donné avec le complexe aura pour conséquence une diminution de ce nombre. Il en résulte un effet opposé, selon la nature du lanthanide étudié, consistant à

une baisse en termes de relaxivité pour l'IRM et une augmentation du signal de luminescence, dans le cas de l'imagerie optique.

La synthèse de ces complexes, ainsi que la caractérisation physico-chimique sont discutées au chapitre 2, où l'accent est mis sur les propriétés magnétiques et l'évaluation de changement de la relaxivité en présence des NTs. Ainsi, dans un premier temps, les temps de vie de luminescence du complexe Eu^{3+} et Tb^{3+} ont été mesurés dans l'eau et le D_2O et ont permis de mettre en évidence la présence d'une seule molécule d'eau dans la sphère de coordination de ces trois complexes.

Dans le but de déterminer les paramètres mis en jeu dans la relaxivité des complexes de Gd^{3+} , des mesures de temps de relaxation T_1 à différents champs magnétiques et températures ont été menées, complétées par des études RMN de l' ^{17}O à températures variables, ainsi que des mesures du déplacement chimique paramagnétique de l' ^{17}O . Ces dernières, étant proportionnels à la concentration en Gd^{3+} et à q , ont pu confirmer le nombre d'hydratation obtenu par les mesures de luminescence. Les complexes Gd^{3+} de L^5 , L^6 et L^7 ont présenté des relaxivités de 6.1, 7.7 et 4.4 $\text{mM}^{-1}\text{s}^{-1}$, respectivement, à 20 MHz et 37°C. L'analyse de l'ensemble des données expérimentales a été menée à l'aide de la théorie de Solomon-Bloembergen-Morgan et ont permis d'estimer les paramètres de relaxation microscopiques des trois complexes. En particulier, les valeurs calculées pour la vitesse d'échange d'eau confirment que les complexes GdL^5 et GdL^6 se situent dans la région d'échange rapide ($k_{\text{ex}}^{298} = 14.2 \times 10^6 \text{ s}^{-1}$ et $k_{\text{ex}}^{298} = 13.0 \times 10^6 \text{ s}^{-1}$, respectivement), alors que le GdL^7 est dans la région d'échange lent ($k_{\text{ex}}^{298} = 0.7 \times 10^6 \text{ s}^{-1}$).

Pour démontrer l'utilité de ses complexes comme agents « intelligents », leurs relaxivités en fonction de la concentration en divers NTs ont été mesurées à 60 MHz et 37°C dans l'HEPES. Aucune influence sur la relaxivité du complexe GdL^7 n'est observée. En revanche, GdL^5 et GdL^6 ont montré un profil de réponse relativement similaire avec une diminution de relaxivité allant jusqu'au 75% en présence des NTs α -amino-acides, dans la gamme de concentrations millimolaires. Une diminution peu significative est mesurée en présence de l'acétylcholine, qui n'est pas un amino-acide. Toutefois, les complexes GdL^5 et GdL^6 s'avèrent aussi sensibles vis-à-

vis du bicarbonate, un anion endogène présent à des concentrations de l'ordre de 20-25 mM *in vivo*.

Le mécanisme de diminution de relaxivité en présence de NTs a été étudié grâce à la mesure de temps de vie de luminescence des complexes de TbL⁵ ainsi que celle de changement de l'intensité du signal luminescence en présence de la glycine. Elles ont démontré que le nombre de molécules d'eau dans la sphère interne diminue effectivement en présence de NTs, dû à l'interaction du groupement carboxylate avec le centre métallique. D'un autre côté, des études de RMN ¹H et 2D-HSQC menées sur le complexe ternaire YL⁵-glutamate n'ont pas permis de conclure quant à l'existence d'interaction entre l'éther couronne et le groupe ammonium du NT.

Etant donnés ces résultats très encourageants obtenus avec les ligands L⁵ et L⁶, l'objectif était ensuite d'envisager des modifications structurales sur le ligand L⁶ en vue d'améliorer ce système. Ainsi, le chapitre 3 porte principalement sur la description de ces améliorations.

Dans une première partie de ce chapitre, une sonde sensible à la présence NTs est présentée, pour laquelle les conditions IRM et de luminescence ont été satisfaites, tout en utilisant un même ligand (L⁸, schéma 2). Compte-tenu de ses propriétés optiques intéressantes, et de sa longueur d'onde d'excitation relativement grande, la benzophénone a été incorporée dans la structure pour sensibiliser l'émission des lanthanides. En particulier, vu l'intérêt du domaine du proche infrarouge pour l'imagerie optique, l'objectif était surtout de sensibiliser les ions Nd³⁺ et Yb³⁺. Ainsi, le ligand L⁸ a été complexé aux lanthanides Gd³⁺, Eu³⁺, Yb³⁺ et Nd³⁺ afin de déterminer leurs propriétés magnétiques et optiques.

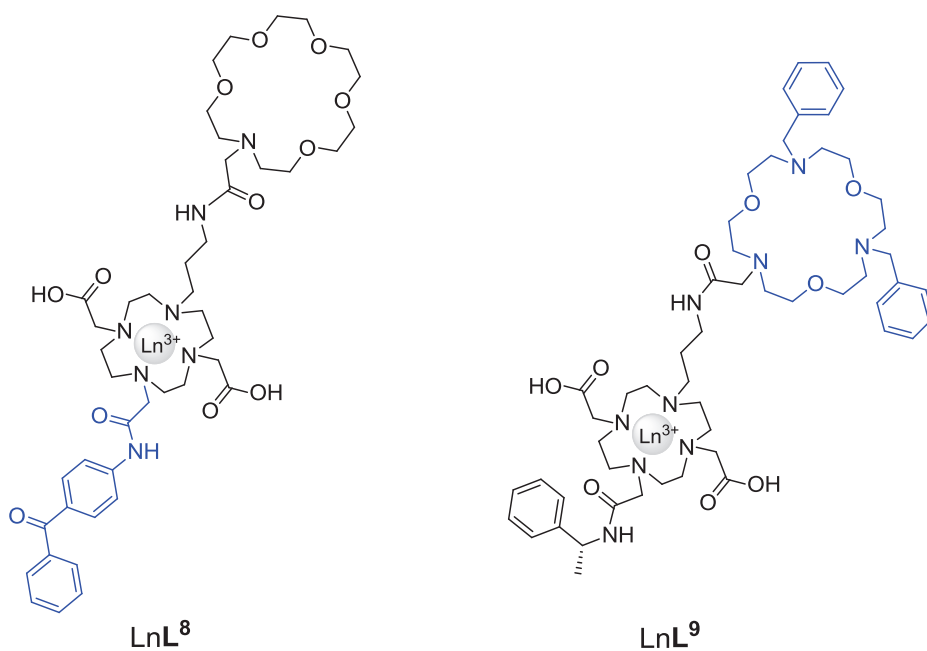


Schéma 2

La relaxivité observée de GdL⁸ est de 6.7 mM⁻¹s⁻¹ à 300 MHz et 37°C, comparé à 7.8 mM⁻¹s⁻¹ dans le cas du GdL⁶ dans les mêmes conditions. Des études de RMN ¹⁷O menées sur le complexe GdL⁸ ont permis de déterminer les paramètres de relaxivité et ont notamment montré que le complexe GdL⁸ a une vitesse d'échange d'eau moins rapide ($k_{ex}^{298} = 5.1 \cdot 10^6 \text{ s}^{-1}$) en comparaison avec celle du complexe GdL⁶ ($k_{ex}^{298} = 13.0 \cdot 10^6 \text{ s}^{-1}$). Ceci peut être justifié par l'effet stérique du motif benzophénone. En plus, les mesures relaxométriques du GdL⁸ en présence de neurotransmetteurs ont montré que l'introduction du motif benzophénone a eu pour effet la diminution de l'affinité pour les NTs vis-à-vis du bicarbonate.

La capacité de la benzophénone à sensibiliser les lanthanides Eu³⁺, Nd³⁺ et d'Yb³⁺ a été prouvée par les spectres d'excitation des complexes montrant un maximum autour de 300 nm, attribué à la benzophénone. Lorsque ces complexes sont soumis à une excitation à cette longueur d'onde, nous avons constaté l'émission caractéristique dans le visible pour le complexe d'Eu³⁺ et dans le proche-infrarouge pour les complexes de Nd³⁺ et Yb³⁺. De plus, les rendements quantiques observés pour les deux derniers sont du même ordre de grandeur que ceux reportés dans la littérature.

Afin d'étudier l'influence des neurotransmetteurs sur la luminescence du complexe LnL⁸, des spectres de luminescence ont été enregistrés en fonction de leur concentration, ainsi que celle du bicarbonate. Nous avons constaté, sur le complexe d'Eu³⁺, une augmentation significative de la luminescence en présence de NTs. Cependant, cette augmentation s'est révélée être plus importante dans le cas du bicarbonate. Ces résultats concordent avec ce qui a été observé dans les études relaxométriques. Par conséquent, ce changement de luminescence peut être corrélé à la diminution du nombre d'hydratation, comme il a été vu précédemment avec les complexes GdL⁵⁻⁶. En outre, le complexe d'Yb³⁺ s'est révélé aussi très sensible aux NTs et au bicarbonate dans le proche infra-rouge. Cependant, et contrairement à ce qui était attendu, le complexe de Nd³⁺ s'est avéré sensible uniquement au bicarbonate. Une telle différence peut être attribuée au fait que le déplacement des oscillateurs O-H de la molécule d'eau lié au métal est compensé par les oscillateurs C-H des neurotransmetteurs dont l'effet est probablement non négligeable au point d'avoir un impact sur le photo-blanchiment de la luminescence de Nd³⁺.

Par ailleurs, l'émission des Yb³⁺ et Nd³⁺ a été observée également en présence de potassium (K⁺). Celui-ci a présenté un effet similaire aux neurotransmetteurs sur le complexe d'Yb³⁺, alors qu'il n'y a pas eu de changement dans le cas de Nd³⁺. Etant donné que le K⁺ se complexe seulement au niveau de l'éther couronne, et donc il n'entraîne pas de changement d'hydratation, il a été suggéré qu'un processus de transfert d'électron photoinduit se produit de la paire électronique libre de l'azote de l'éther couronne vers l'ion Yb³⁺. En conséquence, ce postulat laisse suggérer aussi que, dans le cas particulier d'Yb³⁺, l'augmentation de l'intensité de l'émission en présence de NTs pourrait être due aussi, en plus de la diminution du nombre d'hydratation, à l'inhibition du phénomène PET entraîné par à une éventuelle interaction de l'ammonium avec l'éther couronne.

En outre, ce comportement distinct des Nd³⁺ et Yb³⁺ permettra la mise en place d'une méthode ratiométrique afin d'éliminer la dépendance de la concentration de complexe. L'utilisation d'un mélange des complexes Yb³⁺ et Nd³⁺ produit un effet qui est fonction du ratio de concentration des deux complexes et qui est proportionnel à concentration de NTs.

Parallèlement à l'élaboration du chélateur L^8 , le ligand L^9 (figure 2) a été aussi synthétisé dans le but d'améliorer l'affinité pour les NTs. Etant donné que le monoaza-éther couronne présente une bonne sélectivité pour le K^+ vis-à-vis de l'ammonium primaire, nous avons envisagé de le remplacer par un triaza-éther couronne ayant une sélectivité prononcée en faveur du cation $-NH_3^+$ par rapport au K^+ dans le but de renforcer l'interaction bivalent avec les NTs.

La relaxivité mesurée pour le complexe GdL^9 est de $8.8 \text{ mM}^{-1}\text{s}^{-1}$ à 300 MHz et 37°C , comparé à $7.8 \text{ mM}^{-1}\text{s}^{-1}$ pour le complexe GdL^6 dans les mêmes conditions. Il donne aussi lieu à une vitesse d'échange rapide ($k_{ex}^{298} = 11.8 \times 10^6 \text{ s}^{-1}$) proche de celle de GdL^6 . Les variations de relaxivité de GdL^9 , en présence des NTs, ont permis de constater que l'affinité pour les NTs s'était remarquablement améliorée en comparaison de celle de GdL^6 , mais il ne reste pas moins sélectif vis-à-vis du bicarbonate.

En conclusion, ces composés constituent une classe de sondes IRM et optiques ayant des propriétés relaxométriques intéressantes (relaxivités élevées et vitesse d'échange rapide) et ouvrent donc de nouvelles perspectives dans le développement d'agents bimodaux sensibles aux neurotransmetteurs. Par ailleurs, le complexe de Ln^{3+} à motif benzophénone a montré des résultats très encourageants en termes de propriétés optiques. Néanmoins, l'objectif d'en faire des sondes sélectives n'a pas été atteint et donc certaines améliorations peuvent être envisagées dans cette direction.

Fatima Oukhatar

Curriculum Vitae

Personal Information

Address: 3 Chemin des Pinsons, 31120 Portet sur Garonne

E-mail: Fatima.oukhatar@hotmail.com

Date of birth : 12-01-1981

Education

Since 2008 University of Orléans, France & Max Planck Institute of Tübingen (Germany)

Ph.D. candidate, Physico-Chemistry of Living and Biological Systems

Max Planck Institute fellowship

2007-2008 Joseph Fourier University, Grenoble

MSc. in Bio-Organic & Bio-Inorganic Chemistry

2005-2006 Paul Sabatier University, Toulouse

MSc. in Molecular Chemistry

Research Experience & Training

Since 2008, PhD thesis

Centre de Biophysique Moléculaire UPR 4301, Orléans, France

& Max-Planck Institute for Biological Cybernetics, Tübingen, Germany

- Project: Design, synthesis and evaluation of neurotransmitter responsive probes for magnetic resonance and optical imaging.
- Supervisors: Dr. Eva Jakab toth & Prof. Nikos Logothetis

January – June 2008, Master thesis

Département de Chimie Moléculaire UMR 5250, Grenoble

- Project: Synthesis and *in vitro* evaluation of fluorescent proflavine derivatives as imaging agents of amyloid fibril formation.
- Supervisor : Dr. Sabine Chierici

January-May 2006, Master thesis

Laboratoire d'Hétérochimie Fondamentale et Appliquée, Toulouse

- Project: Synthesis of trifluoromethyl O-carboxy anhydrides and their application as chiral derivatizing agents for assignment of configuration by ^1H and ^{19}F NMR spectroscopy.
- Supervisors: Dr. Didier Bourissou & Prof. Blanca Martin-Vaca

April - June 2005, Trainee

Laboratoire des Aminoacides Peptides et Protéines, Montpellier

- Project: Solid-phase synthesis of enzyme inhibitors peptides
- Supervisor: Dr. Jean-François Hernandez

Abstracts

- **March 2011, Torino (Italy).** Oral presentation “MRI Contrast Agents for Sensing Neurotransmitters”, COST Action D38 Metal-Based Systems for Molecular Imaging Applications, ,
- **September 2011, San Diego (USA).** Poster “MRI Responsive Contrast Agents: Towards Sensing and Imaging of Neurotransmitters”, World Molecular Imaging Congress.

Publications

- Dominique Garin, Fatima Oukhatar, Andrew B Mahon, Andrew C Try, Michel Dubois-Dauphin, Frank M Laferla, Martine Demeunynck, Marcelle Moulin Sallanon, Sabine Chierici, **“Proflavine derivatives as fluorescent imaging agents of amyloid deposits”**, *Bioorganic & medicinal chemistry letters*. **2011**, 21(8), 2203-6.
- Olivier Thillaye du Boullay, Aurélie Alba, Fatima Oukhatar, Blanca Martin-Vaca and Didier Bourissou, **“(1-Naphthyl)(trifluoromethyl) O-Carboxy Anhydride as a Chiral derivatizing Agent: Eclipsed Conformation Enforced by Hydrogen bonding”**, *Organic Letters*, **2008**, 10 (20), 4669-4672

Languages

Arabic (native), French (fluent), English (advanced level), German (Basic knowledge, level A2)

References

- **Dr. Éva JAKAB TÓTH**
Centre de Biophysique Moléculaire, CNRS, Orléans, France
eva.jakabtoth@cns-orleans.fr
+33 (0)2 38 25 76 25
- **Dr. Didier BOURISSOU**
Laboratoire d’Hétérochimie Fondamentale et Appliquée
Toulouse, France
dbouriss@chimie.ups-tlse.fr
+33 (0)5 6155 7737
- **Martine DEMEUNYNCK**
Département de Pharmacochimie Moléculaire, Grenoble, France
martine.demeunynck@ujf-grenoble.fr
+33 (0) 4 76 63 53 14

Fatima Oukhatar

Conception, Synthèse et Caractérisation de Sondes IRM et Optiques Sensibles aux Neurotransmetteurs

Résumé:

Malgré le rôle primordial des neurotransmetteurs (NTs) dans le système nerveux central, leur détection non-invasive *in vivo* reste un défi majeur. L'imagerie par résonance magnétique (IRM), grâce à son excellente résolution spatiale et temporelle, est parmi les techniques de diagnostic les plus performantes. Elle est au centre des développements récents en imagerie moléculaire. En particulier, l'utilisation des agents d'imagerie intelligents qui sont capables de visualiser le statut physico-chimique des tissus commence à avoir une place importante en neuroscience.

Cette étude a pour objectif de concevoir, synthétiser et caractériser *in vitro* des sondes intelligentes à base de cations lanthanide pour la détection *in vivo* des NTs. La conception de nos sondes est basée sur des interactions doubles avec des neurotransmetteurs zwitterioniques: d'une part entre le complexe de Ln^{3+} positivement chargé et le carboxylate du NT et d'autre part entre un ether couronne lié au complexe et la fonction amine du NT.

Plusieurs des sondes synthétisées présentent des relaxivités élevées et ont une réponse relaxométrique remarquable aux NTs, bien que leur sélectivité vis-à-vis de l'ion bicarbonate ne soit pas suffisante. Afin de développer des sondes pour une approche bimodale IRM /optique, nous avons également intégré dans les complexes une benzophenone qui joue le rôle de chromophore pour sensibiliser la luminescence des ions Ln^{3+} émettant dans le proche infra-rouge. Le complexe d' Yb^{3+} correspondant a des propriétés de luminescence très intéressantes avec une forte réponse aux NTs.

Mots clés: lanthanides, IRM, neurotransmetteurs, sondes « intelligentes » d'imagerie, luminescence, imagerie optique

Design, Synthesis and Characterization of Neurotransmitter Responsive Probes for Magnetic Resonance and Optical Imaging

Summary:

In spite of the key role of neurotransmitters (NTs) in signal transduction, their non-invasive *in vivo* monitoring remains an important challenge. Magnetic resonance imaging (MRI) has recently been demonstrated as a promising technique to non-invasively visualize physiological events with excellent temporal and spatial resolution. In particular, smart MRI contrast agents that are able to report on the physico-chemical status of the tissues, start to have a strong impact in neuroscience.

The objective of this work was the design, synthesis and *in vitro* characterization of a series of lanthanide-based probes responsive to NTs with the aim to track *in vivo* concentration changes of NTs using MR or optical imaging. The design of our imaging probes relies on a dual binding approach of zwitterionic NTs to the Ln^{3+} complexes, involving interactions (i) between a positively charged Ln^{3+} chelate and the carboxylate function of the NTs and (ii) between an azacrown ether appended on the chelate and the amine group of the neurotransmitters.

Some of the novel contrast agents were found to exhibit high relaxivities and a remarkable relaxivity response towards NTs, though little selectivity against bicarbonate. In order to apply a bimodal MRI/optical imaging approach, we have also incorporated a benzophenone moiety into the chelate to sensitize the near-infrared emitting Ln^{3+} ions. The Yb^{3+} analogue proved to be highly sensitive to NTs.

Keywords: MRI, smart contrast agents, neurotransmitters, lanthanide, luminescence, optical imaging.



Centre de biophysique moléculaire, CNRS,
Rue Charles Sadron, 45071 Cedex 2 Orléans, France

Max Planck Institute for Biological Cybernetics,
Tübingen, Allemagne

